University of Warsaw

Doctoral Thesis

Multimode Quantum Optics with Spin Waves and Photons

Author:
Michał Parniak

Supervisor:
dr hab. Wojciech Wasilewski

Faculty of Physics

January 2019

Abstract

Multimode Quantum Optics with Spin Waves and Photons

The thesis describes the development of a multimode quantum memory based on laser-cooled gas of rubidium atoms. Starting with the construction of a magneto-optical trap we arrive at implementations of complex quantum protocols realized within the domain of spin waves stored in the memory, with the main achievement being the realization of a spin-wave analogue of the Hong-Ou-Mandel effect.

In Chapter 2 I introduce the theoretical framework needed to plan experiments and explain their results. The theory serves us in designing new protocols based on the ac-Stark effect and phase matching. A full quantum treatment of the light-atom interaction is also presented, with a particular focus on a quantized collective atomic excitations field.

Chapter 3 describes the essential and most innovative parts of the constructed experimental setup.

Chapter 4 presents the quantum memory with the highest capacity achieved so far, based on the Raman light-atom interface. The memory stores light in 665 spatial modes. New experimental and data analysis methods are highlighted.

Chapter 5 introduces the ac-Stark modulation applied to control the collective spin of an atomic ensemble. The results are immediately used in Chapter 6, where the same effect is employed to control the spatial interference of single spin waves. Hong-Ou-Mandel two-particle interference for a pair of spin waves is demonstrated.

Chapter 7 presents a further development of the new control methods with a focus on a sequential quantum memory. The interference of pulses inside the memory stored at different times is demonstrated for the first time.

In Chapter 8 we use our deepened understanding to unveil a new approach to spin waves, where we use them as a pump in a parametric down-conversion process. This allows us to observe and control superradiant emission, for the first time in the case of six-wave mixing. This allows unprecedented control over the superradiant emission pattern in space.

The final Chapter 9 summarizes the thesis and proposed future path of development.

Streszczenie

Wielomodowa optyka kwantowa fal spinowych i fotonów

Niniejsza praca przedstawia rozwój wielomodowej pamięci kwantowej opartej na chłodzonym laserowo gazie atomów rubidu, począwszy od konsturkcji samej pułapki magnetooptycznej aż do implementacji złożonych protokołów kwantowych na przechowywanych w pamięci falach spinowych i zademonstrowania analogu interferencji Hong-Ou-Mandla dla dwóch fal spinowych.

W Rozdziale 2 prezentuję warsztat teoretyczny niezbędny do planowania i wyjaśnania przeprowadzonych eksperymentów. Opracowana teoria służy do projektowania nowych protokołów w oparciu o dynamiczny efekt Starka (ac-Stark) i dopasowanie fazowe. Przedstawiam też w pełni kwantowych opis oddziaływania, ze szczególnym uwzględnieniem opisu pojedycznych kolektywnych wzbudzeń - fal spinowych.

Rozdział 3 opisuje powstały układ doświadczalny, skupiając się na najbardziej innowacyjncyh elementach.

Rozdział 4 prezentuje opis najpojemniejszej na chwilę obecną pamięci kwantowej dla światła, działającej w oparciu o interfejs ramanowski. Zaprezentowana pamięć przechowuje światło w 665 modach przestrzennych. Szczegółowo opisane są nowe metody doświadczalne i analizy danych.

Rozdział 5 opisuje nowy sposób uzyskania kontroli nad kolektywnym spinem zespołu atomów dzięki dynamicznemu efektowi Starka. Wyniki są zastosowane w Rozdziale 6, gdzie kontrolujemy przesztrzenną fazę pojedynczych fal spinowych. Udaje się zademonstrować dwucząstowkową interferencję fal spinowych prowadzącą do ich „sklejenia”, jak w efekcie Hong-Ou-Mandla dla fotonów.

Rozdział 7 prezentuje rozwój tej nowej metody i jej zastosowanie do realizacji pamięci sekwencyjnej. Po raz pierwszy też demonstrujemy interferencję impulsów światła zapisanych do pamięci w różnych momentach.

W Rozdziale 8 opisuję inne podejście do nowych zastosowań fal spinowych, gdzie używamy odpowiednio przygotowanej spójności atomowej do kontroli nadpromienistości. Obserwujemy znaczny efekt nadpromienistego wzmocnenia emisji, po raz pierwszy w procesie mieszania sześciu fal, który dzięki pośredniczącej fali spinowej zapewnia nam niespotykaną do tej pory kontrolę.

Wreszcie rozdział 9 podsumowuje pracę i proponuje dalsze kierunki rozwoju.

Acknowledgements

The accomplishment of the research presented in this thesis wouldn't be possible without a team effort of the entire Quantum Memories Laboratory. I would like to thank the entire team for the joint work, effort and for the creation of an unprecedented place that allows for one to self-develop in a very pleasant way. The team particularly relevant to the quantum memory includes Michał Dąbrowski, Adam Leszczyński, Mateusz Mazelnik and Michał Lipka. I also thank others involved in many projects around, including Radek Chrapkiewicz, Michał Jachura, as well as the newest members of the team, Sebastian Borówka and Kajetan Boroszko. I also gratefully acknowledge the support of our technical and administrative staff: Jarek Iwaszkiewicz, Tomek Kowalczyk, Karol Kosiński, Marek Trzaskowski, Janusz Grochowski, Janusz Rogoziński, Piotr Zbińkowski and Halina Przychodzeń.

Very particular thanks go to Mateusz, with whom I have spent countless hours in the lab, building countless new setups, developing a plethora of software, conceptualizing quite crazy stuff, but also talking about the life of a physicist... I hope that we can this fruitful friendship and scientific collaboration.

With many of the above-mentioned fellow students, we have been participating in the actions of our students' Optics & Photonics society "KNOF". Others with whom I had the pleasure to work with and attend student conferences include (yet are not limited to): Janek Szczepanek, Aleksander Bogucki, Justyna Piwowar, Michał Nawrot, Łukasz Zinkiewicz, Gosia Zinkiewicz and Piotrek Węgrzyn.

On the senior side, I would like to thank the mentors that have led me through my studies from the very beginning. In particular, I greatly benefited from my first lab experiences with prof. Czesław Radzewicz and Piotr Fita, and later instruction from Piotr Wasylczyk. In 2013 I also had the pleasure to benefit from working through the summer in the group of prof. Morgan W. Mitchell in ICFO, to whom I am grateful for this wonderful opportunity.

In most recent years I had the pleasure to initiate a theoretical collaboration with Konrad Banaszek and Rafał Demkowicz-Dobrzański, who have both instructed me also in the early years. I am grateful for their continuing support through our joint project.

Through the years I also shared scientific discussions with many individuals during meetings, conferences, seminars etc... I would like to especially acknowledge Janek Kołodyński, Krzysztof Kaczmarek, Lukáš Slodička (during my visit in Olomouc and his visit in Warsaw), Josh Nunn, Anthony Leung (during a conference in Hong Kong) and Pau Farrera (during conferences and my visit in ICFO).

The last but not least scientific thanks are devoted to Wojtek, who has been my advisor since 2012. Thank you for spending countless hours and significant effort of teaching me both the core physicists' skills as well as those more soft or volatile. I also gratefully acknowledge all our discussions unrelated to physics, as

well as those related to our scientific roles in this world. I hope we can take these experiences boldly into the future.

Special thanks finally go to my friends with whom we have “destroyed” many problems during our undergraduate and master studies, in particular, Michał Papaj, Tomek Maciążek and Rafał Ołdziejewski (with all of whom I still share regular “executive board” meetings), but also Mateusz Machalica, Maciek Ciemny, and many others.

The conducted work would not, however, be worth it without the continuing support of all my friends, including Filip Król, Piotr Kwiatkowski, Tomek Kubrak & Asia Król.

Finally, I thank my parents for the continuing support during all my education and work.

Funding information. My work through this thesis has been funded by the National Science Centre, Poland (NCN) OPUS grant No. 2016/21/B/ST2/02559 of my supervisor and the PRELUDIUM grant No. 2017/25/N/ST2/01163 I received in 2018. An essential funding source has been provided by the Polish Ministry of Science and Higher Education (MNiSW) “Diamentowy Grant” No. DI2013 011943 I received in 2014. I have been supported by the Foundation for Polish Science, co-financed by the European Union under the European Regional Development Fund, as a part of the “Quantum Optical Communication System” project carried out within the TEAM programme (led by prof. Konrad Banaszek).

List of Publications

Main papers:

1. **M. Parniak**†, M. Dąbrowski, M. Mazelanik, A. Leszczyński, M. Lipka, W. Wasilewski, ”Wavevector-multiplexed quantum memory via spatially-resolved single-photon detection", Nature Communications **8**, 2140 (2017), [Par17]
2. A. Leszczyński, M. Mazelanik, M. Lipka, **M. Parniak**†, M. Dąbrowski, W. Wasilewski, "Spatially-resolved control of fictitious magnetic fields in a cold atomic ensemble", Optics Letters **43**, 1147 (2018), [Les18]
3. **M. Parniak***†, M. Mazelanik*, A. Leszczyński, M. Lipka, M. Dąbrowski, W. Wasilewski, "Quantum Optics of Spin Waves Through Ac-Stark Modulation", arXiv:1804.05854, provisionally accepted in *Physical Review Letters* [Par18c]
4. M. Mazelanik*, **M. Parniak***†, A. Leszczyński, M. Lipka, W. Wasilewski, "Coherent spin-wave processor of stored optical pulses", arXiv:1808.00927, accepted in *npj Quantum Information*, [Maz18]
5. M. Mazelanik, A. Leszczyński, M. Lipka, W. Wasilewski, **M. Parniak**, "Spin-wave control of spatial single-photon superradiance", in preparation

Related papers:

6. **M. Parniak**†, A. Leszczyński, W. Wasilewski, "Magneto-optical polarization rotation in a ladder-type atomic system for tunable offset locking", Applied Physics Letters **108**, 161103 (2016), [PLW16b]
7. M. Lipka, **M. Parniak**, W. Wasilewski, "Optical Frequency Locked Loop for long-term stabilization of broad-line DFB lasers frequency difference", Applied Physics B **123**, 238 (2017), [LPW17b]
8. M. Lipka, **M. Parniak**, W. Wasilewski, "Microchannel plate cross-talk mitigation for spatial autocorrelation measurements", Applied Physics Letters **112**, 211105 (2018), [LPW18]
9. A. Leszczyński, **M. Parniak**†, W. Wasilewski, "Phase matching alters spatial multiphoton processes in dense atomic ensembles", Optics Express **25**, 284 (2017), [LPW17a]

10. M. Dąbrowski, M. Mazelanik, **M. Parniak**, A. Leszczyński, M. Lipka, W. Wasilewski, "Certification of high-dimensional entanglement and Einstein-Podolsky-Rosen steering with cold atomic quantum memory", Physical Review A **98**, 042126 (2018), [Dąb18]
11. M. Lipka, A. Leszczyński, M. Mazelanik, **M. Parniak**, W. Wasilewski, "Spatial spin-wave modulator for quantum memory assisted adaptive measurements", submitted

Not related to this thesis:

12. **M. Parniak**†, S. Borówka, K. Boroszko, W. Wasilewski, K. Banaszek, R. Demkowicz-Dobrzański, "Beating the Rayleigh Limit Using Two-Photon Interference", Physical Review Letters **121**, 250503 (2018), [Par18b]
13. **M. Parniak**†, W. Wasilewski, "Interference and nonlinear properties of four-wave-mixing resonances in thermal vapor: Analytical results and experimental verification", Physical Review A **91**, 023418 (2015), [PW15]
14. **M. Parniak**†, A. Leszczyński, W. Wasilewski, "Coupling of four-wave mixing and Raman scattering by ground-state atomic coherence", Physical Review A **93**, 053821 (2016), [PLW16a]
15. **M. Parniak**†, D. Pęcak, W. Wasilewski, "Multimode Raman light-atom interface in warm atomic ensemble as multiple three-mode quantum operations", Journal of Modern Optics **63**, 2039 (2016), [PPW16]
16. **M. Parniak**†, W. Wasilewski, "Direct observation of atomic diffusion in warm rubidium ensembles", Applied Physics B **116**, 415 (2014), [PW14]
17. M. Dąbrowski, **M. Parniak**†, W. Wasilewski, "Einstein-Podolsky-Rosen paradox in a hybrid bipartite system", Optica **4**, 272 (2017), [DPW17]

Equal contributions are denoted by *, while † denotes whether the author of this thesis is the corresponding author.

Contents

Chapter 1

Introduction

Technological development allows us to control effects explained only by quantum mechanics in more elaborate and intricate ways. The range of systems in which quantum effects are demonstrated now ranges from the purely optical systems where entanglement and quantum interference are rudimentary [Zho18] and allow even for loophole-free tests of quantum mechanics [Giu15], to the material systems such as mechanical membranes [Møl17], and simultaneously from the miniature systems such as single atoms [Lop15], spins [Aws18] or superconducting qubits [Son17] to the macroscopic atomic ensembles [Kra11] and large organic molecules [Ger11].

A challenge that remains is to control many of such system in a way precise enough to allow for quantum computation. Even with recent developments in superconducting systems [Kel18], it seems that such technology may still be quite distant.

An alternative is provided by photonic systems. Photons can travel fast along large distances with small losses which makes them great carriers of quantum information, especially at telecommunication wavelengths [Mar17]. The famous Duan-Lukin-Cirac-Zoller (DLCZ) protocol further stimulates many efforts by providing an option to efficiently distribute photonic entanglement [Dua01]. Even simplest quantum computation, however, requires us to interact two photons, which is a non-trivial condition, since photons generally do not interact strongly with each other. A certain solution has been proposed by Knill, Laflamme and Milburn [KLM01], who suggested using multi-photon *interference* to realize effective multi-qubit quantum gates.

Bosonic interference A simplest multi-photon quantum interference effect has been observed by Hong, Ou and Mandel [HOM87], and later greatly explored also in our group [WKF07; JC15; Jac16; Chr16b; Par18b]. In the so-called Hong-Ou-Mandel effect two photons meet at a 50:50 beamsplitter. Due to their indistinguishability and bosonic nature, they will always exit the beamsplitter via the same port. It thus might seem as if the photons actually interact. This inherently quantum two-particle effect serves as an important test of both nonclassicality of the input state as well as the proper operation of the beamsplitter. While nowadays it is easily achievable with photons, recent experiments or theoretical proposals considered similar quantum-interferometric properties of atoms [Kau14; Lop15; BYL18], phonons [Toy15; Hon17], plasmons [HKZ13; Fak14] and photons but in elaborate hybrid systems that involve photon sources of different kind [Jin13; Che15; Qia16; Hon17; Gao18; Vur18; Zop18; RZZK07; Hos11; DeR03]. Notably, the ability to achieve Hong-Ou-Mandel interference is a strong indication of a good control over the system, as it shows that the particles do show non-classical behaviour and that we control their indistinguishability. Demonstration of such interference is a fundamental accomplishment, providing insight into the nature of considered particle or quasi-particle.

This progress illuminates the perspective to combine linear operations, that have always been simple for photons, and nonlinear operations, that can be engineered in material systems. The quantum memory for light, where photons are stored in the form of collective atomic excitations is a good candidate for bedrock to realize this proposal facilitating both fundamental studies and applications in quantum networks.

This thesis demonstrates the two-particle interference of spin waves stored in a multimode, optically-interface quantum memory.

Optical quantum memories As optical quantum memory technologies mature, the the range of their applications increases. We can distinguish two particular modes of operation for an optical quantum memory. In the "emissive" memory we simultaneously generate and store light. The memory generates a two-mode squeezed state, for which one mode is emitted as light and the other mode remains stored in the memory. The stored mode can be retrieved at later times. Quite non-intuitively, such memory stores, in fact, random information generated by itself. As we will show, however, through this thesis, such protocol finds extensive applications.

The "absorptive" memory, on the other hand, can store an external state of light. The process of storage and subsequent retrieval is a beamsplitter transformation between light and the memory mode. It is thus inherently similar to the process of retrieval from emissive memory as well.

Basic memories operating in a single temporal and spatial mode can store only a single optical pulse, which may interfere with another incoming pulse. This operation can only be performed in the presence of the coupling light [Rei12]. Such memories, based either on Raman scattering or electromagnetically induced transparency (EIT), can achieve high efficiencies [VG18], but offer very limited capacity as multiplexing is limited by the number of atomic magnetic sublevels employed [Wan11; Lee14; VG18]. Photonic quantum networks, however, need to extensively utilize multiplexing techniques, exploring photonic spatial and temporal structure, to achieve high-performance [Lun11; Chr16b; Rei16; Mar17; Mun10]. Multimode

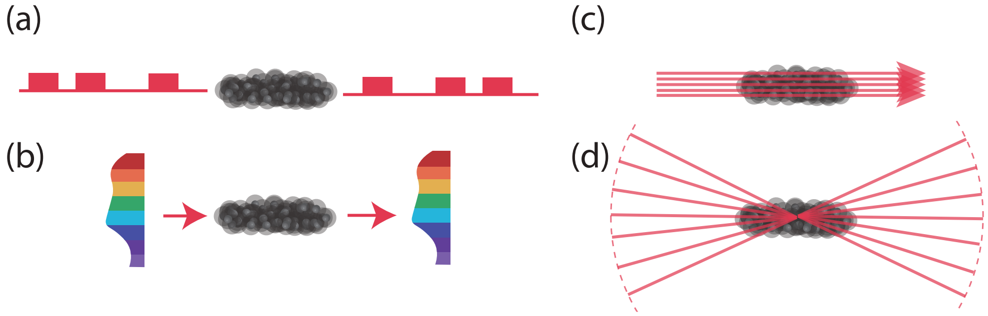

FIGURE 1.1: Various modes of multiplexing an atomic-ensemble quantum memory. Pulses can be stored sequentially as in (a), or we can rather choose spectral encoding of information in the same kind of memory, as in (b). The atomic ensemble can be separated into many small in independent ensembles to store many beams in parallel as in (c), or the same ensemble can store many angular modes (wavevectors), as in (d).

quantum memories, on which we consternate in this thesis [Din13; Pu17], can become part of such networks, but a requirement of implementing complex linear operations on stored excitations arises.

While a single atomic ensemble may be split into an array to offer parallel storage of light [Pu17], such a scheme hinders manipulations within the memory as communication between memory cells must be inherently light-based. It is thus highly desirable to independently store many optical pulses within the same group of atoms. Such a multiplexing scheme may utilize either the spatial [Din13] or temporal degree of freedom [Gün13; KMR17; Tir16]. In the latter case, considered in the context of the atomic-ensemble based quantum memories, the Gradient Echo Memory (GEM) [Nun08; Hos09; Hos11; Spa13; Alb15] scheme stands out as an efficient way to engineer the phase-matching at read-out stage to achieve mode-selective storage and retrieval. A similar feature is inherently offered by the atomic frequency comb (AFC) memories based on ensembles of ions in solids [KMR17; Gün13; Sin14] thanks to their large inhomogeneous broadening. In the spatial degree of freedom, atomic ensembles allow storage of light in many angular-emission modes through spin-wave wavevector multiplexing [Dai12], which we will demonstrate in this thesis. These schemes allow storage of hundreds of optical modes, also when used with non-classical states of light. In conclusion, multiplexing techniques can be either implemented in the spatial/angular domain or the temporal spectral domain, as illustrated in Fig. 1.1.

Processing of light in the memory Manipulation of stored optical pulses, however, remains a substantial challenge, both from technical and fundamental points of view. The AFC memory has been demonstrated to allow pre-programmed interference of two stored pulses with a single output port [Sin17; Sag14].

Most recently similar beamsplitter operations in the AFC memory have also been implemented in a multi-dimensional Hilbert space [Yan18]. Within the GEM scheme, a beamsplitter operation between pre-selected, stored pulses and an input pulse has been realized [Cam12; Cam14]. Remarkably, these schemes allow basic spectral and temporal manipulations of stored light. More work is needed however to reach the regime of efficient and arbitrary manipulations. In particular, the ac-Stark shift caused by an additional light field has been studies in optical-lattice based quantum memories [Dud10], as well as used and proposed as a versatile way to realize the GEM scheme [Spa10] and to control photon-echoes [CH15]. Recent theoretical proposals went beyond the simple gradient shape and suggested engineering the stored spin-wave shape to realize Kapitsa-Dirac diffraction [HGO15] or a quantum memory protected with a disordered password [Su17]. These schemes stand out in relation to an established all-optical technique of manipulating stationary light [BZL03] - since control light is not present during the manipulation process, decoherence is significantly reduced for stored light.

1.1 Introduction to multiplexing

While wavelength-division multiplexing is a well established technique, spatial-mode multiplexing in optical fibres or in free-space also emerges as an essential tool in modern techniques for high-throughput transmission [Wan12; RFN13]. Similarly, as quantum technologies mature, the necessity of multiplexing in photon-based quantum communication becomes clear [Mun10] and much effort is devoted to various schemes exploiting spatial [Sur08; Lan09; Dai12; Din13; Nic13; Par15; Lee16; Che16; DPW17] temporal [Cla10; Col13b; Hum14; Gün15; Cho16; Xio16] or spectral degrees of freedom. Utilization of many modes can finally allow efficient application of the Duan-Lukin-Cirac-Zoller (DLCZ) protocol [Dua01; Sim07; KMR17; Lap17] and offer nearly-deterministic generation of multi-photon states [Ma11; Nun13; CDW17] later applicable in quantum enhanced sensing technologies [Wol12; Mat16] as well as optical quantum computation [Kok07]. Regardless of substantial efforts, the task of achieving a large number of modes remains a challenging endeavour especially in hybrid atom-photon systems.

1.1.1 Temporal multiplexing

Here, as an example, we will recall three distinct schemes of temporally-multiplexed quantum memories. In particular, some quantum memories inherently support many temporal modes. One such example is a ring cavity with an active switching element[1]. Fig. 1.2 presents such a memory, where a train of H-polarized

---

[1] While we could also consider a passive cavity, or even a long optical fibre, to be a photonic quantum memory, the lack of control would eliminate such a solution from the applications considered in this work.

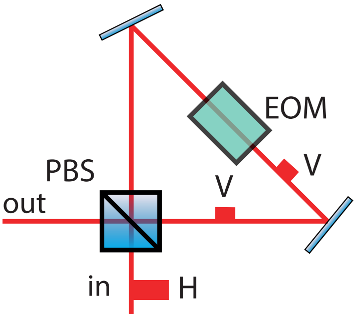

FIGURE 1.2: The temporally multiplexed optical memory based on a cavity. The electro-optic modulator (EOM) manages the memory by keeping the pulses circulating in the cavity or releasing them on demand.

pulses enters a cavity via a polarizing beamsplitter. After travelling through the cavity, the pulses enter through an orthogonal port of the beamsplitter. Normally, the pulses would immediately exit the cavity. Here we introduce an active element, in practice a Pockels cell or an electro-optic modulator, that can switch the polarization to orthogonal V polarization, so the pulses get reflected at the PBS. The pulses will remain in the cavity as long as the active element is switched again. It can be also switched selectively to allow picking of pulses at the stages of storage or release. In the simplest scenario, the maximal duration of the stored train of pulses roughly equals to the cavity-round trip t_r. The pulses can exit the cavity at integer multiples of t_r with an efficiency of η^{2k}, where η is the round-trip amplitude transmitivity (or $1-\eta$ is the round-trip loss). We may translate this relation to an exponential amplitude decay with the total storage time t of $\exp(t/t_r \ln(\eta))$. Note that $\ln(\eta) < 0$. The memory of that kind referred to as a *loop* quantum memory, has seen substantial developments in recent times. *Pang et al.* [Pan18] achieved $\eta = 0.9$ with lifetime reaching ~ 100 ns, while *Kaneda et al.* [Kan15] used a cavity with $\eta = 0.97$ and $t_r = 8.3$ ns. The latter cavity has been used to implement a multiplexed photon source - we will elaborate on that idea in our scheme in Sec. 4.1. The largest number of temporal modes used for photon source multiplexing in cavity-based quantum memory [Kan15] is 30.

Similarly as the above example, the *atomic frequency comb* memory inherently supports many temporal modes [Afz09]. The mechanism for that is, however, completely different. The memory uses an ensemble of ions that is subject to a strong inhomogeneous spectral broadening of the $|g\rangle \to |e\rangle$ transition. First, the ensemble is prepared via optical pumping (in that case called spectral hole burning) in a frequency comb state, which is a periodic structure of highly absorbing peaks with a frequency period Δ. A photon is then absorbed and the stored "spin wave" takes on a form:

$$\sum_{j}^{N} c_j e^{i\delta_j t - ikz_j} |g_1 \dots e_j \dots g_N\rangle. \tag{1.1}$$

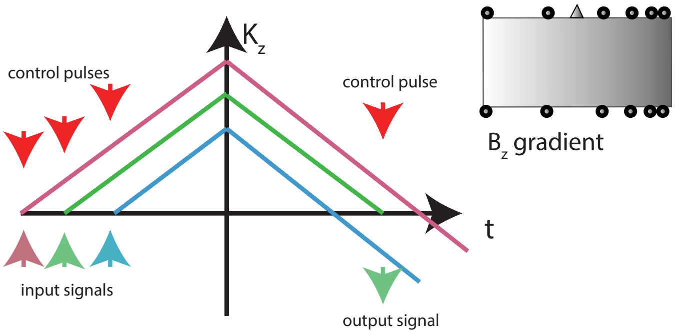

FIGURE 1.3: Gradient Echo Memory realizing a "conveyor belt" for stored optical pulses based on a gradient of magnetic field and an atomic vapour cell.

Since each atom features a different detuning δ_j from the resonance, the excitation is immediately dephased and phase-matched emission cannot occur. Due to the periodic structure, however, the excitation is rephased after the time $\tau = 1/\Delta$ and phase-matched read-out emission occurs. The coefficients c_n contain spectral amplitude and phase information about the input pulse, and thus a temporally-structured light (such as a train of pulses) may be stored. The number of stored temporal modes can be estimated as the ratio of the total bandwidth of inhomogeneous broadening and the peak separation Δ. The AFC memory has also been shown to store single photons (nonclassical light) emitted from distinct sources [Tan15] and serve as a temporally-multimode photon source in a slight modified, DLCZ-like scenario [KMR17; Lap17]. Using more levels one can also map the $|g\rangle \rightarrow |e\rangle$ excitation onto a ground-state spin wave to significantly prolong the memory lifetime.

Finally, *Gradient Echo Memory* (Fig. 1.3) uses the inhomogeneous broadening as well, yet it is induced artificially via a gradient of a longitudinal magnetic field. The scheme has been implemented in an atomic ensemble with a typical Λ level scheme [Hos09]. The memory engineers the phase of the stored atomic excitations to suppress emission from excitations that are phase-mismatched. In this thesis, we will explore the property of phase matching more thoroughly. Here, it is essential to understand that atomic excitation in form of a spin wave with a certain longitudinal wavevector K_z, i.e. $B \sim e^{iK_z z}$ facilitates emission for only a certain specific K_z. Thus if we change K_z by applying a gradient of a magnetic field that shifts the energy between levels associated with the coherence B, we may make the emission from a stored spin wave impossible.

With such scheme, it is then possible to store many pulses subsequently. Such a "conveyor belt" for optical pulses can then be retrieved upon reversing the gradient. It has been proposed to realize such memory using the ac-Stark effect [Spa10], which we will realize here in Chapter 7.

1.1.2 Spatial multiplexing

Multiplexing of spatial modes is a natural choice in many systems. In purely photonic, memoryless systems hundreds of modes have been obtained within the spatial domain of spontaneous parametric down-conversion (SPDC) [Edg12; MDL14; Kre14]. From the informational point of view, these experiments stand close to multimode photonic systems operating in the time-frequency domain [Ros13; Kan15; Xie15; Rei16; Xio16; Cai17]. However, most applications such as the DLCZ protocol [Dua01], enhanced photon generation [Nun13; CDW17; Kan17] or even linear optical quantum computing (LOQC) [Kok07] require or greatly benefit from a multimode quantum memory.

Spatial multiplexing can be thought of either in the real-space domain, where we consider photons' positions or in the wavevector domain, where we rather consider their momenta. An intermediate domain can be spanned by any set of orthogonal modes, such as Laguerre-Gauss mode that correspond to photonic angular momenta.

In quantum memories, an important trend is to build a multiplexed quantum repeater by splitting a trapped atomic ensemble into many cells [Lan09; Nun13]. The idea was recently realized in two dimensions achieving 225 modes [Pu17]. These schemes, however, suffer from the limitation given by difficulty in trapping large ensembles as well as hinder heralded simultaneous excitation of all modes. In consequence, they are rendered useful only for the DLCZ quantum repeater [Dua01] but neither for quantum imaging [Boy08; BGR10; Gen16] nor for enhancing rate of the photonic state generation [Nun13; Xio16; CDW17].

In this work, we will present new developments in wavevector multiplexing. We will demonstrate a quantum memory operating with 665 modes, and later also performing inter-modal operations and integrating temporal and spatial multiplexing. In particular, Sec. 4.7 discusses fundamental limitations on capacity, further also elaborated on in the temporal case in Chapter 7.

1.2 Contributions and development

The following section describes the historical perspective on the development of our quantum memory and constitutes rather a narrative story than a scientific text. Details will be best understood only after reading the remainder of the thesis. My contributions to all the results of this thesis and other research conducted along the way are listed.

The experiments we performed involved a number of individuals who contributed (either in a minor or major way) to the final result, either directly or by working out some methods in earlier experiments, including students and PhD students: Michał Parniak (MP), Radek Chrapkiewicz (RCh), Michał Dąbrowski (MD), Adam Leszczyński (AL), Michał Jachura (MJ), Mateusz Mazelanik (MM),

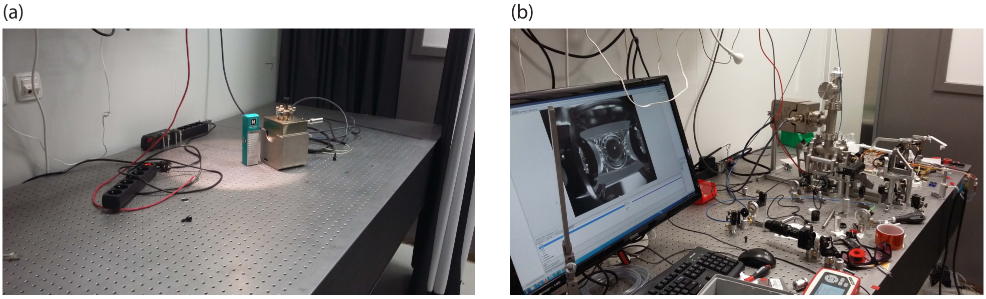

FIGURE 1.4: (a) The ion pump upon the first test run together with a box of grease given to us by M. Zawada. (b) The setup used to trap the first cloud of cold atoms, with the trapped atoms themselves, displayed on the monitor.

Michał Lipka (ML), Sebastian Borówka (SB), Kajetan Boroszko (KBo); technical support staff: Jarek Iwaszkiewicz (JI), Tomek Kowalczyk (TK), Karol Kosiński (KK), Marcin Piasecki (MPi); theoretical collaborators: Konrad Banaszek (KBa), Rafał Demkowicz-Dobrzanski (RDD) and our group leader Wojciech Wasilewski (WW).

The MOT apparatus along with the vacuum system has been designed by WW with input from myself and MD. The laser and control system has been constructed by joining two warm-atoms experiments: the Raman memory experiment constructed by RCh, MD and in the last stages operated by me as well, and the four-wave mixing experiment conducted by me and AL. With the MOT vacuum system and optics we assembled together with WW and MD and the high current source constructed by JI, I was able to obtain the first MOT on May 1 2016 using laser from the four-wave mixing experiment as cooler (which was also amplified via a custom injection-lock system I constructed using the laser controller designed by WW) and repumper. The locking schemes in this experiment proved to be insufficient for cold atoms and thus together with ML and WW, we planned a new locking system using saturated-absorption spectroscopy with the error signal recovered by modulating the light we an EOM and demodulating the AC signal from a fast photodiode. The electronic components for the modulation have been designed and assembled by WW, JI and MPi. ML tested the error signal generation in the experiment. In the meantime, I have adapted the FPGA control program from the four-wave mixing experiment to control the now more complex experiment, in particular allowing control of up to 16 DDS channels. Together with WW we also adapted new laser controllers two feature efficient operation with many laser heads. MM, ML, JI and WW designed additional elements, including the Rb dispensers controller, ultra-fast current switch for MOT coils and an air-proof container for the cooler-slave laser head. First unsuccessful (nearly catastrophic) usage of the Rb dispensers controller released excess rubidium into the vacuum and thus a re-bakeout of the vacuum was performed by MM and ML. In September 2016 we disassembled two warm-atoms experiments and started moving the lasers onto one optical table and MOT setup onto the other. Together with ML, we have installed the first locking setups for cooler and repumper and adjusted our laser controllers and tuned the feedback loops to allow locking. Later we worked on characterizing and optimizing the beat-note lock designed by WW, later also assembled by KK. Others (myself, MD, AL, MM) participated in constructing the laser system that at that time comprised 6 lasers (one of them with the injection-locked amplifier). The MOT setup has been reconstructed in the new place by myself, MD, MM and AL. The alignment proved to be rather tedious due to the small size of the entire structure and as it much later turned out the insufficient diameter of the cooling beam. Despite, with the new locking systems we have been able to immediately observe stable cold atoms cloud. Initially, we have been able to observe the narrow absorption line of cold atoms and influence it with optical pumping. With the evolution of the laser system and FPGA control scheme, we were finally able to measure the optical depth on a camera and observed ODs of around 20-30. In the meantime, MD and MM made and installed large coils for stray magnetic fields compensation. In December 2016 we tried to repeat the Raman scheme from the warm-atoms experiment, expecting macroscopic Raman signal scattered off the optically pumped atomic cloud (as in for example Refs. [CW12; PLW16a]). We indeed observed strong scattering. Unfortunately, as I discovered a week later by testing the transmission of the signal through an optically-pumped warm vapour cell, it was a polarization rotation signal, not associated with the hyperfine coherence. With the new knowledge, we studied the polarization rotation signal (free-induction decay, FID) to understand the behaviour of magnetic fields in the system and simultaneously with MM we designed and tested an efficient optical pumping setup for warm filtering cell. The FID signal allowed us to set proper magnetic fields and minimize fields from eddy currents caused by MOT coil switching off, for which together with MM we installed a special shorted coil. At this time I also programmed the optical molasses sequence to achieve a temperature of $\sim 23\ \mu$K. With ML we constructed a 50 Hz line-synchronization signal generator and I programmed the synchronization into the FPGA with the help of WW. The setup was later improved by TK.

With the new knowledge, we designed setup for write and read beams counter-propagating and intersecting at an angle of 8 degrees and tried to unsuccessfully observe the now filtered signal first on the APD and then on the ICCD camera using a far-field imaging setup designed with the old Mathematica script of WW, RCh and MD. This has lead us to finally install our I-sCMOS sensor that finally indicated that we do observe single scattered photons. Indeed we observed read photons only when we also applied to write laser pulses, however, no spatial correlation at all could be observed and we had significant problems with filtering out the strong laser beams in the very centre. Another problem was a rather slow Matlab interface for data analysis originally designed by RCh. I have completely redesigned this software to include a "user-friendly" object-oriented interface for data analysis in python (Spyder) and new algorithms for analysis. The performance has also been greatly improved and LabVIEW data collection programs redesigned to store all essential experimental parameters and allow convenient file naming. Despite some improvements, correlations could not be observed.

Finally, in March 2017, I was able to figure out that our spatial configuration did not allow phase-matching. With this consideration, I proposed to counter-propagate the beams onto the same optical axis (with fibre cross-coupling). The configuration required a D-shape mirror in the far-field to properly separate photons from laser beams. With MM we used Zemax to design a lens system to image a large angle of scattered photons. We used an EOM to generate side-band at 6.8 GHz and seed the Raman process testing the phase matching. In the meantime ML with inputs from MM and myself constructed the setup for generating pure seed light (with cavity filtering), which we used in later stages. I optimised the magnetic fields very accurately to ensure gain the seed process and the read-out beam was observed almost immediately. After careful elimination of noise sources in April 2017, we observed a single-photon correlation with an initial $g_{rw}^{(2)} = 12.1 \pm 3.5$. With optimizations, that involved calibration with custom Ronchi rulings designed by WW, we finally improved this figure nearly ten-fold. In the next month, I concentrated on writing the paper [Par17] and preparing figures, with significant inputs from MD and MM.

The next experiment in which we wanted to observe both position and momentum correlations required a redesign of the imaging system performed by MM. I performed initial theoretical analysis and identified entropic EPR-steering witnesses as the most proper for our experiment. The initial alignment of the experiment was performed by MM, MD, AL and myself. Later MM and ML reached the optimal resolution and MM and MD performed initial measurements. MM discovered the difficulties in estimating entropies of measured distributions due to a bias of estimators. I proposed and implemented solutions based on Bayesian estimation and parametric max-likelihood estimators, finally discovering a need for additional measurements. At this time I and MD also performed additional measurements of autocorrelation functions in response to reviews of the previous work [Par17]. Final, proper measurements for the EPR experiment were performed by myself and AL. I prepared preliminary figures, which were later improved by MM. MD wrote the article [Dąb18], which was later modified by myself and MM. In particular, we prepared a more general theory.

In the meantime, I also constructed the SPDC photon source (adapted from the setup built by MJ and used in Refs. [Chr16b; Jac16]) and performed the superresolution experiment, including measurements and data analysis, proposed by KBa and RDD, for which I wrote the first version of the paper, later improved by RDD and KBa [Par18b]. I worked also with SB who tested the imaging setup with classical light and KBo who prepared the hardware for motorized stages. With RDD we prepared a consistent theoretical treatment with both simulations and analytical approximations.

After this experiment, I proposed to use the I-sCMOS camera to measure auto-correlation functions of pseudo-thermal light. The experiment required new developments in data analysis due to deleterious cross-talk effects. The proof-of-principle experiment and analysis were conducted by ML, with input to interpretation and writing of the paper from myself and WW.

In October 2017 we used the BoosTA laser amplifier to try to control the phase of atomic spin coherence in the FID experiment. I proposed to generate a fictitious magnetic field via ac-Stark shift as a test before performing complex spatial manipulations. AL implemented the first setup but observed strong decoherence, which we attributed to dephasing due to inhomogeneous illumination. We decided to use a spatial light modulator to engineer the spatial profile of ac-Stark light. The initial setup was constructed by AL, MM, MD, ML and MP. Initial idea was to use machine learning to correct the intensity by looking only at the lifetime of spin coherence. This was programmed mostly by ML, MM and AL. This attempt turned out to be unsuccessful, and an auxiliary camera was used instead. The pattern preparation software was programmed by MM and AL, with later inputs from myself. Much later, with MM (with inputs from AL and KBo) we remade the software in python. AL and MM took the measurements for the experiment and AL analyzed the data with inputs from myself, MM and MD. AL and I wrote the original paper [Les18] with substantial inputs to the revised version from MD, MM and ML.

After this experiment, we returned to the Raman interaction and tried to manipulate the spin wave in its spatial domain. With MM we prepared the setup and observed the diffraction of spin waves on the ac-Stark grating. Soon after we also observed the effect at the single-photon level in the correlation function. This led us to attempt to observe Hong-Ou-Mandel interference of two heralded spin waves. Observation of such effect has long been proposed by WW. I have suggested the specific realisation of using the ac-Stark grating as a beamsplitter. Soon we have been able to observe interference of two seeded (classical) spin waves. With MM we upgraded a lot of software and hardware to allow uninterrupted operation of the system. We installed cooling and temperature stabilization of the spatial light modulator and programmed further automation of the experiment. The efficiency of detection with the I-sCMOS camera turned out to be too low to observe enough four-fold coincidences. We have thus installed avalanche photodiodes and programmed a time-tagger within our FPGA. I also programmed the fast SLM-sequence synchronization feedback loop in an FPGA. By the end of January 2018, we have been able to observe the spin-wave Hong-Ou-Mandel dip. The measurements performed by myself and MM with the help of WW took another month due to rather slow data acquisition rates. We also tried to implement a protocol with FPGA feedback but delays in AOMs were too large even after optimization performed by AL and MD. I wrote the paper (first submitted in April 2018) along with MM and we immediately started the next experiment that involved an ac-Stark gradient echo memory. For this, we have completely rebuilt the amplifier-SLM pattern preparation setup and developed many new protocols. I created simulations of our experiment using XMDS2 and we took measurements together with MM. We wrote the paper which was submitted in August 2018 [Maz18].

During summer 2018 we conducted two experiments in parallel. ML and AL developed methods for spatial shaping of spin-waves with lens-like patterns. ML and AL took the measurements and analyzed the data, with input to interpretation, planning and paper (submitted November 2018) writing from myself, MM and WW. At the same time with MM we installed more access paths for laser beams to the system, locked the 776 nm laser to the two-photon absorption line and observed four-wave mixing in the diamond configuration. Next, we attempted at observing photonic triplets and worked out new methods for the time-delayed six-wave mixing process. I performed final measurements in August 2018 and observed superradiant patterns at the single-photon level on the camera, for which I also developed the theory. In the meantime, I slightly rebuilt the MOT setup to allow higher optical depths by expanding the cooling and repumping laser beams.

In October 2018 we started working on implementing the magnetic GEM protocol to be able to combine it with our ac-Stark methods to implement a Hadamard transform on a train of pulses, in accordance with a theoretical proposal of a superadditive receiver of KBa. With MM we constructed a new two-way coil switch. With MM and AL, we operated GEM with classical light and identified that our magnetic field inhomogeneities are too large to process (interfere) more than two pulses efficiently. We have thus greatly improved the GEM coil design. With this, we have arrived at the present day, since November and December 2018 have been largely devoted to additional measurements for the revised versions of papers [Par18c; Maz18].

1.3 Structure and contents of the thesis

This thesis shows the development of a multiplexed quantum memory based on cold atoms. In this introduction (Sec. 1.1) I have introduced several concepts of multiplexing in optical memories to facilitate further understanding and setting of our results in the context of current research.

Chapter 2 will introduce the theory of the operation of the developed quantum light-matter interface. In particular, both the atomic and optical part start from the basics to arrive at important effects used by the protocols explored further, including the roles of ac-Stark shift and phase matching. The adopted wave-equation approach allows us to link quantum and classical characteristics of the system.

Chapter 3 described the details of the constructed cold-atoms experimental setup, supplemented by novel optical elements such as the generator of the ac-Stark modulation patterns as well as the single-photon sensitive camera. Note that in this chapter we try to concentrate on the elements essential to the operation of the memory as well as particularly novel technical elements, omitting physics of atom cooling and trapping.

As a motivational introduction, Chapter 4 starts with exploring the advantages offered by multiplexing in a multi-photon generation protocol. Next, detailed results of the tests of the multimode quantum memory based on wavevector-multiplexing are presented. The chapter includes the development of many new concepts and data analysis methods. Fundamental limits on multiplexing are also discussed.

Chapter 5 describes an initial experiment demonstrating ac-Stark based control over a spin ensemble. The new method cast in the context of magnetometric spin measurements highlights the new capabilities of our method and lays foundations for more elaborate manipulations.

Chapter 6 describes a first experimental demonstration of quantum Hong-Ou-Mandel interference of two spin waves achieved with ac-Stark modulation. The results are cast in the fundamental context of the endeavours to demonstrate quantum interference of quasi-particles, as well as in the context of potential applications in quantum communications and quantum information processing.

In Chapter 7 these applications are further explored by demonstrating a first spin-wave interferometric processor (SMIP) for stored optical pulses. With the ac-Stark modulation, we program our processor to facilitate storage of many optical pulses and implement interference between the pulse arriving at different times.

Finally, Chapter 8 explores our new understanding of the role of spin waves in atomic ensembles to show that they can be used to structure superradiant emission patterns in complex wave-mixing processes. With the new technique exploration of the properties of superradiance of single photons stand open. In particular, we experimentally establish a new link between superradiance and phase matching previously unobserved in the spatial domain.

Chapter 9 concludes the thesis and proposes further paths of development.

Chapter 2

Light-atom interactions theory

The explanation of the operation of the quantum memory, as well as related wave-mixing protocols, requires accurate treatment in two distinct domains. On one hand, we have classical and quantum optics, that in our case must involve spatial propagation and diffraction of light, as the atomic ensemble we work with is spatially extended. On the other hand, we have the atomic ensemble itself. For this, we need a description of a single atom dynamics in a light field, as well as of the properties of non-classical collective atomic states.

With these requirements, we set the following goals. For the optical part, we will derive a propagation equation that is well suited to treat long pulses propagating at potentially large angles. Such description will be cast in the language of a slowly-varying envelope. Most difficulties here arise due to the requirement for accurate treatment of diffraction at moderate angles. These propagation dynamics will be then expressed in the quantum language of electric field envelope operators.

For the atoms, we will derive the dynamics of a three-level atom starting from very simple principles. We will identify essential terms corresponding to processes in the system, that will allow for easy extensions to more complex (many levels in Chapter 8) or otherwise related (ac-Stark modulation in Chapters 5, 6 and 7) dynamics.

In particular, we will provide both exact equations and easy to understand solutions that point to the importance of phase matching (essential in Chapter 8). This will allow us to identify optimal experimental configurations.

Having found the proper description of the dynamics of atomic coherence, we will build a framework of collective atomic excitations extended to the spatial domain.

Appendix A supplements this Chapter giving many derivations that would be hard to follow in the main text. There, we also join the quantum optical and atomic treatment in a form of quite extensive equations and provide essential solutions that describe processes present in our experiments.

2.1 Quantum optics

2.1.1 Optical wave propagation

Here we begin with the wave equation for the electric field vector amplitude in free space:

$$\triangle \mathbf{E}(\mathbf{r},t) - \frac{1}{c^2}\frac{\partial^2 \mathbf{E}(\mathbf{r},t)}{\partial t^2} = 0 \tag{2.1}$$

A plane wave of the form:

$$\mathbf{E}(\mathbf{r},t) = \frac{1}{2}\mathbf{A}e^{-i\omega t + i\mathbf{k}\cdot\mathbf{r}} + c.c \tag{2.2}$$

is the basic solution of this equation, where $\mathbf{k}$ and $\mathbf{A}$ are parameters: the wavevector and amplitude of oscillation, respectively. In free space, the angular frequency $\omega = |\mathbf{k}|c = kc$ is related to the wavevector via the linear dispersion relation.

In a more specific case light propagates through a dielectric (non-magnetic) medium with polarization $\mathbf{P}(\mathbf{r},t)$:

$$\triangle \mathbf{E}(\mathbf{r},t) - \frac{1}{c^2}\frac{\partial^2 \mathbf{E}(\mathbf{r},t)}{\partial t^2} = \frac{1}{\epsilon_0 c^2}\frac{\partial^2 \mathbf{P}(\mathbf{r},t)}{\partial t^2} \tag{2.3}$$

Note 2.1: Fourier transform convention.

We will define the Fourier transform of a single-variable function $f(x)$ as:

$$\tilde{f}(k) = \frac{1}{\sqrt{2\pi}}\int \mathrm{d}x f(x)e^{-ikx}, \tag{2.4}$$

where the integration spans the entire space. The inverse Fourier transform is:

$$f(x) = \frac{1}{\sqrt{2\pi}}\int \mathrm{d}k \tilde{f}(k)e^{ikx}. \tag{2.5}$$

With such definitions the Fourier transform us unitary.

To simplify the wave equation we will first rewrite in terms of the envelope. Let us now plug in an ansatz inspired by the free-space solution given by Eq. 2.2 in a slightly modified form:

$$\mathbf{E}(\mathbf{r},t) = \frac{1}{2}\mathbf{A}(\mathbf{r},t)e^{-i\omega_0 t + ik_0 z} + c.c., \tag{2.6}$$

where $\mathbf{A}(\mathbf{r}_\perp,t)$ will be the *envelope* of the electric field and ω_0 is the central carrier frequency. An identical transformation is performed for the polarization:

$$\mathbf{P}(\mathbf{r},t) = \frac{1}{2}\boldsymbol{\mathcal{P}}(\mathbf{r},t)e^{-i\omega_0 t + ik_0 z} + c.c., \tag{2.7}$$

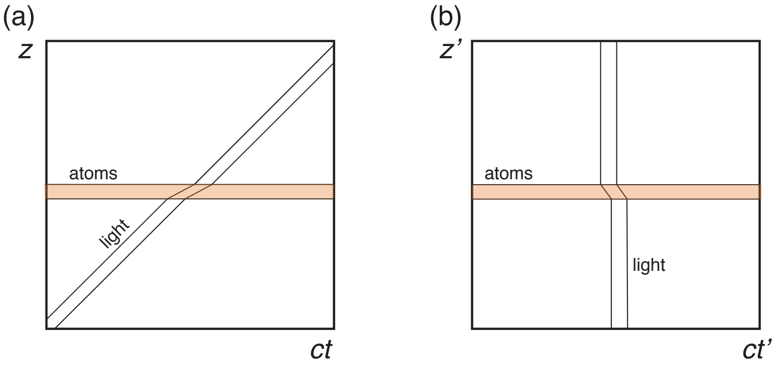

FIGURE 2.1: Pictorial representation of the coordinate transformation from the laboratory frame of reference (a) to the frame of reference co-moving with the pulse (b). As an example the pulse is slowed down (retarded) in a stationary ensemble of atoms.

We may now assume the the envelopes of the electric field and polarization are slowly-varying. Furthermore, we will express the fields in a coordinate system co-moving with the light pulse, by transforming space and time as: $z \to z$, $t \to t - z/c$. The coordinate transformation is depicted in Fig. 2.1. With these assumptions and a set of approximations we arrive at the following equation (expressed in the transverse-Fourier coordinate $\mathbf{k}_\perp$) for the evolution of the envelopes:

$$\boxed{\left[\frac{\partial}{\partial z} - i\left(\sqrt{k_0^2 - k_\perp^2} - k_0\right)\right]\mathbf{A}(\mathbf{k}_\perp, z, t) = \frac{ik_0}{2\epsilon_0}\boldsymbol{\mathcal{P}}(\mathbf{k}_\perp, z, t).} \tag{2.8}$$

The full derivation is presented in Appendix A.2 along with the introduction the the Unidirectional Pulse Propagation Equation (UPPE) in Appendix A.1. Furthermore, Ref. [Cou11] provides a comprehensive comparison of different solutions and treatments.

As a combination of the UPPE and the well-known SVEA (slowly-varying envelope approximation), the equation can be called the *unidirectional slowly varying envelope approximation* (U-SVEA), which I surprisingly did not find in the literature, even though it is a rather simple extension of UPPE. Notably, a plane-wave solution to a homogenous U-SVEA equation (without polarization) has the form:

$$\mathbf{A}(\mathbf{r}, t) = \mathbf{A}_0 e^{ik_x x + ik_y y + i(\sqrt{k_0^2 - k_\perp^2} - k_0)z} \tag{2.9}$$

By expanding Eq. 2.8 for small $k_\perp$ we reproduce the well-known paraxial SVEA equation, valid for much smaller angles:

$$\left(\frac{\partial}{\partial z} + ik_\perp^2\right)\mathbf{A}(\mathbf{k}_\perp, z, t) = \frac{ik_0}{2\epsilon_0}\boldsymbol{\mathcal{P}}(\mathbf{k}_\perp, z, t). \tag{2.10}$$

This can be rewritten in the real space as:

$$\left(\frac{\partial}{\partial z} - \triangle_\perp\right) \mathbf{A}(\mathbf{r}_\perp, z, t) = \frac{ik_0}{2\epsilon_0} \boldsymbol{\mathcal{P}}(\mathbf{r}_\perp, z, t). \tag{2.11}$$

The necessity of using the square root in Eq. 2.8 instead of the first non-vanishing term $k_\perp^2$ represented in Eq. 2.10 stems from a large numerical aperture NA ≈ 0.15 of the imaging system used in our experiment. For nearly plane waves propagating through the ensemble, we could use Eq. 2.11, with $\mathbf{k}_0$ adjusted to the propagation axis. If more than one such wave would propagate through the ensemble at potentially large angles, the paraxial approximation would have to be implemented for each of them separately. In consequence, each wave would have its own frame of reference. If they all interacted with the same atomic coherence, we would have to take into account this transformation for atoms. All of these problems are resolved by using Eq. 2.8 instead and taking the z axis along the atomic ensemble. Usage of Eq. 2.8 becomes a necessity to faithfully represent the wavevector, which is required to resolve phase-matching for cm-long atomic ensembles. Another case is when instead of nearly plane waves we consider strongly focused beams. Indeed, in our setup, an optical mode can be focused down to a $1/e^2$ waist of ~ 5 μm.

As a particular example, let us compare the solution to the U-SVEA equation (Eq. 2.9) to the solution of the simplified paraxial-SVEA equation:

$$\mathbf{A}(\mathbf{r}, t) = \mathbf{A}_0 e^{ik_x x + ik_y y - i(k_x^2 + k_y^2)/(2k_0)z}. \tag{2.12}$$

This simplified solution lacks the additional phase accumulated along the z direction. If we thus calculate the total wavevector of the after plugging in the slowly-varying envelope into Eq. 2.2, we obtain a total wavevector length $|\mathbf{k}|^2 = (k_0 - (k_x^2 + k_y^2)/(2k_0))^2 + k_x^2 + k_y^2 \neq k_0^2$. On the other hand, with the improved U-SVEA equation, we conserve the wavevector as $|\mathbf{k}|^2 = (\sqrt{k_0^2 - k_x^2 - k_y^2} - k_0 + k_0)^2 + k_x^2 + k_y^2 = k_0^2$. This is especially important in the considerations regarding phase matching, since there wavevector-based analysis is essential to explain observed emissions.

Polarization For completeness, here we define the decomposition of the amplitude vector into a set of polarizations:

$$\mathbf{A} = \sum_s A^s \boldsymbol{\epsilon}_s, , \tag{2.13}$$

where $\boldsymbol{\epsilon}_s$ is the polarization versor. The index s may run either through linear polarizations x, y and z, or through two linear polarizations, which we denote $s = +$ ($s = -$) for the right-circular σ_+ (left-circular σ_-) polarization and $s = 0$

corresponds to z-polarized light (π polarization).

Note that here we will remain in the lowest order approximation in terms of wavevectors for polarization, neglecting the tilt of polarization vector for beams propagating at large angles.

2.1.2 Quantization

While the above description correctly describes the evolution of mean electromagnetic fields, to study the noise in all experimental scenarios, and in particular to explore the surprising nonlocal correlations that arise for the photonic system, we need a quantum theory of light. The fully consistent and formally correct quantization of the electromagnetic field requires a relativistic quantum electrodynamics framework. On the other hand, in practice, we often find classical solutions of wave equations and "put hats" on the output amplitudes. A trade-off between the two approaches, which we use here, consists in decomposing the electromagnetic field into a set of classical harmonic oscillators, where each mode of the field is a separate oscillator. The canonical positions and momenta of these oscillators are then quantized by proposing canonical commutation relations. A single quantum of this quantum harmonic oscillator has the energy of one photon, similarly as in the original proposal of Planck for the description of the radiation of a black body. The evolution of the system is governed by the wave equation for the electric field operator. The quantum electric field amplitude operator can be expressed in terms of creation and annihilation operators, defined as in a quantum harmonic oscillator, of a discrete set of spatial modes $U_{ls}(\mathbf{r})$ and polarizations s:

$$\hat{\mathbf{E}}(\mathbf{r},t) = \sum_{sl} i\sqrt{\frac{\hbar\omega_l}{2\epsilon_0}}(\hat{a}_{sl}e^{-i\omega_l t}U_{sl}(\mathbf{r}) + h.c.)\boldsymbol{\epsilon}_s \tag{2.14}$$

Each mode is characterized by a specific frequency of oscillation ω_{sl}. The operators obey the following commutation relations:

$$[\hat{a}_{sl}, \hat{a}^\dagger_{s'l'}] = \delta_{ss'}\delta_{ll'} \tag{2.15}$$

$$[\hat{a}_{sl}, \hat{a}_{s'l'}] = 0 \tag{2.16}$$

if the electric field operator obeys the wave Eq. 2.1, which can also be expressed in terms of equations for the mode functions. Equivalently, the temporal evolution may be expressed by Heisenberg equations with the field Hamiltonian, while the spatial evolution via the canonical momentum operator. Here we rewrite the electric field operator in terms of the carrier wave and a slowly varying envelope operator[1]:

$$\hat{\mathbf{E}}(\mathbf{r},t) = \frac{1}{2}\hat{\mathbf{A}}(\mathbf{r},t)e^{-i\omega_0 t + ik_0 z} + h.c., \tag{2.17}$$

The total number of photons in the mode is given by the photon number operator:

$$\hat{n}_{sl} = \hat{a}^\dagger_{sl}\hat{a}_{sl}. \tag{2.18}$$

We can also sum such operators for all modes and obtain the operator for the total number of photons $\hat{n}_{\mathrm{tot}}$.

Coherent states Coherent states are eigenstates of the annihilation operator. The expectation value is ${}_{sl}\langle\alpha|\hat{a}_{sl}|\alpha\rangle_{sl} = \alpha$. They also correspond to classical states of a harmonic oscillator. Importantly, the expectation value of the photon number operator is ${}_{sl}\langle\alpha|\hat{a}^\dagger_{sl}\hat{a}_{sl}|\alpha\rangle_{sl} = |\alpha|^2$ and its variance[2]

$$\mathrm{Var}(\hat{n}_{sl}) = {}_{sl}\langle\alpha|\hat{n}_{sl}(\hat{n}_{sl} - 1) - |\alpha|^2|\alpha\rangle_{sl} = |\alpha|^2, \tag{2.19}$$

thus the relative noise in photon number measurement scales as $\frac{1}{\sqrt{n}}$, which is called the *shot noise* level.

Fock states The creation operator can generate Fock states, that have the form:

$$|n\rangle_{sl} = \frac{(\hat{a}^\dagger_{sl})^n}{\sqrt{n!}}|0\rangle, \tag{2.20}$$

where by $|0\rangle$ we denote the vacuum state. In particular, $|1\rangle_{sl}$ is a *single photon* residing in mode *sl*. Any eigenstate of the photon number operator with an eigenvalue of 1 will be called a single photon. Another important class of states are coherent states, that are defined as:

$$|\alpha\rangle_{sl} = e^{-|\alpha^2|/2}\sum_n \alpha^n(\hat{a}^\dagger_{sl})^n|0\rangle. \tag{2.21}$$

---

[1] This operator is proportional to a position-dependent photon annihilation operator. It has been shown that this interpretation, while valid in the Fourier domain, is problematic in the spatial domain as a photon cannot be localized to a volume smaller than several λ^3. The properties of the “spatial wave function” of a photon are thus a subject of a >50-year-old lively debate [Man66; Sip95] summarized in a review by *Białynicki-Birula* [BB05] and with proper theoretical tools a photon wave function can be properly defined (as opposed to the position operator for photon [NW49] as proved by *Newton and Wigner*). Here we partially avoid this problem by working in a quasi-monochromatic approximation and interpreting $\hat{\mathbf{A}}$ as simply a decomposition of the field operator. Still, in the position basis it should be treated as applying to the $\sim\lambda^3$ volume around the given position.

[2] The operator for the second moment of photon number is $\hat{a}^\dagger\hat{a}^\dagger\hat{a}\hat{a} = \hat{n}(\hat{n} - 1)$.

Squeezed vacuum An important state for our considerations is called a two-mode squeezed state (or squeezed vacuum). We will treat it from a slightly different point of view than above, by considering the Heisenberg-picture evolution of operators for two modes with operators $\hat{a}$ and $\hat{b}$ as:

$$\hat{a}' = \cosh(\xi)\hat{a} + \sinh(\xi)\hat{b}^\dagger = \hat{U}^\dagger \hat{a}\hat{U}, \tag{2.22}$$

$$\hat{b}' = \cosh(\xi)\hat{b} - \sinh(\xi)\hat{a}^\dagger = \hat{U}^\dagger \hat{b}\hat{U}, \tag{2.23}$$

where $\hat{U}$ is a certain unitary transformation that also gives the Schrodinger-picture evolution for states as $|\psi'\rangle = \hat{U}|\psi\rangle$. To find how an input vacuum state evolves, we use the fact that the state is annihilated by $\hat{a}$ and that $\hat{U}^\dagger\hat{U} = \mathbb{1}$:

$$0 = \hat{a}|0\rangle = \hat{U}\hat{a}\hat{U}^\dagger \underbrace{\hat{U}|0\rangle}_{|\psi'\rangle} \tag{2.24}$$

The $\hat{U}\hat{a}\hat{U}^\dagger$ operation is an inverse of 2.22 and thus corresponds to squeezing with the squeezing parameter of $-\xi$ and can be written explicitly. On the other hand, we can write $|\psi'\rangle$ in the Fock state basis and by comparing the two expression find its decomposition as:

$$|\psi'\rangle = \frac{1}{\cosh(\xi)} \sum_n^\infty \tanh^n(\xi)|n,n\rangle = \frac{1}{\cosh(\xi)} e^{\tanh(\xi)\hat{a}^\dagger\hat{b}^\dagger}|0\rangle. \tag{2.25}$$

We can find that the mean photon number in each mode is then $\sinh(\xi)$, while the probability to register a photon in each mode is $\tanh(\xi)$.

Hong-Ou-Mandel effect The two-photon interference is a cornerstone of quantum optics. In their seminal experiment [HOM87], Hong, Ou and Mandel populated modes a and b with single photons, i.e. $\hat{a}^\dagger\hat{b}^\dagger|0\rangle = |11\rangle_{ab}$. The modes where then transformed on a 50:50 beamsplitter into modes c and d as:

$$\hat{c} = \frac{1}{\sqrt{2}}(\hat{a} + \hat{b}), \tag{2.26}$$

$$\hat{d} = \frac{1}{\sqrt{2}}(\hat{a} - \hat{b}). \tag{2.27}$$

By reversing the transformation we can easily find the state in terms of new modes as:

$$\hat{a}^\dagger\hat{b}^\dagger|0\rangle = \frac{1}{2}(\hat{c}^\dagger + \hat{d}^\dagger)(\hat{c}^\dagger - \hat{d}^\dagger) = \frac{1}{2}(\hat{c}^{\dagger 2} - \hat{d}^{\dagger 2})|0\rangle = \frac{1}{\sqrt{2}}(|20\rangle_{cd} - |02\rangle_{cd}), \tag{2.28}$$

which shows that the photons always exit together from a beamsplitter. Such behaviour is particularly characteristic of any Fock-state bosonic excitations, as will be demonstrated experimentally in Chapter 6 for spin waves.

2.1.3 Identifying nonclassical light

Any classical state of light described by a density operator $\hat{\rho}$ can be written as a mixture of coherent states:

$$\hat{\rho} = \int \mathrm{d}^2\alpha P(\alpha)|\alpha\rangle\langle\alpha|, \tag{2.29}$$

where $P(\alpha)$ is called the Glauber-Sudarshan P-representation. For classical states we require $P > 0$. The negativity of P function can thus be considered the witness of nonclassicality. In general however, it is hard to measure the entire P function. We thus require some distinct inequalities, for which the violation will indicate nonclassicality.

One such example is best suited to identify nonclassical correlations in two-mode squeezed vacuum. For such case we will rely on the measurements of Glauber correlation functions:

$$g_{ab}^{(2)} = \frac{\langle\hat{a}^\dagger\hat{a}\hat{b}^\dagger\hat{b}\rangle}{\langle\hat{a}^\dagger\hat{a}\rangle\langle\hat{b}^\dagger\hat{b}\rangle}, \tag{2.30}$$

$$g_{aa}^{(2)} = \frac{\langle\hat{a}^\dagger\hat{a}^\dagger\hat{a}\hat{a}\rangle}{\langle\hat{a}^\dagger\hat{a}\rangle^2}. \tag{2.31}$$

Classically, these correlation functions must satisfy the Cauchy-Schwarz inequality:

$$[g_{ab}^{(2)}]^2 \leq g_{aa}^{(2)} g_{bb}^{(2)}. \tag{2.32}$$

Typically, modes a and b will be thermal, and to show nonclassicality we require only that $g_{ab}^{(2)} > 2$, since for thermal states we have $g_{aa}^{(2)} = g_{bb}^{(2)} = 2$. Care is required however and autocorrelations functions should always be measured as well (see the "Deceitfully large cross-correlation" paragraph below). This is also true for the two-mode squeezed vacuum for which the cross-correlation is:

$$g_{ab}^{(2)} = 1 + \frac{1}{\tanh(\xi)} = 1 + \frac{1}{p} = 2 + \frac{1}{\sinh(\xi)}. \tag{2.33}$$

It is thus clear that in order to violate the Cauchy-Schwarz inequality significantly, we need low photon generation rates.

The second important example relates two a single photon Fock state $|1\rangle$. For such state, we will measure its second-order auto-correlation $g_{aa}^{(2)}$ to demonstrate its nonclassicality. An ideal single photon will attain the value of 0. The phe-

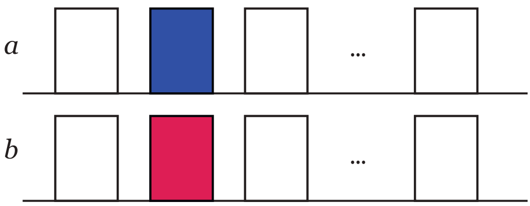

FIGURE 2.2: A pair of pulse trains in which only one time bin in each train contains a coherent state of light. If the time bin is the same in both trains, they are highly-correlated and naive considerations might even indicate nonclassicality.

nomenon is called photon antibunching, and any light with $g^{(2)}_{aa} < 1$ is called antibunched and is nonclassical. Note that this property is specific for autocorrelation functions.

The proofs of this, as well as the Cauchy-Schwarz inequality, are presented in Appendix A.4.

Finally, let us mention that the auto-correlation function may also be concerning conditional counts, for example an important example for the two-mode squeezed vacuum is:

$$g^{(2)}_{aa|b} = \frac{\langle \hat{a}^\dagger \hat{a}^\dagger \hat{a} \hat{a} \hat{b}^\dagger \hat{b} \rangle \langle \hat{b}^\dagger \hat{b} \rangle}{\langle \hat{a}^\dagger \hat{a} \hat{b}^\dagger \hat{b} \rangle^2} = \frac{2p^2(2+p)}{(1-p)^3}, \tag{2.34}$$

with $p = \tanh(\xi)$. By heralding a photon in mode b we observe that the photon in mode a is indeed a single photon, yielding a low value of the auto-correlation function for small p.

We can also link the cross correlation to the heralded auto-correlation in the limit of $p \ll 1$, obtaining:

$$g^{(2)}_{aa|b} \approx \frac{4}{g^{(2)}_{ab}}. \tag{2.35}$$

Deceitfully large cross-correlation As a cautionary example, let us consider a pair of modes a and b, measured with avalanche photodiodes. We shall send a coherent state $|\alpha, \alpha\rangle$ onto each of the photodiodes with probability p and vacuum with $1-p$. The density matrix of the two-mode state can be written as:

$$\hat{\rho} = p|\alpha, \alpha\rangle\langle\alpha, \alpha| + (1-p)|0, 0\rangle\langle 0, 0|. \tag{2.36}$$

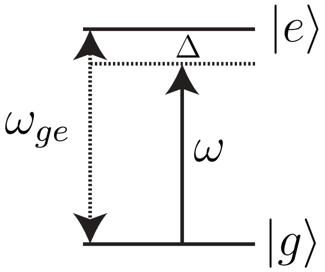

FIGURE 2.3: A level scheme for a generic two-level atom. The optical field with frequency ω is detuned from the atomic resonance by Δ.

Figure 2.2 illustrates this experimental setting. The measured mean photon number in each mode is $p|\alpha|^2$. The correlation function can be calculated as:

$$g^{(2)}_{ab} = \frac{\mathrm{Tr}(\hat{n}_a\hat{n}_b\hat{\rho})}{(p|\alpha|^2)^2} = \frac{p|\alpha|^4}{p^2|\alpha|^4} = \frac{1}{p}. \tag{2.37}$$

Thus, with small p the cross-correlation becomes arbitrarily large, even though the input state is clearly classical. Obviously, we can also find that $g^{(2)}_{aa}$ and $g^{(2)}_{bb}$ both equal $\frac{1}{p}$, which solves the apparent problem as the Cauchy–Schwarz parameter equals 1. The example however provides an important warning that classical fluctuations can generate very high values of $g^{(2)}_{ab}$.

2.2 A two-level atom

In this section, we introduce the light-atom interactions theory starting from the academic example of a two-level atom.

Basic Hamiltonian As a basic building block, a primitive, for any further theoretical considerations here I introduce a two-level atom interacting with a single mode of a classical, optical field. This simple model can later be extended in a variety of ways, including those important for us: spatial propagation, quantization of the optical field and adding more energy levels to the atom Here we consider a two-level atom with a ground state $|g\rangle$ and an excited state $|e\rangle$. The total Hamiltonian for the atom is generally subdivided into two parts:

$$\hat{H} = \hat{H}_B + \hat{V}. \tag{2.38}$$

The basic Hamiltonian $\hat{H}_B$ describes a non-interaction atoms. We may reference the energy of the system to the energy of the ground state and assume $\langle g|\hat{H}_B|g\rangle =$

0. For the energy of the excited state we than have $\langle e|\hat{H}_B|e\rangle = \hbar\omega_0$. The basic Hamiltonian $\hat{H}_B$ is then:

$$\hat{H}_B = \hbar\omega_{ge}|e\rangle\langle e|. \tag{2.39}$$

The second part $\hat{V}$ corresponds to light-matter interaction. Here we will use the dipole approximation and write the interaction term simply as the energy of a dipole in an external field:

$$\hat{V} = -\mathbf{E}\cdot\hat{\mathbf{d}}, \tag{2.40}$$

where the electric field vector is taken as in Eq. 2.2 with $\mathbf{r} = 0$ as for now we consider a single atom and there are no spatial dependencies since we assume that the field does not vary within the atom and $\hat{\mathbf{d}}$ is the dipole moment operator. Later we can replace the constant amplitude vector $\mathbf{A}$ with a slowly varying amplitude to study slowly-varying atom processes in space and time.

Quantum mechanically, the dipole moment operator is given by $-e\hat{\mathbf{r}}$, where $\hat{\mathbf{r}}$ is the vector of position operators for the electron associated with the transition (in our case always the same valence electron) where and the charge of the electron equal $-e$. The matrix elements of the operator can be calculated as $\langle\psi|\hat{\mathbf{d}}|\phi\rangle = \langle\psi| - e\hat{\mathbf{r}}|\phi\rangle$. The expectation values on non-interaction Hamiltonian eigenstates of an isolated atom vanish. In particular, in Hamiltonian eigenbasis $\hat{\mathbf{d}}$ is strictly non-diagonal. Note that $\hat{\mathbf{d}}$ is a vector of operators. Each of these operators corresponds to one polarization, which yields a decomposition:

$$\hat{\mathbf{d}} = \sum_s \hat{d}^s \boldsymbol{\epsilon}_s. \tag{2.41}$$

For example, $\hat{d}^x = -e\hat{x}$, $\hat{d}^y = -e\hat{y}$ and $\hat{d}^z = -e\hat{z}$. For circular polarizations we have $\hat{d}^+ = -e(\hat{x} + i\hat{y})$ and $\hat{d}^- = -e(\hat{x} - i\hat{y})$.

Interaction picture For the two-level atom, we may limit ourselves to the terms $\langle g|\hat{\mathbf{d}}|e\rangle = \mathbf{d}_{ge}$ and $\langle g|\hat{\mathbf{d}}|e\rangle = \mathbf{d}_{eg}$. In particular note that $\mathbf{d}_{eg} = \mathbf{d}_{ge}^*$ which further simplifies the expressions. We may now write the interaction Hamiltonian in the basis of eigenstates of $\hat{H}_B$:

$$\hat{V} = -\frac{1}{2}(\mathbf{A}\cdot\mathbf{d}_{ge}e^{-i\omega t} + \mathbf{A}^*\cdot\mathbf{d}_{ge}e^{i\omega t})\hat{\sigma}_{ge} - \frac{1}{2}(\mathbf{A}\cdot\mathbf{d}_{eg}e^{-i\omega t} + \mathbf{A}^*\cdot\mathbf{d}_{eg}e^{i\omega t})\hat{\sigma}_{eg}, \tag{2.42}$$

where $\hat{\sigma}_{ge} = |g\rangle\langle e|$ etc.

The above Hamiltonian contains a non-trivial time-dependence that does not adhere to simple treatment. To allow for a simple solution, we first express the above Hamiltonian in the interaction picture associated with $\hat{H}_0 = \hbar\omega\hat{\sigma}_{ee}$, which corresponds to a frame-of-reference co-rotating with the optical field. The interaction Hamiltonian in the interaction picture is then:

$$\hat{H}_I = \exp(i\hat{H}_0 t/\hbar)(\hat{H} - \hat{H}_0)\exp(-i\hat{H}_0 t/\hbar) =$$
$$= -\hbar\Delta\hat{\sigma}_{ee} - \frac{1}{2}\mathbf{d}_{ge}\cdot(\mathbf{A}e^{-2i\omega t} + \mathbf{A}^*)\hat{\sigma}_{ge} - \frac{1}{2}\mathbf{d}_{eg}\cdot(\mathbf{A}^* e^{2i\omega t} + \mathbf{A})\hat{\sigma}_{eg}, \quad (2.43)$$

where $\Delta = \omega - \omega_{ge}$ is the *detuning* of the optical field from the atomic resonance. We now disregard the terms rotating with a frequency of 2ω under the assumption that these rapid oscillations will be averaged out in the final result, which constitutes the rotating wave approximation (RWA). See Sec. A.5 for a more rigorous justification. It is now convenient to express the strength of the interaction by a *Rabi frequency*, defined as $\Omega = \frac{\mathbf{A}\cdot\mathbf{d_{eg}}}{\hbar}$, obtaining the final simple result:

$$\hat{H}'_I = -\hbar\Delta|1\rangle\langle 1| - \hbar\frac{\Omega^*}{2}|0\rangle\langle 1| - \hbar\frac{\Omega}{2}|1\rangle\langle 0|. \quad (2.44)$$

From now on we will remain in the interaction picture unless otherwise stated.

Relaxation Let us now write a general equation describing time evolution of a density matrix $\hat{\rho}$. The most general, yet not particularly informative form of the equations is:

$$\dot{\hat{\rho}} = \mathcal{L}(\hat{\rho}), \quad (2.45)$$

where $\mathcal{L}$ is a linear operator on the space of density matrices, called a Lindblad superoperator. A semi-phenomenological way to write the full evolution is comprehensively described in [ABR10]. The equation takes on a form:

$$\dot{\hat{\rho}} = -\frac{i}{\hbar}[\hat{H}'_I, \hat{\rho}] - \frac{1}{2}\{\hat{\Gamma}, \hat{\rho}\} + \hat{\Lambda}, \quad (2.46)$$

where is the $\{\cdot,\cdot\}$ anticommutator. The first part is a standard Hamiltonian evolution known from the von Neumann equation. The relaxation matrix, which models decoherence of the excited state due to spontaneous emission, is:

$$\hat{\Gamma} = \Gamma\hat{\sigma}_{ee}. \quad (2.47)$$

To maintain the trace of the density matrix equal 1, or equivalently guarantee $\mathrm{Tr}(\dot{\hat{\rho}}) = 0$, we add the repopulation term:

$$\hat{\Lambda} = \Gamma\hat{\sigma}_{gg}\rho_{ee}. \quad (2.48)$$

A more general framework for decoherence is provided by the spontaneous emission supeoperator, as nicely introduced in Ref. [ABR10]. The superoperator $\hat{F}$ is constructed so that a trace with a density matrix $\mathrm{Tr}(\hat{\rho}\hat{F})$ can be added to Eq.

2.46. The approach constitutes a specific case of a treatment of an open quantum systems via the master equation.

2.2.1 Stationary states

Initial insight to the solution of the evolution equation is provided by considering the stationary state. The stationary solution of Eq. 2.46, calculated for $t \to \infty$, for the two-level atom has an illuminating form. The coherences take a form:

$$\rho_{ee} = \frac{|\Omega|^2}{\Gamma^2 + 2|\Omega|^2 + 4\Delta^2}, \tag{2.49}$$

$$\rho_{eg} = -\frac{2(\Delta - i\Gamma/2)\Omega}{\Gamma^2 + 2|\Omega|^2 + 4\Delta^2}. \tag{2.50}$$

In the regime dominated by relaxation $\Omega \ll \Gamma$, or equivalently in the first order of perturbation in terms of Ω/Γ we obtain:

$$\rho_{eg} =\approx -\frac{\Omega}{2(\Delta + i\Gamma/2)}. \tag{2.51}$$

The expression will allow us to reproduce Lorentzian shapes of dispersion and absorption. The exact expression given by Eq. 2.49 and Eq. 2.50 provide the rate of fluorescence associated with excited-state population and incorporate the effects of power broadening, as witnessed by the $|\Omega|^2$ terms in the denominators.

2.2.2 Polarization and susceptibility

Before considering propagation of light through an ensemble of two-level atoms, we must link the local single-atom coherence to macroscopic polarization that appears in the propagation equation. We will define a polarization at some point r by considering all atoms within a small volume V around r. Since for now we work within the regime of classical optics, we take the state of all atoms N atoms within that volume to be a separable tensor-product state. We assume all these atoms are in the same state $\forall_{i\in V}\, \hat{\rho}_i = \hat{\rho}$. The dipole moment operator for i-th atom $\hat{\mathbf{d}}^{(j)}$ acts only on that atom and formally is an identity operation $\mathbb{1}$ on all other atoms. The polarization is then calculated as an expectation value of the total dipole moment divided by the volume:

$$\mathbf{P} = \frac{1}{V}\mathrm{Tr}\Big(\bigotimes_i^N \hat{\rho}_i \sum_j^N \hat{\mathbf{d}}^{(j)}\Big) = \frac{1}{V}\sum_j^N \prod_i^N \mathrm{Tr}(\hat{\rho}_i \hat{\mathbf{d}}^{(j)}) = \frac{N}{V}\mathrm{Tr}(\hat{\rho}\hat{\mathbf{d}}), \tag{2.52}$$

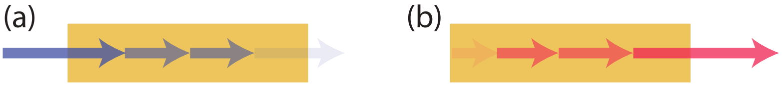

FIGURE 2.4: Absorption (a) and amplification of light (b) in an atomic medium. In (a) the medium contains atomic in the ground state. Induced coherence ρ_{eg} (polarization) results in absorption of incident light field. In (b) a pre-existing coherence ρ_{eg} leads to a directional emission of a new light field.

where we can replace $\frac{N}{V}$ by local atom-number density $n(\mathbf{r})$ to obtain the textbook formula:

$$\boxed{\mathbf{P}(\mathbf{r},t) = n(\mathbf{r})\mathrm{Tr}(\hat{\rho}(\mathbf{r},t)\hat{\mathbf{d}}),} \tag{2.53}$$

where $\hat{\rho}(\mathbf{r},t)$ is a small-volume-averaged density matrix.

To calculate the polarization in the considered case let us return to the laboratory frame of reference (LAB). Here, the dipole moment operator has the simple form $\hat{\mathbf{d}} = \mathbf{d}_{ge}\hat{\sigma}_{ge} + \mathbf{d}_{eg}\hat{\sigma}_{eg}$. The denisty matrix however must be re-transformed from the frame of reference rotating with the field:

$$\hat{\rho}_{\mathrm{LAB}} = \exp(-i\hat{H}_0 t/\hbar)\hat{\rho}\exp(i\hat{H}_0 t/\hbar). \tag{2.54}$$

The coherence term in the LAB frame of reference is:

$$\rho_{eg,\mathrm{LAB}} = -\frac{\Omega}{2(\Delta + i\Gamma/2)}e^{-i\omega t}. \tag{2.55}$$

The macroscopic polarization calculated using Eq. 2.53 becomes:

$$\mathbf{P} = -n\frac{\Omega\mathbf{d}_{ge}}{2(\Delta + i\Gamma/2)}e^{-i\omega t} + \mathrm{c.c.}. \tag{2.56}$$

It can be now expressed in terms of its (slowly-varying) amplitude, as defined in Eq. 2.7:

$$\boldsymbol{\mathcal{P}} = -n\frac{\Omega\mathbf{d}_{ge}}{(\Delta + i\Gamma/2)}. \tag{2.57}$$

Finally, we can define the *linear susceptibility* χ, so that $\boldsymbol{\mathcal{P}} = \epsilon_0\chi\mathbf{A}$:

$$\chi = -n\frac{|\mathbf{d}_{ge}|^2}{\hbar\epsilon_0(\Delta + i\Gamma/2)}. \tag{2.58}$$

2.2.3 Propagation

Here we will give two basic results in the propagation scenario. First, assuming a plane wave spatial propagation with negligible influence of0 diffraction terms, within the one-dimensional slowly-varying envelope approximation we have (cf. Eq. 2.11):

$$2i\frac{\partial \mathbf{A}}{\partial z} = -\frac{\omega}{c\epsilon_0}\mathbf{P}. \tag{2.59}$$

The solution yield the basic law of absorption and dispersion:

$$\mathbf{A}(z) = \mathbf{A}(0)\exp\left(-n\frac{ik}{2\hbar\epsilon_0}\frac{|d_{01}|^2}{\Delta + i\Gamma/2}z\right). \tag{2.60}$$

We observe that light intensity decreases exponentially as it propagates along the ensemble. The absorption is strongest on resonance at $\Delta = 0$. Furthermore, the exponent also contains an imaginary component leading to accumulation of an additional phase along propagation, which constitutes the atomic dispersion. The example is depicted in Fig. 2.4(a). In the second example (Fig. 2.4(b)) we have no input light, but the medium of length L contains an initial constant coherence ρ_{eg}. If we for now neglect the effects such as re-absorption of light and temporal evolution of the coherence, at $t = 0$ at the output we obtain the following amplitude:

$$\mathbf{A}_{\text{out}} = \frac{ik}{2\epsilon_0}nL\mathbf{d}_{01}\rho_{10}. \tag{2.61}$$

We see that the field intensity increases linearly with the length of the atomic ensemble.

2.3 Multi-level atom

We can now directly apply the methods worked out in the previous section to study the properties of multi-level atoms, where the levels are coupled by many optical fields. We can distinguish to particular reasons to go beyond the simple model of a two-level atom. First, real atoms are inherently multi-level, and even a single monochromatic coherent field will couple many levels. The extended model is thus required to better describe the physical reality. Most importantly, however, including even one more level leads to qualitatively new effects, such as two-photon absorption, Raman scattering and electromagnetically induced transparency.

2.3.1 Raman transitions with three-level system

We consider a system of three levels coupled with two optical fields, as in Fig. 2.5, called the lambda (Λ) system. We will assume that the two field can be treated separately. This means that the electric field can be rewritten as $\mathbf{E} = \mathbf{E}_1 + \mathbf{E}_2$, where E_1 dominantly oscillates at frequency ω_1 and E_2 at ω_2. Two transitions in the atom can be treated separately as long as the spectrum of both beams is smaller than $|\omega_1 - \omega_2|$ and the detunings also satisfy $|\delta|, |\Delta| \ll |\omega_1 - \omega_2|$. The condition on the spectrum:

$$\left|\frac{\partial \mathbf{A}_1}{\partial t}\right| + \left|\frac{\partial \mathbf{A}_2}{\partial t}\right| \ll |\omega_1 - \omega_2| \left(|\mathbf{A}_1| + |\mathbf{A}_2|\right) \tag{2.62}$$

also allows separating the propagation equation into two independent equations for two fields. Let us first consider the atomic part of the evolution, by taking $r = 0$. Such configuration and approximations allows obtaining the time independent hamiltonian in the rotating frame defined by $\hat{H}_0 = \hbar(\omega_1 - \omega_2)\hat{\sigma}_{hh} + \hbar(\omega_1 + \omega_2)\hat{\sigma}_{ee}$:

$$\hat{H}_I = -\frac{\hbar}{2}\begin{pmatrix} 0 & 0 & \Omega_1^* \\ 0 & 2\delta & \Omega_2^* \\ \Omega_1 & \Omega_2 & -2\Delta \end{pmatrix}, \tag{2.63}$$

where Ω_i are Rabi frequencies of respective fields on the relevant transitions. For the decoherence terms, we assume the decay of excited state with the rate Γ and decay of the ground-state coherence with the rate γ.

To solve the results set of equations for density matrix elements we employ the *adiabatic elimination*. In this approximation we assume that the fields are far detuned from their respective resonances $|\Delta| \gg \Gamma$ and in consequence the excited states does not get populated, i.e. $\rho_{ee} = 0$. Furthermore, we assume that the excited state coherences, ρ_{eg} and ρ_{eh} follow the evolution of the ground-state manifold adiabatically, and thus we take $\dot{\rho}_{eg} = \dot{\rho}_{eh} = 0$. With this assumptions we can write these coherences as a function of ground-state coherences and populations:

$$\rho_{eg} = -\frac{\Omega_1\rho_{gg} + \Omega_2\rho_{hg}}{i(\gamma/2 + \Gamma) - 2\Delta}, \tag{2.64}$$

$$\rho_{eh} = -\frac{\Omega_1\rho_{gh} + \Omega_2\rho_{hh}}{i(\gamma/2 + \Gamma) - 2(\delta + \Delta)}, \tag{2.65}$$

The coherence of interest will evolve according to the following equation:

$$\dot{\rho}_{hg} = -\frac{\Omega_1\Omega_2^*}{\gamma + 2\Gamma + 4i\Delta} - \left(\frac{|\Omega_2|^2}{\gamma + 2\Gamma + 4i\Delta} + \frac{|\Omega_1|^2}{\gamma + 2\Gamma - 4i(\delta + \Delta)} + \frac{\gamma}{2} - i\delta\right)\rho_{hg}. \tag{2.66}$$

We will now look at two distinct situations of interest. First, we assume that the Ω_2 field is the strong coupling field and Ω_1 field is a weak signal field and we remain in the limit $\rho_{gg} = 1$ and $\rho_{hh} = 0$ (see Fig. 2.5(a)). It is also reasonable to assume that the rate of spin-wave dephasing is small and thus $\gamma \ll \Gamma$. We obtain the following simplified equation:

$$\dot{\rho}_{hg} = -\frac{\Omega_1\Omega_2^*}{2\Gamma + 4i\Delta} - \left(\frac{|\Omega_2|^2}{2\Gamma + 4i\Delta} + \frac{\gamma}{2} - i\delta\right)\rho_{hg}. \tag{2.67}$$

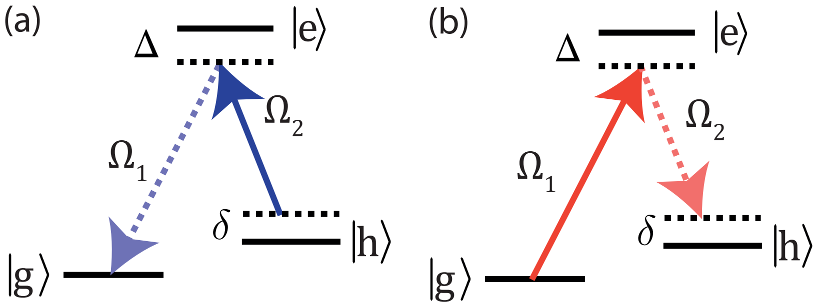

FIGURE 2.5: The three-level Λ system in two distinct situations. In both cases, most atoms reside in $|g\rangle$. In (a) the strong field Ω_2 couples the weak field Ω_1 to the ground-state atomic coherence ρ_{hg}. In this scenario, excitations are exchanged between Ω_1 field and the atomic coherence. In (b) Ω_1 field is strong and couples the weak Ω_2 field to the same coherence. This scenario leads to amplification of the ρ_{hg} coherence and Ω_2 field. In both cases, Δ and δ denote single- and two-photon detunings, respectively.

To facilitate understanding, we rewrite the real and imaginary parts separately and obtain the following decomposition of the terms in the equation:

$$\dot{\rho}_{hg} = -\underbrace{\frac{\Omega_1\Omega_2^*}{2\Gamma + 4i\Delta}}_{\text{Raman}} + i\left(\underbrace{\frac{\Delta|\Omega_2|^2}{\Gamma^2 + 4\Delta^2}}_{\text{ac-Stark shift}} + \delta\right)\rho_{hg} - \left(\frac{1}{2}\gamma + \underbrace{\frac{\Gamma|\Omega_2|^2}{2\Gamma^2 + 8\Delta^2}}_{\text{power broadening}}\right)\rho_{hg}. \tag{2.68}$$

As now clearly seen, they subsequently correspond to the Raman interaction, the total frequency shift (ac-Stark shift plus the two-photon detuning) and losses (intrinsic losses plus power broadening).

The same can be done for the the case of weak Ω_2 field and strong Ω_1 field:

$$\dot{\rho}_{hg} = -\underbrace{\frac{\Omega_1\Omega_2^*}{2\Gamma + 4i\Delta}}_{\text{Raman}} + i\left(\underbrace{-\frac{(\Delta+\delta)|\Omega_1|^2}{\Gamma^2 + 4(\Delta+\delta)^2}}_{\text{ac-Stark shift}} + \delta\right)\rho_{hg} - \left(\frac{1}{2}\gamma + \underbrace{\frac{\Gamma|\Omega_1|^2}{2\Gamma^2 + 8(\Delta+\delta)^2}}_{\text{power broadening}}\right)\rho_{hg}. \tag{2.69}$$

Note 2.2: Beyond adiabatic elimination.

To go beyond the adiabaticity but keep the expression manageable, it is worth assuming that $\rho_{ee} = 0$ but coherences may evolve rapidly. We also take $\rho_{gg} \approx 1$ and $\rho_{hh} \approx 0$. We than obtain three rather than just one equation:

$$\dot{\rho}_{hg} = \frac{1}{2} i \left((2\delta + i\gamma)\rho_{hg} + \Omega_2^* \rho_{eg} - \Omega_1^* \rho_{eh} \right) \tag{2.70}$$

$$\dot{\rho}_{eg} = \frac{1}{2} i \left((-2\Delta + i\Gamma)\rho_{eg} + \Omega_2 \rho_{hg} + \Omega_1 \right) \tag{2.71}$$

$$\dot{\rho}_{eh} = \frac{1}{2} i \left(\Omega_1 \rho_{hg}^* + \rho_{eh}(i\gamma + i\Gamma - 2(\delta + \Delta)) \right) \tag{2.72}$$

and the relevant polarizations are $\mathcal{P}_1 = n\rho_{eg} d_{ge}$ and $\mathcal{P}_2 = n\rho_{eh} d_{he}$. This system of equations does not provide an easy analytical solutions, as opposed to the fully adiabatic approximation. Furthermore, it becomes much difficult to employ in simulations. The main reasons is surprisingly not the higher number of equations (3 atomic equations and two field equations, as opposed to 1 atomic and 1 field equation in the adiabatic case), but rather the requirement of much higher temporal resolution, resulting from fast Rabi oscillations with a frequency of $\sim \Delta$. Inclusion of all populations yields an exact set of 6 atomic equations, just slightly more difficult to simulate.

2.3.2 Light-atom cross-coupling

Finally, we can link the evolution of atomic coherence to the evolution of the optical field. First, we write the expression for the full atomic polarization, separated into parts oscillating at frequencies ω_1 and ω_2. Additionally, we will make a substitution $B = \sqrt{n}\rho_{hg}$, where B will be understood as a field of atomic coherence. To argument this substitution, we point out that on one hand it is intuitive that such field will be best described by the coherence multiplied by the atomic density, since we would like the field to only be present where the atoms are actually present. The importance of the square root however emerges only as we will rewrite the equations for quantum operators rather than classical functions (Sec. 2.4). The coherence described by B will be thus called *spin wave.*

Here, the optical polarization is calculated by plugging the results from Eqs. 2.64 and 2.65 into Eq. 2.53. It takes the following form:

$$\mathbf{P}_1 = \underbrace{-\frac{\mathbf{d}_{ge}}{\hbar} \left(\sqrt{n} \frac{\mathbf{d}_{eh} \cdot \mathbf{A}_2 B e^{i(k_2 - k_1)z}}{i\Gamma - 2\Delta} + n \frac{\mathbf{d}_{eg} \cdot \mathbf{A}_1}{i\Gamma - 2\Delta} \right)}_{\frac{1}{2}\mathcal{P}_1} e^{ik_1 z - i\omega_1 t} + c.c \tag{2.73}$$

$$\mathbf{P}_2 = \underbrace{-\frac{\mathbf{d}_{he}}{\hbar} \left(\sqrt{n} \frac{\mathbf{d}_{eg} \cdot \mathbf{A}_1 B^* e^{i(k_1 - k_2)z}}{i\Gamma - 2(\delta + \Delta)} \right)}_{\frac{1}{2}\mathcal{P}_2} e^{ik_2 z - i\omega_2 t} + c.c \tag{2.74}$$

As we have seen in Sec. 2.2.2, such polarization is inherently linked to emission and absorption of light.

2.3.3 Phase matching

With these relations we may now consider specific processes and their spatial properties. We believe that the analysis presented here, while not based strictly on the propagation equations, will provide a proper intuition towards further analysis and set the more involved considerations in Sec. 2.3.4, Sec. 7.1 as well as Sec. A.9 in the proper context.

Read interaction Let us start with a scenario in which a strong read laser field $\mathbf{A}_2 = \mathbf{A}_R$ couples a weak read signal (anti-Stokes) field $\mathbf{A}_1 = \mathbf{A}_r$ to the spin wave B through an optical polarization $\mathbf{P}_1 = \mathbf{P}_r$. Both fields are written in terms of the free-space solution (Eq. 2.9) to the U-SVEA equation:

$$\mathbf{A}_r = \mathbf{A}_{r0} e^{ik_x^r x + ik_y^r y + i(\sqrt{k_r^2 - k_{r\perp}^2} - k_r)z} \tag{2.75}$$

$$\mathbf{A}_R = \mathbf{A}_{R0} e^{ik_x^R x + ik_y^R y + i(\sqrt{k_R^2 - k_{R\perp}^2} - k_R)z} \tag{2.76}$$

Let us also assume that the spin wave has a general form $B = B_0 e^{i\mathbf{K}\cdot\mathbf{r}}$. We will also assume that the atomic ensemble is very long along the z direction. If we now plug in Eq. 2.76 into Eq. 2.73 we can observe that the first term associated with a spin wave will have the following spatial dependence:

$$\mathbf{P}_r \propto e^{i(K_x + k_x^R) + i(K_y + k_y^R) + i\sqrt{k_R^2 - (k_x^R)^2 - (k_y^R)^2}} \tag{2.77}$$

Through this proportionality, we immediately see that the direction of emission is thus set by K_x and K_y of the spin wave and k_x^R, k_y^R of the drive field. For the emission to be efficient in such situation, we require emissions from all atoms interfere constructively. Equivalently, the oscillation along z must match a wave described by Eq. 2.75. This condition then reads:

$$\Delta K_z = \sqrt{k_R^2 - (k_x^R)^2 - (k_y^R)^2} - \sqrt{k_r^2 - (k_x^r)^2 - (k_y^r)^2} + K_z = 0 \tag{2.78}$$

Which along with the condition for the perpendicular wavevector:

$$\mathbf{k}_{r\perp} = \mathbf{K}_\perp + \mathbf{k}_{R\perp} \tag{2.79}$$

constitutes the phase matching condition. If we now plug in the condition for perpendicular wavevector into Eq. 2.78, eliminating $\mathbf{k}_r$, we obtain an equation describing a sphere in K-space. Typically we will consider one transverse dimension (either K_x or K_y) and K_z and discuss a circle. These are the wavevectors of spin waves that can be efficiently mapped onto light:

$$(K_x - k_x^R)^2 + (K_y - k_y^R)^2 + (K_z + \sqrt{k_R^2 - (k_x^R)^2 - (k_y^R)^2})^2 = k_r^2 \tag{2.80}$$

Let us now analyse what happens as the wavevector of the coupling field k_R is changing. For simplicity, we consider a tilt in the x direction by an angle of α from the situation where $k_x^R = k_y^R = 0$. We see that the centrepoint of the circle is shifted with respect to its original position at $(0, 0, -k_R)$ to $(k_R \sin(\alpha), 0, -k_R \cos(\alpha))$. The radius of the circle does not change. Clearly, such tilt only causes a rotation of the centrepoint around the origin. In future considerations, we will adopt an alternative view when we will rather choose to rotate the coordinate system[3]. A particularly important example will be a rotation of 180 degrees.

Exactly the same condition is derived if we assume that we want to map the field $\mathbf{A}_r$ (Eq. 2.75) onto the atomic coherence. Then, we need to consider the equation describing evolution of the spin wave:

$$\frac{\partial B}{\partial t} = -\sqrt{n}\frac{\mathbf{d}_{he} \cdot \mathbf{A}_R^*/\hbar^2 e^{i(k_r - k_R)z}}{2\Gamma + 4i\Delta}\mathbf{d}_{eg} \cdot \mathbf{A}_r - \left(\frac{|\mathbf{d}_{eh} \cdot \mathbf{A}_R|^2/\hbar^2}{2\Gamma + 4i\Delta} + \frac{\gamma}{2} - i\delta\right) B. \tag{2.81}$$

Here, the first term describes generation of spin wave due to incident field. The generated spin wave will have the wavevector:

$$\mathbf{K} = \left(k_x^r - k_x^R, k_y^r - k_y^R, \sqrt{k_r^2 - (k_x^r)^2 - (k_y^r)^2} - \sqrt{k_R^2 - (k_x^R)^2 - (k_y^R)^2}\right) \tag{2.82}$$

Notably, the spin waves with these wavevectors coincide with the spin waves retrievable from the memory, i.e. those for which the wavevectors satisfy Eq. 2.80. Finally, let us note that in both cases under the conditions of perfect phase matching, we have:

$$\mathbf{k}_r = \mathbf{k}_R + \mathbf{K} \tag{2.83}$$

Write interaction We will now consider an opposite situation, taking $\mathbf{A}_2 = \mathbf{A}_w$ as a weak write signal (Stokes) field and $\mathbf{A}_2 = \mathbf{A}_W$ as a strong coupling write laser field. The field amplitudes are again described by:

$$\mathbf{A}_w = \mathbf{A}_{w0} e^{ik_x^w x + ik_y^w y + i(\sqrt{k_w^2 - k_{w\perp}^2} - k_w)z} \tag{2.84}$$

$$\mathbf{A}_W = \mathbf{A}_{W0} e^{ik_x^W x + ik_y^W y + i(\sqrt{k_W^2 - k_{W\perp}^2} - k_W)z} \tag{2.85}$$

By writing the evolution of the spin wave as:

$$\frac{\partial B}{\partial t} = -\sqrt{n}\frac{\mathbf{d}_{eg}\mathbf{A}_W/\hbar^2 e^{i(k_W - k_w)z}}{2\Gamma + 4i(\Delta + \delta)}\mathbf{d}_{he} \cdot \mathbf{A}_w^* - \left(\frac{|\mathbf{d}_{eg} \cdot \mathbf{A}_W|^2/\hbar^2}{2\Gamma - 4i(\Delta + \delta)} + \frac{\gamma}{2} - i\delta\right) B. \tag{2.86}$$

---

[3] The only potential problem with such equivalence is the question whether in the case of a non-zero phase-mismatch we should calculate ΔK_z along the old or the new K_z axis. The answer does not seem as simple as in practice an exact shape of the atomic cloud would have to be taken into account. The correction, however, is rather small

From the first part of the equation to which we plug in both Eq. 2.84 and Eq. 2.85 we observe that now the spin wave will have a wavevector of:

$$\mathbf{K} = (k_x^W - k_x^w, k_y^W - k_y^w, \sqrt{k_W^2 - (k_x^W)^2 - (k_y^W)^2} - \sqrt{k_w^2 - (k_x^w)^2 - (k_y^w)^2}) \tag{2.87}$$

which is clearly distinct than in the read interaction, as here the optical field $\mathbf{A}_w$ contributes as its complex conjugate. For this reason, the signs in the spin-wave wavevector are reversed. In the write interaction, both spin waves and the optical field are parametrically amplified. At the single-photon level, we understand the interaction as a scattering of photon from a write coupling field to produce a scatter write (Stokes) photon and a spin wave with properly matched wavevector. Equivalently, we may again write, in analogy to Eq. 2.83:

$$\mathbf{k}_w = \mathbf{k}_W - \mathbf{K}. \tag{2.88}$$

Using this relation for the z component we have:

$$\sqrt{k_W^2 - (k_x^W)^2 - (k_y^W)^2} - \sqrt{k_w^2 - (k_x^w)^2 - (k_y^w)^2} = K_z. \tag{2.89}$$

If we now again eliminate $\mathbf{k}_w$ using 2.87 and rearrange, we obtain:

$$(K_x - k_x^W)^2 + (K_y - k_y^W)^2 + (K_z - \sqrt{k_W^2 - (k_x^W)^2 - (k_y^W)^2})^2 = k_w^2, \tag{2.90}$$

which again describes a circle in the K-space.

Write-read memory Let us now join the two processes together and consider the conditions under which the photons scattered in the write interaction can be retrieved in the read interaction. This conundrum is well described by a graph of wavevectors, including the wavevectors of the pump, as seen in Fig. 2.6(a). We can observe that as the photons are scattered at larger angles, a phase mismatch ΔK_z arises during read. We believe it is convenient to express the same scenario in terms of wavevectors of spin waves that are generated and retrievable, as described by Eqs. 2.80 and 2.90. In Fig. 2.6(b,c,d) we mark these wavevectors in the space spanned by K_x and K_z, for the case where the coupling beams are collinear and propagate along z. We see that indeed as previously observed the wavevectors of spin waves generated in the write interaction do not overlap with those efficiently retrieved in the read interaction. Equivalently, circles described by Eqs. 2.80 and 2.90 are distinct.

In the experiment, we need to consider an optimal arrangement of write and read beams. As seen in Fig. 2.6, spin waves for which the write and read interaction is efficient are distinct. We illustrate it specifically in Fig. 2.6(b). A spin wave created in the write interaction, in general, is not efficiently read out in the

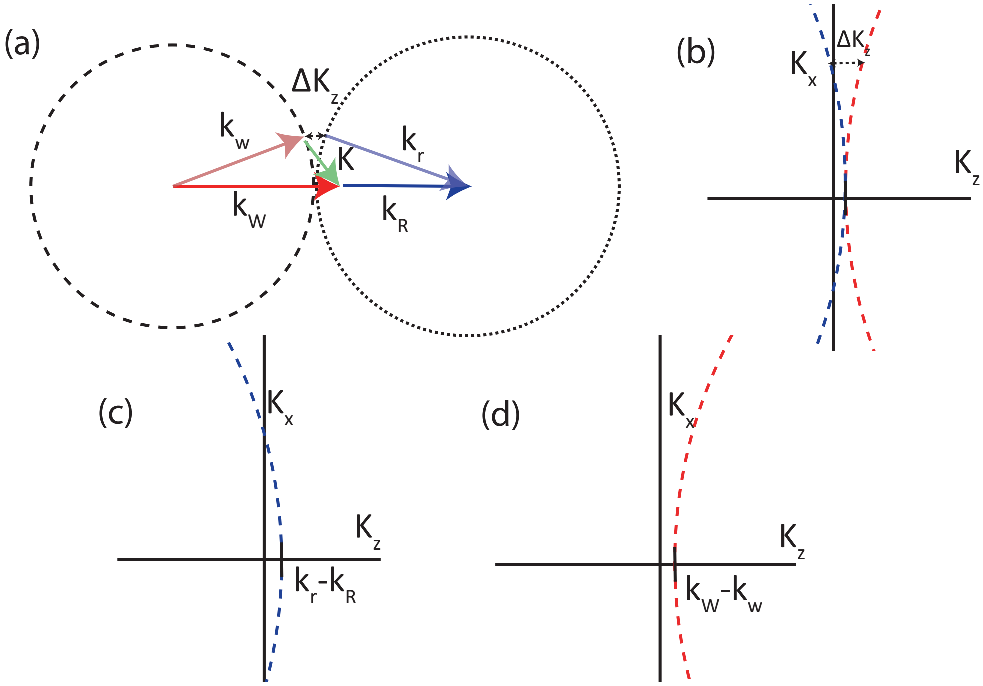

FIGURE 2.6: Illustration of the addition of wavevectors in the entire process along with the wavevector mismatch ΔK_z along the z direction. In (b) we draw overlayed sets of spin-wave wavevectors from the write and read processes in the co-propagating, described by Eqs. 2.80 and 2.90 with $\mathbf{k}_W$ and $\mathbf{k}_R$ set along the z axis. The set of wavevectors of spin waves in the (K_x, K_z) space that facilitate good phase matching during the read (c) and write (d) interaction are also presented separately. For the read interaction we take $k_R > k_r$ and for the write interaction $k_W < k_w$. This corresponds to the particular configuration depicted in Fig. 2.5. The choice depends in general on the specific atomic level configuration selected.

read interaction. A particular spin wave, created with a certain K_x, is then read out with an efficiency determined by the longitudinal wavevector mismatch ΔK_z. We can thus see that if the write and read control beams co-propagate, perfect phase matching occurs only at $K_x = 0$. As the angle of scattering grows, the phase matching degrades. For the Rubidium-87 atom, K_z at $K_x = 0$ corresponds to the difference in energies equal $\hbar\Delta_{\mathrm{HFS}}$ between levels $|g\rangle$ and $|h\rangle$, which we choose to be sublevels from the $F = 1$ and $F = 2$ manifolds, respectively. The zero-point wavevector component will be denoted by $K_{z0} = \Delta_{\mathrm{HFS}}/c = 0.14$ rad/mm, or $\Lambda_{z0} = 44$ mm.

The situation is quite different if the beams counter-propagate, as depicted in Fig. 2.7(b). We obtain the figure by rotating the coordinate system for the

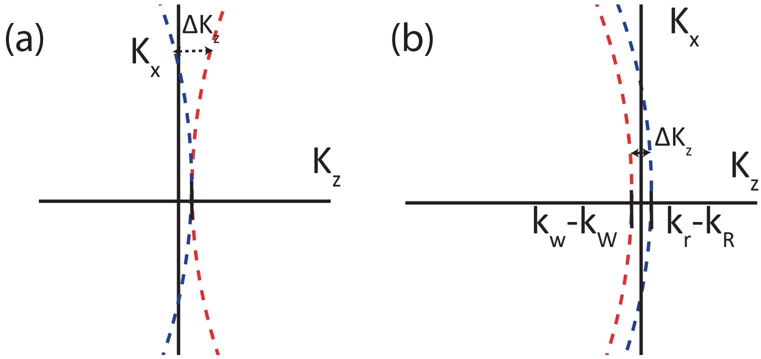

FIGURE 2.7: Overlaid sets of spin waves from the write and read processes in the (a) co-propagating and (b) counter-propagating configurations.

spin-wave wavevectors associated with the write interaction (red) by 180 degrees. In the original coordinate system, the circle is then described by:

$$(K_x)^2 + (K_y)^2 + (K_z + k_W)^2 = k_w^2, \tag{2.91}$$

Note that in order to obtain this result strictly, one needs to redefine the envelope in the U-SVEA equation to propagate mostly along $-z$. We believe however, that our argument of rotating the coordinate system from the previous section is convincingly extensible for full rotations.

In this new situation, there is a phase-mismatch at $K_x = 0$ equal $\Delta K_z = 2K_{z0}$, but it stays roughly constant as K_x is increased. With a typical length of the atomic ensemble, this phase mismatch is non-negligible. Note, however, that Fig. 2.7 is not to scale; in an actual scenario there are small differences in curvatures of the rings, and on such scale, the ΔK_z at $K_x = 0$ is very small. Still, we can observe that the read-out of spin waves created even at large angles remain phase matched very well. In fact, the difference in curvatures causes the difference K_{z0} to cancel out at the scattering angle of approx. 4 degrees. The counter-propagating configuration is consequently the best choice if we want to observe write photons and then read spin waves at large scattering angles. As witnessed in Fig. 2.7(a), it is not the case in the co-propagating scenario.

It is, however, important to note that the two configurations respond differently to a small tilt between write and read coupling beam axe, which we again introduce in the figure via rotation of the coordinate system. In the co-propagating scenario depicted in Fig. 2.8(a) the phase matching is roughly preserved and even improved for a certain angle. In the counter-propagating scenario, as in Fig. 2.8(b) the tilt introduces a large phase-mismatch ΔK_z for most angles. Only photons emitted exactly along one specific direction (the intersection of arcs in Fig. 2.8(b)), that give rise to spin waves later retrieved along the read beam

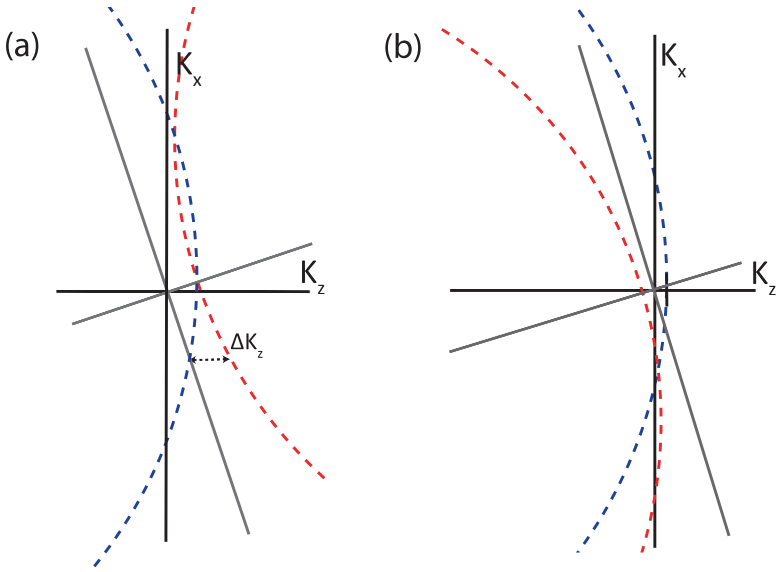

FIGURE 2.8: Overlayed sets of spin waves from the write and read processes in the (a) co-propagating and (b) counter-propagating configurations, yet with an additional tilt. Black axes correspond to the read laser frame-of-reference and greyed axes to write laser.

remain phase-matched. This shows that tilting write and read beams in the counter-propagating configuration does not provide proper phase matching characteristics (which we learned experimentally, as I mentioned in the introduction).

2.3.4 Coupled equations

Let us now write the actual coupled equations that govern the two processes discussed. Considering the full pair of equations accurately is essential to properly predict the efficiency of the memory. These will be the equations solved numerically in Chapter 7. We will use to simplified one-dimensional propagation equation (Eq. 2.11), keeping in mind that it can be extended to the full U-SVEA (Eq. 2.8). Finally, we rewrite Eq. 2.68 in terms of field amplitudes, keeping in mind that the two slowly varying amplitudes were written in terms of different wavevector (k_1 and k_2). Furthermore, we will substitute $B = \sqrt{n}\rho_{hg}$ as before. Together with the evolution given by the polarization given by Eq. 2.73 they give a set of coupled equations:

$$\frac{\partial \mathbf{A}_1}{\partial z} = -\frac{ik_1}{\epsilon_0\hbar}\sqrt{n}\mathbf{d}_{ge}\frac{\mathbf{d}_{eh}\cdot\mathbf{A}_2}{i\Gamma - 2\Delta}e^{i(k_2-k_1)z}B - \frac{ik_1}{\epsilon_0\hbar}n\mathbf{d}_{ge}\frac{\mathbf{d}_{eg}\cdot\mathbf{A}_1}{i\Gamma-2\Delta}, \tag{2.92}$$

$$\frac{\partial B}{\partial t} = -\sqrt{n}\frac{\mathbf{d}_{he}\cdot\mathbf{A}_2^*/\hbar^2 e^{i(k_1-k_2)z}}{2\Gamma+4i\Delta}\mathbf{d}_{eg}\cdot\mathbf{A}_1 - \left(\frac{|\mathbf{d}_{eh}\cdot\mathbf{A}_2|^2/\hbar^2}{2\Gamma+4i\Delta}+\frac{\gamma}{2}-i\delta\right)B. \tag{2.93}$$

As we will demonstrate later with quantum fields, these equations result in a beamsplitter-type interaction between the field $\mathbf{A}_1$ and the atomic coherence field B. The excitations are thus exchanged between the optical field and the atomic coherence.

In the alternative case ($|\Omega_2| \ll |\Omega_1|$), as depicted in Fig. 2.5(b) we obtain:

$$\frac{\partial \mathbf{A}_2}{\partial z} = -\frac{ik_2}{\epsilon_0\hbar}\sqrt{n}\mathbf{d}_{he}\frac{\mathbf{d}_{eg}\mathbf{A}_1}{i\Gamma-2(\Delta+\delta)}e^{i(k_1-k_2)z}B^*, \tag{2.94}$$

$$\frac{\partial B}{\partial t} = -\sqrt{n}\frac{\mathbf{d}_{eg}\mathbf{A}_1/\hbar^2 e^{i(k_1-k_2)z}}{2\Gamma+4i(\Delta+\delta)}\mathbf{d}_{he}\cdot\mathbf{A}_2^* - \left(\frac{|\mathbf{d}_{eg}\cdot\mathbf{A}_1|^2/\hbar^2}{2\Gamma-4i(\Delta+\delta)}+\frac{\gamma}{2}-i\delta\right)B. \tag{2.95}$$

In this case both the optical field $\mathbf{A}_1$ and the atomic coherence field B will be amplified. Here, the energy comes from the strong drive field $\mathbf{A}_2$, for which we have assumed a non-depletion regime.

2.3.5 Two-photon absorption

Conveniently, the very same model as in Sec. 2.2.2 allows explanation of two-photon absorption and optical pumping in a three-level ladder (Ξ) system with levels $|g\rangle$, $|e\rangle$ and $|f\rangle$. We are particularly interested in coherence between the excited levels, that leads to absorption to light at the $|e\rangle \to |f\rangle$ transition. In turn, in the steady state, we will obtain a population of the $|f\rangle$ state, that will lead to fluorescence. The actual system in rubidium allows an alternative decay path through a transition at 420 nm, as illustrated on the cover of this thesis. The steady state coherences in the far-detuned regime are:

$$\rho_{ff} = \frac{|\Omega_1|^2|\Omega_2|^2}{16(\Delta^2+\Gamma_1^2/4)(\delta^2+\Gamma_2^2/4)}. \tag{2.96}$$

$$\rho_{fe} = -\frac{|\Omega_1|^2\Omega_2}{8(\Delta^2+\Gamma_1^2/4)(\delta+i\Gamma_2/2)}. \tag{2.97}$$

One can see that absorption of light at $|e\rangle \to |f\rangle$ transiton occurs only if we illuminate the atoms with strong Ω_1 field.

2.3.6 Ac-Stark shift

We have seen that the ac-Stark shift affects the operation of the Raman light-atom interface. On the other hand, it can also allow desired control over the atomic spins. With a far off-resonant laser light $\Delta \gg \Gamma$ we can selectively change the phases in distinct magnetic sublevels and neglect the deleterious effects of incoherent excitations that scale as $1/\Delta^2$, while the ac-Stark shift scales as $1/\Delta$.

Here we concentrate on the ac-Stark shift of the ground-state energies. It is tempting to calculate the ac-Stark shift of a certain ground state $|g\rangle$ by simply adding the shifts induced at different transitions (to different excited states) $|e_1\rangle, \ldots, |e_n\rangle$:

$$\Delta_S = \sum_n \frac{|\langle g|\mathbf{A}\cdot\hat{\mathbf{d}}|e_n\rangle|^2}{4\hbar^2\Delta_n}. \tag{2.98}$$

While such approach would indeed works in some isolated cases and the above formula is true as far as the energy shift is concerned, it fails to capture important dynamics. Let us consider an illustrative example of a $F = 1$ manifold coupled to a single $F = 0$, $m_F = 0$ excited state via x-polarized light, as in Fig. 2.9(c). By performing the adiabatic elimination similarly as in Sec. 2.3.1, we obtain the following Hamiltonian governing the evolution of the ground state under the ac-Stark shift inducing field, which we will call the *effective ac-Stark shift Hamiltonian*:

$$H_S = \hbar \begin{pmatrix} \frac{|\Omega_1|^2}{4\Delta} & 0 & \frac{\Omega_1^*\Omega_2}{4\Delta} \\ 0 & 0 & 0 \\ \frac{\Omega_1\Omega_2^*}{4\Delta} & 0 & \frac{|\Omega_2|^2}{4\Delta} \end{pmatrix}, \tag{2.99}$$

where we have used Ω_1 and Ω_2 as two Rabi frequencies to show to via which transitions they contribute. Yet, from now on we can assume $\Omega_1 = \Omega_2 = \Omega$, which corresponds to linear x polarization. While we clearly see that the $F = 1$, $m_F = 0$ level is not shifted, the levels $F = 1$, $m_F = \pm 1$ are shifted by the same amount. However, we observe that an additional off-diagonal term between the latter states appears that is of the same order in power and detuning as the ac-Stark shift itself. This term describes a two-photon Rabi oscillation between these levels with an effective Rabi frequency $\Omega_R = \Omega_1\Omega_2^*/(4\Delta) = |\Omega|^2/(4\Delta)$, similarly as for the case of Raman transitions. If we thus prepare the atom in one of these states (or in a superposition of one of these states and a state from another ground-state hyperfine manifold), via the effective ac-Stark shift Hamiltonian the state will be rotated within the $F = 1$ manifold. By for example starting in $m_F = 1$ we end up in $m_F = -1$ upon acquiring a π ac-Stark phase shift. To avoid this effect one must engineer a Hamiltonian diagonal in the desired basis. In general, the expression for the ac-Stark Hamiltonian element between ground state levels $|g\rangle$

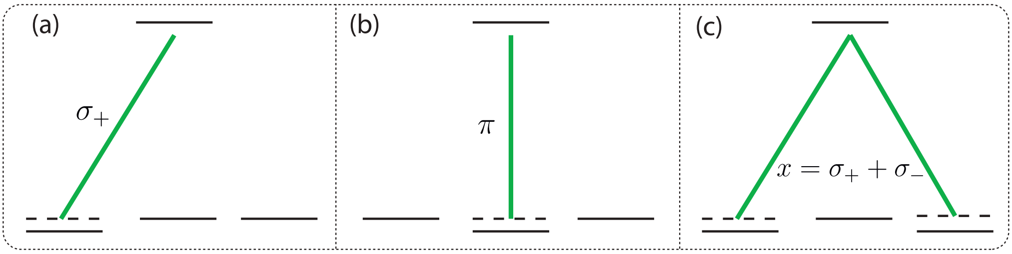

FIGURE 2.9: Three different ac-Stark shift scenarios in the ground state $F = 1$ manifold coupled to an excited state $F = 1$ manifold. While in (a) and (b) we only shift the energy of one atomic level, in (c) we shift two atomic levels and facilitate a Raman interaction between them.

and $|h\rangle$ can be written as:

$$\langle g|H_S|h\rangle = \sum_n \frac{\langle g|\mathbf{A} \cdot \hat{\mathbf{d}}|e_n\rangle\langle h|\mathbf{A} \cdot \hat{\mathbf{d}}|e_n\rangle^*}{4\hbar\Delta_n} \tag{2.100}$$

A scheme more suited to our application can be facilitated by circular σ_+, σ_- polarizations or the π-polarized light. As easily seen in Fig. 2.9(b), the π-polarized light does not couple different ground-state levels in a Raman-like fashion, and provides a diagonal effective ac-Stark shift Hamiltonian.

Finally, we elucidate on another solution to the problem of state evolution (mixing) within the manifold. Returning to the example, we can add an axial magnetic field B_z and thus set the quantization axis along the z direction. The Hamiltonian is then modified to include an additional term

$$\sum_{m_F=-F}^{F} m_F B_z \mu_B g_F |m_F\rangle\langle m_F|. \tag{2.101}$$

The levels $F = 1$, $m_F = \pm 1$ coupled via the ac-Stark shift inducing light are thus shifted[4] by $2B_z\mu_B g_F$. The shift is equivalent to a two-photon detuning δ, which changes the pattern of the Rabi oscillation. In particular, its frequency increases as $\sqrt{\delta^2 + |\Omega_R|^2}$, but most importantly the amplitude of population oscillation is reduced by a factor of $|\Omega_R|^2/(\delta^2 + |\Omega_R|^2)$. Thus, with a high enough magnetic field so that $\delta = B_z\mu_B g_F \gg \Omega_R$ the atom mostly remains in the initial state and only desirably acquires the phase due to the ac-Stark shift.

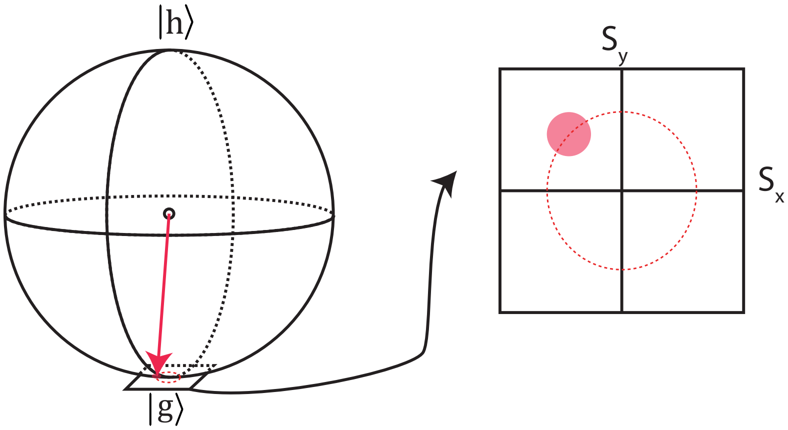

FIGURE 2.10: Pictorial representation of the Holstein-Primakoff approximation. The state of N atoms is represented by a vector on a Bloch sphere of the collective spin $\hat{S}$. The bottom corresponds to all atoms in the $|g\rangle$. If the state remains close to $|g\rangle$, we may approximate its properties by considering them on a plane rather than a sphere. The obtained phase space resembles to phase space for photons, and thus has all the desirable bosonic properties. Within the approximation, quadratures are proportional to the spin operators $\hat{S}_x$, $\hat{S}_y$. A localized state depicted here corresponds to a coherent spin state. Remarkably, however, many nonclassical states of spins, such as Fock states, can be generated, analogously as in the photonic phase space.

2.4 Spin waves

2.4.1 Spin-wave density operators

We have previously consider an amplitude of a classical spin wave B. To transfer the above framework into the quantum regime, we will consider a continuous version of the spin-wave creation operator. The operator is defined within a small volume δV, which must contain enough atoms $n(\mathbf{r})\delta V$ for the Holstein-Primakoff approximation [HP40] to hold. The approximation assumes that only a small number of atoms is actually excited, which we depict in Fig. 2.10. We define this operator as[5]:

$$\hat{B}^{\dagger}(\mathbf{r}) = \frac{1}{\sqrt{n(\mathbf{r})\delta V}} \sum_{i \in \delta V(\mathbf{r})} \hat{\sigma}_{hg}^{(i)} \tag{2.102}$$

Note that $\hat{\sigma}_{hg}^{(i)}$ is a shorthand notation for a larger operator:

$$\hat{\sigma}_{hg}^{(i)} \equiv \mathbb{1} \otimes \ldots \otimes \underset{i}{\hat{\sigma}_{hg}} \otimes \ldots \otimes \mathbb{1}, \tag{2.103}$$

---

[4] Note that we neglect any changes in single-photon detunings due to Zeeman shifts

[5] A similar framework has been followed by J. Nunn [Nun08].

which runs over all atoms within a specified volume and $\hat{\sigma}_{hg}$ stands on the i-th place, while for all other atoms we have the identity operation $\mathbb{1}$. With such definition the operator posses a set of desirable properties. In particular, the commutator between $B(\mathbf{r})$ and $B(\mathbf{r}')$ where the volumes $\delta V(\mathbf{r})$ and $\delta V(\mathbf{r}')$ do not overlap (or overlap completely if $\mathbf{r} = \mathbf{r}'$) is:

$$[\hat{B}(\mathbf{r}), \hat{B}^{\dagger}(\mathbf{r}')] = \frac{1}{\sqrt{n(\mathbf{r})n(\mathbf{r}')(\delta V)^2}} \sum_{i\in\delta V(\mathbf{r}), j\in\delta V(\mathbf{r}')} [\hat{\sigma}_{gh}^{(i)}, \hat{\sigma}_{hg}^{(j)}]. \tag{2.104}$$

Clearly the operators inside the sum commute unless $i = j$. In case $\mathbf{r} \neq \mathbf{r}'$ this always happens (the products of operators concern completely different atoms) and the above commutator equals 0. Otherwise, we can calculate its expectation value on the ground state $|0\rangle = |g_1\rangle \otimes \ldots \otimes |g_N\rangle$:

$$[\hat{B}(\mathbf{r}), \hat{B}^{\dagger}(\mathbf{r})] = \frac{1}{n(\mathbf{r})(\delta V)^2} \sum_{i\in\delta V(\mathbf{r})} (\hat{\sigma}_{gg}^{(i)} - \hat{\sigma}_{hh}^{(i)}) \xrightarrow[\langle 0|.|0\rangle]{} \frac{1}{n(\mathbf{r})(\delta V)^2} n(\mathbf{r})\delta V = \\ = \frac{1}{\delta V} \tag{2.105}$$

Finally, the commutator can be written generally in the limit $\delta V \to 0$ as:

$$[\hat{B}(\mathbf{r}), \hat{B}^{\dagger}(\mathbf{r}')] = \delta(\mathbf{r} - \mathbf{r}'). \tag{2.106}$$

2.4.2 Coherent spin-wave states

It is instructive to consider the operator evaluated on a separable spin-wave state of the form:

$$|\beta\rangle = \bigotimes_{i}^{N} (|g_i\rangle + \beta(\mathbf{r}_i)|h_i\rangle) \tag{2.107}$$

where $\beta(\mathbf{r})$ is the spatial amplitude distribution and $N|\beta(\mathbf{r})|^2 \ll 1$ so that we may disregard the normalization constant. We also assume that within a volume $\delta V(\mathbf{r})$ the function $\beta(\mathbf{r})$ does not vary for for any pair of atoms i and j within the volume $\beta(\mathbf{r}_i) = \beta(\mathbf{r}_j) = \beta(\mathbf{r})$. We then observe that the expectation value of the $\hat{B}(\mathbf{r})$ operator becomes, as the summation over the atoms in volume $\delta V(\mathbf{r})$ is trivial:

$$\langle\beta|\hat{B}(\mathbf{r})|\beta\rangle = \frac{1}{\sqrt{n(\mathbf{r})}\delta V} \sum_{i\in\delta V(\mathbf{r})} \beta(\mathbf{r}_i) = \frac{1}{\sqrt{n(\mathbf{r})}\delta V} \delta V n(\mathbf{r})\beta(\mathbf{r}) = \sqrt{n(\mathbf{r})}\beta(\mathbf{r}), \tag{2.108}$$

which is proportional to the amplitude of classical atomic polarization.

The state defined by Eq. 2.107, which we rewrite here for a plane-wave spin wave:

$$|\sqrt{N}\beta\rangle_{\mathbf{K},sep} = (1+|\beta|^2)^{-N/2}\bigotimes_i^N(|g_i\rangle + \beta e^{i\mathbf{Kr}_i}|h_i\rangle) \tag{2.109}$$

is in fact equivalent to a coherent spin-wave state defined in terms of spin-wave operators:

$$|\sqrt{N}\beta\rangle_{\mathbf{K},coh} = e^{-N|\beta|^2/2}\sum_m^\infty(\hat{b}_\mathbf{K}^\dagger)^m(\sqrt{N}\beta)^m|0\rangle. \tag{2.110}$$

See also Appendix A.6 for further considerations regarding the local density operator for spin waves and Appendix A.8 for the proof of separability of a coherent spin-wave state as defined above (Eq. 2.110).

2.4.3 Wavevector space

Since as noted before the $\hat{B}(\mathbf{r})$ operator from Eq. 2.102 only takes a small number of atoms, it is better to consider its analogue in the wavevector space, as it takes all atoms in the ensemble:

$$\boxed{\hat{B}^\dagger(\mathbf{K}) = \frac{1}{(2\pi)^{3/2}}\sum_i \frac{1}{\sqrt{n(\mathbf{r}_i)}}e^{i\mathbf{Kr}_i}\hat{\sigma}_{hg}^{(i)}}. \tag{2.111}$$

With this definition we avoid the problems with defining the small volume of operation δV. As shown in Appendix A.7, this operator also posses all the desirable commutation properties, i.e behaves like a bosonic density operator.

2.4.4 Discrete mode bases

Let us now consider a certain mode function $u_l(\mathbf{r})$ (along with its Fourier transform $\tilde{u}_l(\mathbf{K})$) describing a spatial shape of the spin wave. An operator creating a single spin wave in such particular mode is:

$$\hat{b}_l^\dagger = \int \mathrm{d}\mathbf{K}\hat{B}^\dagger(\mathbf{K})\tilde{u}_l(\mathbf{K}) = \int \mathrm{d}\mathbf{r}\hat{B}^\dagger(\mathbf{r})u_l(\mathbf{r}) \tag{2.112}$$

A particularly interesting class of mode functions are plane waves limited by the atom number density. For the mode function we take:

$$u_\mathbf{K}(\mathbf{r}) = \sqrt{\frac{n(\mathbf{r})}{N}}e^{i\mathbf{Kr}} \tag{2.113}$$

To calculate the creation operator we use to explicit form of the Fourier transform of the above mode function:

$$\begin{aligned}\hat{b}^\dagger_{\mathbf{K}} &= \int \mathrm{d}\mathbf{K}'\hat{B}^\dagger(\mathbf{K}') \int \frac{1}{(2\pi)^{3/2}}\mathrm{d}\mathbf{r}'\sqrt{\frac{n(\mathbf{r}')}{N}}e^{+i\mathbf{K}\mathbf{r}'}e^{-i\mathbf{K}'\mathbf{r}'} = \\ &= \frac{1}{(2\pi)^3}\int \mathrm{d}\mathbf{K}'\int \mathrm{d}\mathbf{r}'\sum_i \sqrt{\frac{n(\mathbf{r}')}{N}}e^{i\mathbf{K}\mathbf{r}'}e^{-i\mathbf{K}'\mathbf{r}'}\frac{1}{\sqrt{n(\mathbf{r}_i)}}e^{i\mathbf{K}'\mathbf{r}_i}\hat{\sigma}^{(i)}_{hg} = \\ &= \sum_i \int \mathrm{d}\mathbf{r}' e^{i\mathbf{K}\mathbf{r}'}\frac{\sqrt{n(\mathbf{r}')}}{\sqrt{Nn(\mathbf{r}_i)}}\delta(\mathbf{r}'-\mathbf{r}_i)\hat{\sigma}^{(i)}_{hg} = \boxed{\frac{1}{\sqrt{N}}\sum_i e^{i\mathbf{K}\mathbf{r}_i}\hat{\sigma}^{(i)}_{hg}} \qquad (2.114)\end{aligned}$$

which is the most standard spin wave creation operator known in the literature. The operator creates a single collective excitation, yet now each atom contains the spatial phase term $e^{i\mathbf{K}\mathbf{r}_i}$. This phase-dependence is in fact a plane wave and the finite extent of the atomic ensemble is implicitly encoded in the summation over the atoms.

The commutator for this discrete spin-wave operator, evaluated on the ground state, is again calculated by replacing summation by integration:

$$[\hat{b}_{\mathbf{K}}, \hat{b}^\dagger_{\mathbf{K}'}] = \frac{1}{N}\sum_i e^{i(\mathbf{K}-\mathbf{K}')\mathbf{r}_i}(\hat{\sigma}^{(i)}_{gg} - \hat{\sigma}^{(i)}_{hh}) = \frac{1}{N}\int \mathrm{d}\mathbf{r} n(\mathbf{r})e^{i(\mathbf{K}-\mathbf{K}')\mathbf{r}} \qquad (2.115)$$

Note that the above expression is equal to the overlap between respective mode functions calculated as $\int \mathrm{d}\mathbf{r}u_{\mathbf{K}}(\mathbf{r})u^*_{\mathbf{K}'}(\mathbf{r})$. If we go to an infinite atomic ensemble of volume $V \to \infty$ with a constant $n(\mathbf{r}) = N/V$ the above expression reduces to:

$$[\hat{b}_{\mathbf{K}}, \hat{b}^\dagger_{\mathbf{K}'}] = \frac{1}{V}\int_V \mathrm{d}\mathbf{r}e^{i(\mathbf{K}-\mathbf{K}')\mathbf{r}} \xrightarrow[V\to\infty]{} \delta_{KK'}. \qquad (2.116)$$

With these properties we can use the introduced operators to construct various spin-wave states, in an analogy to photonic states.

2.4.5 Decoherence in a thermal ensemble

The spin waves carry spatial phase information, and this information is inherently susceptible to random atomic motion[6]. In particular, a spin wave originally created as $|\psi\rangle = \hat{b}^\dagger_{\mathbf{K}}|0\rangle$ randomly evolves into a distinct state given by:

$$|\psi'\rangle = \frac{1}{\sqrt{N}}\sum_i e^{i\mathbf{K}\mathbf{r}'_i}\hat{\sigma}^{(i)}_{hg}|0\rangle, \qquad (2.117)$$

---

[6] The derivation here roughly follows the idea presented by K. S. Choi [Cho11].

since every atom previously at position $\mathbf{r}_i$ moves to $\mathbf{r}'_i$. Since in simplest scenario we desire the spin-wave state to remain unchanged, the overlap between the two states given by will show us the effective decoherence:

$$|\langle\psi'|\psi\rangle|^2 = \frac{1}{N^2}\left|\sum_i e^{i\mathbf{K}(\mathbf{r}_i-\mathbf{r}'_i)}\right|^2 \tag{2.118}$$

We can calculate this overlap given the statistical distribution of atomic displacements $\mathbf{r}_i - \mathbf{r}'_i$ in the ensemble. In particular, we are interested only in displacements along the direction of $\mathbf{K}$. The displacement of interest $\hat{e}_{\mathbf{K}}(\mathbf{r}_i - \mathbf{r}'_i)$ is then distributed in the same way as the velocity along the direction of $\mathbf{K}$, thus $\hat{e}_{\mathbf{K}}(\mathbf{r}_i - \mathbf{r}'_i) = v^i_{\mathbf{K}}t$, where $v^i_{\mathbf{K}}$ is the velocity of atom i along the direction $\mathbf{K}$ and t is the evolution time. Such velocity follows the one-dimensional Maxwell-Boltzmann distribution $v_{\mathbf{K}} \sim \sqrt{\frac{m}{2\pi k_B T}}e^{-mv^2_{\mathbf{K}}/(2k_B T)}$, where m is the mass of Rb atom. Our overlap can thus be calculated as the average value on the thermal ensemble:

$$|\langle\psi'|\psi\rangle|^2 = \left|\int \mathrm{d}v_{\mathbf{K}}\sqrt{\frac{m}{2\pi k_B T}}e^{i|\mathbf{K}|v_{\mathbf{K}}t}e^{-\frac{mv^2_{\mathbf{K}}}{2k_B T}}\right|^2 = e^{-|\mathbf{K}|^2 t^2 \frac{k_B T}{m}}. \tag{2.119}$$

The decoherence thus follows a Gaussian decay e^{-t^2/τ^2} with a characteristic time τ and the associated decoherence rate:

$$\tau^{-1} = \Gamma = |\mathbf{K}|\sqrt{\frac{k_B T}{m}}. \tag{2.120}$$

Remarkably, $\sqrt{\frac{k_B T}{m}} = v_{\mathrm{rms}}$ is the root-mean square of a velocity component.

Note that this relation is quite different from what is observed in warm atomic ensembles, where decoherence is due to diffusion of atoms in a buffer gas environment. The motion is thus diffusive rather than ballistic. There the decay is exponential in time ($e^{-t/\tau}$) with the decay rate $\Gamma = D|\mathbf{K}|^2$, where D is the diffusion coefficient [PW14].

Chapter 3

Cold-atom experimental setup

3.1 Single-photon resolving camera

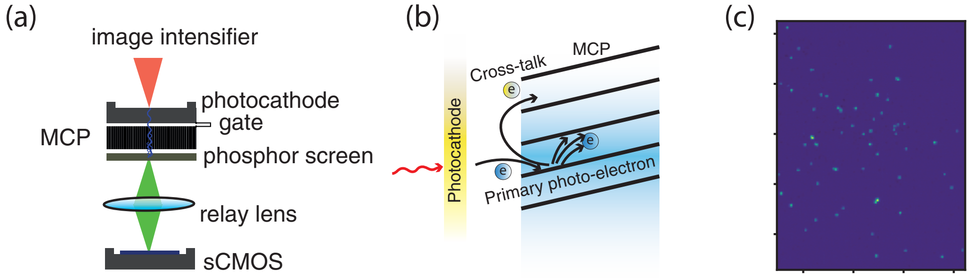

FIGURE 3.1: A simplified schematic of the I-sCMOS camera (a) and the process of electron multiplication in the MCP (b) along with generation of spurious cross-talk. An actual lens used in the device is a high numerical-aperture imaging system composed of 6 lenses. An example frame registered by sCMOS camera is shown in (c). Dots correspond to single-photon detection, or inherently, dark counts.

An essential component of the detection setup is a spatially-resolved single photon detector comprising an image intensifier based on a microchannel plate coupled with fast and sensitive scientific complementary metal-oxide semiconductor (sCMOS) sensor. The entire intensified sCMOS camera (I-sCMOS) allows for spatially-resolved detection of single photons. The device is depicted in Fig. 3.1(a).

The image intensifier is a so-called third generation device from Hamamatsu (model V7090D). The intensifier consists of a photocathode, a double-stage microchannel plate (MCP) and a phosphor screen. The GaAs photocathode has a 20% quantum efficiency (manufacturer guarantees min. 18%). Photoelectrons emitted from the photocathode are attracted to the MCP thanks to a voltage differential of 200 V. The voltage can be rapidly gated thanks to a Photek GM300-3 module. The electrons are then accelerated and multiplied thanks to the MCP voltage of 0.25 up to 1.75 kV, with a typical multiplication factor of 10^5. The MCP is composed of nearly 10 million microchannels, ca. 6 μm diameter each. As shown in Fig. 3.1(b), some electrons might get reflected from the MCP and enter an adjacent microchannel to yield a deleterious cross-talk effect. This effect typically prevents proper measurement of autocorrelations in a single region and imposes the need to use sophisticated post-processing [LPW18].

Electrons leaving MCP are accelerated by a high voltage of 6 kV and hit the phosphor screen producing bright flashes of green light. The phosphor flashes decay in about 200 ns and are highly random in terms of total brightness due to the stochastic electron multiplication process. A specialized lens (Stanford Computer Optics, $f/\# = 1.1$) is used to image these flashes onto the sCMOS sensor. The sCMOS sensor is a fast and low-noise 5.5 MPix Andor Zyla camera. If used with a very small frame, it allow acquisition rates of up to 6000 fps. An example image from the camera is shown in Fig. 3.1(c).

The registered flashed are processed in real time. Each flash is fit with a local Gaussian to recover its centroid. These detections are stored in the form of positions for further analysis, which greatly reduces the amount of stored data, compared with storing full frames. Low noise of the camera guarantees that the average intensity of the brightest pixel is 500 times higher than the noise level. We thus avoid losing counts due to the discrimination process or generating spurious dark counts by setting the detection threshold too low.

The basic dark count level of the device is typically of the order of 0.2/px/s (which we calculate for a pixel of the sCMOS camera), which in fact is very low. For a typical measurement on a large area of 2×10^4 px during 1 μs we obtain approx. 5×10^{-3} dark counts. Typical mode area of a photon in the far field we register is only of the order of tens of pixels, yielding very low dark count rate per mode. This corresponds to ca. 10 darks counts per second and per mode, which is characteristic of best available avalanche photodiodes. This figure could be brought down even further by reducing the modes size or cooling of the electron amplifier or the photocathode.

The I-sCMOS device has been used in our group for several experiments and various papers (not covered by this thesis) contain details of its operation in various modes and scenarios: [CWB14; Chr16b; DCW14; Par18b; LPW18; Chr16a; Dąb18].

3.2 Magnetooptical trap

Trapping atoms in a magneto-optical trap (MOT), that simultaneously guarantees very low motional temperatures ($\sim$ 100 μK), is a well-established technology [Phi98]. With proper optimization, the setup becomes only slightly more complex than its analogue using warm atomic vapours. Yet, the performance and the level of control over the trapped atomic ensemble are unmatched.

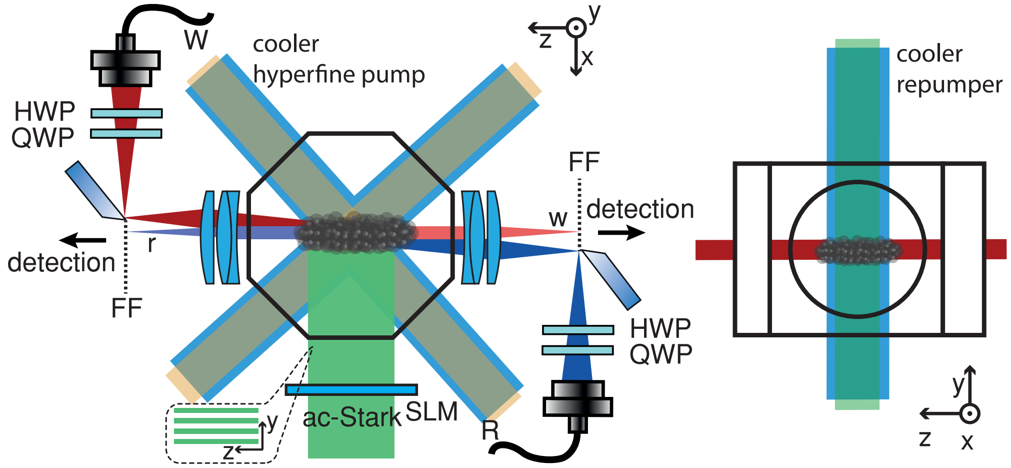

FIGURE 3.2: Schematic of the core of the experimental setup with marked write/read lasers and write/read photon modes. The write and read beams are counter-propagating and are separated from the generated photons in the far field (FF) of the atomic ensemble. The photons are collected from the MOT via a set of high field-of-view lens. The ac-Stark modulation beam shaped with a spatial light modulator (SLM) is applied from the side.

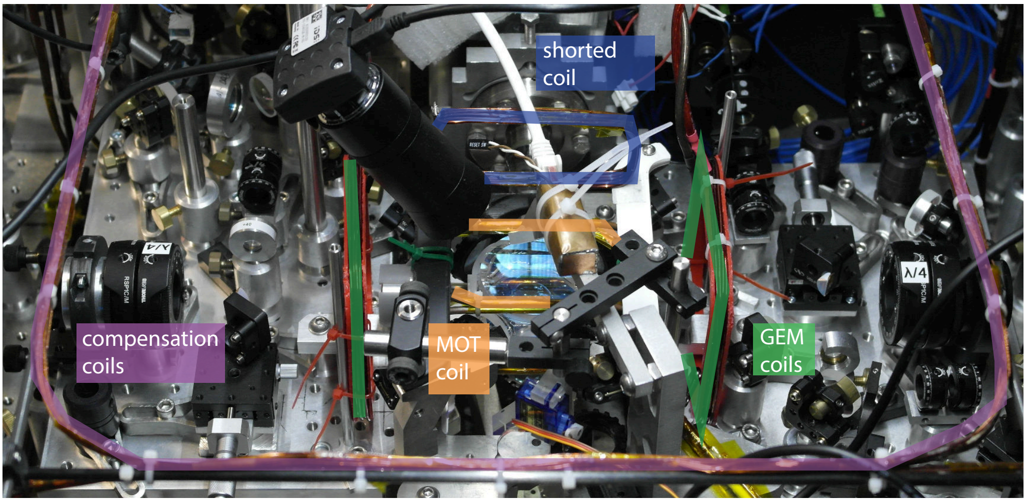

FIGURE 3.3: Essential magnetic coils installed around the MOT: the small trapping coil, shorted coil for eddy currents compensation and large coils generating a static bias field and compensating any other residual fields. The magnetic fields are monitored with a semiconductor magnetometer (HMC2003). GEM coils are installed for future applications.

For the experiments presented in this thesis, we have assembled a standard magneto-optical trap setup, with several additional goals in mind. In particular,

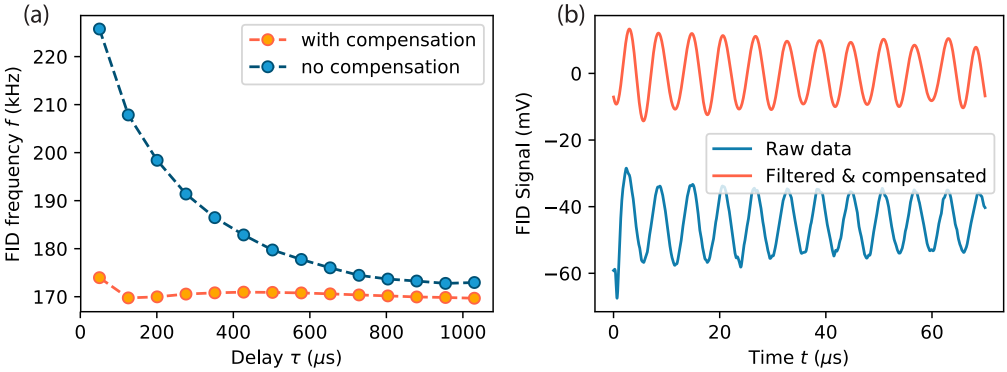

FIGURE 3.4: Compensation of magnetic fields induced by eddy currents created after switching off the MOT coils. For this measurement, we apply a small transverse instead of the longitudinal magnetic field to obtain a strong spin-precession signal by probing atoms with linearly polarized light (FID, free-induction decay). The atoms are first prepared in the $F = 1$, $m_F = 1$ state. We then apply 50 μs long probing sequences. Before each sequence atoms are again optically pumped. From each sequence, we extract the central oscillation frequency (proportional to the magnetic field with a constant 1.4 kHz/mG) and plot it as a function of delay after the MOT coils are switched off. We observe that without a shorted coil the spurious fields change on a 0.5 ms timescale, while an additional coil guarantees their rapid stabilization.

the atomic quantum can store quantum information only in a well-controlled magnetic field. This requirement causes the need to rapidly switch off the trapping magnetic field. Second, a high optical depth is highly beneficial for the memory. Finally, good optical access to the chamber is needed to perform a variety of light-based manipulations. The setup has been largely inspired by recent experiments in Canberra [Spa13] and Hong Kong [Zha12].

Figure 3.2 presents to the core of the MOT setup. The cooling beam is sent to the octagonal glass chamber from six sides. The repumping beam is sent only in the vertical direction along with the cooling light. The beams are expanded to their maximum diameters of 2.5 cm, limited by the apertures of vacuum chamber windows.

The trapping magnetic fields are produced with 125 A current in a low-inductance MOT coil, designed similarly as in [Zha12]. Such configuration supports gradients of 25 G/cm in the MOT. The elongated shape of the MOT coil guarantees an elongated shape of the trapped atomic ensemble. A coil switch based on MOSFET transistors has been designed to turn off the magnetic field in less than a few μs. The circuit features an additional high-inductance current-storage coil to allow rapid activation of the MOT coil as well. See Fig. 3.3 for the overview of coils installed around the setup.

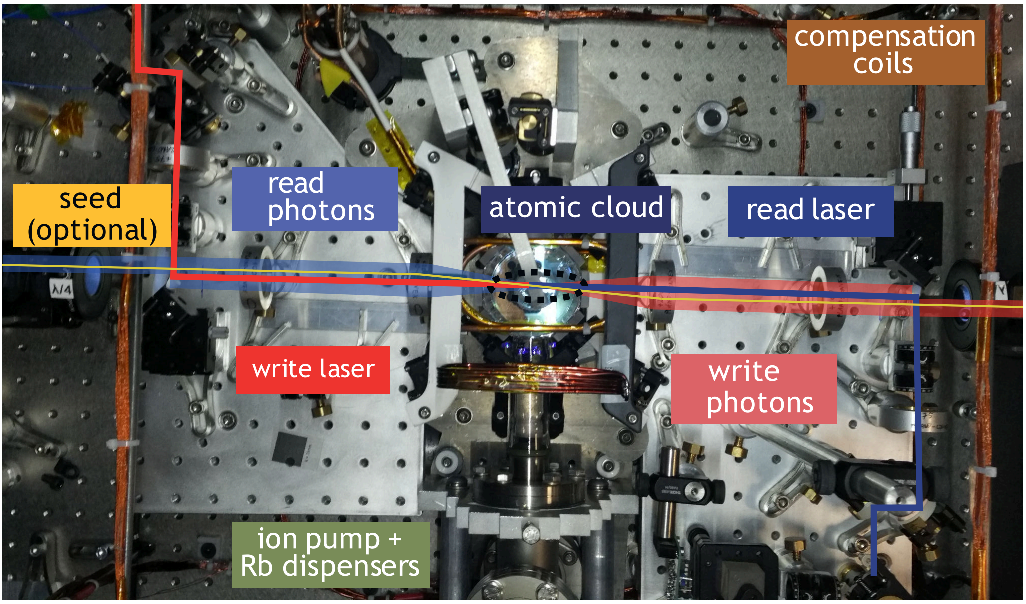

FIGURE 3.5: Essential magnetic coils installed around the MOT: the small trapping coil, shorted coil for eddy currents compensation and large coils generating a static bias field and compensating any other residual fields. The magnetic fields are monitored with a semiconductor magnetometer (HMC2003).

Additional large coils around the entire setup allow setting a constant bias field. Furthermore, we have installed a shorted coil above the MOT chamber to compensate for the eddy currents induced in the metal elements below the chamber. The position and shape of the coil have been determined experimentally. In particular, we performed an additional experiment and set a small bias field in the x direction, so that we obtained a strong spin-precession signal, as the atoms are z polarized with an optical pump. A weak, linearly polarized beam is then sent into the setup to observe the polarization rotation signal (or more precisely the rotation of polarization axis with respect to initial direction as measured on a balanced photodetector), also known as the free-induction decay (FID) of the atomic spin coherence. See Fig. 3.4(b) for an example trace of the FID signal. By measuring the FID signal we observed that indeed our setup allows rapid decay of stray magnetic fields after MOT coils are turned off. See Fig. 3.4(a) for the final result with and without the shorted compensation coil. Chapter 5 provides more detailed descriptions of FID measurements.

During operation of the quantum memory, that is for the proper experiment, we set an approximately 50 mG bias magnetic field along the z direction, which allows better optical pumping and selection of a proper magnetic sublevel.

For the quantum memory, we use several additional beams. A hyperfine pump

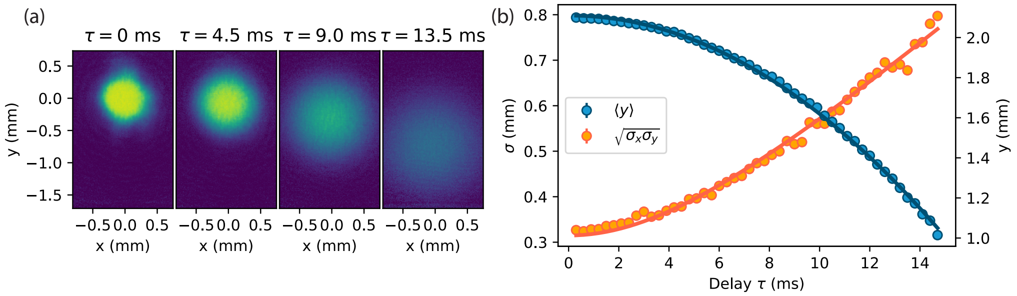

FIGURE 3.6: Free thermal expansions of the atomic cloud observed in absorption of a weak probe light. We fit the average width of the cloud to obtain the temperature of 23 μK. We also observe the free fall of atoms in the gravitational field.

laser is sent along with the cooling beams. Write and read lasers are sent through a lens system, as shown in both Figs. 3.2 and 3.5. The Zeeman Pump laser is also sent approximately along the write laser beam. The lens system has been modelled in Zemax to allow collection of a large span of emission angles from the MOT. The final objective is composed of one doublet and one singlet lens and captures photons emitted at an angle of up to 12 degrees from the z axis. The system is optimized also in terms of aberrations. D-shaped mirrors are used to separate photons from the lasers in the far field.

The far field, as marked in Fig. 3.2, is then imaged onto the I-sCMOS camera. There, only long lenses are used so no significant aberrations are introduced. The system allows transmission of photons through long atomic vapour filters. Alternatively, we use single-mode fibres for the collection of photons. The fibres are equipped with custom collimators, which focus the fibre mode in the far field. In the MOT, fibre modes are several times smaller than the size of the atomic ensemble.

Fig. 3.7 presents the typical timing sequence of the experiment, used both in the configurations based on detection with the single photon-resolving I-sCMOS camera (panel a) or avalanche photodiodes coupled to single mode fibres (panel b). Such sequence illustrates a typical operation of a DLCZ quantum memory, that is the main subject of Chapters 4 and 6. With slight modifications it will serve as a basis for sequences used in Chapters 7 and 8.

The sequence is typically repeated at the 420 Hz refresh rate of the spatial light modulator (SLM). In a single cycle, the atoms are trapped for 1.8 ms in the case of the I-sCMOS experiment. Avalanche photodiodes can be used instead of the I-sCMOS, for which we can repeat the experimental sequence faster. Then, typically 1.1 ms is used for cooling. With a relatively high Rb vapour pressure ($\sim 10^{-7}$ mbar) and cooling laser (70 mW total power) as well as a detuning of 15 up to 25 MHz to the red from the $5^2S_{1/2}$ $F = 2 \rightarrow 5^2P_{3/2}$ $F = 3$ transition

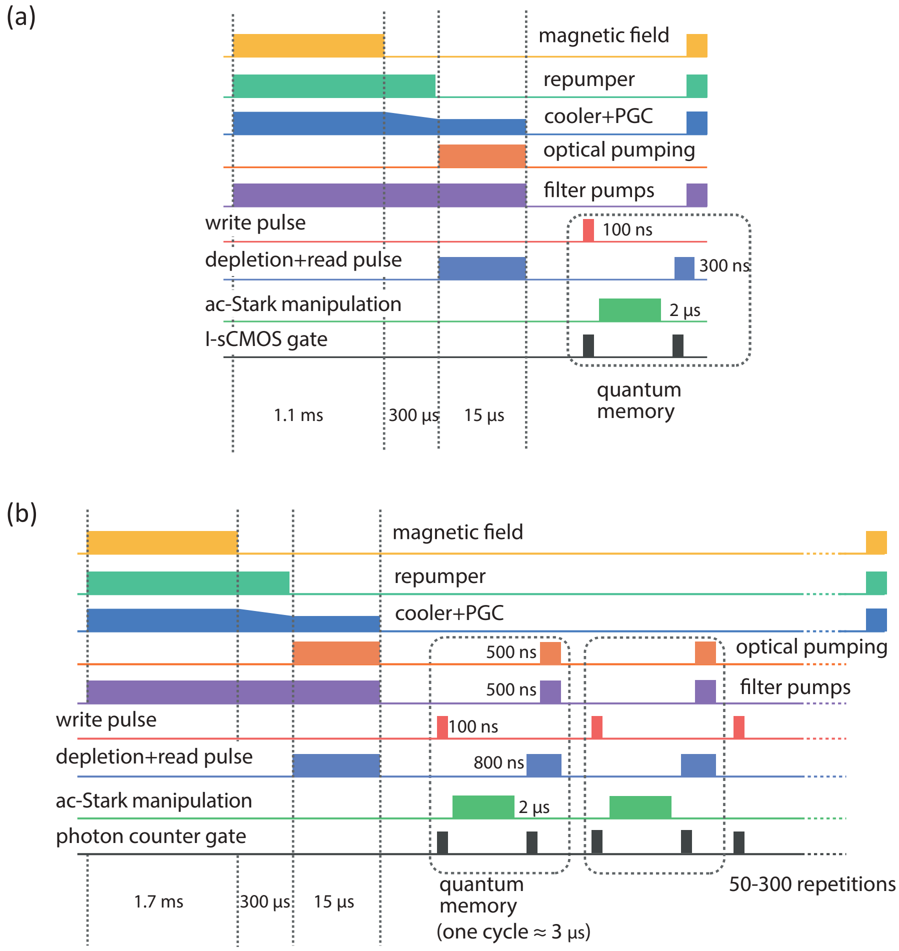

FIGURE 3.7: Timing sequence of the experiment. Panel (a) portrays the timing sequence used when wavevector-resolved detection using an I-sCMOS camera is performed. Due to camera frame rate limitation, only one cycle of QM per one MOT is performed. In (b) we show the timing sequence for the experiment using few-mode detection using APDs. One MOT cycle fits up to 300 QM cycles. In both cases the sequence is repeated at the rate of 420 Hz.

the sequence allows us to maintain a stable atom number in the MOT. We found that by tuning the laser closer to the resonance allows trapping the atoms faster, yet causes reaching lower final optical depths.

The number of atoms saturates after only approx. 10 s that include thousands of MOT cycles, yielding an optical depth of 30 up to 200 (strongly depending on how many times the quantum memory cycle is repeated), as measured at the $5^2S_{1/2}\ F = 2 \rightarrow 5^2P_{3/2}\ F = 3$ closed transition of the D2 line. Trapping is followed by polarization gradient cooling in optical molasses (PGC) with the cooling laser detuning increased to 31 MHz that allows us to reach a temperature of 23.2 ± 0.4 μK. We verify the temperature via a standard time-of-flight measurement, as illustrated in Fig. 3.6.

The atoms are finally prepared in the $F = 1$, $m_F = 1$ state through optical pumping with $> 70\%$ efficiency, using one laser (15 mW power) tuned to the $5^2S_{1/2}$ $F = 2 \rightarrow 5^2P_{1/2}$ $F = 2$ transition which we call the "Hyperfine Pump" and another circularly-polarized laser ("Zeeman Pump", 10 mW power) tuned to the $5^2S_{1/2}$ $F = 1 \rightarrow 5^2P_{3/2}$ $F = 1$ transition.

A single QM cycle consists of a 100 ns long write pulse (varying power, typically ~ 2 μW), optionally a 2 μs long ac-Stark spin-wave manipulation pulse, and 300 ns read laser pulse (300 μW power). The write pulse is left-circularly polarized and red-detuned by 25 MHz from $5^2S_{1/2}$, $F = 1 \rightarrow 5^2P_{3/2}$, $F = 2$ transition). The counter-propagating read laser pulse is right-circularly polarized and resonant with $5^2S_{1/2}$, $F = 2 \rightarrow 5^2P_{1/2}$, $F = 2$ transition. See also Fig. 3.2 for experimental geometry.

All lasers are locked to either cooler or repumper laser through a beat-note offset lock [LPW17b]. In the I-sCMOS experiment, the image intensifier gate is open during writing and reading. The sCMOS camera captures photon flashes during both gates, in separate spatial regions of the image intensifier. In the APD experiment, the memory cycle is followed by a short 500 ns clear pulse (consisting of the read laser pulse, optical pumping and additional pumping of filtering cells to maintain hyperfine polarization). The APD gate is typically kept open only during the initial 80 ns of the read pulse, to optimize the signal-to-noise ratio.

3.3 Generation of coherent spin-wave states

To generate a highly-populated coherent spin-wave state we can seed the write optical field in the write interaction, to allow for parametric amplification of both the seed light and the spin wave. The process is governed by a squeezing Hamiltonian so both the seed light and the spin waves are amplified; however, for strong and coherent seed light, the generated spin-wave state is close to a coherent state. The seed light, detuned by the Rubidium-87 hyperfine splitting from the write laser light needs to be phase-coherent with the write laser for the process to be efficient. We use an electro-optic modulator (EOM) fed with an SHF (super high frequency - an official designation for the 3 to 30 GHz frequency range) signal with central frequency $f_{\mathrm{SHF}} = 6.834$ GHz to generate sidebands (see Fig. 3.8 for experimental schematic). The SHF signal is additionally modulated using a 60 MHz sine wave from a direct digital synthesizer (DDS). Modulated light consisting of harmonic frequency components separated by f_{SHF} is sent to an FP-cavity and its reflected portion is directed onto a fast photodiode. The photodiode re-

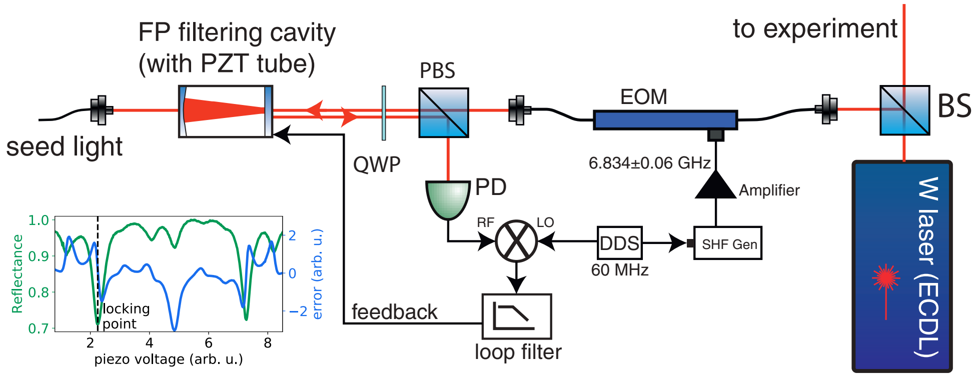

FIGURE 3.8: Generation of seed light. To generate phase-coherent light detuned from the write laser by exactly the Rubidium-87 hyperfine splitting, we send some of the write laser light into an electro-optic modulator (EOM) producing sidebands at $f_{\mathrm{SHF}} = \pm 6.834$ GHz. A Fabry-Pérot (FP) scanning cavity is used to filter out all sidebands except the desired one. For this, we additionally modulate the f_{SHF} frequency at $f_{\mathrm{RF}} = 60$ MHz. Light reflected from the cavity is registered using a photodiode (PD) and the signal is mixed with the $f_{\mathrm{RF}} = 60$ MHz modulation, producing a locking signal for the cavity (inset).

gisters beat-notes (RF) at 60 MHz, which are then mixed with the 60 MHz local oscillator (LO) signal. After the loop filter, we obtain a locking signal, which thanks to a proper choice of relative phases between LO and RF allows locking only at the desired sideband (the locking signal slopes for positive and negative shifts differs in sign). For seeding purposes we are interested only in the term which is shifted by $-f_{\mathrm{SHF}}$ from the original laser frequency. The cavity reflects the fundamental unmodulated light and other sidebands, resulting in 26 dB net attenuation of all unwanted components.

The system can then be used to seed the Raman process. As demonstrated in Fig. 3.5 the seed beam is sent along with the write beam, imitating a scattered photon. We are also able to send two seed beams simultaneously, with a simple setup illustrated in Fig. 3.10.The system is prepared in the full analogy with the spontaneous scheme. Then, in the transmission of seed light strong amplification is observed, as in Fig. 3.9(a). The amplification strongly depends on the two-photon detuning δ. At non-zero detuning, oscillations are observed at the frequency determined by the detuning. Note that here we calculate the two-photon detuning from the ac-Stark shifted resonance. Notably, if after a delay we send only the write laser pulse (Fig. 3.9(b)), we observe strong emission in the direction of seed light. This is due to continued parametric amplification, now seeded by the spin wave present in the ensemble. The process is one of the easiest ways to confirm proper operation of the memory, at least for classical light.

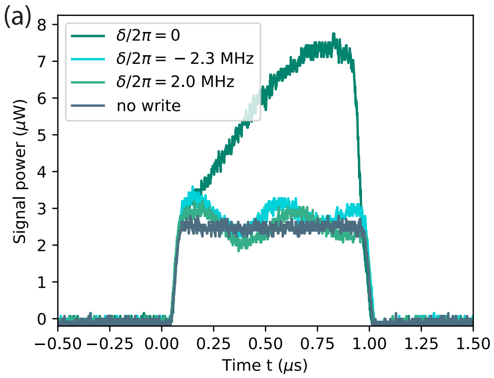

FIGURE 3.9: Parametric amplification of spin waves and seed light (a) as well as continued amplification after a delay, which arises due to the presence of spin waves. In (a) we can achieve a total gain of 3.7 dB a the single-photon detuning $\Delta/2\pi = -57$ MHz from the $F = 2,\ 5P_{3/2}$ level.

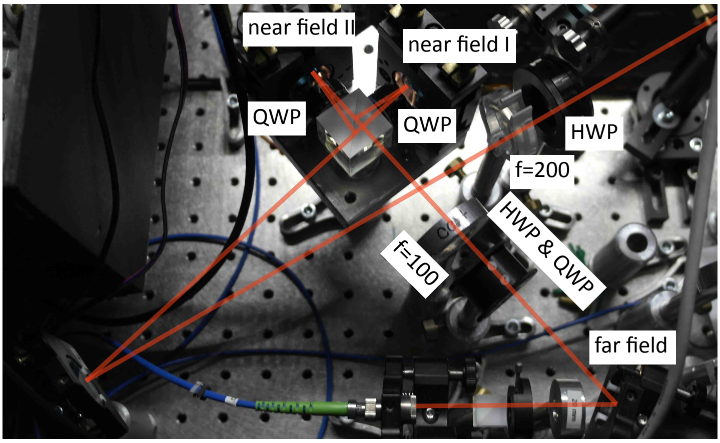

FIGURE 3.10: Setup for generating two seed beam sent at an angle. The two beams enter with a diagonal polarization at a PBS. The two polarizations are reflected by two mirrors at different angles. The mirrors are then imaged onto the MOT, so the angle of the mirror is mapped onto the angle-of-incidence of each seed beam.

3.4 Filtering

Two separate rubidium vapour cells are used to filter out stray write and read laser light from write and read photons. The 10-cm-long cells are paraffin-coated and contain 99.4% isotopically pure ^{87}Rb as well as buffer gases (Precision Glassblowing, 1 Torr Kr for both write and read filters) that keep the pumped atoms in the interaction region. The cells are pumped with 50 mW of resonant laser light (with $5^2S_{1/2},\ F = 2 \rightarrow 5^2P_{1/2}$ and $5^2S_{1/2},\ F = 1 \rightarrow 5^2P_{3/2}$ for write and read

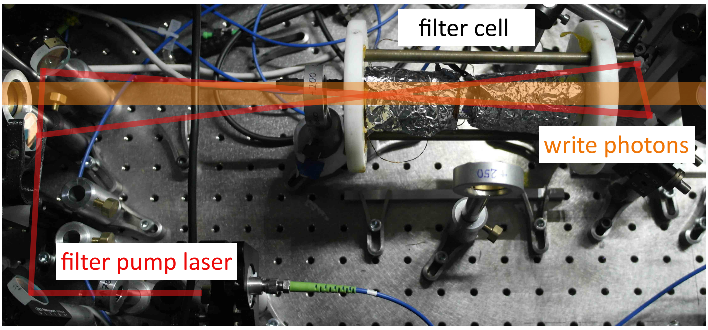

FIGURE 3.11: The photograph of the filter setup. Write photons pass through the filter once, from right to left. The filter pump laser is sent through the cell a total of four times.

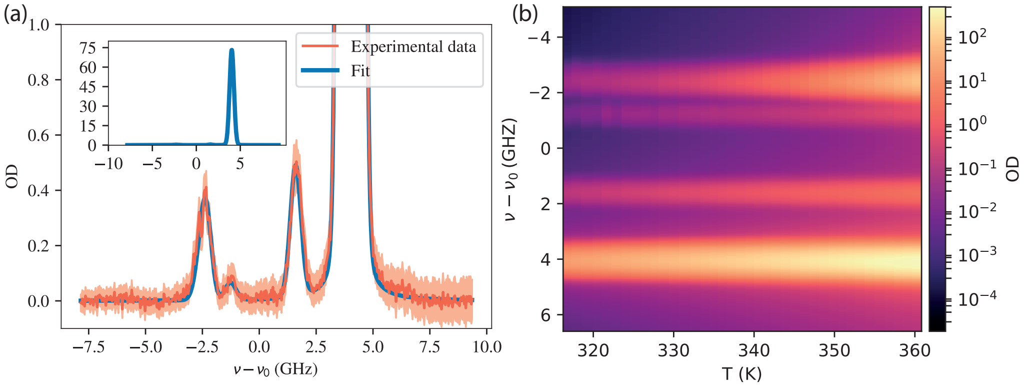

FIGURE 3.12: Characterization of one of the filtering systems. In (a) the data points (at the temperature of 320 K) correspond to a measurement of absorption of the weak probe beam while the fit is the theoretical prediction of OD based on a Voigt-profile absorption model including optical pumping. The inset shows the OD in a larger scale (only the fitted function), demonstrating very high attenuation of write laser light ($\nu - \nu_0 = 4.3$ GHz detuning). Simultaneously, high transmission of photons ($\nu - \nu_0 = -2.5$ GHz detuning) is achieved. Detuning is given with respect to the line centroid at ν_0. Two more central absorption peaks correspond to a residual amount of ^{85}Rb in the filtering glass cell. Panel (b) presents the OD through a range of temperature. Above ca. 340 K we observe a quench in the optical pumping efficiency due to radiation trapping. Note that even though the residual Rubidium-85 is not directly pumped, for this isotope we also observe a significant population imbalance.

photon filters, respectively). Along the developments presented in this thesis, the setups have been improved from double-pass to quadruple-pass, as seen in Fig. 3.11. One of the cells has also been changed to a 5 Torr N_2 cell without paraffin coating. For this new cell, we have observed quite different characteristics, typically requiring lower temperatures.

The optical pumping is active at all times except when the image intensifier gate is open. Figure 3.12 presents a characterization of the write filter (we measured the comparable characteristics also for the read photons filter). Both filters are characterized by OD > 70 for the laser light and approx. 65% transmission for single photons generated inside the atomic quantum memory. We have seen that it is essential to purify write and read laser light and remove any broadband components. In particular, we observed strong Raman scattering in optical fibres that would later pass through the filters and contribute to noise. It was thus important to place narrowband interference filters right after the fibre collimator output.

3.5 Ac-Stark beam shaping

The final essential part required for the proposed experiments is a setup to generate desired light patterns. With such patterns, we want to imprint a spatially dependent phase induced via the ac-Stark shift onto the atomic ensemble. Precise shaping of the ac-Stark beam is essential to obtain the desired effect. This is essential even if a spatially-constant intensity is desired.

For accurate shaping of the beam we use a spatial light modulator (SLM, Holoeye Pluto) coupled with a charge-coupled device (CCD) camera (Basler Scout scA1400-17fm). The SLM is illuminated with an elliptically shaped beam from a semiconductor taper amplifier (Toptica, BoosTA) seeded with a light from an ECDL (Toptica DL 100) locked using an offset-lock setup. Temporal ac-Stark pulse profile is controlled with an acousto-optic modulator. Both the CCD camera and the atomic ensemble are situated in the same image plane of the SLM ($\times 1.7$ magnification). Importantly, the same lenses are used and the only difference between the camera plane and the atomic cloud plane is a flip mirror instead of a vacuum chamber window on the beam path. With this, we achieve the best possible representation of light intensity in the vacuum chamber, distorted by a minimal number of optical elements.

The camera can then provide feedback to the computer program that controls the SLM, which is used to actually generate the desired pattern, with a particular focus on intensity homogeneity. The program operates by first mapping the SLM coordinates onto the camera pixels using a National Instruments Vision module, and then iteratively adjusting the SLM display to achieve an intensity distribution closest to the target one. The optimization procedure begins with a white rectangle displayed on the SLM. Next, at each iteration, the error distribution i.e. the difference between pattern observed on the camera and the target is calculated. According to that error, the SLM pattern is changed proportionally.

In later stages of the experiment (Chapter 7) we have improved the setup to feature two patterns that may be selected rapidly. The setup is featured in Fig.

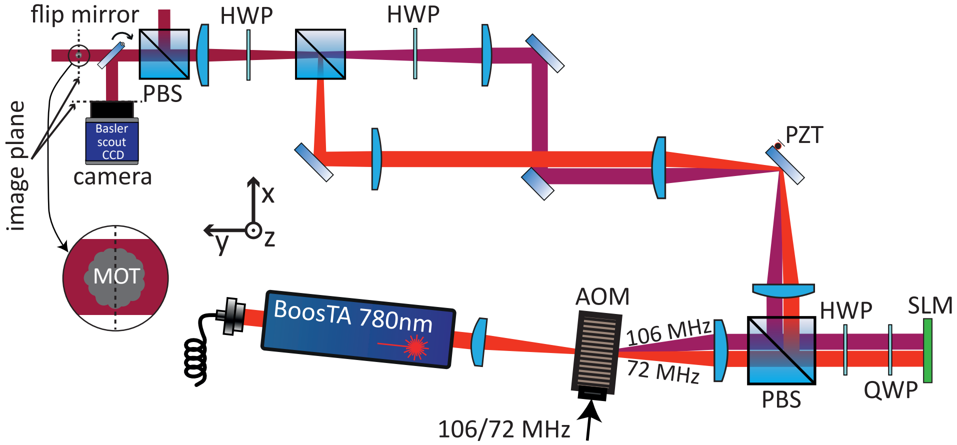

FIGURE 3.13: Schematic illustrating the rapidly-reprogrammable double pattern imaging system (HWP - half-wave plate, QWP - quarter-wave plate, PZT - piezoelectric transducer, AOM - acousto-optic modulator). The AOM diffracts the input beam onto disparate regions of the SLM, which are then simultaneously imaged onto the MOT after being combined on the polarizing beamsplitter (PBS). The final PBS projects both light fields onto the z polarization. Desired patterns are prepared using an iterative optimization algorithm with camera-based feedback.

3.13, An acousto-optical modulator (AOM) situated in the far field of the spatial light modulator (SLM) is used to control the position of the beam at the SLM and carve out ~ 2 μs long pulses. With this setup, we may select which region of the SLM is illuminated by changing the frequency of the AOM, which is done in real time using a direct digital synthesizer (DDS). On the SLM matrix, we display two patterns in two disparate regions. The SLM surface is then imaged onto a D-shape mirror which sends each pattern on a different path. The two paths are joined on a polarizing beamsplitter (PBS) before the vacuum chamber, but now the two patterns overlap. Note that in the current configuration we lose half of the power at the final PBS. An additional mirror placed in the far-field of the SLM is used for fine adjustment of grating position in the vertical direction with the help of a piezoelectric transducer (PZT).

3.6 Two-photon transitions setup and locking

Higher excited levels in the Rb atom give access to many interesting physical processes such as a plenitude of four-wave mixing processes or Rydberg physics. We have selected one of the simplest ways to access some of these phenomena by selecting a convenient $5D_{3/2}$ manifold, which can be excited via two-photon transitions involving $5P_{3/2}$ manifold (780 and 776 nm) as well as $5P_{1/2}$ mani-

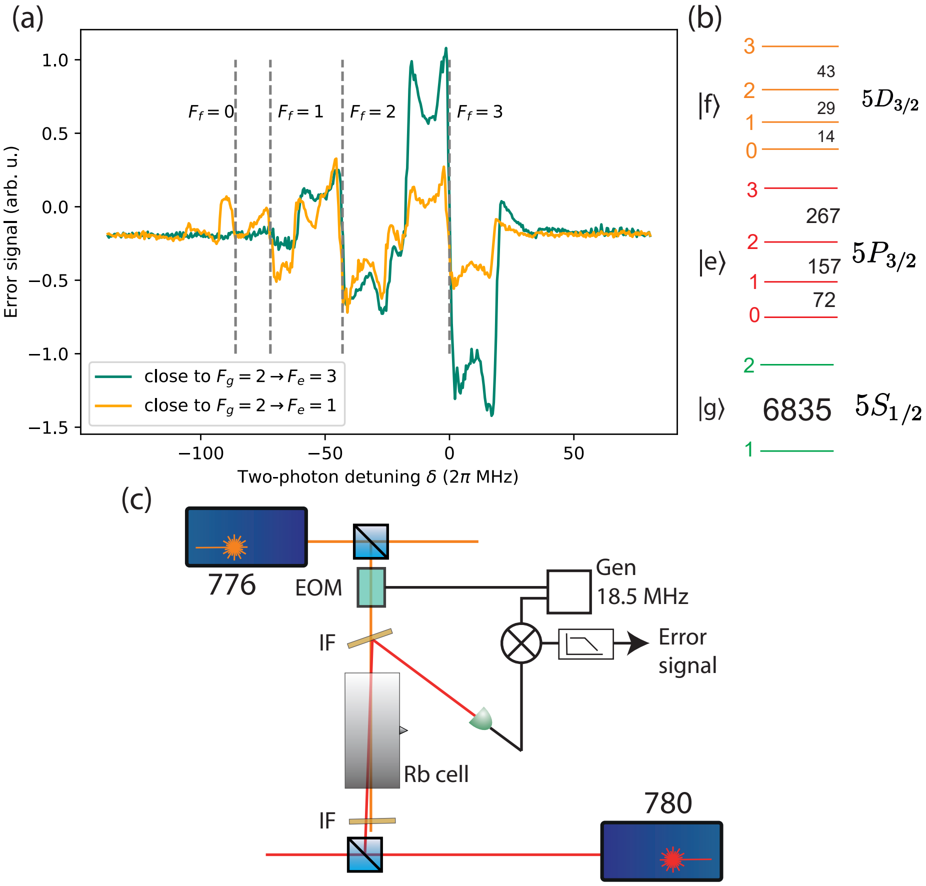

FIGURE 3.14: Modulation transfer spectroscopy setup for locking the 776 nm laser to the two-photon resonance. The obtained error signal at two different single-photon detunings within the Doppler-broadened line is presented in (a). The two-photon detuning δ is measured from the resonance corresponding to $F_f = 3$. In (b) we show the relevant hyperfine energy levels with spacings between them given in MHz. Panel (c) presents the experimental setup, described in the text.

fold (795 and 762 nm). All transitions thus lie close to each other in terms of wavelength and same elements (mirrors, lenses) may be used for all the beams. These transitions have been explored in our group in the context of four-wave mixing and magneto-optical polarization rotation in warm atoms before [PW15; PLW16b; LPW17a; PLW16a]. The 776 nm laser was thus easily calibrated using a standard diode initially intended for for 780 nm. In warm atoms however we typically operated far from the single-photon resonance, thus the locking setup presented in [PLW16b] had to be modified. The new locking setup (Fig. 3.14(c)) is based on technique called modulation transfer spectroscopy. In this technique, as opposed to the simpler frequency modulation spectroscopy, we do not modulate the probe light. Instead, we modulate the pump (coupling) light using a phase-only EOM equipped with a custom resonant circuit, here at 776 nm, and probe the system with an unmodulated beam, here at 780 nm. The probe beam is then measured and its RF (18.5 MHz) signal demodulated (mixed) with the pump modulation. The modulation is thus only transferred to the probe beam, and detectable in the demodulated signal if the two beams interact in the vapour cell. Finally, the RF signal is demodulated with a mixer and a low-pass filter.

A significant advantage of this scheme is the stability of the error signal offset, as out of resonance we will simply not have any signal. Furthermore, we become nearly immune to the residual amplitude modulation of the EOM, as the amplitude modulation is transduced weakly by the atoms.

The very mechanism of the modulation transfer, in fact, varies with the modulation frequency. At low frequencies (kHz) it may be understood as simply a slow sweeping of an EIT peak or dip. At higher frequencies (MHz) the mechanism is actually a four-wave mixing process between the pump, probe and the sidebands.

The obtained error signal as we scan the 776 nm laser is presented in Fig. 3.14(a). All four levels of the highest excited state manifold are visible. By changing the single photon detuning within the Doppler-broadened line corresponding to the $F_g = 2$ manifold we observe relative changes of various components that arise due to selection rules.

Chapter 4

The Multimode Quantum Memory

In this chapter demonstrate a massive improvement in the number of modes processed by quantum memory. The experimental realization is accomplished through multiplexing of angular emission modes of a single quantum memory and by employing a spatially-resolved single-photon detection. The setup is shown to generate photons in 665 pairwise-coupled modes, exploring the regime of multimode capacity with simultaneous extremely low noise-level achieved with stringent, spatially-multimode yet simple and robust filtering. We use a single-photon resolving camera to measure both correlations and auto-correlation unambiguously proving quantum character of light. Note that throughout our results no background subtraction is performed - in contrast to any previous experiments with single-photon sensitive cameras [Edg12; MDL14; CDW17; DPW17]. We achieve the quantum memory lifetime of more than 50 μs which combined with the multimode capacity invites real-time feedback processing of stored excitations and paves the way towards promptly achieving fast generation of single and multi-photon states [Nun13; CDW17].

We will start with a motivational introduction describing a multi-photon generation protocol based on the developed quantum memory. Next, in Sec. 4.2 we briefly describe the operation of the memory, as its essentials are already covered in Chapters 2 and 3. Subsequent sections describe the main experimental results. The results presented here are largely based on Ref. [Par17], where parts of the text and some figures are published. This Chapter however contains many additional figures and descriptions.

4.1 Quasi-deterministic photons

First, we propose the potential application of our scheme as a platform for multi-photon state generation. Figure 4.1 pictures a protocol utilizing the multi-pixel capability of the single-photon resolving camera to enhance the generation of multi-photon states. The essential advantage over recently introduced quantum

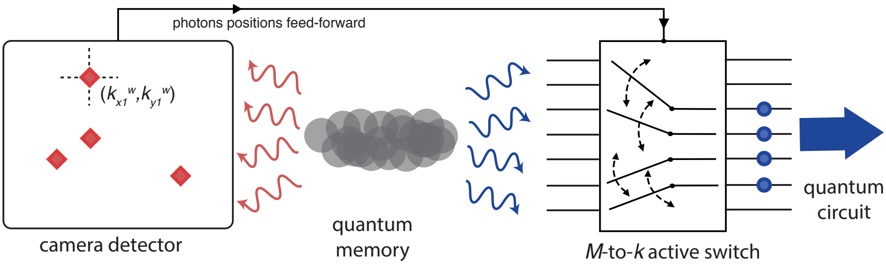

FIGURE 4.1: Single photon spatial routing and multiplexing for multi-photon state generation: a single-photon resolving camera registers write photons emitted from the quantum memory. Each detection heralds the creation of a spin-wave excitation in the atomic ensemble quantum memory with a wavevector determined by the wavevector $(k^{w}_{x,i}, k^{w}_{y,i})$ at which i-th photon was registered, which is calculated from the registered photon position and camera calibration. If a desired photon number k has been registered, the photonic M-to-k switch is reconfigured to channel photons from conjugate directions stored and subsequently the read-out pulse is applied to convert stored spin-wave excitations to the requested number of photons, which will be used later, e.g. in the quantum circuit.

memory arrays [Pu17] is simultaneous excitation and access to many modes. The protocol is being managed by a classical memory storing the wavevectors of registered photons and the which-mode information. This information is finally used to route the photons retrieved in the read-out process from the quantum memory. A photonic switch is used to direct photons to a quantum circuit or to conditionally generate arbitrary states through multi-photon interference. Furthermore, since a small number of photons is generated per each frame, one could adapt in real-time the number of trials to create exactly the desired number of excitations in the quantum memory. By keeping the mean photon number per shot small we virtually eliminate the malicious pairs in a single mode. This gives us a slight advantage over a simpler scheme [CDW17] in which a single excitation shot is used. Extensions of this proposal are numerous, including usage of spin-wave echos to conditionally manipulate the atomic excitations [Hos09]. The experimental results presented below constitute the most essential step towards the realization of the proposed protocol.

To give estimates of performance of the multi-photon generation protocol let us first consider a scenario where to goal is to generate a k photons. We use a set of photon-pair sources based on two-mode squeezing, which we will denote s and i for signal and idler, that remain in low photon generation rate regime $\langle\hat{n}\rangle = \sinh(\xi) \approx p \ll 1$, where by p we denote a probability to generate a photon pair. The single photon in the idler mode is heralded by detecting a photon in the signal mode, and its quality is certified by a low value of second-order correlation

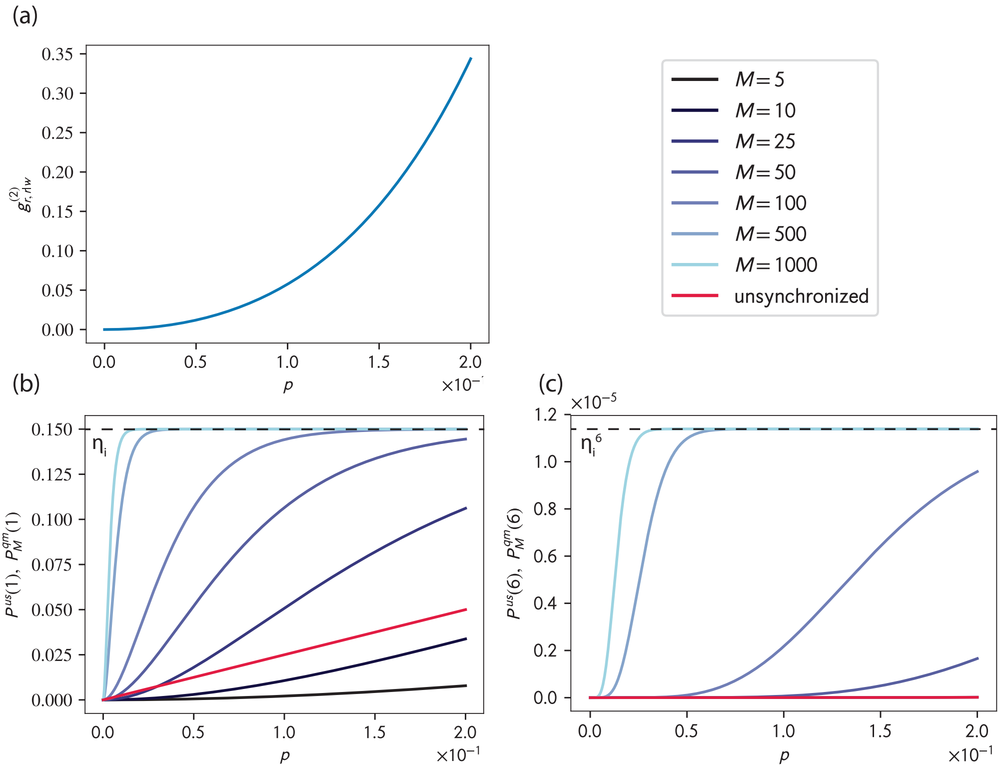

FIGURE 4.2: Performance of the multi-photon generation protocol. (a) The read photon auto-correlation function dependence on the photon-pair generation rate p. Only small probability p guarantees pure single photons. Panels (b,c) depict probabilities to generate a desired number of $k = 1$ or 6 photons in the unsynchronized $P^{us}(k)$ and quantum-memory-enhanced $P^{qm}(k)$ scenario, for a set of numbers of modes M as indicated in the legend. We assume equal detection probabilities of both heralding and heralded photons of 50% as well as memory read-out efficiency of 30%. Importantly, we observe that for high numbers of modes M the generation probabilities quickly saturate at the their maxima determined only by read-out and detection probabilities.

function:

$$g^{(2)}_{i,i|s} = \frac{2p^2(2+p)}{(1-p)^3} \tag{4.1}$$

We will denote transmission in the two modes by η_s and η_i. Without a quantum memory, we need k of such sources. Each of them can herald a single photon with probability $p\eta_s$. Thus, the probability to herald k photons will be $(p\eta_s)^k$. With a quantum memory that harnesses M modes we adopt a different strategy. Each of these modes again generates a photon pair with probability p. To be able to herald k photons, and then redirect them into a desired spatial/temporal mode upon read-out, we require that the setup generates at least k photons. In

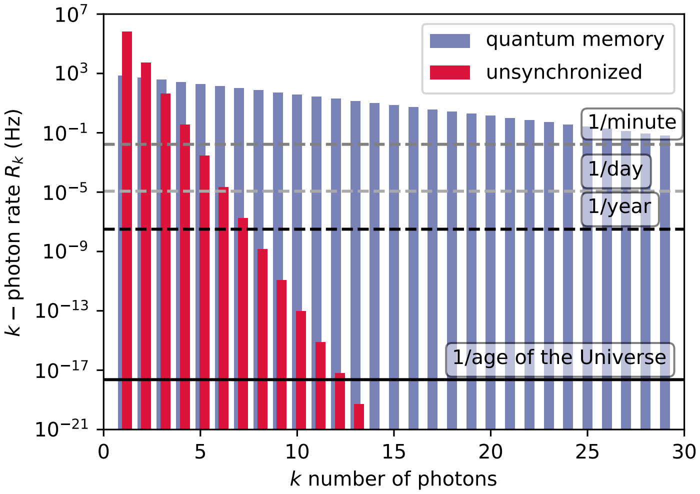

FIGURE 4.3: Estimates of the k-photon generation rates in a highly optimized scenario with a set of SPDC sources (repetition rate 80 MHz, $p = 10^{-2}$, detection efficiency 90%) and a multimode quantum memory source (repetition rate 1 kHz, $p = 10^{-2}$, number of modes $M = 4000$, write photon detection (heralding) efficiency 20%, read photon detection efficiency 90%, memory read-out efficiency 80%).

particular the probability to herald exactly k photons is:

$$p_k = \binom{M}{k} (p\eta_s)^k (1 - p\eta_s)^{M-k} \tag{4.2}$$

which is a binomail distribution. The probability to herald at least k photons is given by its cumulative distribution function:

$$p_{\geq k} = \sum_{j=k}^{M} \binom{M}{j} (p\eta_s)^j (1 - p\eta_s)^{M-j} = I_{p\eta_s}(k, n - k + 1), \tag{4.3}$$

where $I_x(a, b)$ is a regularized incomplete Beta function[1]. Finally, in both cases we have losses in the idler arm which multiply our rates by $(\eta_i)^k$, and thus they equal (us - unsynchronized, qm - quantum memory):

$$P^{us}(k) = (p\eta_s\eta_i)^k \tag{4.4}$$

$$P_M^{qm}(k) = I_{p\eta_s}(k, n - k + 1)(\eta_i)^k \tag{4.5}$$

Finally, we make a direct comparison with a parametric down-conversion source

---

[1] The Beta function is specifically defined as the cumulative distribution function of the binomial distribution

and give optimistic, yet still realistic, estimates of expected photon rates. We optimistically assume detection efficiency of single-mode detectors equal 90%, of camera detector equal 20% and quantum memory read-out efficiency of 80% with $M = 4000$ modes and $p = 10^{-2}$. For the SPDC source, we take experimental repetition rate of 80 MHz, that corresponds to our Ti:Sapphire oscillator (MaiTai), while for the quantum memory we take 1 kHz that corresponds to the best camera frame rate we can currently achieve, although there are perspectives to reach even 100 kHz. With these parameters, we plot the expected k-photon rate R_k in both scenarios in Fig. 4.3. We observe that the SPDC source only performs better when we generate 1 or 2 photons; for any number above that, the multiplexed quantum memory dominates. In particular, with reasonable rates of 1/hour, we could generate up to 18-photon-states. The waiting time for such state with an SPDC source is far longer than the currently estimated age of the Universe 13.8×10^9 years. Importantly, we observe that the low detection efficiency of the camera detector is compensated by a large number of modes.

4.2 Quantum memory setup

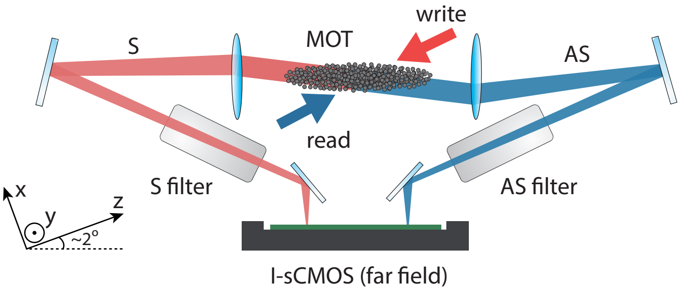

Figure 4.4: Schematic of the main part of the experimental setup. The atomic ensemble released from the magneto-optical trap (MOT) is illuminated with orthogonal, circularly-polarized write and read laser beams. Angles at which write (w) and read (r) photons (produced through Raman scattering) are emitted from the atomic ensemble are imaged on the single-photon resolving I-sCMOS sensor, composed of an sCMOS camera and an image intensifier. Optically pumped atomic cells (w and r filters) filter out the residual laser light and stray fluorescence

Here we very briefly remind the experimental setting described in Chapter 3. For the quantum memory, we use an engineered atomic ensemble of cold rubidium-87 atoms generated within a magneto-optical trap (MOT) and cooled using polarization-gradient cooling (PGC) scheme, as depicted in Fig. 4.5. During this experiment with the roughly 1 cm-long cigar-shape ensemble ($\sigma_z \approx 5$ mm) of radius $\sigma_\perp = \sigma_x = \sigma_y = 0.3 \pm 0.05$ mm (taken as $1/e^2$ the radius of the

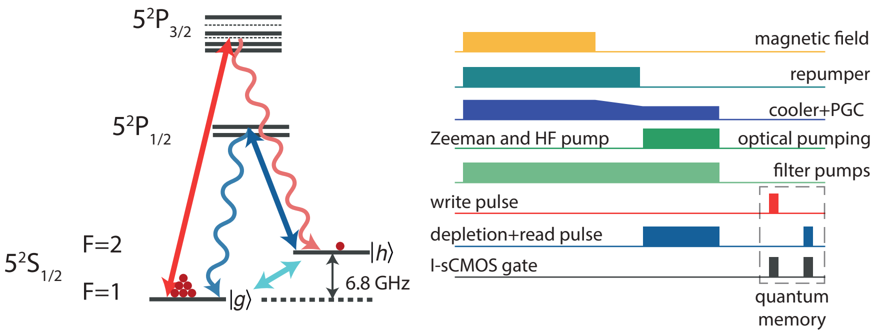

FIGURE 4.5: Atomic level configuration [relevant colours correspond to the pulse sequence in the right panel]. In the process of write-in and read-out the spin-wave is created or annihilated, respectively. The wavy arrows correspond to w (red) and r (blue) photons. Pulse sequence used in the experiment consists of trapping magnetic field switching, laser cooling and optical pumping (with depletion) preparation stages, as well as short write and read laser pulses (quantum memory stage) producing write and read photons.

atomic column density) containing $N = 10^8$ atoms we achieved optical depth OD $= 40$ as measured on the closed $F = 2 \rightarrow F = 3$ transition, which limits the memory read-out efficiency [Zha12; Cho16]. Quantum memory operates once atoms are released from MOT with the magnetic field gradients switched off. We prepare 70% of atoms in the $F = 1$, $m_F = 1$ state and the rest of atoms in the $F = 1$, $m_F = 0$ state through optical pumping. The inefficiency of the optical pumping can be attributed to various effects: high optical depth, imperfect beam overlap, or imperfect light polarization. Atom-photon interface is achieved with two lasers: write, which is red-detuned from $5^2S_{1/2},\ F = 1 \rightarrow 5^2P_{3/2},\ F = 2$ transition and read laser tuned to $5^2S_{1/2},\ F = 2 \rightarrow 5^2P_{1/2},\ F = 2$ transition.

To generate the multimode, multi-photon state we illuminate the ensemble with a write pulse containing 10^7 photons ($\sim 2\ \mu$W power levels) with wavevector $\mathbf{k}_\mathrm{W}$ tilted at an angle of 2° to the ensemble longitudinal axis in the xz plane. We take the axis defined by counter-propagating read and write beams as the z axis of the frame of reference. Write (w) photons scattered in the Raman process are registered on the I-sCMOS camera located in the far-field with respect to the atomic ensemble. A scattered photon with a transverse wavevector $\mathbf{k}_w$ is accompanied by a collective atomic excitation (spin wave) with a spatial phase dependence, as previously derived in Eq. 2.114:

$$\hat{b}^\dagger_\mathbf{K}|0\rangle = N^{-1/2}\sum_{j=1}^{N}\exp\left(i\mathbf{K}\cdot\mathbf{r}_j\right)|g_1\ldots h_j\ldots g_N\rangle, \tag{4.6}$$

where $\mathbf{K} = \mathbf{k}_w - \mathbf{k}_W$ is the spin-wave wavevector, $\mathbf{r}_j$ is the position of j-th atom, $|g_j\rangle$ ($|h_j\rangle$) corresponds to the $5^2S_{1/2}$, $F = 1$ ($F = 2$) state and the summation is carried over all N atoms in the ensemble.

To learn about the spin-wave we convert it to a read (r) photon through resonant Raman scattering (read-out process) with a read pulse with wavevector $\mathbf{k}_R$ containing 10^8 ($\sim$ 1 mW power level) photons. Wavevector of the r photon is determined by the stored atomic excitation $\mathbf{k}_r = \mathbf{K} + \mathbf{k}_R$. We estimate the read-out efficiency as $\chi_R = 35 \pm 2\%$ (taken as the ratio of coincidence rate to write photons rate and accounted for losses). Read photons are registered in a separate region of the same I-sCMOS sensor.

Spatially-insensitive filtering is essential for the memory to take advantage of its inherent multimode capacity. Commonly used frequency filtering cavities [Lan09; Cla10; Che16] transmit only one spatial mode. To overcome this issue we use two separate optically-pumped hot rubidium vapour cells with buffer gas and paraffin coating. The cells are pumped by strong lasers during the cooling and trapping period of the MOT. Additional interference filters are used to separate stray pump laser light from single photons.

Finally, photons originating from the atomic quantum memory are imaged onto the I-sCMOS sensor through a nearly diffraction-limited imaging setup. The sensor is located in the Fourier plane of the atomic ensemble. Positions of photons registered on the camera are calibrated as transverse emission angles, directly proportional to transverse wavevector components. The I-sCMOS camera has the quantum efficiency of 20% and the combined average transmission of the imaging and filtering system is 40%. The net efficiencies in write and read arms are equal $\eta_w \approx \eta_r \approx 8\%$,

4.3 Data analysis

When collecting large statistics the spatial degree of freedom with parallelized detection provides an advantage over single-mode experiments [Nic13; Par15]. If one considers each mode as a separate realization of the experiment we are able to collect statistics at a rate of 3×10^5 effective experiments per second. This rate is very similar to what is obtained in single-mode experiments, however, the multimode scheme offers much more versatility as increasing the memory storage time to many μs decreases the rate very insignificantly, contrasted with a dramatic drop in the rate in the single-mode experiments. For example, with 30 μs storage time our effective experimental rate remains at 300 kHz, as it is anyway limited by the read-out speed of the sCMOS camera. For the corresponding single-mode experiment the absolute maximum stands at 33 kHz. With faster camera acquisition rate the advantage of the multimode scenario would become overwhelming.

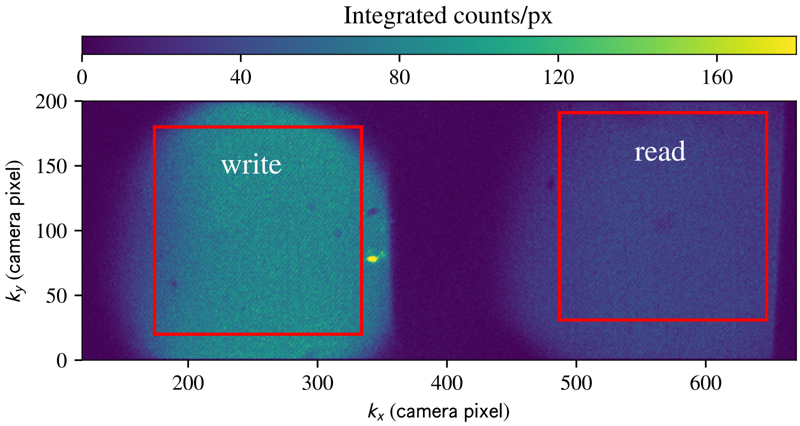

FIGURE 4.6: Integrated photon counts as seen directly on the I-sCMOS camera, as well as post-selected write and read photon regions. Axes correspond to k_x and k_y wavevector, but are not calibrated here. A sharp cutoff on the right side of each region corresponds to a D-shape mirror. Other visible apertures are due to optical elements such as lenses and mirrors. An overexposed dot on the right side of the write region is a speckle from scattered write laser light.

Here, to obtain proper statistics we have collected 10^7 camera frames. For a pair of small conjugate square-shaped region-of-interests (ROI) with side length $\kappa = 160$ rad/mm and a net write photon detection probability of $p_w = 4 \times 10^{-2}$ we register very few accidental coincidences, i.e. 90% of coincidences come from conjugate modes. This figure of merit changes with a mean photon number and thus the number of observed modes, as due to limited detection efficiencies we will sometimes register a pair of photons from two different pairwise-coupled modes. For two conjugate ROIs with side lengths $\kappa = 340$ rad/mm (i.e. 43 mrad) corresponding to a nearly full field of view composed of hundreds of modes, we have registered a total number of 1.6×10^5 coincidences of which 4.4×10^4 came from conjugate mode pairs.

Collection of photon counts with a multi-pixel detector requires new experimental and data analysis tools. To verify the anti-correlation between momenta of write and read photons both in x and y coordinates, we count the coincidences for each pair of camera pixels corresponding to wavevector coordinates (k_x^w, k_y^w) and (k_x^r, k_y^r). Figure 4.8(a) portrays the number of coincidences for a large field of view as a function of (k_x^r, k_y^r) momenta summed over the x coordinates. Notably, thanks to a very high signal-to-noise ratio we do not subtract the accidental and noise background in contrast to hitherto schemes [Edg12; MDL14; CDW17; DPW17]. We observe a clear anti-correlated behavior which we model by the quantum amplitude of the generated write–read photon pair in the y dimension, given by:

$$\Psi_y(k_y^w, k_y^r) = \mathcal{N} \exp\left(-\frac{(k_y^2 + k_y^r)^2}{4\kappa_y^w}\right) \Theta(k_y^w + \kappa)\Theta(k_y^r + \kappa)\Theta(-k_y^w - \kappa)\Theta(-k_y^r - \kappa), \tag{4.7}$$

where κ_y is a correlation length in the y dimension and $\mathcal{N}$ is a normalization constant. Note that the extent (support) of this wavefunction must be bounded in order to find a proper normalization, which here we express in the form of Heaviside's theta (step) function.

The number of coincidences is proportional to $|\Psi_y(k_y^w, k_y^r)|^2$. If we thus disregard accidental coincidences and possibly non-trivial phase dependencies, we may find the wavefunction as a square root of the spatial coincidence distribution. An identical expression describes photons behavior in x dimension – see inset in Fig. 4.8(a).

For the Gaussian-shaped atomic ensemble the size of the emission mode should be related to ensemble transverse dimension $\sigma_\perp = 0.3 \pm 0.05$ mm, corresponding to wavevector spread of $1/\sigma_\perp = 3.3 \pm 0.5$ rad/mm in the far-field for light at the wavelength of write photons. To precisely determine the mode widths $\kappa_{x,y}$, in Fig. 4.8(b) we plot the coincidences in terms of sum of wavevector variables. Gaussian fit yields values of $\kappa_x = 4.45 \pm 0.02$ rad/mm and $\kappa_y = 4.76 \pm 0.02$ rad/mm for x and y dimension, respectively. Consequently, we can consider the generated entangled state [Lee16; DPW17] to be nearly symmetrical in terms of x and y spatial dimensions. This wavevector spread is very close to the limit $1/\sigma_\perp$ given by the diffraction at the atomic ensemble and confirms the quality of the imaging system for conjugate modes.

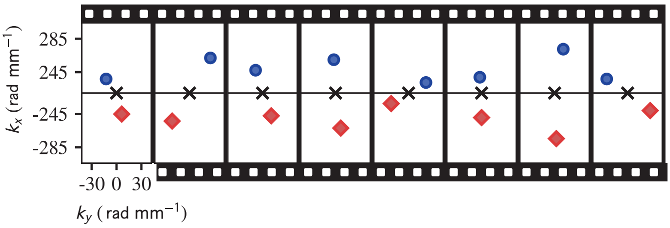

FIGURE 4.7: Example subsequent frames in the write (bottom) and read (top) regions demonstrating correlated photon pairs in each camera frame. Note that while most frames will contain no photon or a photon only in a single region, almost all (>90%) frames with a coincidence event will contain a correlated photon pair for the detection probability of write photon $p_w = 1.2 \times 10^{-2}$

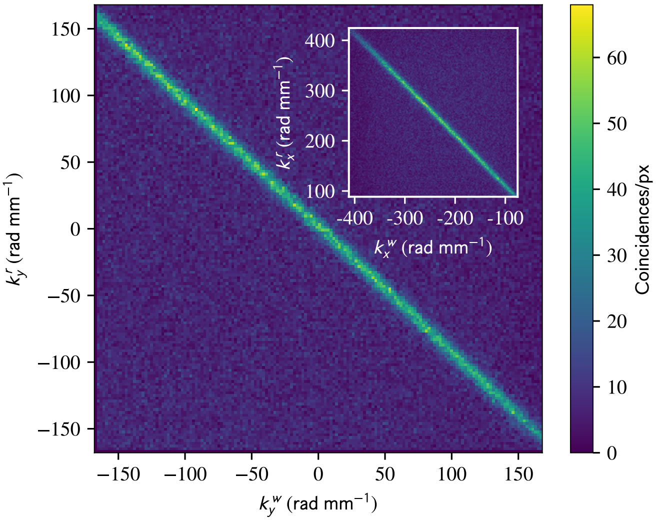

FIGURE 4.8: Spatial properties of the generated biphoton state: all write–read photon coincidences obtained from 10^7 frames marked with their k_y wavevector components (k_x for the inset) for zero memory storage time, demonstrating high degree of momenta anti-correlation.

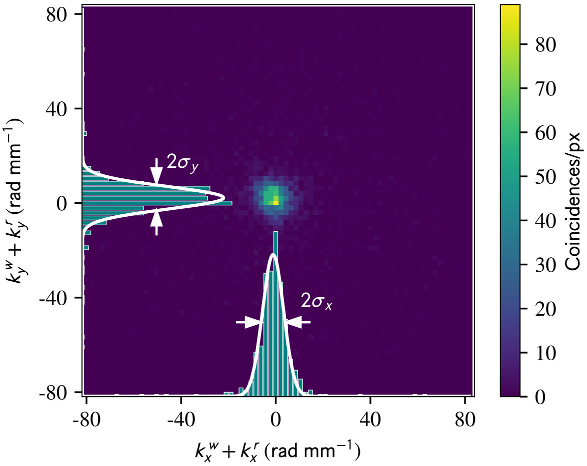

FIGURE 4.9: Same coincidences as in Fig. 4.8 counted in the center-of-mass variables $(k_x^w + k_x^r)$ and $(k_y^w + k_y^r)$. The central peak is fitted with a two-dimensional Gaussian to obtain its centre and width. One-dimensional distributions correspond to cross-section counts selected for central pixels. Both here and in Fig. 4.8 the plots disregard the perpendicular component and neither accidental nor noise background subtraction is performed.

4.4 Capacity estimation

From the fundamental point of view, multimode states of light can be considered either as continuous-variable systems [Tas11] or highly-dimensional entangled states [Fic16] offering large dimensionality of available Hilbert space and in turn providing high informational capacity. Estimation of the informational capacity of continuous-variable entangled states of light has attracted some attention of its own due to broad applications of such states [MDL14; DPW17]. Various measures of this capacity have been discussed e.g. on the information-theoretical basis [Sch13]. Here we estimate the number of independent mode pairs observed in write and read arms using the Schmidt mode decomposition [GRE99; LE04]. For a single-dimensional photon pair amplitude given by Eq. 4.7 and cropped to a finite region we find a decomposition into the Schmidt modes as:

$$\Psi_y(k_y^w, k_y^r) = \sum_{j=0}^{\infty} \lambda_j u_j(k_y^w) v_j^*(k_y^r), \tag{4.8}$$

where λ_j are singular values corresponding to contributions of each mode while u_j and v_j^* are orthogonal sets of eigenfunctions. Effective number of independent mode pairs is given by:

$$M = 1/\sum_{j=0}^{\infty} \lambda_j^4. \tag{4.9}$$

Such decomposition can in principle correspond to modes given in the intensievly-studied orbital-angular-momentum (Gauss-Laguerre) basis [Din13; Nic13; Fic16] or another orthogonal basis.

To correctly determine the number of modes we use a similar procedure as proposed by *Law* and *Eberly* [LE04]. The procedure has been first introduced by *Grobe et al.* [GRE99] for the case of electron wavefunctions. Focusing on one dimension, we generate a normalized biphoton amplitudes according to equation (4.7), with various widths $\kappa_{x,y}$, on a square two-dimensional k_y^w–k_y^r grid. We numerically find the eigenmode decomposition of the generated matrix and calculate the number of modes according to equation (4.8). Figure 4.10 presents example of results for $\kappa = 420$ rad/mm while the solid line corresponds to a fit of $A\kappa/2\kappa_{x,y}$ relation which we verified numerically for various sets of parameters and obtained $A = 0.565$.

Note that for a Gaussian-shaped wavefunction with long axis width κ_G we would expect $M_{x,y} \approx \frac{1}{2}\kappa_G/\kappa_{x,y}$. The factor of 2 in our case corresponds to taking κ to be a full width rather than half-width. The actual enhancement due to sharp cutoff is 0.565 vs. 0.5. The strict result (valid for all ratios) is [LE04]:

$$M_{x,y} = \frac{1}{2}\left(\frac{\kappa_G}{\kappa_{x,y}} + \frac{\kappa_{x,y}}{\kappa_G}\right) \tag{4.10}$$

Note that for a biphoton amplitude on a rectangular (non-square) grid numerical singular value decomposition (SVD) might be used to give analogous results.

Finally, we obtain $M_x = 26.7 \pm 0.1$ and $M_y = 24.9 \pm 0.1$. Finally, for the total number of modes M, which is the product of the number of modes in each spatial dimension, we get $M = M_x M_y = 665 \pm 4$.

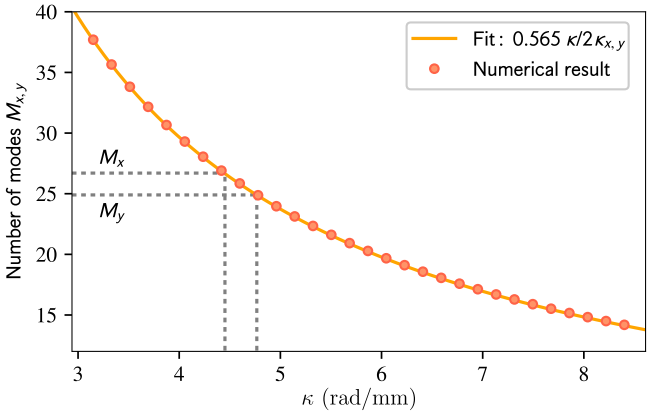

FIGURE 4.10: Result of the eigenmode decomposition for the number of modes. Dots represent the results from numerical decomposition while the solid line is the simplified prediction of 0.565 $\kappa/2\kappa_{x,y}$. Dotted grey lines correspond to values of $\kappa_{x,y}$ we obtain in our experimental setup and corresponding numbers of modes M_x and M_y.

4.5 Nonclassical photon-number correlations

The presented spatial correlations at a single-photon level require further analysis to confirm the actual generation of multi-photon quantum states of light. Nonclassicality of the correlations (and hence the memory) may be assessed by looking at the second-order correlation function:

$$g^{(2)}_{rw} = \frac{\langle \hat{n}_r \hat{n}_w \rangle}{\langle \hat{n}_r \rangle \langle \hat{n}_w \rangle} \approx \frac{p_{r,w}}{p_r p_w}, \tag{4.11}$$

where p_w and p_r are the probabilities of registering a write and an read photon in their respective regions, while p_{rw} is the write–read coincidence probability. Since the expected single mode statistics of write and read light are thermal, the

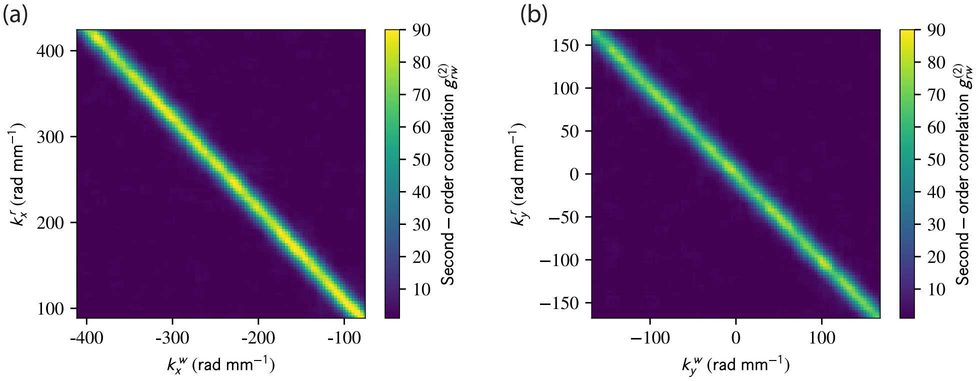

FIGURE 4.11: Nonclassical correlations of photons emitted from the quantum memory. (a,b) - second-order cross-correlation function $g_{rw}^{(2)}$ measured for different positions of ROI in write and read arms, for zero memory storage time. Nonclassical correlations are observed only between conjugate modes, confirming the highly-multimode character of our quantum memory. Data corresponds to w photon probability $p_w = 2 \times 10^{-4}$ per ROI.

maximum value of local $g_{ww}^{(2)}$ and $g_{rr}^{(2)}$ autocorrelation functions is 2. Consequently, a value of $g_{rw}^{(2)} > 2$ yields violation of the Cauchy-Schwarz inequality:

$$R = \frac{[g_{rw}^{(2)}]^2}{g_{ww}^{(2)} g_{rr}^{(2)}} \leq 1 \tag{4.12}$$

and thus proves nonclassical character of the generated state of light.

4.5.1 ROI-based analysis

To perform the measurements we utilize the inherent photon-number-resolving capability of the I-sCMOS detector guaranteed by the spatial resolution and independence of electron multiplication channels [CWB14]. We verify non-classical photon number correlations in many modes by selecting a set of ROIs in both write and read arms and calculating $g_{rw}^{(2)}$ for all accessible combinations. For the data presented in Figs. 4.11 and 4.12 to obtain a single $g_{rw}^{(2)}$ map we have selected 100 regions in a column (oriented in the y-direction) in write and read arms and calculated value of $g_{rw}^{(2)}$ for each pair of regions (note these regions are partially overlapping). We collect these results for 25 different conjugate positions of columns in the x-direction (i.e. $k_x^w + k_x^r = 0$) and estimate mean and standard deviation for further analysis. Results presented in Figs. 4.11(a,b) clearly confirm the multimode capacity discussed in previous sections. For the experimental data presented in Fig. 4.11(b) we obtain $g_{rw}^{(2)} = 72 \pm 5$ at the diagonal compared with

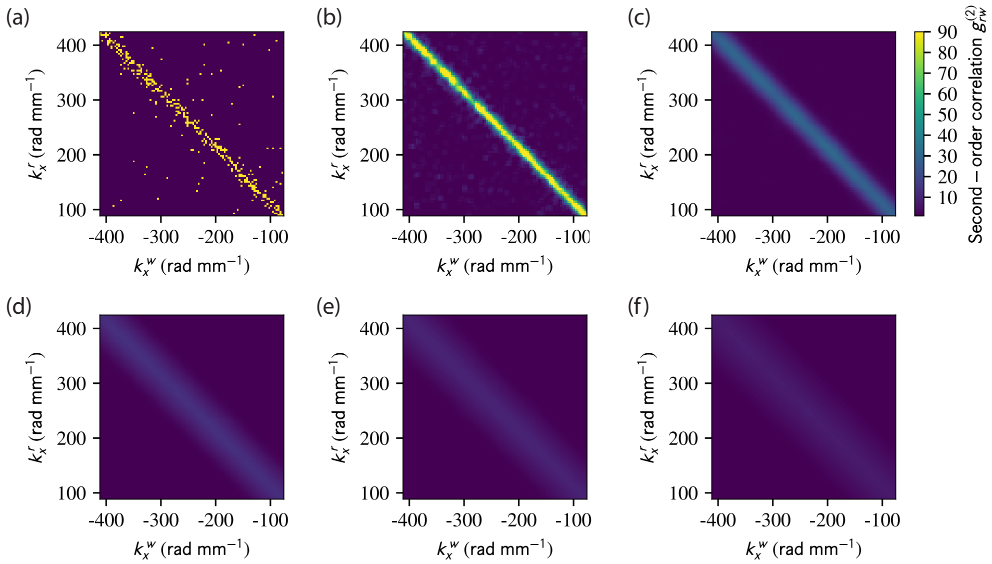

FIGURE 4.12: Correlation functions obtained for different choices of ROI side lengths κ, with κ increasing from (a) to (f). A choice of smaller κ results in better spatial resolution and higher value of correlation function at the cost of worse statistics and thus high statistical uncertainties and fluctuations even in the correlated regions. Large κ, as in bottom row gives lower $g_{rw}^{(2)}$ and large spatial spread, severely limiting the number of observed modes. For further considerations, and for Fig. 4.11, we choose the intermediate scenario depicted in (c).

$g_{rw}^{(2)} = 1.0 \pm 0.4$ for a set of uncorrelated regions, where the errors correspond to one standard deviation. Next, we select a single pair of square-shaped conjugate ROIs in write and read arms. Figure 4.13 presents the measured $g_{rw}^{(2)}$ at $\tau = 0$ storage time for varying size of ROI with a constant photon flux per pixel. To calculate the value of $g_{rw}^{(2)}$ for Fig. 4.13 we have additionally averaged over all conjugate regions (corresponding to averaging over the diagonal in Fig. 4.11(b)) and inferring the errorbars (one standard deviation). Figure 4.12 presents the maps corresponding to different choices of κ, demonstrating the trade-off between proper statistics and better results in terms of $g_{rw}^{(2)}$ and spatial correlation (resolution). With the decreasing size of ROI the write photon detection probability p_w decreases and we observe $g_{rw}^{(2)}$ cross-correlation well above the classical limit of 2 which perfectly matches our theoretical predictions.

To make the prediction let us consider a collection of M squeezed modes pairs. Assuming the probability p of *generating* (as opposed to registering) write photon in a single mode and efficiencies in the write and read arms equal η_w and $\eta_r \chi_R$, respectively, with χ_R being the retrieval efficiency, we obtain the probability of

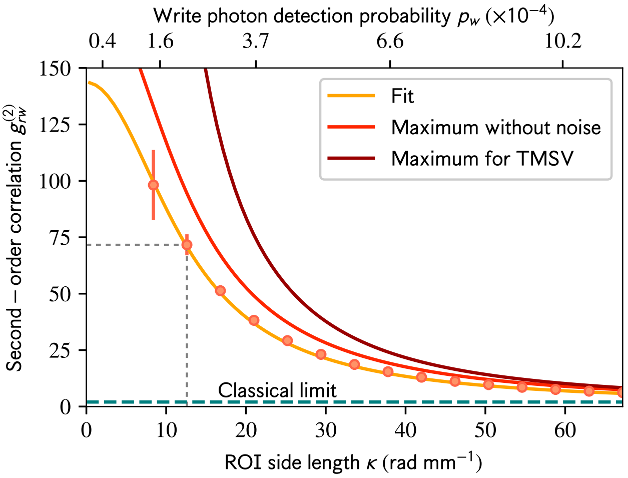

FIGURE 4.13: Second-order correlation $g_{rw}^{(2)}$ for write and read photons measured at $\tau = 0$ storage time using different sizes of ROI in the analysis. Smaller ROIs inherently correspond to lower p_w and consequently give higher values of $g_{rw}^{(2)}$. Our theoretical prediction for $g_{rw}^{(2)}$ calculated for the measured mode size closely adheres to experimental results. Other curves correspond to the maximum value of $g_{rw}^{(2)}$ without noise in the read photon arm and the maximum theoretical result for two-mode squeezed vacuum state (TMSV) with given probability p_w. Grey dashed lines mark the regime of operation and analysis (same ROI side length κ) used in the measurement shown in Fig. 4.11.

registering a coincidence from any two conjugate modes $pM\eta_w\eta_r\chi_R$. If we now consider a pair of square-shaped ROIs with the side length κ containing M modes for which we again assume the probability p per mode to *generate* a photon pair, the coincidence rate is reduced, as not all coincidences will fall into the ROI. This effect is more pronounced for the smaller size of ROI. In particular, if we consider that the write photon is detected inside its respective ROI, we seek the probability that its conjugate read photon will be detected in conjugate ROI (i.e. with conjugate center). We may calculate this probability by considering photon pairs distributed in momentum space according to equation (4.7). By considering write photons in the given ROI we calculate the conditional probability $f(\kappa)$ of registering read photon in the conjugate ROI in the read arm, which gives us:

$$\begin{aligned} f(\kappa) &= \left(\int_{-\frac{\kappa}{2}}^{\frac{\kappa}{2}} \mathrm{d}k_w \int_{-\frac{\kappa}{2}}^{\frac{\kappa}{2}} \mathrm{d}k_r \frac{1}{\sqrt{2\pi}\kappa\kappa_{x,y}} e^{-(k_w+k_r)^2/2\kappa_{x,y}^2} \right)^2 \\ &= \left(\operatorname{erf}\left(\frac{\sqrt{2}\kappa}{2\kappa_{x,y}} \right) + \sqrt{\frac{1}{2\pi}} \frac{2\kappa_{x,y}}{\kappa} \left(e^{-\kappa^2/2\kappa_{x,y}^2} - 1 \right) \right)^2, \end{aligned} \tag{4.13}$$

where squaring is due to the two-dimensional character of the problem. Finally,

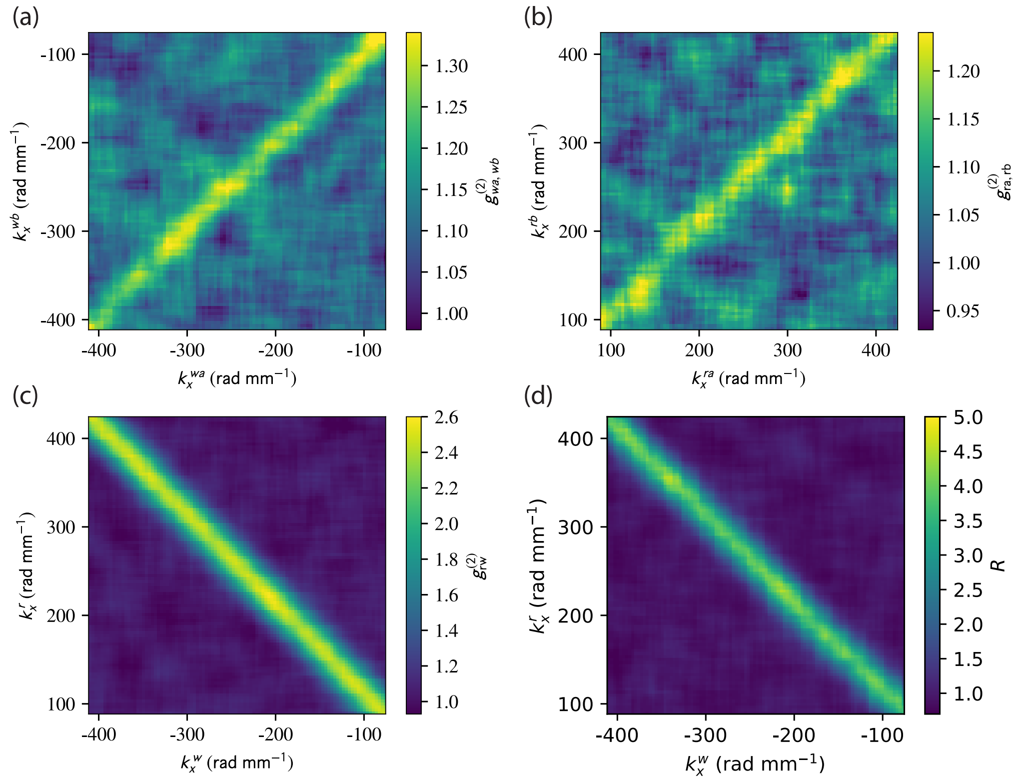

FIGURE 4.14: **Results of the autocorrelation measurements.** (a-c) Results of the measurement of $g^{(2)}_{ww}$, $g^{(2)}_{rr}$ and $g^{(2)}_{rw}$, respectively and (d) inferred value of Cauchy-Schwarz violation R.

to estimate the net coincidence probability we additionally consider the total number of accidental coincidences which is very well approximated by a product of probabilities in write and read arms $p_w p_r$. The results is not actually strict, since it arises only due to the presence of noise and losses. If we only had losses, the number of accidentals due to pairing of photons from different modes would actually be higher. Nevertheless, the approximate and intuitive results is widely used in the literature; see Refs. [Che06; Zha09; Alb15; Lap17; DPW17].

The net write–read coincidence probability thus equals:

$$p_{r,w} = pMf(\kappa)\eta_w\eta_r\chi_R + p_w p_r. \tag{4.14}$$

We compare this result with a maximum value achievable without noise in the read arm, as well as maximum theoretical value for two-mode, squeezed vacuum state (TMSV) for the given p_w, achievable only if coherent spatial filtering (using e.g. single-mode fibres or cavities) is applied. In Fig. 4.13, as κ becomes smaller

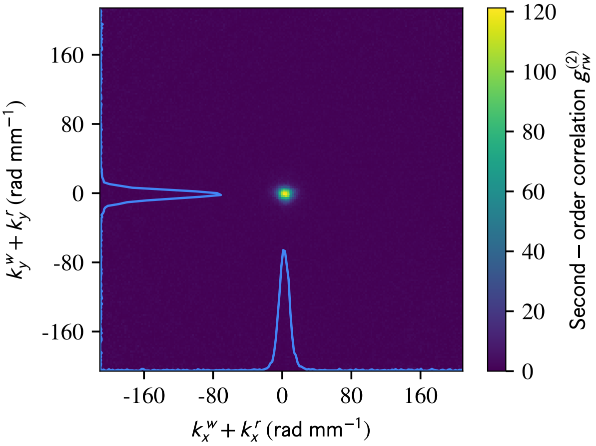

FIGURE 4.15: Cross-correlation function calculated using the framework from Sec. 4.5.3 for the data from Fig. 4.9 and other related. With the fine spatial sampling achieved here we attain the value of 120 for $g_{rw}^{(2)}$.

than the actual correlation length $\kappa_{x,y}$, the curve flattens-off due to the $f(\kappa)$ factor limiting the number of coincidences.

4.5.2 Autocorrelations

Even though we expect the photon statistics in write and read arms to exhibit maximum values of autocorrelation functions of 2, to implicitly demonstrate violation of Cauchy-Schwartz inequality (4.12), we have performed additional measurements of $g_{ww}^{(2)}$ and $g_{rr}^{(2)}$ using a slightly modified experimental setup. To facilitate this experiment we have modified a part of the experimental setup to allow measurement of autocorrelation functions $g_{ww}^{(2)}$ and $g_{rr}^{(2)}$. A high extinction-ratio Wollaston prism was placed in front of the image intensifier and a pair of half-wave plates was used to rotate the polarization of write and read photons. The Wollaston prism split the photons into two beams (both for write and read arm) at the 50:50 ratio in the vertical direction, so four distinct regions were observed on the camera ($w1$, $w2$, $r1$ and $r2$). After compensating for the change in angle-of-incidence due to refraction at the Wollaston prism we have analyzed the correlations between regions $w1$-$w2$ and $r1$-$r2$ to obtain estimates of autocorrelation functions. The results are presented in Fig. 4.14.

Due to inherently low number of w-w and r-r coincidences in this measurement we have increased the mean photon number (and thus the second-order cross-correlation function is relatively low) in the write arm to $\langle \hat{n}_w \rangle = 1.2$ (note that the probability per pixel is still low and thus the approximation $\langle \hat{n}_w \rangle \approx p_w$ for a

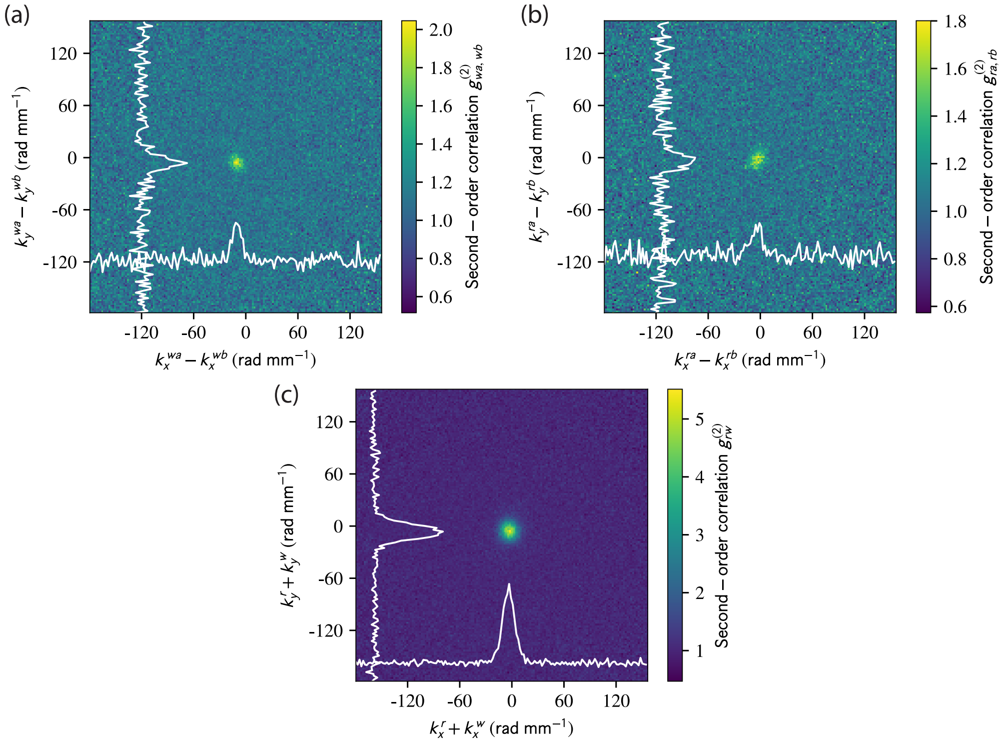

FIGURE 4.16: Cross-correlation and auto-correlation calculated using the framework from Sec. 4.5.3 for the data with high generation probability p in order to obtain fair statistics for auto-coincidences.

small region still applies). Additionally, a larger analysis region with side length $\kappa = 25.2$ rad/mm was used, resulting in visibly wider diagonal correlation. By averaging diagonal, correlated region we found mean values of $g^{(2)}_{ww} = 1.29 \pm 0.04$, $g^{(2)}_{rr} = 1.18 \pm 0.04$ and $g^{(2)}_{rw} = 2.45 \pm 0.04$. For a set of uncorrelated regions we found $g^{(2)}_{ww} = 1.07 \pm 0.04$, $g^{(2)}_{rr} = 1.04 \pm 0.03$ and $g^{(2)}_{rw} = 1.02 \pm 0.05$, proving that indeed both $g^{(2)}_{ww}$, $g^{(2)}_{rr} \leq 2$. These values are consequently higher than the expected value of 1 in the ideal case scenario, which is due to significant classical long-term fluctuations during the measurement. Figure 4.14(d) shows inferred value o R demonstrating significant violation of the Cauchy-Schwartz inequality at the diagonal. By averaging the diagonal values we find $R = 4.0 \pm 0.2$, significantly violating inequality (4.12). For uncorrelated regions the value is $R = 0.68 \pm 0.06$. Errors correspond to one standard deviation. Analogous results were obtained for the y-dimension.

4.5.3 Second-order correlations in "centre-of-mass" variables

We saw that for the spatially-resolved maps of $g^{(2)}_{rw}$ either very large statistics or large size of ROI (κ) are required to provide informative results. Yet, the analysis in terms of the normalized correlation functions, such as $g^{(2)}_{rw}$, has advantages also when considering the wavefunction approach. While in Appendix 4.4 we intuitively assumed that the spatial distribution of coincidences is proportional to $|\Psi|^2$ (expressed in appropriate spatial coordinates), a more formal approach is given by the link between $g^{(2)}_{rw}$ and $|\Psi|^2$, that can be derived similarly as the link between Ψ and the first-order correlation function $g^{(1)}_{rw}$ as in Sec. A.11.1 (in particular cf. Eq. A.72):

$$g^{(2)}_{rw} = 1 + \alpha|\Psi|^2, \tag{4.15}$$

where α is a proportionality constant depending on the degree of squeezing.

To obtain a fair signal in this framework we will thus express the cross-correlation in terms of sum-difference (EPR) variables. With such, the data is contracted two two instead of four dimensions. The cross-correlation is calculated as:

$$g^{(2)}_{rw}(k^r_x + k^w_x, k^r_y + k^w_y) = \frac{\int \langle \hat{n}_r(k^r_x, k^r_y)\hat{n}_w(k^w_x, k^w_y)\rangle \mathrm{d}(k^r_x - k^w_x)\mathrm{d}(k^r_y - k^w_y)}{\int \langle \hat{n}_r(k^r_x, k^r_y)\rangle\langle \hat{n}_w(k^w_x, k^w_y)\rangle \mathrm{d}(k^r_x - k^w_x)\mathrm{d}(k^r_y - k^w_y)}. \tag{4.16}$$

The essential idea conveyed by this formula is that we average the unnormalized cross-correlation (nominator) and the product of means (denominator) to obtain the cross-correlation in the variables of interest.

In Fig. 4.15, which is obtained with the same data as Fig. 4.9 and others related, we immediately observed that all the value of cross-correlation reaches its maximum in the very centre, as expected. Furthermore, thanks to the fine sampling, as opposed to the ROI-based analysis, we obtain the value of $g^{(2)}_{rw}$ of approx. 120. The same method is then applied to analyse the data from Fig. 4.14 and obtain both cross- and auto-coincidences, with slightly modified formula averaging over sum rather than a difference of wavevectors. In Fig. 4.16 obtain higher values of all correlation functions than before, still confirming that $g^{(2)}_{rr}$ and $g^{(2)}_{ww}$ are below 2.

4.6 Storage capabilities

Cold atomic ensemble prepared in MOT typically offers μs up to ms coherence times, limited mainly by atomic motion, atom losses and stray magnetic fields. We characterize the memory storage time by analyzing the $g^{(2)}_{rw}$ correlation function when the read laser is applied after a variable storage time t following the write pulse. Figure 4.11(d) presents the average $g^{(2)}_{rw}$ calculated for 1,000 pairs of correlated square-shaped ROIs with side length $\kappa = 21$ rad/mm and $p_w = 1.9 \times 10^{-3}$ per entire ROI, each comprising approximately 5 modes. Data sets in Fig. 4.11(d) correspond to two different angles at which the photons were scattered, hence spin-waves with different wavevectors — higher scattering angles (and thus spin-waves with larger wavenumbers) correspond to shorter decay times. Similar procedure as described for Figs. 4.11 and 4.12 was used to calculate values and standard deviations here (Fig. 4.17), however we used far less regions to average as we required that regions correspond to appropriate spin-wave wavevector K_x.

We observe a quantum-beating oscillation on a double exponential decay of correlations due to the presence of two types of spin-waves arising as a result of imperfect optical pumping. Due to the axial magnetic field of 36 mG, the two types of spin-waves accumulate different phases over the storage time which leads to their constructive or destructive interference at the read-out stage.

We model this evolution, and in particular, the evolution of $g^{(2)}_{rw}$ correlation function following *Zhao et al.* [Zha09], but including the effect of interference of different spin-waves as well as the reduced number of coincidence counts due to incoherent spatial filtering. The result is the following expression for the second-order correlation function (starting from Eq. 4.14):

$$g^{(2)}_{rw} = 1 + \frac{p\eta_w\eta_r\chi_R(t)f(\kappa)}{p\eta_w(p\eta_r\chi_R(t)+\xi)}, \tag{4.17}$$

where ξ is a contribution of noise in the read photon arm. The retrieval efficiency is modeled as an interference of two fields arising due to two atomic coherences by the following time-dependent expression:

$$\chi_{\mathrm{R}}(t) = |\alpha_1 \exp(-t^2/2\tau_1^2) + \alpha_2 \exp(i\omega t)\exp(-t^2/2\tau_2^2)|^2, \tag{4.18}$$

where α_1 and α_2 are contributions of spin-waves between $F=1,\ m_F=1 \leftrightarrow F=2,\ m_F=-1$ and $F=1,\ m_F=0 \leftrightarrow F=2,\ m_F=-2$ transitions, respectively. The fit yields $\alpha_1 = 0.58$ and $\alpha_2 = 0.04$, clearly confirming dominant role of the clock-transition (between $F=1,\ m_F=1$ and $F=2,\ m_F=-1$ states) spin-wave[2]. The relative phase between the two spin-waves changes as one of them accumulates additional phase due to a Zeeman energy shift $\hbar\omega = 2\pi\hbar \times 51$ kHz in the axial magnetic field.

We observe this interference effect as an oscillation with a Larmor period of $T_L = 2\pi/\omega_L = 19.5\ \mu$s. For all spin waves, we measure lifetimes larger than 50 μs. In particular for the clock-transition spin-wave with small $K_x = 100$ rad/mm we obtain the lifetime of over 100 μs. The main source of decoherence is the

---

[2] The clock transition is insensitive to magnetic field up to the first order, i.e. only quadratic Zeeman shift is present. Transitions of such kind are often employed in atomic clocks.

random atomic motion governed by the Maxwell-Boltzmann velocity distribution [Zha09]. The lifetimes are bounded by wavevector-dependent decoherence rate $\Gamma_T = |\mathbf{K}|v_{\mathrm{rms}}$, with $v_{\mathrm{rms}} = \sqrt{\frac{k_B T}{m}} \approx 4.5$ cm s^{-1} (as in Eq. 2.120).

The sharp drop in $g^{(2)}_{rw}$ in the very beginning (two initial experimental points) is attributed to an increase of noise fluorescence as a result of an influx of unpumped thermal atoms into the interaction region. This noise might be eliminated by optical pumping of thermal atoms or by using a two-stage MOT with differential pumping. See Fig. 4.18 for the measured temporal evolution of noise fluorescence.

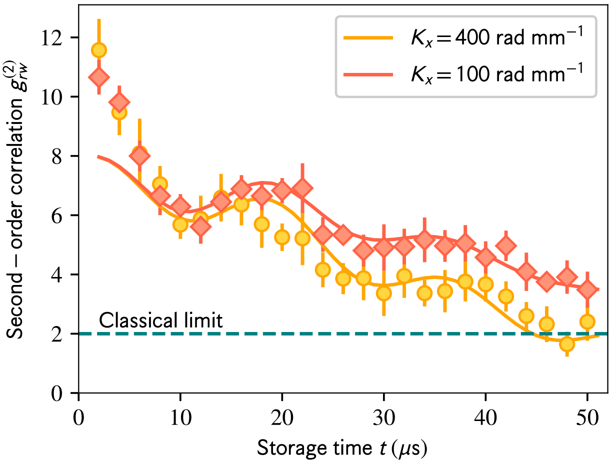

FIGURE 4.17: Second-order correlation $g^{(2)}_{rw}$ as a function of storage time, measured for two different angles of scattering corresponding to stored spin-waves with distinct K_x. Data was taken with a higher write photon detection probability of $p_w = 1.9 \times 10^{-3}$ as compared to Figs. 4.11 through 4.13 and thus the value of the correlation function is smaller. Nonclassical correlations for spin-waves with smaller wavenumber are confirmed for the storage time t up to 50 μs. Theoretical model of the time-evolution of $g^{(2)}_{rw}$ (solid lines, given by Eq. 4.17) exhibits good agreement with experimental data, except for the initial drop that we attribute to an increase of noise fluorescence of thermal atoms.

4.7 Discussion and Conclusions

We have demonstrated a quantum memory-enabled source of spatially-structured nonclassical light based on a principle of wavevector multiplexing. Simultaneous operation on many collective atomic excitations allows us to generate a multimode quantum state of light. The memory preserves nonclassical correlations up to 50 μs and exhibits excellent noise properties, in contrast to the hitherto used warm-atomic vapour schemes [CDW17; DPW17]. Simultaneous detection using

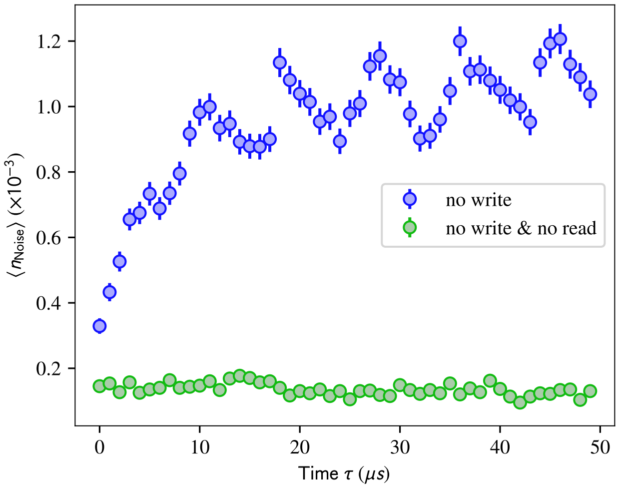

FIGURE 4.18: Noise level as a function of storage time. The mean number of registered noise photons in the read arm with (blue dots) and without (green dots) the read laser. The write laser was off in both cases. The noise level without the read laser corresponds to mostly dark counts and residual stray light. With the read laser we observe fluorescence of atoms residing in $F = 2$ manifold of the ground state. The initial increase of this fluorescence is due to the influx of room-temperature atoms present in the vacuum chamber into the interaction region. The optical pumping ensures that at the zero storage time the fluorescence is minimized. We attribute the oscillation in the noise photons signal to partial spin polarization of room-temperature atoms.

a state-of-the-art single-photon resolving camera is an ideal scheme to implement enhanced photon generation protocols [Nun13; MDW16; CDW17]. Additionally, a two-dimensional detector is both necessary and well-suited to the access high quantum information capacity of multimode states of light, which is unachievable with single-mode fibres [Edg12]. Furthermore, simultaneous detection of the entire transverse field of view could be essential in fundamental tests such as demonstration of the Einstein-Podolsky-Rosen paradox [EPR35] without the Bell sampling loophole [MDL14].

Our results clearly demonstrate the ability of multimode quantum memory to emit a single photon with high probability. In particular, we measured write photon detection probability of $p_w^{\mathrm{total}} = 0.21$ (as in data from Fig. 4.11) and simultaneously extremely low probability of registering a photon per mode equal $p_w^{\mathrm{per\ mode}} = 3.8 \times 10^{-4}$ that drastically minimizes the probability of generating a photon pair in a single mode and proves memory efficacy in enhanced generation of photons. Excellent quality of single photons has been verified through measurements of $g_{rw}^{(2)}$ cross-correlation function. Our quantum memory also exhibits

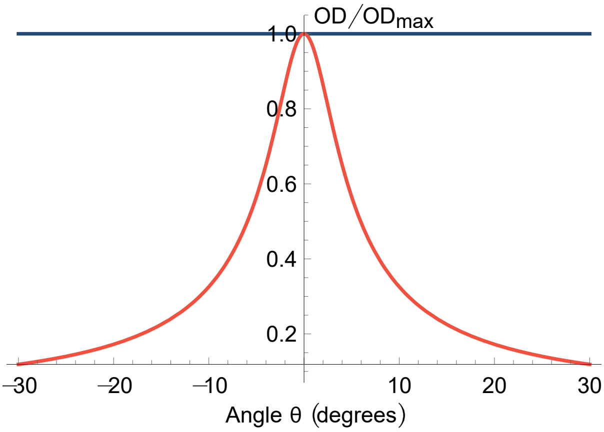

FIGURE 4.19: Relative, mean optical depth of a Gaussian atomic ensemble with an aspect ratio of 16, when looking from an angle θ.

an excellent time-bandwidth product of more than 500, which is an important figure of merit in terms of probability of retrieving all the photons stored in the memory (see Fig. 4.1), as well as prospective integration with time-bin multiplexing [Nun13]. We envisage that hundreds of μs memory lifetime, contrasted with noise-free yet low storage-time solutions [Kac18], and 100 ns operation time are excellent parameters when it comes to integration with fast electronic or photonic circuits for real-time feedback [Ma11; HAK11]. With 665 modes the memory compares favourably with the previous implementation in warm atoms [CDW17], where no nonclassical $g_{wr}^{(2)}$ was observed and only 8 spatial modes were processed (if considered in terms of the definition given in this this thesis - note that Refs. [CDW17; DPW17; MDL14] used a different definition for M).

The number of available modes is limited by the imaging system. In a cold atomic ensemble generated within a released MOT we expect that the final limit for the number of modes will be set by the lifetime of long-wavevector spin-waves as well as the phase-matching at the retrieval stage. To keep the lifetime within the tens-of-microseconds regime, the maximum scattering angles should be smaller than 6 degrees while the phase-matching happens to place a similar limitation [Sur08; LPW17a]. We thus predict that the number of readily available modes may reach thousands under realistic experimental conditions. However, with novel spin-wave manipulation techniques [HGO15] or by placing the atoms in an optical lattice [Rad10] at least another order-of-magnitude improvement could be achieved, allowing our setup to serve as a universal platform for quantum state preparation.

A more fundamental limit is related to how many modes can be efficiently retrieved. This figure is inherently linked to the optical depth, and in general we expect that the retrieval efficiency scales as $1 - \chi \propto 1/\mathrm{OD}$ [Nun08]. If we now consider modes propagating at large angles to the atomic ensemble, they will effectively experience lower ODs (see Fig. 4.19), as their propagation path through the ensemble is shorter. We may introduce a rule of thumb by requiring that the angle of propagation does not exceed the inverse aspect ratio of the ensemble. For our case, the maximum angle would be $\sigma_\perp/\sigma_z = 60$ mrad $= 3.5$ degrees. With this simplified treatment we may estimate the total number of modes in wavevector multiplexing as the squared ratio of this angle to the total angular size of a single mode given by $\lambda/(2\pi\sigma_\perp)$, so that:

$$M = \left(\frac{2\pi\sigma_\perp^2}{\lambda\sigma_z}\right)^2 \approx 20000. \tag{4.19}$$

Notably, this figure is proportional to the square of the Fresnel number $\mathcal{F} = \sigma_\perp^2/(\lambda\sigma_z)$ of the atomic ensemble [GGZS12].

We also want to make a note on the predictions made in Ref. [GGZS12] and others references therein. Here we considered the write-read protocol, for which, as we have seen in Chapter 2, counter-propagating configuration (backwards retrieval) is better for phase matching. The phase matching is thus good enough, that we preserve the $\sim \mathcal{F}^2$ scaling. On the other hand, for forward retrieval phase matching would limit the number of modes to $\sim \mathcal{F}$. We argument it by considering the maximum angle of scattering that leads to creation of spin waves that later can efficiently retrieved in terms of phase matching. We will require that (cf. Fig. 2.7(a)):

$$\Delta K_z\sigma_z = (k_R - \sqrt{k_r^2 - \theta^2 k_r^2} + k_W - \sqrt{k_w^2 - \theta^2 k_w^2})\sigma_z \approx (k_r + k_w)\theta^2\sigma_z/2 < 1. \tag{4.20}$$

Taking $k_r \approx k_w \approx 2\pi/\lambda$ we get that the angle $\theta < \sqrt{\lambda/2\pi\sigma_z}$. The angular size of the mode is again $\lambda/(2\pi\sigma_\perp)$, so after dividing and squaring this two quantities we arrive and $2\pi\sigma_\perp^2/(\lambda\sigma_z) \sim \mathcal{F}$.

The situation is quite reverse in Ref. [GGZS12], where two read processes (for writing external light to the memory and retrieving it) are considered. We then have a $\sim \mathcal{F}$ scaling for backwards retrieval and $\sim \mathcal{F}^2$ scaling for forward retrieval. In the subsequent chapters we will see, however, that through various manipulation techniques we can mitigate any problems with phase matching, so we can adopt the $\sim \mathcal{F}^2$ scaling as more fundamental.

Quite notably, the very same arguments hold for a memory with spatial (rather than wavevector) multiplexing, as the one in Ref. [Pu17]. For such memory the modes are tightly focused Gaussian beams. We require that such beams are large enough in the centre of the ensemble so that during propagation through the ensemble in remains smaller in its transverse dimension than the ensemble itself. The size turns out to be larger than $\lambda\sigma_z/(2\pi\sigma_\perp)$ and thus if we count how many such beams we can accommodate within the ensemble size, we arrive at the same scaling as in Eq. 4.19. The role of phase matching for forward retrieval becomes clear after considering diffraction.

Finally, in all cases, at very large ODs we can also expect that even high angles will still facilitate good retrieval efficiency. In the scenarios that facilitate proper phase matching, we could then obtain even larger numbers of modes than $\sim \mathcal{F}^2$. On the other hand, larger ODs are typically obtained by producing longer ensembles, which reduces $\mathcal{F}$, and thus a requirement of finding an optimal trade-off arises for future multimode quantum memory implementations.

While we have focused on the application of our quantum memory as a light source in multiplexed communication and computation protocols [Nun13; CDW17], our scheme is also perfectly matched to expedite quantum communication in free-space [Wan12] or with multimode or multi-core fibres [RFN13], quantum imaging and image processing at the single-photon level, as well as quantum-enhanced metrology [Wol12; Mat16]. Spatial photon-number quantum correlations are readily applicable in quantum imaging techniques and the memory capability could help quantum ghost imaging or sub-shot noise imaging along the way to practical applications [BGR10; Gen16]. Furthermore, the quantum-beat signal between two spin-wave excitations demonstrates the ability of our quantum memory to store a superposition of a few spin-waves in many modes and paves the way towards manipulations within and between the Zeeman sublevels as well as with the spatial degree of freedom.

Chapter 5

Collective spin control via ac-Stark shift

In this Chapter, we present experimental implementations of ac-Stark control of atomic spins. First, we manipulate the collective spin polarization and observe its influence on the transmitted light. The results are based on [Les18], yet different theory is used than in the original paper to better suit subsequent considerations.

The concept of fictitious magnetic fields used in this Chapter has ben proposed by Cohen-Tannoudji [CTDR72] and relies on the properties of optically-induced vector ac-Stark shift and is a viable way of performing such spin manipulations [Mor09; Par01], due to its inherently off-resonant and thus absorption-free nature. Moreover, application of fictitious magnetic fields to spin ensembles proves to be a feasible way to reach high sensitivities to real magnetic fields by means of all-optical methods [Zhi14; Lin17; Sun17]. Spatial control of the applied effective potential paves the way towards novel applications such as high spatial-resolution magnetometry [Ven07], magnetic field imaging [Kos11], magnetic gradiometry [DSK13], super-resolved imaging [HZ12] or implicitly generation of tunable gauge potentials on ultracold atoms [Gol14]. Precise spatial control could also enable efficient operation of photon echos [RSM90; Zie98] used in gradient-echo quantum memories [Spa10; CH15], precise atom manipulation [Par01; Par02] as well as novel atom trapping techniques [SLR14; Alb16].

Our goal, on the other hand, was to work out new tools and methods for spatially-resolved controlled of structured spin-wave states. Starting with a manipulation of a classical total spin and performing measurements within the well-known schemes of magnetometry provides a great polygon to test those new tools.

5.1 Idea

We begin with a demonstration of spatially-resolved control of a vector ac-Stark shift on a cold rubidium ensemble. The idea relies on the decomposition of the ac-Stark shift Hamiltonian of the $F = 1$ ground-state manifold into three terms:

scalar, vector and tensor. This decomposition yields many new insights, in particular into intricacies of QND measurement and light-spin coupling. A bunch of works (see Refs. [GSM06; Ech08; Col13a]) describes its properties, yet here we will only treat it as motivation. In particular, the so-called vector part of the Hamiltonian has a form reminiscent of the Hamiltonian of an atom in an external magnetic field. Rather then using the symmetries of the Hamiltonian, here we can show it simply by considering all the transitions involved. Such an approach is better suited to what follows in Chapter 6, since there we will consider a hyperfine coherence between $F = 1$ and $F = 2$ manifolds.

Let us first choose the quantization axis of our system along the axis of propagation of the ac-Stark laser. As shown in Fig. 5.2, this axis for us will be the x axis, as the ac-Stark beam illuminates the atomic ensemble from the side. In this frame of reference, the right-circularly polarized ac-Stark beam detuned interacts with all transitions shown in Fig. 5.1. The magnetic sublevels $m_F = -1$ to $m_F = 1$ are thus shifted accordingly. If we now assume that the ac-Stark light is far-detuned, i.e. δ_S is larger than the hyperfine splitting of the excited state manifold $5P_{3/2}$, all transitions will contribute simply by their relative amplitudes. Within such approximation, we find that the shift may be expressed as:

$$\Delta_S(m_F) = \frac{\alpha_0}{\delta_S} + \frac{\alpha_1}{\delta_S} m_F. \tag{5.1}$$

with $\alpha_0 = \frac{|\mathcal{E}_S d|^2}{12\hbar}$ and $\alpha_1 = \frac{|\mathcal{E}_S d|^2}{48\hbar}$, where $\mathcal{E}_S$ is ac-Stark beam amplitude and

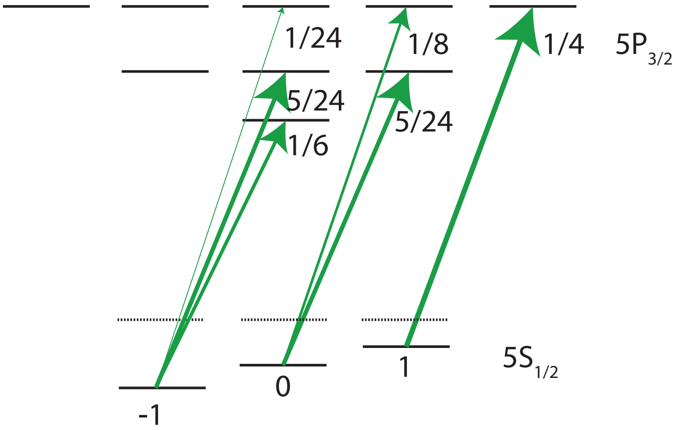

FIGURE 5.1: The ac-Stark shift caused in the $F = 1$ ground-state manifold by an applied strong, far off-resonant circularly-polarized field propagating along the quantization axis. Numbers correspond to relevant transition strength. Dashed lines mark the energies of unshifted levels.

$d = \langle J = 1/2||er||J = 3/2\rangle = 3.58 \times 10^{-19}$ Cm is the dipole matrix element. Importantly, there is no term proportional to m_F^2, which would constitute the tensor part of the interaction. The linear term is the same shift as would be induced by the magnetic field set along the propagation direction. Let us thus write its influence as a simple Hamiltonian (the vector ac-Stark shift Hamiltonian):

$$\hat{H}_S^{(1)} = s\frac{\hbar\alpha_1}{\delta_S}\hat{F}_x, \tag{5.2}$$

where $s = \pm 1$ corresponds to polarization and $\hat{F}$ is the operator of the total spin of a single atom. In particular $\hat{F}_x$ is its x component. The proportionality constant is directly related to the light intensity I_S as:

$$\alpha_1 = \frac{I_S d^2}{24c\epsilon_0\hbar}. \tag{5.3}$$

The form of Hamiltonian from Eq. 5.2 is indeed reminiscent of the Hamiltonian for an atom in an external magnetic field applied along the x direction, so we can define a fictitious magnetic field [CTDR72]:

$$\mathbf{B}_\mathrm{f} = s\frac{1}{g_F\mu_B}\frac{\hbar\alpha_1}{\delta_S}\hat{e}_\mathbf{k}, \tag{5.4}$$

where: $\hat{e}_\mathbf{k} = \mathbf{k}/|\mathbf{k}|$ and $\mathbf{k}$ – wavevector of the laser beam propagating along the x direction. When atomic ensemble is also influenced by a real magnetic field $\mathbf{B}$, taking into account all of the above approximations, the total Hamiltonian can be written in a traditional form:

$$\hat{H} = g_F\mu_B(\mathbf{B} + \mathbf{B}_\mathrm{f})\hat{\mathbf{F}}. \tag{5.5}$$

In consequence, atomic spins exposed to the ac-Stark beam precess around the effective magnetic field $\mathbf{B}_\mathrm{eff} = \mathbf{B} + \mathbf{B}_\mathrm{f}$ with the Larmor frequency $\omega_\mathrm{L} = g_F\mu_B B_\mathrm{eff}/\hbar$. From these formulas, we now see that the sign of the vector ac-Stark shift will shift both with polarization ($s \to -s$) and propagation direction ($\mathbf{k} \to -\mathbf{k}$).

5.2 Spin precession-based characterization

Using a phase-only spatial light modulator (SLM) we shape the spatial profile of an off-resonant laser pulse that induces the ac-Stark shift on the atoms. To characterize the interaction we will observe the effect of the applied fictitious magnetic field on polarization rotation signal, that measures the total spin projection on the z axis $\langle\hat{F}_z\rangle$. Such measurement is traditionally named a free-induction decay (FID) signal [Smi11; Beh13].

The model presented above did not consider incoherent excitation of atoms

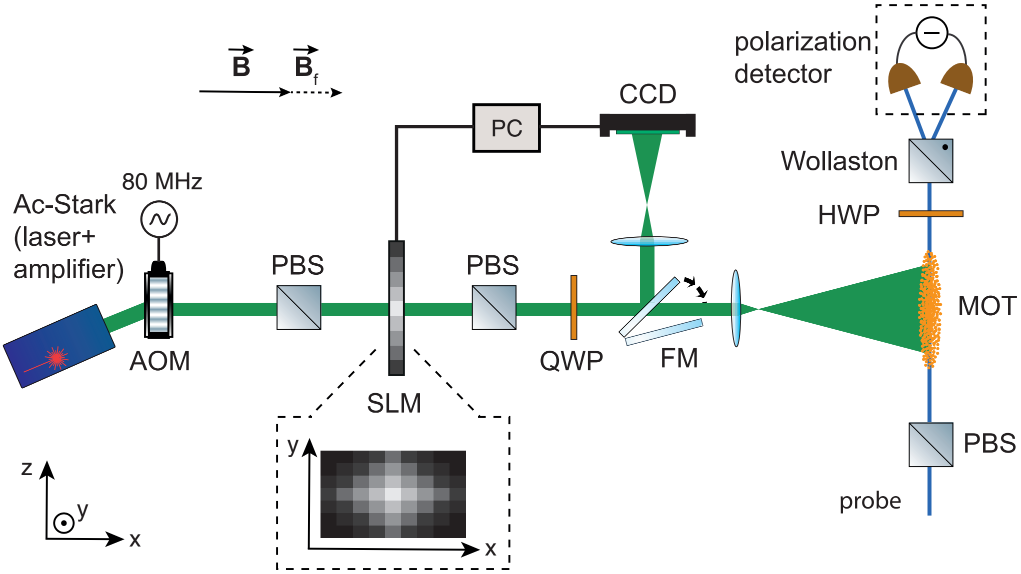

FIGURE 5.2: Schematic of the experimental setup. Atoms released from the magneto-optical trap (MOT) are illuminated by two beams: linearly polarized probe and circularly polarized ac-Stark beam. ac-Stark beam intensity at the output of acousto-optic modulator (AOM) is shaped using reflective spatial light modulator (SLM), drawn in the transmission configuration for simplicity. Flip mirror (FM) switches SLM image between MOT and the CCD camera (which is a simplified version of the more general-purpose setup depicted in Fig. 3.13) Differential photodiode registers polarization rotation of the probe light. PBS, polarizing beamsplitter; HWP (QWP), half-wave (quarter-wave) plate.

and subsequent re-emission of light, including the $F = 2$ manifold. In the leading order of perturbation calculation the rate Γ_{scatt} of this incoherent scattering scales as $\Gamma_{\text{scatt}} \sim 1/\delta_S^2$, as evident from the considerations in Sec. 2.3.1. Therefore, in the far-detuned regime of our experiment ($\delta_S \gg \Gamma$) we expect this contribution to be insignificant.

In the experimental sequence here, repeated synchronously with the 50 Hz SLM refresh rate (note that we later change this rate to effectively 420 Hz), the atoms are first cooled and trapped for 19.6 ms and then the MOT coils are turned off to allow for 300 μs cooling in optical molasses. The 50 Hz refresh rate was selected to synchronize with perturbations from the electrical grid and resulting magnetic field. While the 50 Hz frequency of the SLM did not match the 50 Hz of the grid perfectly, it still allowed minute-long stable measurements.

In fact, it is possible to synchronize the SLM the electric grid. The frequency of the SLM is determined by the clock of the graphics card in the control computer. We have been able to replace a quartz oscillator there with an external 27 MHz DDS source. A microcontroller was then used to phase lock the 50 Hz line signal with the SLM synchronization signal by slightly varying the 27 MHz clock

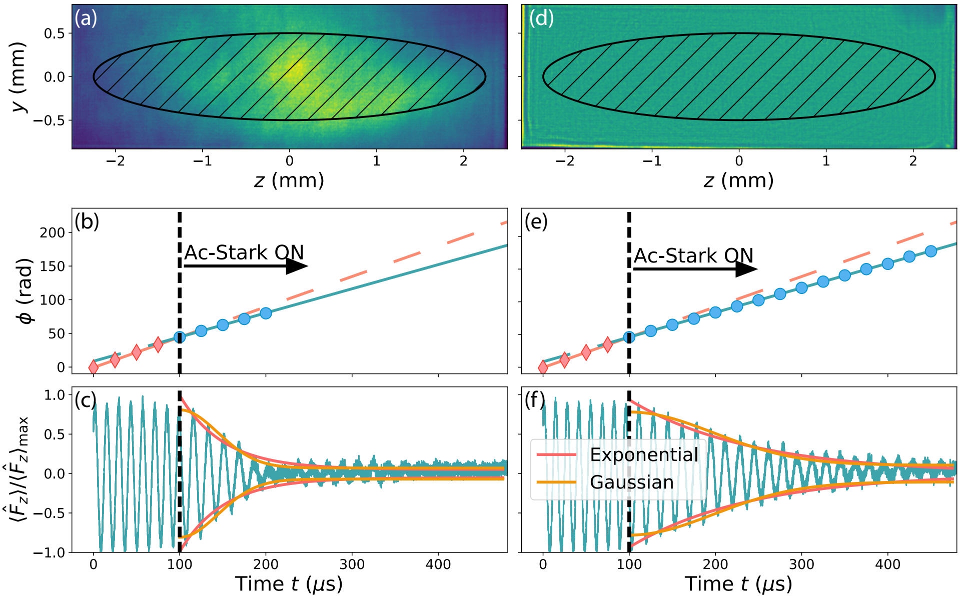

FIGURE 5.3: Influence of the ac-Stark beam intensity inhomogeneity on the FID lifetime τ for $B_{\mathrm{eff}} = B - B_{\mathrm{f}}$. (a) Intensity distribution I_0 of σ_--polarized ac-Stark beam registered on the CCD camera, without SLM correction. The shaded ellipse visualizes MOT position. (b) Phase ϕ retrieved from the FID signal oscillations presented (along with its envelope) in (c). The envelope is fitted with an exponential and Gaussian decay for comparison. Diamonds (dots) correspond to the phase ϕ measured before (after) turning on the ac-Stark beam, along with the linear fits (errorbars within data points). Analogous data for intensity distribution I_C, corrected using SLM to obtain a flat profile of the beam in the MOT plane, are presented in (d)–(f).

signal. The setup turned out to be unnecessary after all, yet it may have potential applications if lower magnetic fields are used along the ac-Stark modulation.

Residual magnetic fields from eddy currents decay after 100 μs, as we have shown in Fig. 3.4. Once the MOT is fully switched off we pump the atoms to the $5^2S_{1/2}$, $F = 1$ state with $\langle F_z \rangle = 1$. Then, after 100 μs of atomic spins rotation driven only by an external magnetic field $\mathbf{B} = B\hat{e}_x$ with amplitude $B = 100$ mG, we illuminate atomic ensemble with a circularly polarized ac-Stark beam. The beam is far-detuned from the $5^2S_{1/2}$, $F = 1 \to 5^2P_{3/2}$ atomic transition and propagates along the x direction. This experimental configuration results in the net magnetic field $\mathbf{B}_{\mathrm{eff}} = \mathbf{B} + \mathbf{B}_{\mathrm{f}}$ pointing along the x axis.

Average spin projection $\langle \hat{F}_z \rangle$ onto the z axis is measured by registering polarization rotation of a weak linearly polarized probe beam propagating along the z direction, using a Wollaston prism and a differential photodiode (DPD). The probe beam of 1 μW power is detuned by 100 MHz from the $5^2S_{1/2}$, $F =$

$1 \rightarrow 5^2P_{3/2}$, $F = 2$ transition, minimizing the deleterious effect of incoherent excitations and tensor interaction. To avoid spin decoherence due to intensity inhomogeneities of the ac-Stark beam we correct the spatial profile using a phase-only reflective SLM and a polarizing beamsplitter (PBS), as has been described in Sec. 3.5.

As the sign of the fictitious magnetic field $\mathbf{B}_\mathrm{f}$ changes with the light polarization s (Eq. 5.4), the absolute value of the fictitious magnetic field B_f adds to or subtracts from the real magnetic field B. In Fig. 5.3 the influence of the ac-Stark effect (with $\delta_S = -2\pi \times 30$ GHz) on the typical spin-precession signal (FID) is presented for the case where the fictitious magnetic field $\mathbf{B}_\mathrm{f}$ of amplitude $B_\mathrm{f} = 20$ mG is subtracted from the real magnetic field $\mathbf{B}$. Using the Hilbert transform we retrieve the phase and envelope (analytical signal) of the measured FID signal. This allows recovering only the essential parameters with high precision without fitting of the full sinusoidal FID signal. In the left column of Fig. 5.3 we plot the spatial intensity profile I_0 of the ac-Stark beam without any SLM correction procedure (a), the total accumulated phase of the FID signal (b), and the FID signal itself (c). The envelope is fitted with exponential and Gaussian decay functions for comparison. We observe that they both provide a reasonable fit and later we choose to adopt the times fitted to an exponential decay. The right column (d)–(f) portrays corresponding data for the spatial intensity profile I_C already corrected with the SLM. The average intensity of $160\,\mathrm{mW/cm}^2$ is selected so that the mean Larmor (FID) frequency shift is the same for both I_C and I_0 intensity profiles. When the ac-Stark beam is applied, much shorter lifetime τ is observed for the uncorrected, highly inhomogeneous case (Fig. 5.3(c)).

To explain the inherently finite lifetime τ of the spin-precession signal let us now consider the three most essential sources of decoherence for the case of ac-Stark shift spin control. The first one is any kind of spin decoherence occurring even without the ac-Stark beam, i.e. intrinsic decay, This includes dephasing due to magnetic field inhomogeneities (occurs at a rate < 1 kHz thus negligible in the further analysis) and most importantly interaction of atoms with the probe beam. This includes incoherent excitation as well as higher-order interaction (tensor) not predicted by the simple polarization-rotation model. We minimize these effect using weak probe light (ca. microwatt power) detuned by 100 MHz from the $5^2S_{1/2}$, $F = 1 \rightarrow 5^2P_{3/2}$, $F = 2$ transition. We obtain the FID lifetime (for $\omega_\mathrm{L} = 2\pi \times 74$ kHz) of about $\tau_0 = 700$ μs.

The second source – associated with the manipulation itself is absorption and subsequent re-emission of light caused by the ac-Stark beam quantified by the scattering rate Γ_scatt. This effect is proportional to I_S/Δ^2 (see Sec. 2.3.1) while the Larmor frequency shift (ac-Stark shift) scales as I_S/Δ (Eq. 5.5). Therefore, the way to minimize incoherent scattering is to increase Δ and I_S proportionally. The last, significant source of decoherence is the dephasing caused by the intensity inhomogeneities of the ac-Stark laser beam characterized by the lifetime τ_S, calculated as:

$$\tau_S^{-1} = \tau^{-1} - \tau_0^{-1}. \tag{5.6}$$

As shown in Fig. 5.3, SLM-corrected ac-Stark beam intensity distribution I_C increases the FID lifetime τ significantly compared to the situation with uncorrected intensity profile I_0. To explicitly confirm this, in Fig. 5.4 we plot the lifetime τ_S along with a fit to a simple relation $\tau_S \propto |\delta_S|$, the ac-Stark induced Larmor frequency shift $\Delta\omega_L$ as well as the mean phase accumulated within the FID lifetime $\varphi_S = \tau_S \Delta\omega_L$, as a functions of ac-Stark beam detuning Δ. Two columns depict

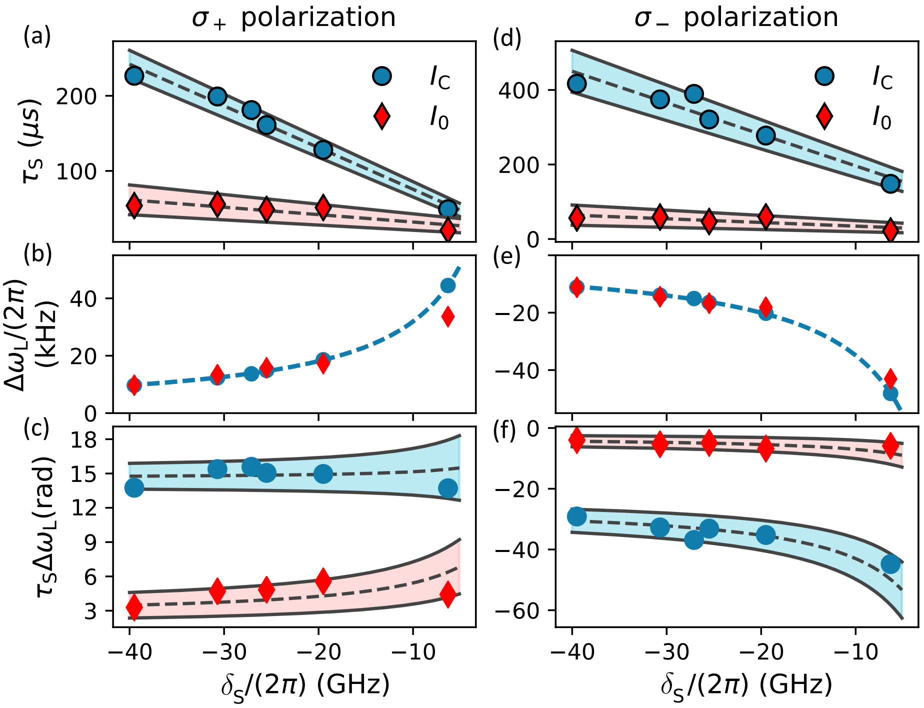

FIGURE 5.4: Dependence of the FID signal on the detuning δ_S for the ac-Stark beam intensity profile with (I_C) and without (I_0) SLM correction. Measured ac-Stark induced dephasing lifetime τ_S along with a fitted function (dashed line) (a), Larmor frequency shift $\Delta\omega_L$ (b) and total phase $\varphi_S = \tau_S\Delta\omega_L$ (c) accumulated within spin coherence lifetime (the product of values from (a) and (b)) for σ_+ polarization of the ac-Stark beam. Shading regions around dashed lines (theoretical fit) correspond to fitting uncertainties (determined for (a) and (c) from standard covariance matrix of the linear fit parameters). In (b) the theoretical scaling I/δ_S is marked by the dashed line for intensity $I_S = 160$ mW/cm^2 (errorbars within data points). Analogous quantities for σ_- polarization of the ac-Stark beam are plotted in (d)–(f). Maximum achievable frequency shift presented here corresponds to a fictitious magnetic field with amplitude $B_f = 70$ mG.

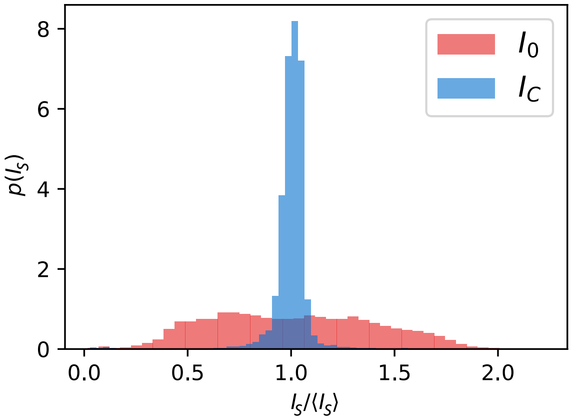

FIGURE 5.5: Histogram of relative intensities ($I_S/\langle I_S\rangle$) before and after correction using the SLM, corresponding to Figs. 5.3(a,d). Strong reduction of spatial intensity variations is observed.

results for both σ_+ and σ_- polarized ac-Stark light. The uncorrected ac-Stark beam mean intensity is chosen to preserve the same FID frequency as with corrected beam profile. Figures 5.4(b) and 5.4(e) confirm the theoretical prediction δ_S^{-1} given by Eq. 5.4. The curve fitted to data corresponds to average light intensity $I_S = 160\ \mathrm{mW/cm^2}$ which is consistent with an independent measurement of light power. The total phase φ_S accumulated within FID lifetime exhibits nearly δ_S-independent behaviour which indeed confirms the dominant role of the ac-Stark shift inhomogeneities on the decoherence phenomenon. Most importantly, thanks to homogenization the possible phase φ_S that the spin can accumulate within one $1/e$ characteristic lifetime τ_S increases from $\varphi_\mathrm{S} = 5$ rad to about $\varphi_\mathrm{S} = 15$ rad for both σ_+ and σ_- polarizations of the ac-Stark beam.

A supporting view is provided by considering the statistics of ac-Stark light intensity. We analyse the intensity maps from Figs. 5.3(a) and 5.3(d) and plot the relative intensity statistics, registered in each pixel, in Fig. 5.5. Indeed we observe that with homogenization the distribution of intensity statistics is much narrower. The observed distribution can be understood as a spectrum of resulting FID signal. From simple Fourier-transform considerations, we may understand that a broader spectrum leads to a much faster decay. The exact shape of the spectrum will also determine the manner in which the FID signal decays. In particular, Gaussian statistics lead to Gaussian-shaped decay, and Lorentzian statistics would lead to exponential decay. The statistics we actually observe seem to be neither. As has been illustrated in Figs. 5.3(c) and 5.3(f) both shapes roughly reproduce the observed shape of FID envelope decay.

5.3 Generating beat-notes

Using the SLM we can easily shape the intensity I_C of the ac-Stark beam into arbitrary patterns – one particular example is depicted in Fig. 5.6. Here, atoms are illuminated with the staircase spatially-modulated ac-Stark beam (with $\delta_S = -2\pi \times 30$ GHz), visualized in insets in Fig. 5.6. Thus, several groups of spins oscillate with equidistant frequencies, forming a frequency comb. With more intensity steps, or equivalently with more teeth in the frequency comb, we can achieve a lower ratio of the revival duration to the time where the amplitude of the FID signal is small. This time scales linearly with the number of teeth. For only two-intensity levels (Fig. 5.6(a)) the FID signal has a cosine envelope and collapses only for a moment, but for four-level staircase (Fig. 5.6(c)) the FID signal almost completely disappears for about 80 μs.

5.4 Conclusions

To conclude, we have demonstrated spatially-resolved control of the fictitious magnetic field generated using the ac-Stark effect. We have shown that inhomogeneities of the ac-Stark beam are the main source of dephasing. After homogenization using SLM we have achieved a phase shift of over 15 rad within the

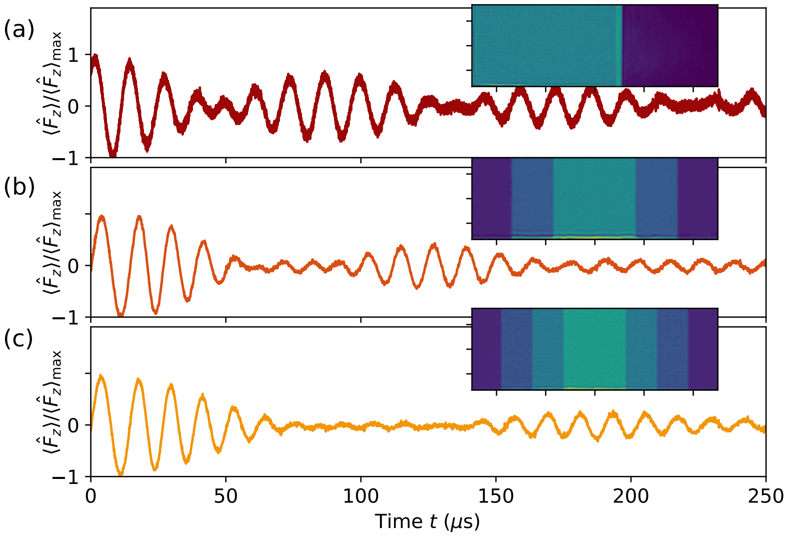

FIGURE 5.6: Temporal dynamics of the FID signal for staircase intensity profiles. Measured beat-note FID signal for two intensity steps (a) as well as collapse-and-revival FID signal for three (b) and four (c) intensity steps. The insets present measured modulation patterns I_S.

$1/e$ the lifetime of the spin coherence, which is several times longer than without spatial intensity corrections. We have also presented the possibility to engineer complex temporal dynamics of the FID signal by sculpting the ac-Stark beam intensity, from frequency shift through beat-note, to collapse-and-revival behaviour. The control over spatial and temporal aspects of light in comparison to the real magnetic field makes our method very robust and useful in high-resolution magnetometry [Kos11] or magnetic gradiometry [DSK13], giving prospects to readily improve the sensitivity and precision. The results of this chapter constitute a solid foundation for subsequent spatial manipulations of spin waves.

Chapter 6

Spin wave interferometry

In this Chapter, we demonstrate the two-particle (Hong-Ou-Mandel) interference of a pair of spin waves residing in the quantum memory. Through that, we also show that the spatial structure of spin waves can be manipulated via the off-resonant ac-Stark shift. The results are based on Ref. [Par18c], with substantial modification in relation to the original arXiv preprint.

Through spin-wave diffraction (cf. Kapitza-Dirac effect [KD33]) based beam-splitter transformation, we realize the Hanbury Brown-Twiss (HBT) type measurement in the spin-wave domain [HBT56], demonstrating precise control and nonclassical statistics of atomic excitations. Most importantly, however, we observe interference of two spin waves – an analogue of the HOM effect for photons. Thanks to the reversible photon-spin wave mapping via the Duan-Lukin-Cirac-Zoller (DLCZ) protocol multimode Raman interface as presented in Chapter 4, these techniques enable encoding states from a high-dimensional Hilbert space into the spatial structure of spin waves to facilitate not only new quantum communication schemes [Fic16], but also high data rate classical telecommunication [Wan12; RFN13]. We propose that a quantum repeater equipped with such coprocessing capability could perform error correction [JTL07; Che07; Zha07; Mur14] or small-scale computation on transmitted quantum data.

6.1 Properties of ac-Stark modulation

To engineer ground-state spin waves in our spatially-multimode quantum memory we employ an off-resonant strong laser shaped with a spatial light modulator (Fig. 6.1), inducing a spatially-dependent differential ac-Stark shift $\Delta_S(\mathbf{r})$ between levels $|g\rangle$ and $|h\rangle$, directly proportional to light intensity. With negligible absorption and a small transverse size of the ensemble we assume a constant intensity along the propagation axis x of the S beam and thus write $\Delta_S(\mathbf{r}) = \Delta_S(y, z)$. The ac-Stark shift leads the spin waves to accumulate an additional, spatially-dependent phase $\varphi_S(y, z) = \Delta_S(y, z)T$ over the interaction time $T \sim 2$ μs with a typical $\Delta_S/2\pi \sim 36$ kHz obtained with 35 mW/cm^2 intensity of S light detuned from the respective resonance by $\delta_S/2\pi = 1.43$ GHz.

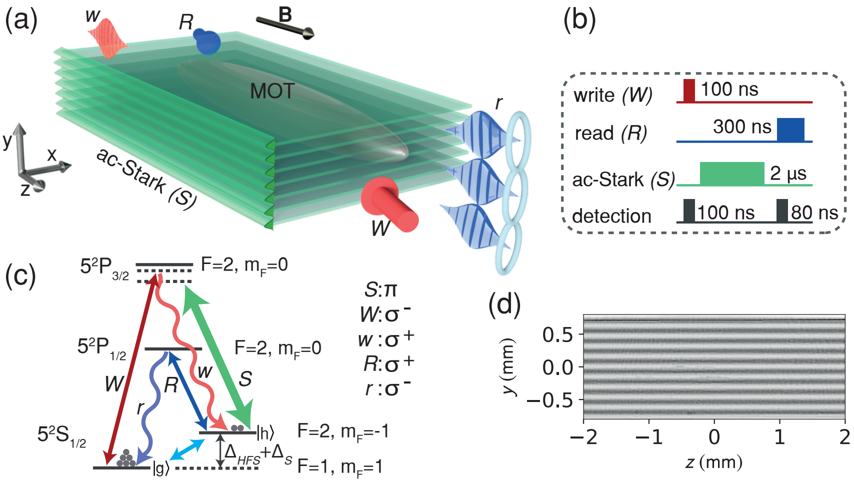

FIGURE 6.1: Experimental setup for generating and manipulating spin waves: (a) detection of a single write photon w scattered from write laser W heralds creation of a spin wave inside the atomic ensemble. The spin wave is then manipulated using an ac-Stark light pattern (b) generated with a far-detuned laser S. The spin wave can then be converted by the read laser R to a read photon r with a reshaped spatial mode; (c) the relevant energy level configuration: $|g\rangle = |5^2S_{1/2}\ F = 1, m_F = 1\rangle$ and $|h\rangle = |5^2S_{1/2}\ F = 2, m_F = -1\rangle$. The write laser is red-detuned from the $5^2S_{1/2}\ F = 1 \to 5^2P_{3/2}\ F = 2$ transition by 25 MHz, the read laser is resonant with the $5^2S_{1/2}\ F = 2 \to 5^2P_{1/2}\ F = 2$ transition and the ac-Stark laser S is red-detuned from the $5^2S_{1/2}\ F = 2 \to 5^2P_{3/2}$ line centroid by 1.43 GHz. During QM operation we keep constant bias magnetic field $\mathbf{B} = (50\text{ mG})\hat{e}_z$.

To theoretically evaluate the performance of the ac-Stark modulation at the single-excitation level, it is crucial to consider both the level of decoherence caused by manipulation and the spurious noise produced. The manipulation should also influence the coherence in a proper way, i.e. the states $|g\rangle$ $(F = 1,\ m_F = 1)$ and $|h\rangle$ $(F = 2,\ m_F = -1)$ should be eigenstates of the effective ac-Stark splitting Hamiltonian, as given by Eq. 2.100. Otherwise, the spin wave is transferred to a different combination of magnetic sublevels, which may lead to beat-notes as well as decoherence due to magnetic field inhomogeneities, which we discussed in Sec. 2.3.6. Further theoretical analysis of the modulation scheme in terms of atomic dynamics is presented in Appendix C.

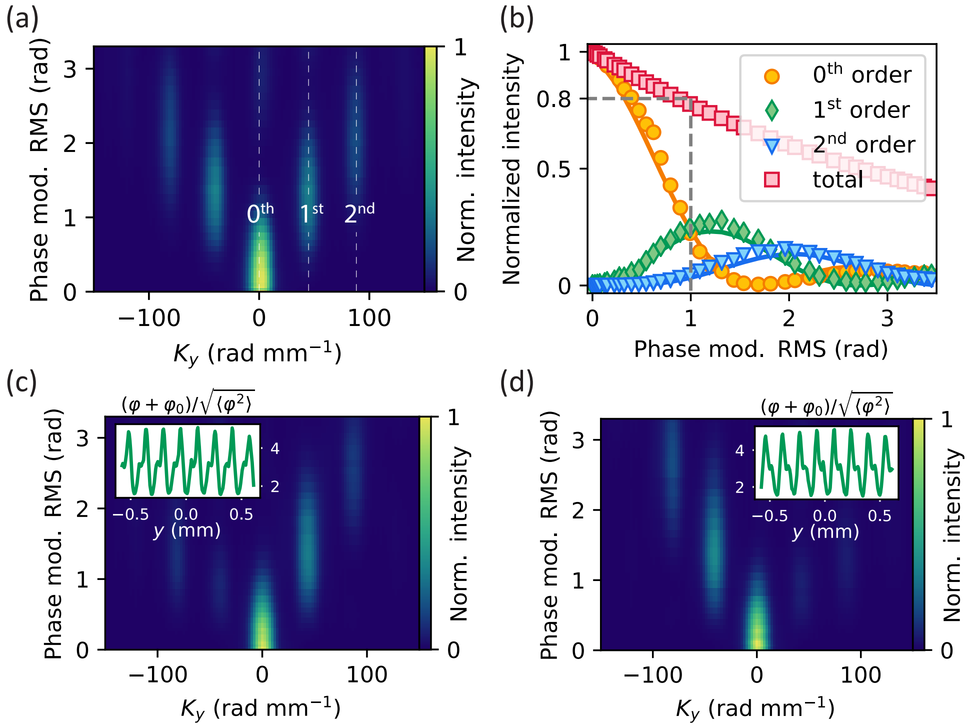

FIGURE 6.2: Measured performance of the spin-wave phase modulator: (a) light intensity emitted from a spin wave as a function of a pure sine modulation RMS amplitude $\sqrt{\langle\varphi_S^2\rangle}$ and the wavevector K_y component; (b) intensities in diffraction orders 0 to 2, marked in (a). In (c,d) we change the modulation to include a term with higher frequency (insets - phase modulation patterns). Depending on the relative phase between the two terms we observe diffraction predominantly in the selected direction.

6.2 Spatial ac-Stark manipulation

The spatial manipulation in the spin-wave domain can be written within the Heisenberg picture as:

$$\hat{\tilde{b}}^{\dagger}_{\mathbf{K}} = N^{-1/2}\sum_{n}^{N} e^{i\mathbf{K}\cdot\mathbf{r}_n + i\varphi_S(\mathbf{r}_n)}|h_n\rangle\langle g_n| = \int \mathscr{F}[e^{i\varphi_S(\mathbf{r})}](\mathbf{k})\hat{b}^{\dagger}_{\mathbf{K}+\mathbf{k}}\mathrm{d}\mathbf{k}, \tag{6.1}$$

where $\mathscr{F}$ represents the Fourier transform in the spatial domain. With periodic $\varphi_S(\mathbf{r})$, the transformation becomes a Fourier series, realizing a multi-output spin-wave beamsplitter in two momentum-space dimensions (K_x, K_z).

We first select φ_S to be a sine wave $\varphi_S(y) = \chi\sin(k_g y + \vartheta)$, where k_g is the grating wavevector. For technical reasons the sine modulation has been accompanied by a constant component φ_0. This was due to the inability to display low (and obviously also negative) intensities on the SLM. We have later improved that issue by performing independent gamma-curve calibrations of multiple SLM regions, so that we could set $\varphi_0 = \chi$ and the modulation ranged from 0 to 2χ. With such modulation all spin waves are diffracted into subsequent orders with central y wavevector components $K_y + mk_g$, $m \in \mathbb{Z}$ and amplitudes of subsequent orders depending on strength of phase modulation quantified by its root mean square (RMS) amplitude $\sqrt{\langle\varphi_S^2\rangle}$. For benchmarking we generate a coherent spin-wave state with excitation number $\bar{n} \approx 10^5$, by seeding the Raman process with a coherent state of light tuned to $|g\rangle \leftrightarrow |h\rangle$ two-photon transition along with the W laser, as has been described in Sec. 3.3. In Fig. 6.2(a) we depict the wavevector-resolved intensity of light emitted from spin waves as a function of phase modulation strength. By integrating the intensities in the discernible diffraction orders we compare the experimental result with the expected behaviour [Fig. 6.2(b)], finding excellent agreement and confirming the proposed mechanism for spin-wave diffraction.

To explicitly express the transformation of the spin-wave creation operator $\hat{b}^\dagger_{K_y} \xrightarrow{\varphi_S(y)} \hat{\tilde{b}}^\dagger_{K_y}$, describing the result of imprinting on atoms a sine-shaped phase pattern $\varphi_S(y) = \chi\sin(k_g y + \vartheta)$ we may use the well-known Jacobi-Anger identity to expand the modulation term into more convenient form:

$$\exp(i\chi\sin(k_g y + \vartheta)) = \sum_{n=-\infty}^{\infty} J_n(\chi)\exp(in(k_g y + \vartheta)), \tag{6.2}$$

where J_n is the n-th Bessel function of the first kind. With this expansion we easily obtain that:

$$\hat{\tilde{b}}^\dagger_{K_y} = \sum_{n=-\infty}^{\infty} J_n(\chi)\exp(in\vartheta)\hat{b}^\dagger_{K_y+nk_g}. \tag{6.3}$$

Using this formula with χ chosen so that $J_0(\chi) = J_1(\chi)$ and neglecting terms with $n > 1$, we get the transformation via which a 50:50 beamsplitter can be realized, which we will demonstrate in Sec. 6.5.

6.3 Directional modulation

For the purpose of quantum engineering of spin waves, we now show that through precise control of the phase modulation pattern we achieve the desired amplitudes of diffraction orders, creating a controllable 1−to−N quantum network, where the zeroth order remains one of the output ports. Figures 6.2(c,d) depict the wavevector-resolved spin-wave density. With this we show that spin waves are predominantly diffracted in the selected direction through a proper asymmetrical modulation, here composed of a sine wave with two frequencies with controlled relative phase. To generate these asymmetric spin-wave patterns, we use different phase modulation. The modified version includes a "second-harmonic" term:

$$\varphi_S(y) = \chi_1 \sin(k_g y + \vartheta_1) + \chi_2 \sin(2k_g + \vartheta_2). \tag{6.4}$$

By taking $\chi_1/\chi_2 = 2.5$, we observe that spin-wave diffraction occurs predominantly in one direction (as in Figs. 6.2(c) and 6.2(d)). By changing the relative phase between the two terms above, i.e. $\Delta\vartheta = \vartheta_1 - \vartheta_2$, we can steer the direction of diffraction. In particular, for Fig. 6.2(c) we selected $\Delta\vartheta = 0$ and for Fig. 6.2(d) we set $\Delta\vartheta = \pi$.

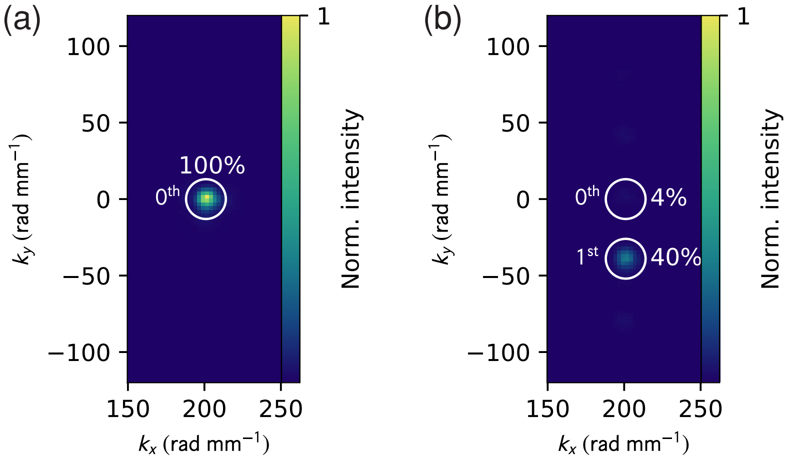

FIGURE 6.3: Wavevector-resolved light intensity emitted from a spin wave, (a) before and (b) after a "blazed" grating modulation is applied in order to transfer all excitations into the first diffraction order.

Directing photons into a specific mode As another example, we demonstrate how to diffract one spin-wave mode into a single (distinct) mode. This can be simply achieved by selecting a linear ramp $\varphi_S(y) = \alpha y$, that transforms $\hat{b}_{\mathbf{K}}$ into $\hat{b}_{\mathbf{K}+\alpha e \hat{e}_y}$. Such pattern, however, may require high laser intensities to significantly transform the mode. A good alternative is to wrap the phase shift ramp and obtain a "blazed" diffraction grating. The periodicity of this grating will determine the wavevector shift, and its amplitude is inherently 2π. Figure 6.3 presents an example manipulation with such grating, where we achieve 40% transfer efficiency and only 4% of excitations remain in the zeroth order. This figure of merit can be greatly improved if we can minimize current intensity deviations from the desired pattern of roughly 10% by preparing a more uniform illumination of the spatial light modulator and designing a system with higher imaging resolution. Such

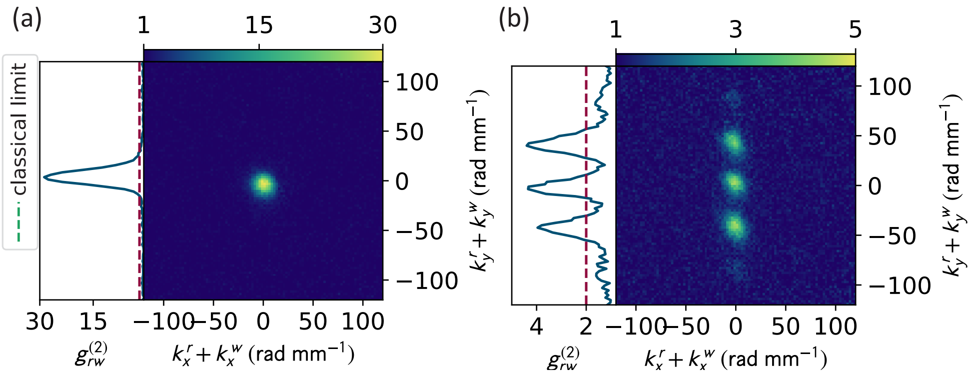

FIGURE 6.4: Second-order cross-correlation functions in the centre-of-mass wavevectors variables as measured in the coincidence measurements using the I-sCMOS camera. A reference measurement (a) of second-order cross-correlation $g^{(2)}_{rw}$ reveals a single peak at $k^r_y + k^w_y = 0$, demonstrating momentum anti-correlations. By reshaping the spin waves with a sine modulation pattern with wavevector k_g, we modify the correlation function (b) to feature two additional peaks at $k^r_y + k^w_y = \pm k_g$. The correlations are calculated as given by Eq. 4.16.

more elaborate manipulation patterns will be thoroughly discussed in Chapter 7.

6.4 Spin-wave splitting observed in spatial correlations

With the spin-wave modulation operating with high populations, we now evaluate its performance at the single excitation level. We probabilistically generate spin waves heralded by detection of w photons on an I-sCMOS camera situated in the far-field of the atomic ensemble. Quantum character of excitations is certified by the second-order correlation function $g^{(2)}_{rw} = \langle \hat{n}_r \hat{n}_w \rangle / \langle \hat{n}_r \rangle \langle \hat{n}_w \rangle > 2$, which we express in terms of wavevector-sum variables, as given by Eq. 4.16. If the spin waves are converted to photons without manipulation, a single peak at $k^r_x + k^w_x = k^r_y + k^w_y = 0$ is observed, as in Fig. 6.4(a), since in general $\mathbf{k}^w + \mathbf{k}^r = \mathbf{k}^W + \mathbf{k}^R$ and we select $\mathbf{k}^W_\perp = -\mathbf{k}^R_\perp$ (the counter-propagating configuration). With sinusoidal phase modulation with RMS = 1.0 rad and wavevector k_g applied along the y-direction during storage, the peak is split into three equal diffraction orders [Fig. 6.4(b)] with very little contribution to higher orders, thus we may write that the $\hat{b}_\mathbf{K}$ operator is transformed into a sum of three operators:

$$\hat{\hat{b}}_\mathbf{K} = (\hat{b}_\mathbf{K} + e^{i\vartheta} \hat{b}_{\mathbf{K}+k_g \hat{e}_y} - e^{-i\vartheta} \hat{b}_{\mathbf{K}-k_g \hat{e}_y})/\sqrt{3}. \tag{6.5}$$

We certify quantum photon-number correlations in each peak, demonstrating that our modulation scheme preserves statistical properties of a spin wave, by operating with high efficiency and without adding spurious noise.

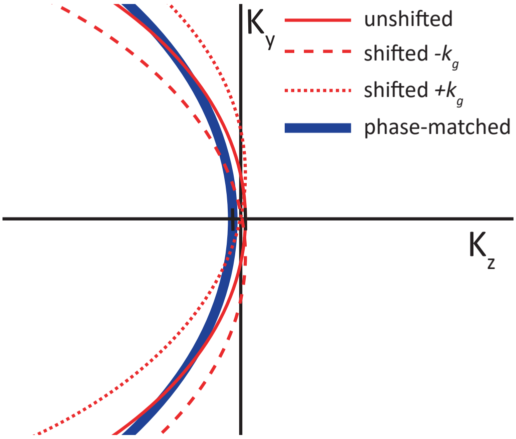

FIGURE 6.5: Pictorial explanation of the phase-matching issue. During the write process, we herald spin waves the wavevectors of which are marked with the solid red line in the (K_y, K_z) plane. As discussed in Sec. 2.3.2, they are well phase-matched during read-out (solid blue line indicates the spin-wave wavevectors phase-matched perfectly during read-out). However, as we shift the spin-wave wavevectors via the ac-Stark modulation in the K_y direction, the phase matching changes significantly. Spin waves shifted by $-k_g$ are now very well phase matched only at small positive K_y, and conversely, spin waves shifted by $+k_g$ are phase-matched at small negative K_y. In consequence, only the regions around $K_y = 0$ allow phase matching of both shifted and unshifted spin waves. This fact is directly observed experimentally in Fig. 6.6.

It is important that we only consider spin waves with relatively small K_y. If the scattering angle is too large, our modulation might make the spin waves phase-mismatched during the read-out process. Indeed, by considering the read-out efficiency of a plane-wave spin-wave reshaped with a sine grating with k_g, we arrive at a very good agreement between measured coincidence map presented in Fig. 6.6(a) and the theoretical prediction [Fig. 6.6(b)] for phase-matching efficiency (here normalized to unity), calculated according to Eq. A.58. The results indicate that the phase-matching is the most essential wavevector-dependent factor to the net read-out efficiency. The main observed effect is the fact that only spin waves with small K_y can be read-out efficiently after modulation. Figure 6.5 demonstrates a pictorial representation of the situation in the spin-wave wavevector space.

The remaining spin-wave are not lost but can be retrieved through manipulating their K_z wavevector components to restore the phase-matching. The problem can thus be alleviated through the use of the ac-Stark gradient in the z-direction or rotation of the grating in the y-z plane, as we will demonstrate in Chapter 7. Furthermore, it is worth noting that the region for which the read-out is naturally efficient encompasses hundreds of usable modes (in terms of Schmidt decomposition).

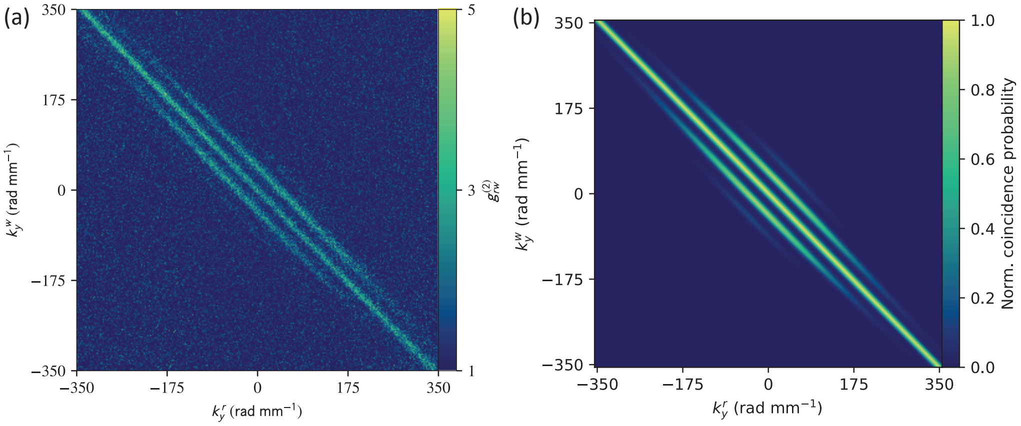

FIGURE 6.6: Influence of phase matching on the read-out of diffracted spin-waves. Panel (a) portrays normalized write-read coincidences in the form of the second-order correlation function (obtained from the same data as Fig. 6.4(b)). We compare this experimental result with the calculated normalized read-out efficiency of the reshaped spin-waves presented in panel (b) [corresponding to the same write photons as in (a)]. A strong influence of phase-matching is evident, as read-out is only efficient for values of k_y^r (and consequently also K_y) around 0.

Let us now consider the dependence of the unconditional $g^{(2)}$ function on modulation RMS amplitude. For this we resort to single-mode detection (Fig. 6.9(b)). Choosing two Gaussian-shaped modes (mode field radius $\sigma = 10.3$ rad mm^{-1}) separated by $\Delta K_y = k_g$ (i.e rc and rd) and neglecting the contribution of weak thermal state split into the rc mode (i.e. assuming modes va and vb reside in vacuum) we can write (following Eq. 6.2):

$$g^{(2)}_{wa,rc} = 1 + \alpha J_0(\chi)^2 e^{-\gamma\chi}, \tag{6.6}$$

$$g^{(2)}_{wa,rd} = 1 + \alpha J_1(\chi)^2 e^{-\gamma\chi}. \tag{6.7}$$

As $\chi = \sqrt{2\langle\varphi^2\rangle}$. We heuristically include the exponential decay with a constant γ to model dephasing due to deviations of the ac-Stark grating from a perfect sine wave. The results for the fit parameters are $\alpha = 23.1 \pm 0.3$ and $\gamma = 0.27 \pm 0.05$ rad^{-1}. The cross-correlation function without the modulation applied corresponds to $g^{(2)}_{wa,rc}$ (no modulation) $= \alpha + 1 = 24.1 \pm 0.3$. This allows us to estimate the total efficiency at $\sqrt{\langle\varphi^2\rangle} = 1$ rad as 84%. The fit results are presented in Fig. 6.7 along with the efficiency corresponding to $e^{-\gamma\chi}$.

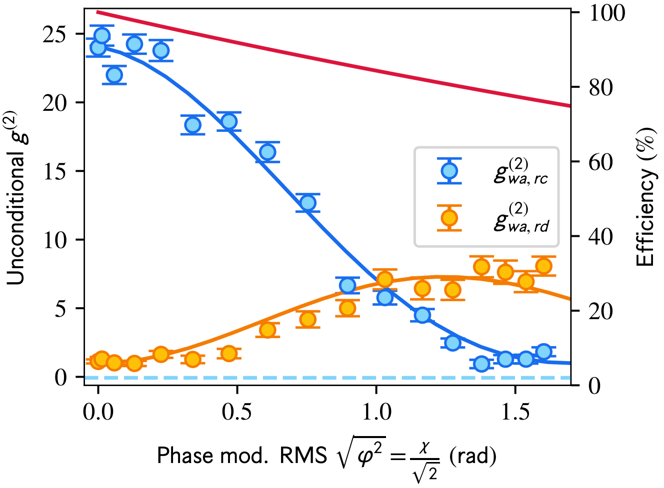

FIGURE 6.7: Beam-splitter operation at the single spin-wave level. Measured second order correlation between the wa write photon mode for two read-out detection modes rc ($k_y^r + k_y^w = 0$) and rd ($k_y^r + k_y^w = k_g$) as a function of phase modulation RMS $\sqrt{\langle\varphi^2\rangle}$ (left axis; dashed line corresponds to 0), and predicted total diffraction efficiency in all modes (red line, right axis). Curves correspond to the theoretical prediction with a the initial correlation and decay as fit parameters.

6.5 Hong-Ou-Mandel interference

We now use the presented manipulation to observe interferometric properties of spin waves. We select a pair of Gaussian-shaped modes (mode field radius $\kappa = 10.3$ rad mm^{-1}) for the w photon (wa and wb) corresponding to spin-wave modes (ra and rb) with $K_y^{ra/rb} = \pm\Delta K_y/2 = \pm 45$ rad mm^{-1} and equal $K_x^{ra} = K_x^{rb} \approx 200$ rad mm^{-1} ($\Delta K_x = 0$) [Fig. 6.8]. By heralding a pair of w photons, we generate a spin wave pair $\hat{b}^\dagger_{ra}\hat{b}^\dagger_{rb}|0\rangle = |11\rangle_{ra,rb}$. With a proper phase modulation each spin wave gets equally distributed into three equidistant modes. We select the grating period $k_g = \Delta K_y = 90$ rad mm^{-1}, so that after manipulation we may write operators for resulting modes rc and rd as

$$\hat{b}^\dagger_{rc} = (\hat{b}^\dagger_{ra} + e^{-i\vartheta}\hat{b}^\dagger_{rb} - e^{i\vartheta}\hat{b}^\dagger_{va})/\sqrt{3} \tag{6.8}$$

and

$$\hat{b}^\dagger_{rd} = (\hat{b}^\dagger_{rb} + e^{-i\vartheta}\hat{b}^\dagger_{vb} - e^{i\vartheta}\hat{b}^\dagger_{ra})/\sqrt{3}. \tag{6.9}$$

Let us now assume that the modes are well-overlapped, that is $\Delta K_x = 0$ and $\Delta K_y = k_g$ and modes va and vb with $K_y^{va/vb} = \pm\frac{3}{2}\Delta K_y$ reside in vacuum (no excitation is heralded in this modes and we neglect their thermal occupations).

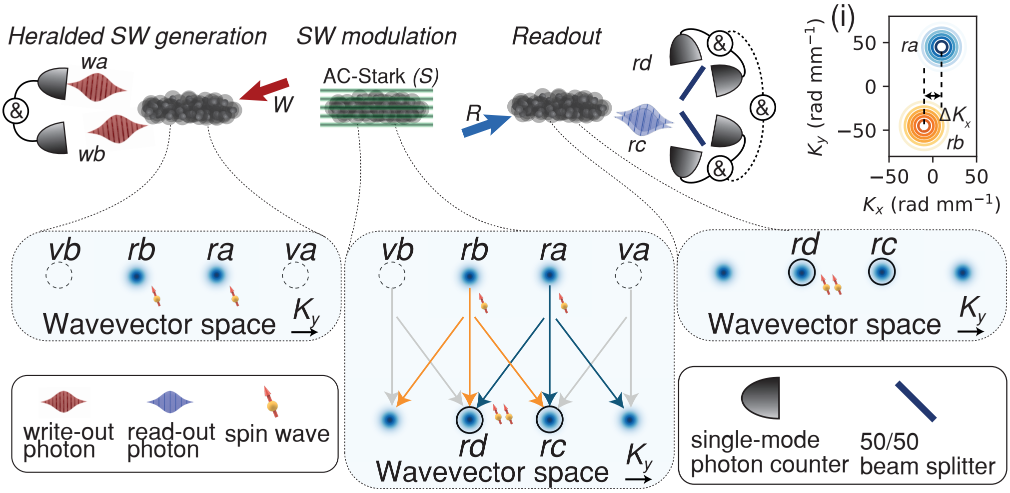

FIGURE 6.8: The protocol for quantum interference of spin waves. Detection of two w photons in modes wa and wb (selected through single-mode fibres) heralds generation of a spin wave pair in modes ra and rb. The three-way splitter is then used to interfere the two spin waves. By detecting the spin waves through photons converted to rc and rd modes we observe bunching due to their bosonic nature. Inset (i) presents the input spin-wave modes in the $(K_x,\ K_y)$ plane. Photonic detection modes are always set to collect photons emitted from heralded spin-wave modes.

In such scenario the Hong-Ou-Mandel interference will occur, as during the manipulation photons in adjacent modes will "meet". The full output state is given by a density matrix, since we trace out the unobserved modes:

$$\hat{\rho}_{rc,rd} = \frac{1}{9}|00\rangle_{rc,rd}\langle 00| + \frac{2}{9}|01\rangle_{rc,rd}\langle 01| + \frac{2}{9}|10\rangle_{rc,rd}\langle 10| + \frac{4}{9}|\psi\rangle\langle\psi| \tag{6.10}$$

with

$$|\psi\rangle = (e^{i\vartheta}|20\rangle + e^{-i\vartheta}|02\rangle)/\sqrt{2}. \tag{6.11}$$

The interference is observable in the heralded cross-correlation:

$$g^{(2)}_{rc,rd|wa,wb} = \frac{\langle \hat{n}_{rc}\hat{n}_{rd}\hat{n}_{wa}\hat{n}_{wb}\rangle\langle\hat{n}_{wa}\hat{n}_{wb}\rangle}{\langle\hat{n}_{rc}\hat{n}_{wa}\hat{n}_{wb}\rangle\langle\hat{n}_{rd}\hat{n}_{wa}\hat{n}_{wb}\rangle} \tag{6.12}$$

counting coincidences between photons emitted from modes rc and rd – these coincidences vanish due to quantum interference. Simultaneously, the number of self coincidences quantified by $g^{(2)}_{rc,rc|wa,wb}$ (or $g^{(2)}_{rd,rd|wa,wb}$) increases. With no interference, obtained for example by setting a large ΔK_x, we expect $g^{(2)}_{rc,rd|wa,wb} = 1$. Due to loss into the unobserved modes as well as the input of vacuum from modes "above" and "below" in the wavevector space, the HOM interference occurs properly 4 out of 9 times, as seen in Eq. 6.12. Since we only observe proper coincidences, we reject all the scenarios where less than 2 photons in the read-out are detected. The entire situation is presented in Fig. 6.8.

In the experiment we first set $g^{(2)}_{wr} \approx 20$ by adjusting the write laser power and obtaining a proper pair generation rate. We then apply the modulation that yields all cross-correlations, such as $g^{(2)}_{wa,rc} = g^{(2)}_{wa,rd} \approx 6$ [Figs. 6.7 and 6.10(c)], with the goal that they should be equal as then we obtain a 50:50 beamsplitter.

The initial extrinsic read-out efficiency, defined as the ratio of $w - r$ coincidences to the number of w counts is 4%, which corresponds to $\chi_R \approx 30\%$ intrinsic memory efficiency after correcting for losses (50% in the optical in filtering system) and detection efficiency (50% detection efficiency of photodiodes, 60% fibre cross-coupling efficiency). The efficiency of the modulation (at all discernible orders) is over 80%. With the initial coincidence $w - r$ rate of 40 Hz we detect from 0.1 up to 0.5 quadruple coincidences per minute. With our current optical depth of 200 (as measured at the closed $F = 2 \to F = 3$ transition) we can achieve efficiencies of over 60% for classical pulses, however since a large detuning and power of the R laser with ~ 1 μs long pulses is required, we currently achieve better overall performance at 30% efficiency with only 80 ns long pulses and the R laser tuned on resonance, which is mainly due to dark counts as well as filtration performance.

Figure 6.10(a) depicts the results obtained as we change the overlap between shifted modes by varying ΔK_x. If the modes are overlapping at $\Delta K_x = 0$, we obtain a value of $g^{(2)}_{rc,rd|wa,wb} = 0.20 \pm 0.06$, which certifies the observation of two-spin-wave HOM interference. Traditionally, the value below 0.5 is thought to certify nonclassical interference, as it can only be obtained by sending single photons on the beamsplitter. Note that, however, no inequality in principle bounds the cross-correlation from below for a pair of modes.

Simultaneously, taking the $g^{(2)}_{rc,rc|wa,wb}$ auto-correlation we observe more than a two-fold increase from 0.5 ± 0.4 to 1.3 ± 0.2 compared with the case of non-overlapping modes, showing that the pair of spin waves is bunched and resides in a single mode.

The theoretical prediction (curves), detailed in Appendix D, is made by first considering that each pair of contributing modes is squeezed to the same degree with the probability to generate a photon-spin wave pair $p = 0.05$, then implementing the given beamsplitter network and finally adding the influence of dark counts at the detection stage.

6.6 Spin-wave HBT experiment

A distinct quantum protocol is implemented by postselecting only w photon detection events in the wa mode [Fig. 6.10(b)]. The so-called Hanbury Brown-Twiss

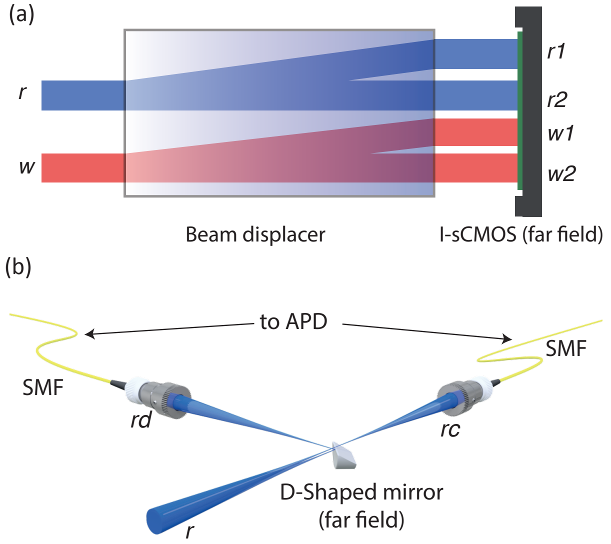

FIGURE 6.9: Two detection schemes used throughout the experiment. In panel (a) a two-dimensional camera sensor (photocathode of an image intensifier, I-sCMOS) situated in the far field with respect to the atomic ensemble detects single write (w) and read (r) photons in four distinct regions thanks to separation achieved with a calcite beam displacer. For cross-correlation measurements, we add the photon counts from two regions corresponding to either write or read light. In panel (b) an example setup (one of the two used, for write and read photons) allowing detection of two far-field modes separated in K_x and K_y. Single-mode fibres (SMF) collimators are aligned using XY translation stages. In terms of the wavevector-space fibre modes correspond to Gaussian shaped mode functions $u_\perp(\mathbf{K}_\perp) \propto e^{\frac{-|\mathbf{K}_\perp|^2}{4\kappa^2}}$.

measurement of a single photon comprises splitting the photon on a beamsplitter and registering the lack (reduced number) of coincidences between the two output ports. Here, we effectively implement a HBT measurement of a single spin wave in mode ra without optical beamsplitting. The mode rb is modelled as containing a thermal state $\hat{\rho}_{rb}(\bar{n})$ with $\bar{n} = 0.1$. Value of $g^{(2)}_{rc,rd|wa} = 0.34 \pm 0.01 < 1$ clearly confirms the single excitation character. As the modes are decoupled, we observe a single photon statistics with $g^{(2)}_{rc,rc|wa} = 0.67 \pm 0.08 < 1$ for the rc mode and close to a single-mode thermal statistics with $g^{(2)}_{rd,rd|wa} = 1.65 \pm 0.34$ for the rd mode.

6.7 Phase-averaged coherent states interference

Finally, we directly populate the spin-wave modes ra and rb with coherent state with population $\bar{n} = 0.1$ by sending a weak seed beam along the path of write

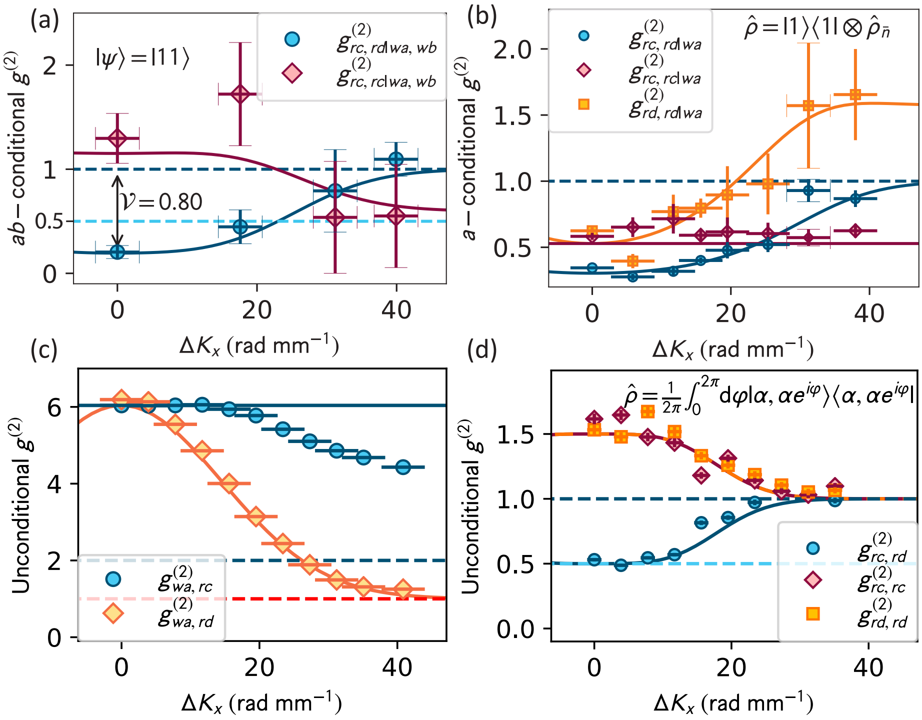

FIGURE 6.10: Demonstration of quantum interference of spin waves: (a) HOM dip as a function of mode wavevector separation. Bunching may be suppressed if the modes ra and rb are separated in the K_x direction of the momentum space; (b) by heralding only the w photon in the wa mode, we implement a HBT experiment, observing non-classical statistics of the spin-wave state; (c) the second-order correlation between w and r photons validating the operation of the three-way splitter with a slight drop in $g^{(2)}_{wa,rc}$ due to residual misalignment as the modes are moved (resulting in reduced fiber coupling efficiency); (d) HOM experiment for coherent input state with phase averaging.

photon. The classical analogue of the HOM effect is observed [Fig. 6.10(d)] as we vary the phase offset of the ac-Stark grating ϑ during a measurement, effectively creating a mixed state at the output. Although here we change the phase of the beamsplitter transformation itself, and not directly the relative phase between two input states, it is equivalent and convenient to write the effective input state as:

$$\hat{\rho} = \frac{1}{2\pi}\int_0^{2\pi} \mathrm{d}\varphi |\alpha, \alpha e^{i\varphi}\rangle\langle\alpha, \alpha e^{i\varphi}|, \tag{6.13}$$

where

$$|\alpha, \alpha e^{i\varphi}\rangle = e^{-|\alpha^2|} e^{\alpha \hat{b}^\dagger_{ra}} e^{\alpha e^{i\varphi} \hat{b}^\dagger_{rb}} |0\rangle. \tag{6.14}$$

For such state at the input, at the output we expect $g^{(2)}_{rc,rd} = 0.5$. This effect, while not inherently quantum, can be though of as a classical analogue of the Hong-Ou-Mandel interference and used to certify multi-photon interfernce in various systems [Jin13]. In the experiment we indeed observe $g^{(2)}_{rc,rd} = 0.53 \pm 0.02$ at $\Delta K_x = 0$ which confirms the high visibility (47% out of 50% maximal). Note that in Fig. 6.10(d) a narrower distribution is observed than in other panels, as in this case as we used a distinct mode function with $\kappa = 6.8$ rad mm^{-1}.

6.8 Conclusions and Perspectives

This demonstration of HOM interference of spin waves not only exposes their bosonic nature, but paves the way towards implementing complex quantum operations, including more spin-wave modes, that are the primitives of the linear-optical quantum computation scheme [Lad10]. The only hitherto successful attempt at HOM interference of spin waves relied on two different magnetic sublevels coupled through Raman transitions [Li16]. Such an approach could also be extended to the spatial domain, yet we believe that the ac-Stark modulation provides more versatility in terms of implemented operations due to inherent access to all wavevectors. Our experiment could furthermore greatly benefit from the deterministic spin wave generation protocol based on Rydberg blockade [Li16], to improve our current heralded spin wave pair generation rate.

With the proposed techniques a multiplexed source of heralded l-photon can be realized [Nun13; Par17] using a single atomic ensemble, as we already described in Sec. 4.1. With the ac-Stark manipulation capability, routing of single photons could be performed within the memory itself, in the domain of spin waves.

The same idea could also be used to design a multiplexed quantum repeater following the proposals presented in [Col07; JTL07; Che07; Zha07]. While more advanced error correction codes for quantum repeaters have already been proposed [Jia09; Mun10; GWT16; Mur14; Mur16], but require a multi-qubit (non-universal) quantum computer at each node. Such advanced quantum information processing capability is hard to achieve in practice with linear optics [Lad10], but photons stored as Rydberg spin waves for which nonlinear interactions can be engineered [Pey12; Dis16; Pet17] could provide such capability when combined with our linear-operations scheme. While hitherto experiments with Rydberg excitations (spin waves) have been performed in spatially single-mode regime [Pet17], extending the capabilities to the continuous-variable multidimensional space could serve as a full photon-coupled platform for simple quantum information processing. Quantum computation and simulation schemes within such a system endowed with the spatial resolution could range from direct nonlinear quantum gates [Pet17], through testing effective field theories [Gul16; JBB16], to a plenitude of more elaborate scenarios involving the formation of topological spin-wave states [Mag15]. We envisage that to bring the Rydberg schemes into the wavevector-multiplexed domain we would need a few times larger blockade radius than currently achieved $\sim 20\ \mu$m to support many spin-wave modes. Other parameters, such as density of atoms, should also be considered.

Chapter 7

Spin wave processing

In this Chapter, we present the first realization of the ac-Stark-based spin-wave multiport interferometric processor (SMIP) and join the advantages of the transverse-wavevector and temporal multiplexing to realize a variety of operations on the stored coherent states of light. The previously untackled regime of complex light patterns used to engineer spin waves is explored, which allows us to tap into the the full three-dimensional potential of the wavevector-multiplexed coherent optical memory. The capacity of such a memory can reach at least $\mathcal{F}^2 \times \mathrm{OD}$, due to the linear scaling of the Gradient Echo Memory with the optical depth [Cho16], as well as quadratic scaling of our spatial multiplexing technique with the Fresnel number (Chapter 4). For our parameters, the capacity figure is of the order of $10^5 \sim 10^6$

We show that thanks to the engineering of the spatial profile of ac-Stark modulation the stored pulses may be processed, interfered and conditionally retrieved. The scheme features both reprogrammable reordering and interference of pulses within the multiple-input, multiple-output paradigm, essential to realize true unitary operations. In the paper, we first introduce the protocol by deriving its theoretical principles and realizing a scheme reminiscent of the Gradient Echo Memory [Hos09]. Next, we realize a series of programmable beamsplitting experiments in spatial and temporal degrees of freedom. High-visibility interference of a pair of spin-wave modes in which coherent light is stored is demonstrated, as previously seen in the two-spin-wave interference experiment in Chapter 6.

Parts of this Chapter have been posted to arXiv [Maz18] and accepted for publication in *npj Quantum Information*.

7.1 Operation of the light-atom interface

The coherent atomic optical memory based on an elongated ensemble of Rb-87 atoms employs a strong control for which we will denote its slowly-varying amplitude A_C to map a weak signal field with amplitude A_{in} onto the atomic coherence ρ_{hg} between the two meta-stable ground states, for which we take $|g\rangle \rightarrow F=1,\ m_F=-1$, and $|h\rangle \rightarrow F=2,\ m_F=1$ (see Fig. 7.1(b) for the atomic level

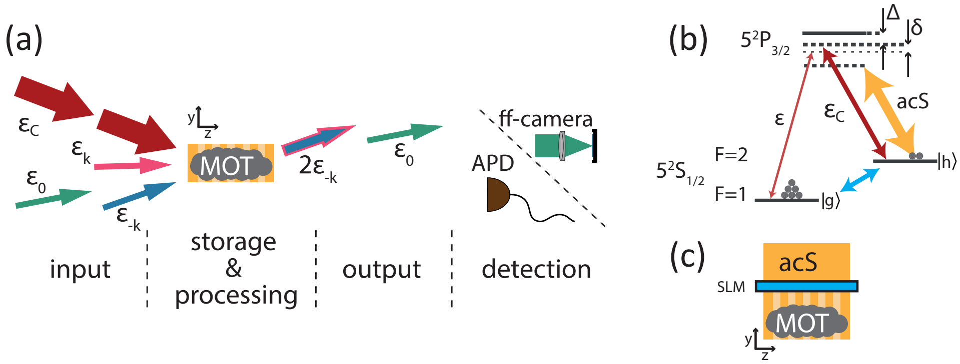

FIGURE 7.1: Spin-wave processing with ac-Stark modulation. (a) - Pulses are sent to SMIP in different time-space modes, then ac-Stark manipulation is applied and at the end, pulses are released. In particular, we use the setup from Fig. 3.10 to send two signal beams at different angles. Released pulses can be detected either on Avalanche Photodiode (APD) or sCMOS camera situated in the far-field (ff) for temporal or angular resolution, respectively. (b) - Rubidium-87 energy level configuration utilized for storing and processing coherent light pulses. (d) - Projection of the panel **b** on perpendicular plane exposing 2-d (y, z) ac-Stark modulation capabilities using Spatial Light Modulator (SLM).

scheme). The experimental sequence is slightly simplified in relation to the one used in Chapters 4 and 6, where the DLCZ protocol was used. Here, the atoms are first optically pumped to the $|g\rangle$ state and control and signal fields (both $\lambda = 780\,\text{nm}$) operate with opposite circular polarizations. Typically we use 300 ns long pulses for storage and retrieval of atomic coherence. For the coupling laser, we used the D2-line laser that was used as write laser in the previous chapters. Then, we could use the beam path of seed light to send in signals (also at two different angles simultaneously, thanks to the setup from Fig. 3.10).

The interaction is well characterized by a set of coupled equations relevant for the read interaction, as described in Sec. 2.3.2. Here, we consider them in their one-dimensional form, yet include the phase-matching factor accounting for the fact that the signal field propagates at an angle to the coupling field. In particular, Fig. 7.1(a) illustrates the geometry in which the coupling and signal fields co-propagate through an elongated atomic ensemble. Below, we identify the terms relevant for our consideration (see Sec. 2.3.2 through Sec. 2.3.4 for relevant derivations and argumentation):

$$\frac{\partial A}{\partial z} = \underbrace{-\frac{ik}{\epsilon_0\hbar}\sqrt{n}d_{ge}\frac{d_{eh}A_C}{i\Gamma-2\Delta}e^{iK'_{z0}z}B}_{\text{Exchange (Raman)}} - \underbrace{\frac{ik}{\epsilon_0\hbar}nd_{ge}\frac{d_{eg}A}{i\Gamma-2\Delta}}_{\text{Dispersion and absorption}}, \tag{7.1}$$

$$\frac{\partial B}{\partial t} = \underbrace{-\sqrt{n}\frac{d_{he}A_C^*/\hbar^2 e^{-iK'_{z0}z}}{2\Gamma+4i\Delta}d_{eg}A}_{\text{Exchange (Raman)}} - \left(\underbrace{\frac{|d_{eh}A_C|^2/\hbar^2}{2\Gamma+4i\Delta}}_{\substack{\text{Coupling}-\text{induced broadening}\\ \text{and ac-Stark shift}}} + \underbrace{\frac{\gamma}{2}}_{\text{Intrinsic decay}} - \underbrace{i\delta}_{\substack{\text{Two-photon}\\ \text{detuning}}} - \underbrace{i\Delta_S}_{\text{Ac}-\text{Stark shift}}\right)B. \tag{7.2}$$

During various parts of the operation of the protocol, only some parts of the equation are employed. In particular, the induced ac-Stark shift Δ_S is never applied along with the coupling light A_C. Assuming that the coupling beam diameter is significantly larger than the transverse size of the ensemble, neglecting losses and assuming a perfectly-matched two-photon detuning, we may actually solve the coupled equations within the first order in the coupling strength and obtain a simple result by which a signal field integral at a particular angle given by transverse wavevector $\mathcal{E}(k_x,k_y)=\int_0^T A(k_x,k_y,t)\mathrm{d}t$ couples to a spin wave:

$$B(K_x,K_y,K_z) \propto \int \mathrm{d}\kappa_x \mathrm{d}\kappa_y s_n(K_x-\kappa_x, K_y-\kappa_y, K_z-K'_{z0})\mathcal{E}(\kappa_x,\kappa_y) \tag{7.3}$$

where

$$K'_{z0} = \sqrt{\omega^2/c^2 - k_x^2 - k_y^2} - \omega_C/c, \tag{7.4}$$

δ is a Dirac delta function and ω and ω_C are frequencies of signal and coupling fields, respectively. Note that here we consider the spin wave in the full wavevector domain and so we take a three-dimensional convolution with the Fourier transformed square-root of the atom-number density s_n. For $k_x=k_y=0$ the longitudinal wavevector simplifies to a constant component $K'_{z0}=K_{z0}=\Delta_{\mathrm{HFS}}/c \approx 0.14\ \mathrm{rad\ mm}^{-1}$, where $\Delta_{\mathrm{HFS}} \approx 2\pi \times 6.8$ GHz is the nominal frequency splitting between levels $|g\rangle$ and $|h\rangle$. In this chapter, we will work with spin waves centred around a certain K_x and close to $K_y=0$. In such case, there is a specific $K_z=K'_{z0}$ for which the spin waves are efficiently retrieved (and onto which signal light is mapped). To exclude this constant offset in K_z we will thus work with shifted spin waves defined as:

$$\tilde{B}(K_x,K_y,K_z) = B(K_x,K_y,K_z-K'_{z0}). \tag{7.5}$$

Importantly, after mapping the optical field we will now obtain a spin-wave excitation expressed as $\tilde{B}$ that has $K_z=0$ rather than a non-zero component. This shift is used to simplify further discussions.

The process of reverse mapping or retrieval driven by the same coupling field occurs in a symmetric way. Essentially, an atomic spin-wave excitation will be mapped onto an optical field proportional to $\tilde{B}$ in terms of the transverse wavevector dependence only if $K_z = 0$. This requirement arises due to the phase-matching condition. In particular, due to phase matching the allowed spread in the K_z space is inversely proportional to the atomic cloud length σ_z and most importantly spin waves with large K_z component ($K_z \sigma_z \gg 1$) will remain stored in the memory. This remains true unless we change the the frame of reference significantly by selecting much different K_x, K_y and change them substantially by δK_x, δK_y, as the actual phase matching is satisfied on a $K_z = 0$ plane only for original (unmodified) spin waves. When we modify the transverse wavevector component the plane tilts and for large K_x (K_y) the spin wave becomes phase-mismatched. However, for small K_x (K_y) and δK_x (δK_y) the phase mismatch $\Delta K_z \approx \frac{\lambda}{4\pi}((K_x + \delta K_x)^2 - K_x^2)$ is small and thus we may use the phase-matching planar approximation to learn which spin waves are retrievable.

In Fig. 7.2 we present the phase-matching situations in terms of the spin-wave field B in the cases where an initial spin wave is shifted in the K_z (b) or K_x (a) direction. We observe that the phase matching condition is preserved in the second case around $K_y = 0$, and expectedly broken in (b). In other words, the planar approximation corresponds to neglecting the curvature of these phase-matching rings and working only around $K_y = 0$.

7.2 Simulation

In all subsequent cases, the coupled equations are simulated using the XMDS2 package [DHJ13]. In the simulation we also add a small imaginary component to the ac-Stark shift $\Delta_S \to (1 + i\mathrm{sgn}(\Delta_S)\gamma_S)\Delta_S$ with $\gamma_S \sim 0.1$, which effectively simulates dephasing due to inhomogeneous ac-Stark light intensity.

We determine the coupling constant effective optical depth by observing single-photon off-resonant absorption. This allows us to experimentally determine its value as OD ≈ 11, as measured on the relevant transition corresponding to signal light. For the coupling field, we take short pulses with smooth slopes (modelling ~ 100 ns experimental rise times) and peak $\Omega_C \approx 2\pi \times 9$ MHz $= 1.5\Gamma$. Typical signal field intensities correspond to peak $\Omega \approx 2\pi \times 50$ kHz. The evolution is simulated on a two-dimensional z-t grid. For the intrinsic decoherence rate, we take $\gamma/2\pi = 10\,\mathrm{kHz}$. Appendix E includes an example code used in the simulation.

7.3 Spin-wave manipulation with the ac-Stark effect

As discussed above, only a limited space, or more precisely a thin three-dimensional volume (in the planar approximation) around $K_z = 0$ plane in the wavevector space may be populated by spin waves by means of read interaction. To manipulate the spin waves within and beyond this volume we use an additional far off-resonant beam (marked in Fig. 7.1(b) as acS) that induces an additional differential ac-Stark shift between levels $|g\rangle$ and $|h\rangle$ of Δ_S that effectively adds to Δ_{HFS}. The ac-Stark beam propagating along the x-direction is z-polarized and red-detuned by approx. 1 GHz from the $|h\rangle \to |e\rangle$ transition induces $\Delta_S/2\pi$ ~100 kHz ac-Stark shift with $\sim$ 100 mW beam power. The atomic level configuration involved is discussed in Appendix C. As before, this shift causes the atomic coherence ρ_{hg}, and thus the spin wave, to accumulate an additional phase $\varphi_S = \Delta_S T$ over the interaction time T. Typically we use ac-Stark pulses of approx. $T \sim 2$ μs duration. By spatially shaping the ac-Stark beam intensity $I_S(y,z)$ a spatially-dependent phase shift $\varphi_S(y,z) \propto I_S(y,z)$, which due to the geometry of the

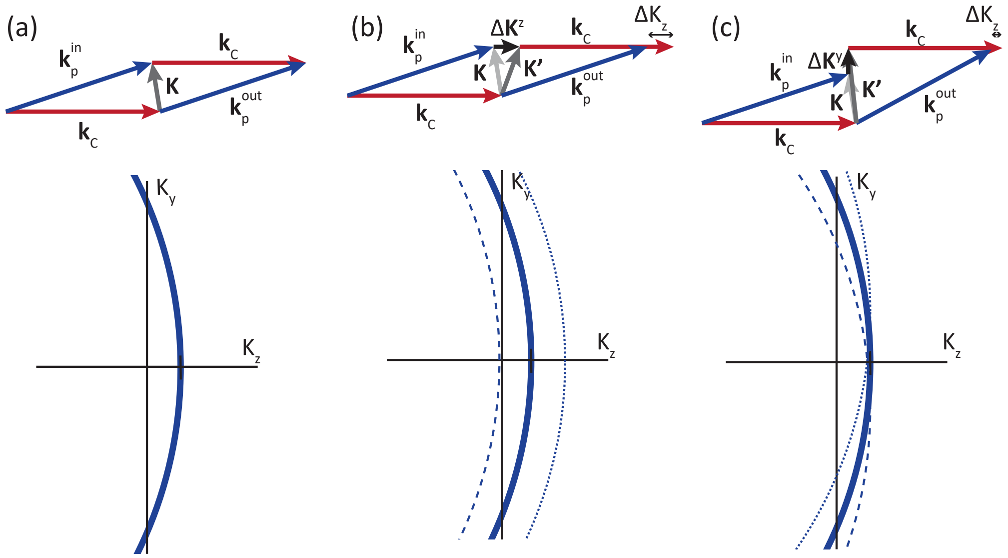

FIGURE 7.2: Phase matching during read-out from the memory. (a) Perfect phase matching can occur ($\Delta K_z = 0$) if the spin wave is not modified. (b) The modification $\Delta\mathbf{K}^z$ of the longitudinal wavevector of spin wave $\mathbf{K}$ leads to a non-zero phase mismatch ΔK_z. If this phase mismatch $\Delta K_z \gg 1/\sigma_z$, read-out can be completely suppressed. (c) The change of transverse coordinate $\Delta\mathbf{K}^y$ leads to a change of emission angle during read-out. Such modification is feasible if the spin wave has a small transverse wavevector $\mathbf{K} \cdot \hat{e}_y$ and if the applied change is small ΔK^y, due to resulting inherent longitudinal phase mismatch ΔK_z.

experiment is limited to two dimensions (see Figure 7.1). Any spin wave is then reshaped as:

$$\tilde{B}(K_x, K_y, K_z) \xrightarrow{\varphi_S(x,z)} \int \mathscr{F}[\exp(i\varphi_S(y,z))](k_y, k_z)\tilde{B}(K_x, K_y{+}k_y, K_z{+}k_z)\mathrm{d}k_y\mathrm{d}k_z. \tag{7.6}$$

Contrary to what was the main point in Chapter 6, here we will concentrate on the modulation in the longitudinal dimension z. In such case, the basic example is an ac-Stark analogue of the GEM, in which a phase shift linear in z ($\varphi_S = \beta z$), with β being proportional to the gradient of ac-Stark laser intensity gradient.

In the traditional magnetic GEM (operated between $F = 1$, $m_F = 1$ and $F = 2$, $m_F = 1$ as in [Cho16]), the shift is induced by a magnetic field gradient $B_z = \nu z$ with ν being the magnetic field gradient. The phase analogous to φ_S, which we here denote φ_B, accumulated during a time T is then given by:

$$\varphi_B = \frac{2g_F\mu_B\nu z T}{\hbar}. \tag{7.7}$$

The spin wave is shifted in the K_z direction by $2g_F\mu_B\nu z t/\hbar$. Here, the ac-Stark light intensity is linear in z and we obtain the same effect and the spin wave is shifted by β.

Here we work with optical modes characterized by small wavevector (angular) spread and therefore the spin waves are well-localized in the wavevector space. Discrete mode transformation in such a space are most conveniently performed by a spatially periodic ac-Stark modulation. Taking a spatial period $2\pi/k_S$ of the modulation in the form $\varphi_S(y,z) = \varphi_S^{\mathrm{per}}(\mathbf{k}_S \cdot (y,z))$ we may express the spin-wave transformation using Fourier series as:

$$\tilde{B}(\mathbf{K}) \xrightarrow{\varphi_S(x,z)} \sum_{n=-\infty}^{+\infty} c_n\tilde{B}(\mathbf{K} + n\mathbf{k}_S), \tag{7.8}$$

with Fourier coefficients c_n defined as:

$$c_n = \frac{1}{2\pi}\int_0^{2\pi} \exp(i\varphi_S^{\mathrm{per}}(\xi) - in\xi)\mathrm{d}\xi. \tag{7.9}$$

The main idea is to be able to input or output pulses to/from the memory sequentially and interfere them as spin waves inside the memory. First, we will simulate these situations in a simplified scenario. Figure 7.3 presents a simplified simulation (assuming perfect write-in and read-out) of a protocol operation within this paradigm. In this exemplary protocol, a pulse is stored and released from the memory. When the pulse is mapped to the ensemble, the created spin wave is phase-modulated using a square-shaped ⎍⎍ (periodic) modulation $\varphi_S(y,z) = \varphi_S^{\text{⎍⎍}}(k_{\text{⎍⎍}}z)$. Such a modulation with a total phase shift of $\pi/2$ distributes the spin

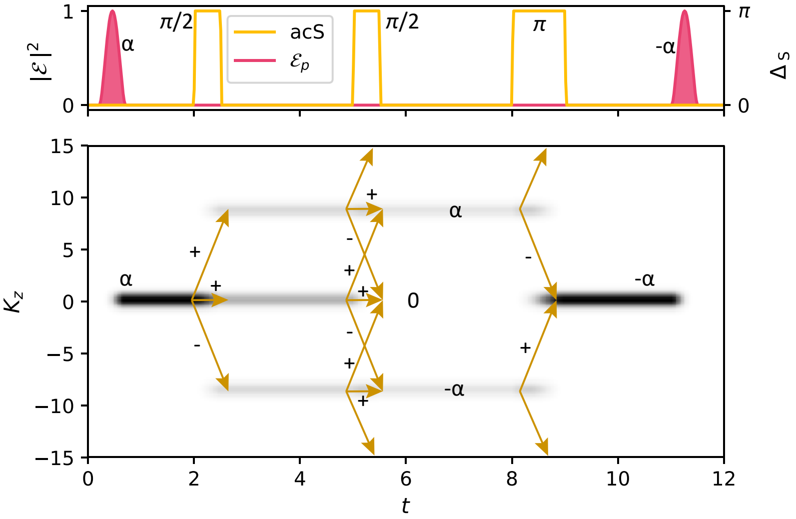

FIGURE 7.3: A simplified simulation of the evolution of $|\tilde{B}(K_z,t)|^2$ showing spin-wave diffraction caused by ac-Stark modulation. For the discernible diffraction orders, we mark also the spin-wave amplitudes (positive or negative). Plus or minus in the arrow labels correspond to a sign of spin wave diffraction order. The relative phase of the grating with respect to the origin of the coordinate system is selected so that all amplitudes are real. Units for wavevectors are arbitrary, yet approximately to scale with the current experimental scenario.

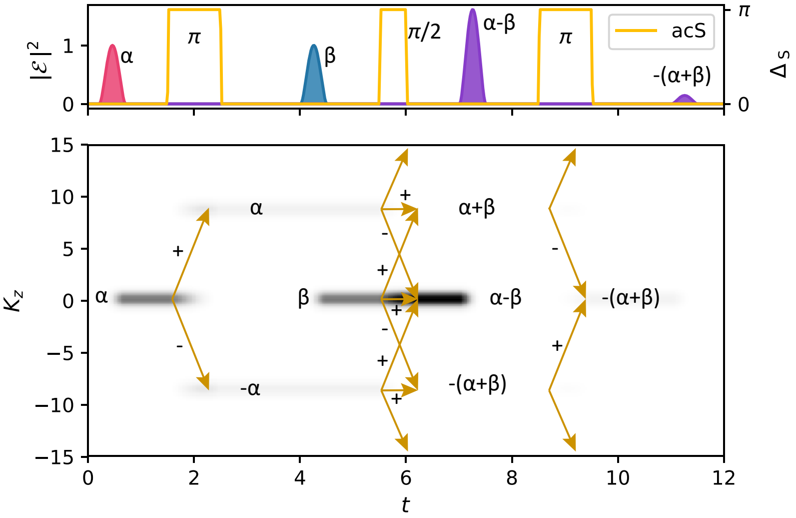

FIGURE 7.4: A simplified simulation of the evolution of $|\tilde{B}(K_z,t)|^2$ showing interference of two pulses subsequently stored as spin waves. Relative amplitudes of the diffraction orders are marked. Initial phase difference between input pulses is π.

Pattern	$\mathcal{A}$	c_{-1}	c_0	c_1
∼	1.435	≈ -0.548	≈ 0.548	≈ 0.548
	2.405	≈ -0.51	≈ 0	≈ 0.51
⊓⊔⊓	$\pi/2$	$-\frac{\sqrt{2}}{\pi}$	$\frac{1}{\sqrt{2}}$	$\frac{\sqrt{2}}{\pi}$
	π	$-\frac{2}{\pi}$	0	$\frac{2}{\pi}$
	2π	0	-1	0
⊿⊿⊿	$\pi/2$	$\frac{2\sqrt{2}}{5\pi}$	$\frac{2\sqrt{2}}{\pi}$	$-\frac{2\sqrt{2}}{3\pi}$
	π	$\frac{2}{3\pi}$	$\frac{2}{\pi}$	$-\frac{2}{\pi}$
	2π	0	0	-1
⋁⋁	$\pi/2$	$-\frac{2\sqrt{2}}{3\pi}$	$\frac{2\sqrt{2}}{\pi}$	$\frac{2\sqrt{2}}{3\pi}$
	π	$-\frac{1}{2}$	$\frac{2}{\pi}$	$\frac{1}{2}$
	2π	$-\frac{4}{3\pi}$	0	$\frac{4}{3\pi}$
	4π	$\frac{8}{15\pi}$	0	$-\frac{8}{15\pi}$

TABLE 7.1: Fourier coefficients $c_{-1,0,1}$ for various patterns and ac-Stark modulation amplitudes $\mathcal{A}$.

wave among three diffraction orders, similarly as in Chapter 6. The spin wave is thus still partly readable since it can be retrieved from the $K_z = 0$ order. To make the spin wave completely unreadable, we apply an additional $\pi/2$ modulation of the same kind. The total applied triangle wave of phase modulation thus now ranges from 0 to π and completely removes the spin wave from the zero order. The memory is thus ready to accept a new light pulse to be stored at $K_z = 0$. Finally, the spin wave is restored to the memory by applying the same triangle-wave modulation with an amplitude of π. All higher orders are extinguished and the spin wave is completely returned to the zeroth order.

A distinct protocol within the same simplified framework is present in Fig. 7.4. There, we first store a light pulse as a spin wave α at $K_z = 0$ and subsequently remove it from the zeroth order via the same modulation with a total phase amplitude of π. Next, we store another light pulse in the new spin wave β in the zeroth order. Subsequent application of the modulation leads to interference between the new β and the old spin wave α. Due to particular phases associated with the modulation, the spin waves interfere constructively in the zeroth order. As we then try to return the higher orders that would contain the remainder of spin waves, we observe very weak output pulse. If the spin waves α and β would input with the same phase, rather than a π phase shift as here, they would interfere constructively in the second port. With such, we realize a two-mode beamsplitter for pulses arriving at different times.

Table 7.1 serves as a helper tool to understand and design various protocol. There, we give Fourier coefficients c_n (Eq. 7.9) for a collection of patterns as well as modulation depths (amplitudes). In the sine modulation, the modulation is characterized by Bessel function. With square modulation, the notable feature is a full return to the zeroth order after at $\mathcal{A} = 2\pi$. For the sawtooth wave, the most notable feature is the asymmetry and complete transfer to the first order. For the triangle wave modulation we have anti-symmetric amplitudes for the first order, but most importantly we observe that those spin waves do not return to the zeroth order as $\mathcal{A}$ is a multiple of 2π. This is essential for storage of many pulses. We could also achieve this with sine modulation, yet there we would have to adjust each modulation step to match subsequent zeros of the Bessel function.

Operations of these two simplified protocols will be presented in the real experimental scenario in subsequent sections.

7.4 Reconfigurable ac-Stark Echo Memory

For the experimental demonstration we begin by moving the spin waves outside the zero K_z to allow storage of subsequent incoming optical pulses, as shown in Fig. 7.5. This configuration, most reminiscent of the GEM [Hos09] and already proposed as a way to reverse pulses order in the two-level GEM [HGO15], here operates best with a triangle-shaped $\wedge\!\!\wedge$ grating (pattern A, Fig 7.5(a)), which can be conventionally written in a closed form:

$$\varphi^{\wedge\!\!\wedge}_{\mathrm{acS}}(\xi) = \mathcal{A}^{\wedge\!\!\wedge}\left|2\left(\frac{\xi}{2\pi} - \left\lfloor\frac{\xi}{2\pi} + \frac{1}{2}\right\rfloor\right)\right|, \tag{7.10}$$

with $\mathbf{k}_{\wedge\!\!\wedge} = 9.6\,\mathrm{rad/mm}\,\hat{e}_z$ for which most essentially the zeroth order $c_0^{\wedge\!\!\wedge} \propto |\,\mathrm{sinc}(\mathcal{A}/2)|$ disappears periodically with modulation strength $\mathcal{A}^{\wedge\!\!\wedge}$ (with period equal 2π) except for $\mathcal{A}^{\wedge\!\!\wedge} = 0$. With this scheme, we may thus apply a grating with $\mathcal{A}^{\wedge\!\!\wedge} = 2\pi$ and remove the pulse from the $K_z = 0$ plane. Due to the periodicity of $c_0^{\wedge\!\!\wedge}$ in the modulation strength $\mathcal{A}^{\wedge\!\!\wedge}$, if a subsequent pulse is stored, the first and any previous pulse remains phase-mismatched at consecutive grating operations with amplitude $\mathcal{A}^{\wedge\!\!\wedge} = 2\pi$. To retrieve the pulses we apply a pattern with the same amplitude shifted by a half of period in the spatial domain (pattern B), that restores the spin waves to the $K_z = 0$ plane.

The scheme lends itself to both *first-in, first-out* (FIFO) and *last-in, first-out* (LIFO) operation, as shown in Figs. 7.5(b,c). For the FIFO operation on two pulses, after storage of a second pulse, we apply a shifted pattern B to simultaneously transfer the first pulse back to the $K_z = 0$ plane and phase-mismatch the second pulse. After the first retrieval operation, the phase matching is restored for the second pulse with pattern A. The LIFO queue for pulses has also been performed for three inputs and outputs (Fig. 7.5(c)).

The efficiency of our memory is currently limited by the optical depth of the ensemble as well as available coupling power. By comparing the intensity of light at the input and output of the memory we obtain write-in efficiency for the first pulse of about 59% and 44% for the second pulse. For immediate retrieval (as for the second pulse in LIFO scheme) we achieve 35% efficiency, while net storage and retrieval efficiency are equal 44% × 35% = 15%. For the pulses that are manipulated the efficiency is diminished by dephasing due to the ac-Stark light intensity inhomogeneities [Les18].

7.5 Programmable beamsplitting of stored light

To demonstrate the beamsplitting capability for pulses arriving at different times we use again the triangle-wave modulation in the z-direction, with $k_{\vee\!\vee} = 22\,\mathrm{rad/mm}$. After subsequent storage of two pulses (which is done the same way as in FIFO and LIFO demonstration using pattern A from 7.5(a)) we apply the shifted pattern B for half of period T, modulating the spin wave with amplitude π instead of 2π (see Fig. 7.5(e)). This way the two pulses are combined and $K_z = 0$ component of resulting the spin wave becomes the first output port of the temporal-mode beamsplitter. Then, after the first read-out, we modulate the unread part again with pattern B with amplitude $\mathcal{A} \approx 2.25\pi$ to transfer a part of the second port to readable $K_z = 0$ plane, then the second read-out is performed. Note that it is crucial to always perform the first read-out, as otherwise, the unread spin wave will interfere and spoil the operation of the second output port. It is thus necessary to simulate the operation of this scheme to a full extent, including possibly imperfect first read-out which can affect the second output port. To characterize the interference of two pulses we change the relative phase between the pulses by varying the two-photon detuning δ. Fringes in the intensity registered in the two output ports appear accordingly. Essentially, the phase difference between the two interfering spin waves is the product of the two-photon detuning δ and the time between two first pulses τ. Furthermore, as we move outside the two-photon resonance the interaction becomes inefficient. This behaviour is reminiscent of the well-known Ramsey interference. In Fig. 7.6 we plot the total number of photons collected after the first (port a) and second (port b) read-out as a function of the two-photon detuning δ. The observed behaviour is properly predicted by a full simulation (solid line). The maximal efficiency achievable in this case (triangle-shaped grating) calculated using the provided Fourier formalism assuming perfect read-out is 81% and 60% for port a and b respectively. The relative phase between the pulses can be also modified within the spin-wave domain. To demonstrate this, we implement another interference protocol; instead of splitting the first pulse into many orders we simply shift its K_z component by $k_{\vee\!\vee}$ using sawtooth wave /|/| modulation:

$$\varphi_S^{\text{/|/|}}(\xi) = \mathcal{A}^{\text{/|/|}} \left(\frac{\xi}{2\pi} - \left\lfloor \frac{\xi}{2\pi} \right\rfloor \right) \tag{7.11}$$

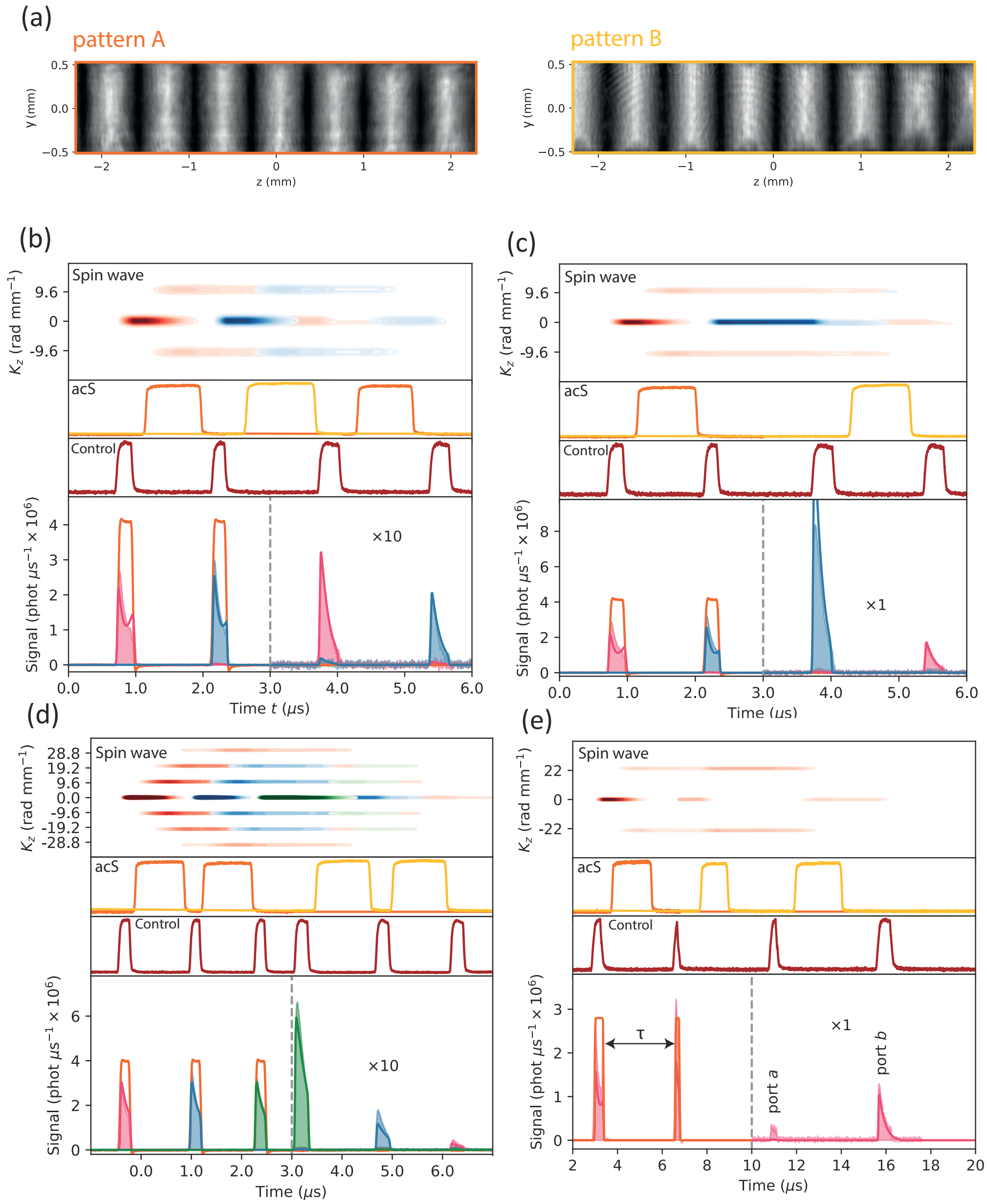

FIGURE 7.5: Operation of the ac-Stark Echo Memory (b-d) and spin-wave Mach-Zehnder interferometer (e). Triangle-wave shaped modulation patterns, shifted by half of a period, are presented in (a).

in the z-direction. Then, the second pulse is written to the memory and the resulting spin wave is modulated using a triangle-shaped grating of depth $\mathcal{A}^{\wedge\!\wedge} \approx 1.16\pi$ satisfying the equation $|c_0^{\wedge\!\wedge}| = |c_1^{\wedge\!\wedge}| = |c_{-1}^{\wedge\!\wedge}| \approx 0.53$. The spatial period of the $\wedge\!\wedge$

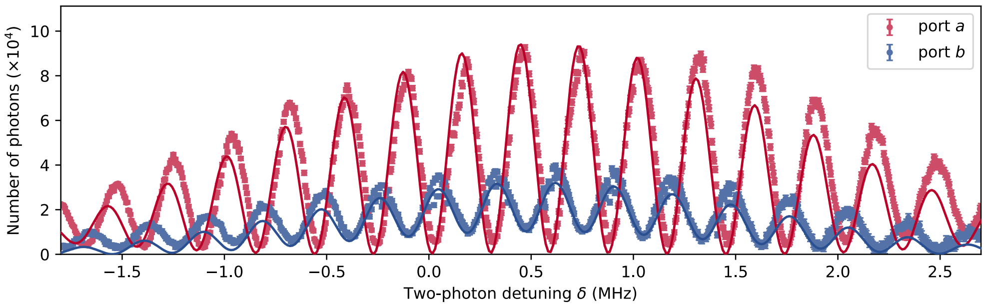

FIGURE 7.6: Ramsey fringes in the spin-wave interferometer, i.e. light intensities registered in two ports (port a, port b) of the beamsplitter as a function of two-photon detuning δ. The errorbars correspond to standard mean error derived from many collected signal traces for each data point.

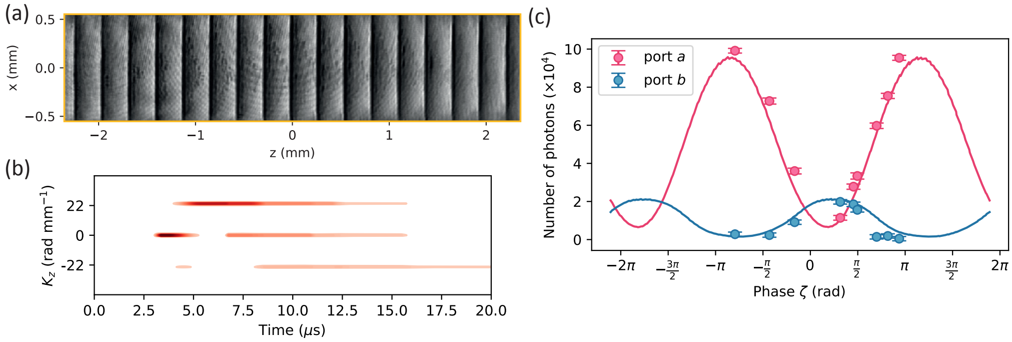

FIGURE 7.7: Asymmetric interferometer with geometric phase control. (a) - The sawtooth-shaped grating (⩘) used to shift the spin waves in one K_z direction. (b) - Simulated time and wavevector resolved spin-wave density $S(K_z, t)$ for a one phase point showing the longitudinal (K_z) spin wave mode-mixing during interferometer operation. The most of the spin wave remaining in the memory after two read-outs is concentrated around $K_z = -22$ rad/mm and $K_z = 44$ rad/mm. Due to the symmetry the contribution outside the K_z range (around $K_z = 44$ rad/mm) will be the same as around $K_z = -22$ rad/mm. (c) - Intensity interference fringes for two consecutively retrieved ports (first - port a, second - port b) as a function of sawtooth ⩘ grating phase ζ. Errorbars correspond to the standard mean error derived from many collected signal traces for each data point.

modulation is chosen to satisfy $\mathbf{k}_{\text{VV}} = \mathbf{k}_{\text{ИИ}} = 22\,\mathrm{rad/mm}\,\hat{e}_z$, thus the pulses are combined in such a manner that the zeroth order of the first pulse overlaps with first diffraction order of the second pulse and conversely. The first interferometer port is again a resulting $K_z = 0$ spin wave component, so it can be completely read-out without any additional manipulations. The second port this time is well defined and lies at a plane with $K_z = k_{\text{VV}}$. Thus, in principle the second port could be restored completely by applying reversed sawtooth pattern NN shifting back the spin wave by $-\mathbf{k}_{\text{ИИ}}$ to the readable region in wavevector space. Due to our setup limitations (see Methods) we probe the second port by applying the VV modulation with an amplitude equal π and subsequently the phase-matched component ($K_z = 0$) is released. The relative phase between interfering components can be manipulated by changing the phase of one of the gratings (ИИ or VV), as for any shifted periodic modulation $\varphi_S^{\text{periodic}}(\xi - \zeta)$ the complex amplitudes of subsequent orders change as $c_n \sim e^{in\zeta}$. We directly witness this behaviour by shifting the sawtooth ИИ grating portrayed in Fig 3a in the z-direction and measuring interference fringes in the total energy of the released pulses. In Fig. 7.7(c) we plot the resulting interference pattern, accompanied by a proper simulation, showing the interference in wavevector space (Fig. 7.7(b)). Theoretical maximum efficiency taken as the ratio of cumulative energy of two output ports to total input energy under perfect read-out conditions is however limited in this case by $2|c_0^{\text{VV}}|^2 \approx 56\%$. Yet, the rest (unread part) of the spin wave remains in the memory and could be in principle retrieved using proper manipulation.

7.6 Transverse space interference and manipulation

To go beyond a single transverse mode we now add the K_y dimension to the scheme. In a simple yet highly robust scenario, we map two equally bright pulses arriving at the same time yet into two different spin waves with $K_y = \pm k$, where $k = 75.4$ rad/mm. We then apply a sinusoidal grating modulation (pattern presented in Fig. 7.8(a)):

$$\varphi_S^{\sim}(\xi) = \mathcal{A}^{\sim}(\sin(\xi + \zeta) + 1)/2, \tag{7.12}$$

with $k = 2k\hat{e}_x$ and $\mathcal{A}^{\sim} \approx 0.92\pi$ that again satisfies $|c_0^{\sim}| = |c_1^{\sim}| = |c_{-1}^{\sim}| = \mathcal{C} \approx 0.55$. In this way the output ports at $K_x = \pm k$ are mixtures of both input ports in the 50:50 ratio. We than again use the fact that shifting the grating position ζ changes the phase at orders ± 1 by $\pm\zeta$. We may thus write the (lossy) beamsplitter transformation as:

$$\begin{pmatrix} \mathcal{E}_{+k}^{\text{out}} \\ \mathcal{E}_{-k}^{\text{out}} \end{pmatrix} = \mathcal{C} \begin{pmatrix} 1 & e^{i\zeta} \\ e^{-i\zeta} & 1 \end{pmatrix} \begin{pmatrix} \mathcal{E}_{+k}^{\text{in}} \\ \mathcal{E}_{-k}^{\text{in}} \end{pmatrix}. \tag{7.13}$$

We scan the phase using a piezo-actuated mirror mount in the far field of the

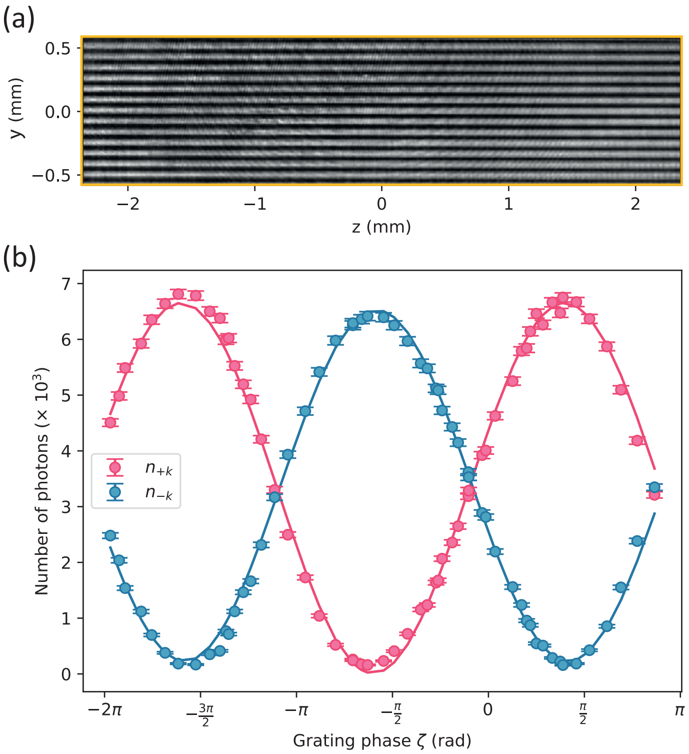

FIGURE 7.8: Spin-wave interference induced by ac-Stark shift manipulation in the transverse-wavevector space. (a) - The sinusoidally-shaped ∼ grating pattern used to apply transverse-mode (K_x) beamsplitter transformation by ac-Stark modulating the spin waves. (b) - Intensity interference fringes for two transverse-mode ports separated by $2k$ detected on the sCMOS camera situated in the far-field of the ensemble. The grating phase ζ is changed using a piezo-actuated mirror.

ensemble (see Methods for details of the imaging setup) and observe high-visibility interference fringes. Notably, we obtain average visibility of 95% by comparing maximum and minimum intensities observed at each port, as portrayed in Fig. 7.8(b). As in the previous section, the theoretical maximal efficiency in this case (assuming perfect read-out) is limited by $2\mathcal{C}^2 \approx 60\%$.

7.7 Discussion

We have demonstrated a reprogrammable device that processes atomic spin waves through interference. Starting with the first demonstration of an ac-Stark controlled atomic memory for light we have extended the concept of ac-Stark control to enable interference of coherent spin-wave states stored in the memory. In particular, the processing is performed simultaneously in two dimensions of the wavevector space. With this, we simultaneously exploit temporal and spatial multiplexing. We show how to perform spin-wave interference between light pulses stored both at different times, as well as sent to the memory at different angles. By switching only a pair of patterns we achieve a substantial degree of reprogrammability and control, which paves the way towards creating complex unitary quantum networks through spin-wave interference.

The demonstrated SMIP lends itself to many critical schemes in quantum and classical telecommunication, including the quantum memory-enabled super-additive communication [Guh11; Kli16; Jar16; CJDD17] or implementation of a receiver operating with an error rate below the standard quantum limit [Bec13] as well as quantum metrology through collective measurements on many optical pulses [DDJK15; Hou18]. The ability of programming interference of stored states provides a robust tool for probing fundamental properties of quantum systems. Recently, a tunable beamsplitter transformation has been used to demonstrate Hong-Ou-Mandel interference between two microwave quantum memories [Gao18]. The techniques presented here pave the way towards programmable complex interference experiments which can be used to reveal fundamental properties of a given quantum system.

As mentioned, the temporal capacity of the memory is limited by the optical depth OD. This is due to the interplay between decoherence and Raman interaction, and thus we are in practice limited by incoherent scattering caused by the control field. With higher OD we can use larger detunings and limit this deleterious influence.

The ac-Stark control owes its versatility to the possibly a very high speed of switching and operation, as compared with the magnetic field gradients. This feature makes it applicable to recently developed short-lived quantum memories that operate in the ladder atomic scheme in warm atomic vapours and achieve very low noise levels [Kac18; Fin18]. The high speed of the ac-Stark control also facilitates real-time feedback processing that could lead to the realization of an even broader class of operations, including enhanced single-photon generation through multiplexing [MDW16; Par17; Nun13; Kan17]. Here, such a scheme could also include engineering of photonic spatial and temporal mode. This could be taken even further with techniques used in stationary-light experiments, where the amplitude of the stored spin-wave is non-destructively reshaped using a multilaser field [Eve16; Par18a].

The universality of the current approach is limited by access only to pure phase modulation of spin waves, that inherently produces many diffraction orders, rather than a specific desired pattern. An interesting approach to achieve universality of performed operations, rather than just control of phase in the wavevector-domain, would be to implement a three-step protocol. It has been demonstrated that for optical frequency-bin modes a pair of electro-optics modulator and a pulse shaper [Lu18]. In our case to obtain arbitrary input-output relation for many stored pulses we would first store the pulses in the memory and apply the phase modulation as presented in the current work. Next, the pulses would be simultaneously read-out and stored again in the memory with an electro-optic modulator changing the phase of each time-bin. Final modulation in the spin-wave domain would yield an arbitrary operation, achieving universality in terms of time-bin input-output operation. In turn, the linear-optical scheme of quantum computation becomes feasible [KLM01]. The number of modes that can be efficiently processed would be limited by the optical depth. In general, a set of concatenated memories, as proposed in [Cam14], could facilitate universal operations within our ac-Stark modulation protocol.

There are also interesting perspective involving just an extension of the current ac-Stark modulation to different and in particular more patterns. As demonstrated, at this point our setup already allows rapid switching between two patterns that could be used in short-lived quantum memories [Kac18; Fin18]. We envisage that the setup may be extended to feature more patterns that could be rapidly reprogrammed, by for example using a two-dimensional AOM to scan the beam through the atomic ensemble, or by using a set of AOMs to transfer many multiplexed images displayed with an SLM. This would unavoidably increase the complexity of the setup. In consequence, fast rapid spatial-light modulators and deformable mirrors that can already be reprogrammed during $\sim 100\ \mu$s could serve as a highly viable solutions[And14]. On the other hand, simpler patterns could also be rapidly generated by sweeping the frequencies in a setup based on acousto-optic deflectors [RB14; Kon18].

Furthermore, note that here we did not use the ac-Stark shift during write and read operations of the optical memory, and thus the two-photon absorption line is not broadened. Thus, the Gradient Echo Memory advantage of avoiding reabsorption of stored light is not yet exploited. Combined with larger optical densities this could significantly improve the efficiency of the presented memory [Spa13].

Finally, by bringing the presented techniques to spin waves that involve a Rydberg state [Wei11; Din16; Dis16; Mir17; Dis17], the attainable range of operations between storage modes could be enriched with nonlinear interactions in order to realize efficient and deterministic quantum gates for photonic states. This could be particularly advantageous in engineering complex correlations within the spatial domain of a Rydberg atomic ensemble [Bus17].

Chapter 8

Spin-wave parametric conversion

In this Chapter, we demonstrate that a spin wave can serve as a pump field in a down-conversion process. New characteristics of single-photon superradiant emission are observed, leading to an improved understanding of spatial properties of the process. Our method can serve as a new tool to engineer state of atoms that radiate in unconventional ways. We also illuminate a perspective of obtaining a two-photon emission from a single spin wave.

The results presented in this Chapter have not yet been published.

8.1 Casaded photon generation

Spatially extended atomic ensembles are a popular medium to generate correlated photon pairs with widely varying properties. The Λ scheme, which forms the basis of the Duan-Lukin-Cirac-Zoller quantum entanglement distribution protocol [Dua01], is well-established in terms of its capabilities to generate photon pairs with both non-trivial temporal [ZSD16] and spatially-multimode structure on which we concentrated in Chapter 4. In particular, if write and read coupling beams are used simultaneously, pairs of photons will be generated without "noticeable" role of the spin waves in the process. Such a scheme is often called the double-Λ configuration (Fig. 8.1(c). Alternative ladder (Fig. 8.1(b)) or diamond (Fig. 8.1(a)) schemes allow generation of two-colour photon pairs, and attract much attention also as a single-photon storage scheme [Kac18] and Rydberg-blockaded medium [Pey12]. High efficiencies of these processes, and resulting high heralding efficiencies for photons are guaranteed by the fulfilment of the phase-matching condition. This is contrasted with seminal photon-pair and entanglement experiments which used a small number of atoms in atomic beams. The atomic-ensemble-based schemes hold an advantage over spontaneous parametric down-conversion processes (SPDC) in nonlinear crystals, that also rely on efficient phase-matching, as the photons are inherently narrowband and atom-resonant, making them suitable for quantum metrology and repeater-based communication [Rad10]. With a purely atomic photon-pair source, potentially difficult engineering of cavity-based SPDC can be avoided [Wol08; Wol11].

The ladder-type (where decay occurs via the same path as excitation) and diamond-type [Bec08; PW15] (where decay and excitation occur via distinct paths) have successfully been used to generate photons with particularly good characteristics. The key advantages of these schemes applied to Rubidium is the possibility to generate one of the photons at the telecom wavelength [Rad10; Bec08; Wil11] and relaxed requirements for filtering, even in room-temperature ensembles [Zha14; Wil11; PKM17], as compared with the Λ scheme. A striking feature of the two-photon decay is the superradiant enhancement of emission [Sri13; Lee17], observed both in ultracold and warm atomic ensembles at high optical depths. The system thus contributes to recent fundamental studies of superradiant emission in cold atoms [KSH17; Roo16; OG18]. Among many intricacies, this behaviour proves the role of atomic coherence in the process. The two pump beams first generate a two-photon coherence between the ground and the highest excited levels. Optimization of this coherence as compared with incoherent excitations of the highest excited state guarantees best signal-to-noise ratio [Cer18]. Emission of the first (signal) photon transfers the two-photon coherence directly to the second (idler) photon transition, leading to simple coherent, phase-matched emission.

Here we show that the properties of a phase-matched cascaded atomic decay can be engineered via proper preparation of the atomic state. In particular, we treat the atomic coherence (spin wave) prepared in the Raman process as one of the fields participating in the parametric conversion process. Hitherto schemes necessarily required that at the atom starts and ends the wave-mixing processes in the same ground state, as dictated by the principles of energy and momentum conservation. This requirement can be leveraged if the ensemble is first prepared in a superposition state, or in other words, some ground-state coherence is present. We generate a strong atomic coherence between $|g\rangle$ and $|h\rangle$ (spin-wave field B) via Raman interaction in the Λ scheme, as depicted in Fig. 8.2(a). The two pump fields (P1 and P2), as in Fig. 8.2(b), then transfer the coherence via a coherent two-photon process to the highest excited state $|c\rangle$. The standard coherent two-photon decay follows by the end of which the atom returns to its ground state $|g\rangle$. The entire process can be viewed as a two-step spontaneous six-wave mixing (6WM) with a time delay. The entire 6WM process again conserves both momentum and energy. By comparison, a standard DLCZ quantum memory, in fact, operates via a four-wave mixing process (4WM) in the Λ scheme with a time delay between write-in and read-out of the atomic spin wave, each involving only two optical fields.

This unorthodox view leads to numerous implications, as the spin wave may be manipulated in various ways, including usage of magnetic [Hos09; Alb15] and optical fields (as in Chapters 6 and 7) via Zeeman and ac-Stark effects, respectively. In our case, the structure of the spin wave could be manipulated, which would subsequently result in a modified atomic state during emission of the idler

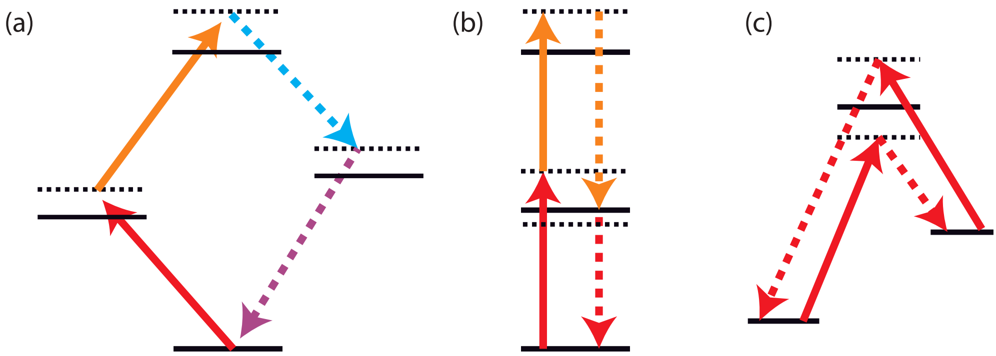

FIGURE 8.1: A general comparison of the (a) diamond, (b) double-ladder (Ξ) and (c) double-Λ configuration for photon pair generation in atomic ensembles. Solid lines correspond to driving beams while dashed lines correspond to generated photons.

photon. Such a modification could serve to change the properties of superradiance facilitating a better understanding of this collective process. From the quantum information perspective, both polarization, temporal and spatial properties of the generated biphoton can be modified, leading to complex multi-degree-of-freedom entangled states.

Finally, it would be particularly interesting to replace one of the strong driving fields in the 6WM process by a quantum field. Essentially, generation of a single spin-wave excitation can be heralded by detecting a photon scattered in the Raman process. Such configuration directly leads to the generation of a correlated three-photon state. Note that the process could also be reversed - first, a single spin-wave would be generated by heralding detection of a photon pair. The resulting state would be a three-partite entangled state of a photon pair and a collective atomic excitation. We envisage that both configurations can be achieved by increasing the two-photon excitation efficiency - currently limited by decoherence caused by the sole Pump 1 field. In this way, the efficiency could even surpass the photon down-conversion probability in three-photon SPDC experiments [Din15; Hüb10]. Furthermore, the spin waves could also be prepared in a deterministic way using Rydberg blockade [Li16]. This could lead to a deterministic generation of entangled photon pairs.

In this Chapter, we first consider the general properties of the scheme and demonstrate nonclassical correlations in the time domain. The next section describes spin-wave control of biphoton correlation in the wavevector domain. Finally, we describe the perspectives and limitations of the scheme.

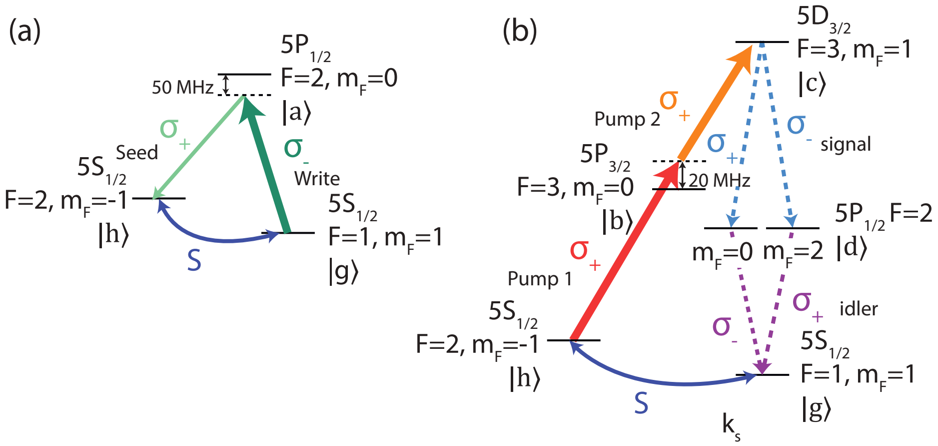

FIGURE 8.2: (a) Rubidium-87 levels configuration used to generate ground state spin wave via seeded Raman scattering in the first step of the delayed 6WM scheme. (b) Relevant energy levels used to generate correlated photon pairs via spontaneously induced two-photon decay closing the 6WM scheme.

8.2 Experiment

With the atomic ensemble prepared via a standard procedure the atoms are optically pumped to the $5S_{1/2}, F = 1, m_F = 1$ state which we denote as $|g\rangle$ (see Fig. 8.2(a)). Then, at the first level of the delayed 6WM process, we employ two phase-coherent optical fields (write and seed, both 795 nm) to generate a strong ground-state spin-wave atomic coherence ρ_{hg} between states $|g\rangle$and $|h\rangle$ for which we take $5S_{1/2}, F = 2, m_F = -1$. The spin wave has a non-trivial spatial dependence $B \propto \exp(i\mathbf{K}\cdot\mathbf{r})$, where $\mathbf{K} = \mathbf{k}_W - \mathbf{k}_{Sd}$ is a spin-wave wavevector and $\mathbf{k}_W$, $\mathbf{k}_{Sd}$ are wavevectors of the write and seed fields, respectively. The spin wave generation process itself can be understood as a seeded (with Seed light) Raman scattering in the Λ system composed of levels $|g\rangle$, $|h\rangle$ and $|a\rangle$ ($5P_{1/2}, F = 2$ with m_F equal either 0 or 2) driven by the strong write light. In such process, both the Seed light and atomic coherence are amplified at the expense of the Write field.

At this point, the spin wave could be stored in the ensemble up to hundreds of microseconds and during this time its spatial structure may be reshaped in various manners as in the previous chapters. Here, for the sake of simplicity, we leave the spin wave pristine and move directly to the second part of the delayed 6WM process where the correlated photon pairs (signal and idler) are generated. In this part, depicted in Fig. 8.2(b) we use two strong laser fields (Pump 1 at 780 nm and Pump 2 at 776 nm) to dynamically transform a substantial part of the ground-state spin wave B into the excited state $|c\rangle(5D_{3/2}, F = 3, m_F = 1)$ coherence $\rho_{cg} = \alpha\rho_{hg}\exp(i(\mathbf{k}_{P1} + \mathbf{k}_{P2})\mathbf{r})$, where $\mathbf{k}_{P1}$, $\mathbf{k}_{P2}$ are the wavevectors of

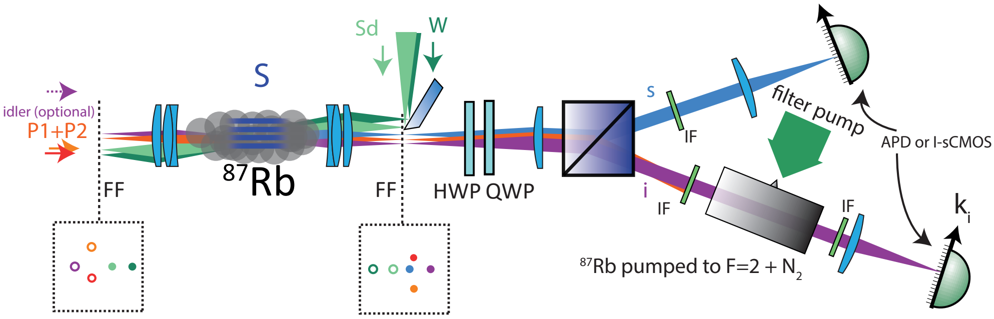

FIGURE 8.3: Experimental setup details. (c) Schematic of the experimental setup used to observe correlated photon pairs generated within the delayed 6WM scheme, including all the crucial elements. The schematic far-field (FF) images provide the information about used angular configuration.

the Pump 1 and 2 respectively and α is the factor governing the time evolution induced by the pump fields. For the convenience we will define the excited-state spin wave as:

$$\mathcal{S} \equiv \sqrt{n}\rho_{cg}\exp(-i(K_z + \sqrt{k_{P1}^2 - k_{P1\perp}^2} + \sqrt{k_{P2}^2 - k_{P2\perp}^2})z), \tag{8.1}$$

where k_s, k_i are wavenumbers of the signal and idler field respectively and n is the atom density distribution. The presence of this coherence enables spontaneously induced coherent two-photon transition to the original ground state level $|g\rangle$, closing the 6WM scheme. The transition happens in two steps: first the spontaneously emitted signal photon transfer the two-photon coherence ρ_{cg} to the intermediate state $|d\rangle$ $(5P_{1/2}F = 2, m_F = 0)$ from which the superradiantly enhanced emission of the idler photon occurs. Thus, the idler photon is emitted always after the signal photon.

Treating the atom-light interaction induced by the weak quantum signal and idler fields as a small perturbation to the free atom density operator evolution, we can write the equations for the slowly varying envelopes of the signal $\hat{A}_s$ and idler $\hat{A}_i$ fields as:

$$\frac{\partial \hat{A}_s}{\partial z} = -ik_s g_s \frac{d_{gd}}{d_{cd}} \hat{A}_i^\dagger \mathcal{S} e^{-i\Delta K_z z}, \tag{8.2}$$

$$\frac{\partial \hat{A}_i}{\partial z} = -ik_i g_i (\hat{A}_i + \frac{d_{dc}}{d_{dg}} \hat{A}_s^\dagger \mathcal{S} e^{-i\Delta K_z z}), \tag{8.3}$$

where we have assumed that signal and idler are frequency anti-correlated. The coupling factors in the no-loss approximation are defined as follows

$$g_s = -\frac{\sqrt{n}|d_{dc}|^2}{\epsilon_0 \hbar} / 2(\omega_s - \omega_{0,dc}), \tag{8.4}$$

$$g_i = -\frac{\sqrt{n}|d_{gd}|^2}{\epsilon_0 \hbar} / 2(\omega_s - \omega_{0,dc}), \tag{8.5}$$

where $\hbar\omega_{0,dc}$ is the frequency separation between levels $|c\rangle$ and $|d\rangle$, ω_s is the signal frequency and

$$\Delta K_z \equiv K_z + \sqrt{k_{P1}^2 - k_{P1\perp}^2} + \sqrt{k_{P2}^2 - k_{P2\perp}^2} - \sqrt{k_s^2 - k_{s\perp}^2} - \sqrt{k_i^2 - k_{i\perp}^2} \tag{8.6}$$

is the 6WM wave-number mismatch. These equations reminiscent of the well known SPDC [Mit09] equations for the constant pump field (whose role in our case is played by the spin wave field $\mathcal{S}$) can be solved within the first order of the perturbation theory to give the description for the situation when signal-idler pairs are produced. As before, in the case of perfect phase matching ($\Delta K_z = 0$) we have:

$$\mathbf{K} = \mathbf{k}_W - \mathbf{k}_{Sd} \tag{8.7}$$

$$\mathbf{K} + \mathbf{k}_{P1} + \mathbf{k}_{P2} = \mathbf{k}_s + \mathbf{k}_i \tag{8.8}$$

From the solution, assuming that the atom density n is described by Gaussian distribution with longitudinal width equal σ_z we can then obtain the space-dependent part of the biphoton wave-function:

$$\psi(\mathbf{k}_{s\perp}, \mathbf{k}_{i\perp}, t_s, t_i) = \psi_t(t_s, t_i) e^{-\Delta K_z(\mathbf{k}_{s\perp}, \mathbf{k}_{i\perp})^2 \sigma_z^2}. \tag{8.9}$$

The temporal part of the solution, however, requires more involved treatment including decoherence. For the experimental needs, it can be approximated with the well-known form [Sri14]:

$$\psi_t(t_s, t_i) = \mathcal{N} e^{-(t_i - t_s)/2\tau_0} \Theta(t_i - t_s) \tag{8.10}$$

Such form stems form the anti-correlation of energies, as encoded in the spectral properties of the process in the constants g_i and g_s, which implies correlation in time. The specific shape of this correlation, however, requires proper treatment of decoherence in the system. To obtain it, we should consider the full coupling of the atom to the continuum of optical modes, within the Wigner-Weiskopf scheme [Jen15]. It could also be modelled effectively, by including an imaginary part in the denominators of g_i and g_s. The spectrum is then Lorentzian, thus we expect an exponential decay of temporal correlation[1].

---

[1] In our lossless approximation we rather obtain a limiting scenario with infinite correlation

The experimental setup details are provided in Fig. 8.3. The signal, idler and all of the control beams (including pumps as well as write and seed) are combined in the far field (FF) of the ensemble and propagate along the z-axis. The imaging setup consisting of two specifically chosen lenses provides a large field of view with minimal aberrations enabling decent resolution in the k-space. The Seed beam has an additional mirror on its path which is placed at the image plane of the ensemble. We use this mirror to change the created spin wave wavevector by changing the angle between write and seed beams. Since the signal and idler fields closing the 6WM process have orthogonal polarization (respectively: $\sigma^+$and σ^- or vice versa, depending on the chosen intermediate state $|d\rangle$ —see Fig. 8.3), we separate them using a half-wave plate and Wollaston prism. Then after passing the interference filters (IF), depending on the situation, they are either detected on the I-sCMOS camera situated in the far-field of the ensemble or coupled to the single-mode fibres connected to Avalanche Photodiodes (APD). When the camera is used we employ additional filtering consisting of a glass cell containing optically pumped to $5S_{1/2}, F = 2$ state Rubidium-87 vapour and buffer gas (N_2). For the alignment purposes, we send an additional beam indicated as an incoming idler in the Fig. 8.3 to seed the signal-idler generation process and observe the classically generated signal beam. For the temporal correlations measurements, we first observe the generated signal beam and maximize its amplitude in the sense of satisfying the phase matching condition $\Delta K_z = 0$. Then we couple this signal beam to the single-mode mode fibre of the signal APD. The particular experimental configuration i.e. control beam angles and propagation direction was chosen to provide broad phase matching spatial spectrum (broad range of angles). In Fig. 8.4 we present the time sequence of the experiment including all the steps described above.

Note that by selecting $F = 3$ manifold as the first intermediate state $|b\rangle$ we avoid performing read-out of the spin wave with the Pump 1 field, that would otherwise occur efficiently if Pump 1 was tuned closer to $F = 2$ excited-state manifold. Still, the Pump 1 field re-scatters excitations to other magnetic states of the $F = 2$ ground-state manifold causing effective decoherence of the spin wave B.

8.3 Results

8.3.1 Temporal correlations

We first present the results for the measurement of temporal correlations in a particular, pre-selected wavevector configuration. As indicated before, we select two distinct polarization configuration in which the dipole moment of the transition

---

$(\tau_0 \to \infty)$

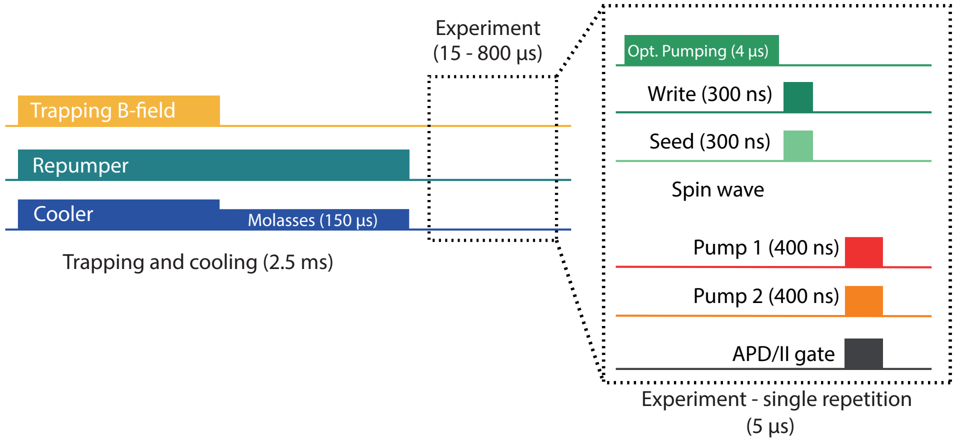

FIGURE 8.4: Time sequence of the experiment detailing the order of all experimental steps leading to correlated photons pairs generation. The experiment is repeated many times in the case of APD detection, and only once in the case of I-sCMOS detection.

for the idler photon differs $\sqrt{6}$ times. In Figs. 8.5(a,b) we present a histogram of signal-idler correlation as a function of mutual delay. We fit the second-order cross correlation as $g_{si}^{(2)}(t_s, t_i) = 1 + |\psi_t(t_s, t_i)|^2$. We observe very strong correlation with the values of $g_{si}^{(2)}$ of the order of 30, with simultaneously measured auto-correlations (Fig. 8.5(c,d)) exhibiting values no larger than 2. These two measurements constitute a strong violation of the Cauchy-Schwarz inequality (Eq. 2.32).

The measurement takes coincidences during the P1+P2 excitation pulse transferring the spin wave, that lasts approx. 100 ns, as well as during a subsequent decay. We observed that if the excitation pulse is applied continuously, decoherence of the spin wave B by pump P1 is strong and the number of coincidences decreases. Quite similarly, even during the decay of the $|c\rangle$ state we observed that the initial period yields slightly higher signal-to-noise ratio (see Fig. 8.6). We attribute this effect to a thermal decay of the spin wave $\mathcal{S}$. Indeed, even with negligible length of K (ground-state spin-wave wavevector), the longitudinal component of $\mathcal{S}$ is $K_{\mathcal{S}}^z = 2\pi(\frac{1}{\lambda_{P1}} + \frac{1}{\lambda_{P2}}) \approx 1600$ rad/mm, yielding $\Gamma_T = 7.2$ MHz (cf. Eq. 2.120).

For the weaker transition we measure the correlation time $\tau_0 = 10.6$ ns and for the stronger transition $\tau_0 = 4.6$ ns. Both these situations suggest a strong role of superradiance in the process, as without superradiant emission enhancement we would expect $\tau_0 \approx 23$ ns. With this, we experimentally prove that superradiance is inherently linked to phase-matched emission [Jen15], and can occur in any wave mixing process. Here, it is demonstrated in 6WM for the first time to our knowledge.

The superradiant rate is generally given by $\Gamma_\mu = (1+\mu)\Gamma$, with μ being the superradiant rate enhancement [Jen15; JC16; Sri13; Sri14]. We would normally expect that the ratio of superradiant rate enhancements for two transitions would be proportional to the ratio of dipole moments square, which in this case would be 6. However, here we observe a ratio only 3.2. This might be attributed to the measurement in Fig. 8.5(b) being at the verge of resolution of our time-tagger, different scaling due to some unknown effects, or likely a combination of the above.

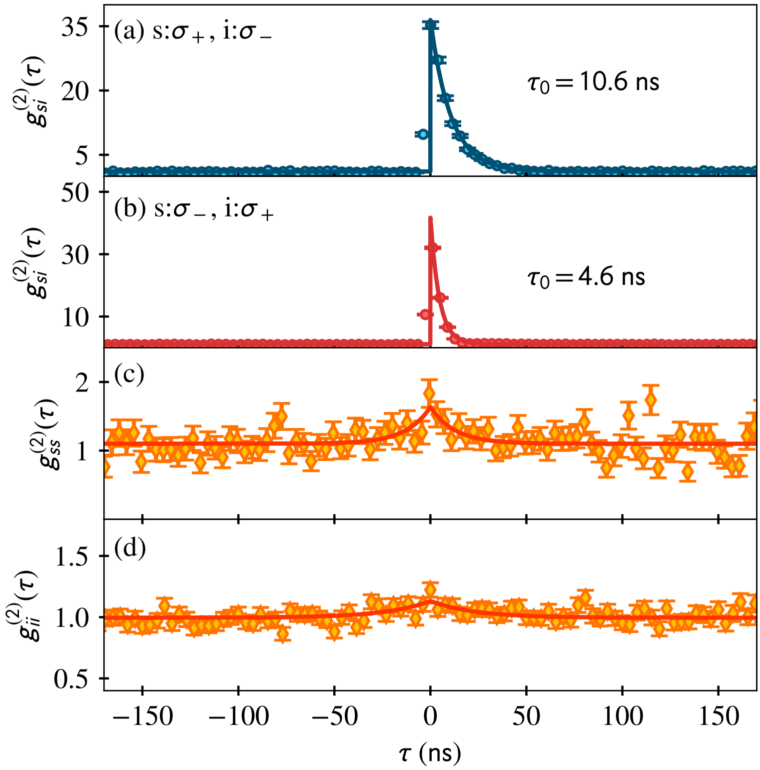

FIGURE 8.5: (a,c) Measured second order correlation functions between signal and idler fields $g^{(2)}_{si}(\tau = t_i - t_s)$ for the two possible decay paths through different intermediate level $|d\rangle$ ((a): $m_F = 0$, (b): $m_F = 2$). (c,d) Measured auto correlation functions $g^{(2)}_{jj}(\tau = t_{j1} - t_{j2})$ for the signal ($j = s$) (c) and idler ($j = i$) (d) fields.

8.3.2 Wavevector-domain correlations.

In the second experiment, we observed signal-idler correlations on the I-sCMOS camera. Using the I-sCMOS camera we collected about 5×10^6 frames for each

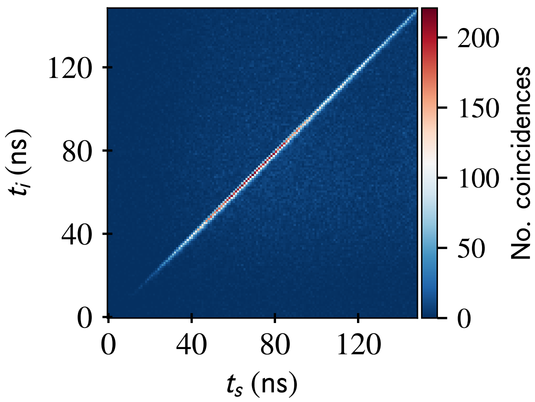

FIGURE 8.6: Temporal signal-idler coincidences for the duration of the excitations pulse (ca. first 100 ns) and subsequent decay.

of five different values of the spin-wave wavevector $\mathbf{K}$. Here the $g_{si}^{(2)}$ is calculated in the wavevector-sum coordinates, as in Sec. 4.5.3, with the only difference that shift the variables by the sum of transverse components of pump wavevectors. In this configuration, we expect that the correlation peak will appear in the spot determined by the initial spin wave. This is indeed what we observed in Figs. 8.7(a-e). Note that the correlations as averaged over the entire duration of the pulse, which we denote by $\langle g_{si}^{(2)} \rangle_T$. The averaging spans for the duration of the pulse This leads to significantly lower values for the cross-correlation, even though pair generation rate is lower here than in Fig. 8.5.

Finally, we also analyse the absolute in which regions the correlated photons are registered. This is most easily recovered by looking at the absolute intensity of registered idler light. The intensity in a perfectly correlated regions is increased approximately two-fold (see Figs. 8.7(f-j)). This can be understood as an interplay between coherent and incoherent emission. The signal photon is emitted in a random direction, leading to a creation of a random optical coherence ρ_{dg}. In most cases, this coherence either does not lead to phase-matched emission or decoheres rapidly due to atomic motion. A photon associated with such excitation is thus emitted in a random direction, in particular also in the phase-matched region. The phase-matched region is quite small, and there the proper phase-matched coherence leads to expected coherent emission of idler photon. Thus starting with a mean spin wave number $\bar{n}$ per pixel, we arrive at still roughly $\bar{n}$ incoherent photons per pixel and additional $\bar{n}$ coherent emission into the phase-matched region. This number may be smaller due to incoherent excitation of spin wave field B, incoherent transfer to spin wave $\mathcal{S}$, as well as its motional decoherence.

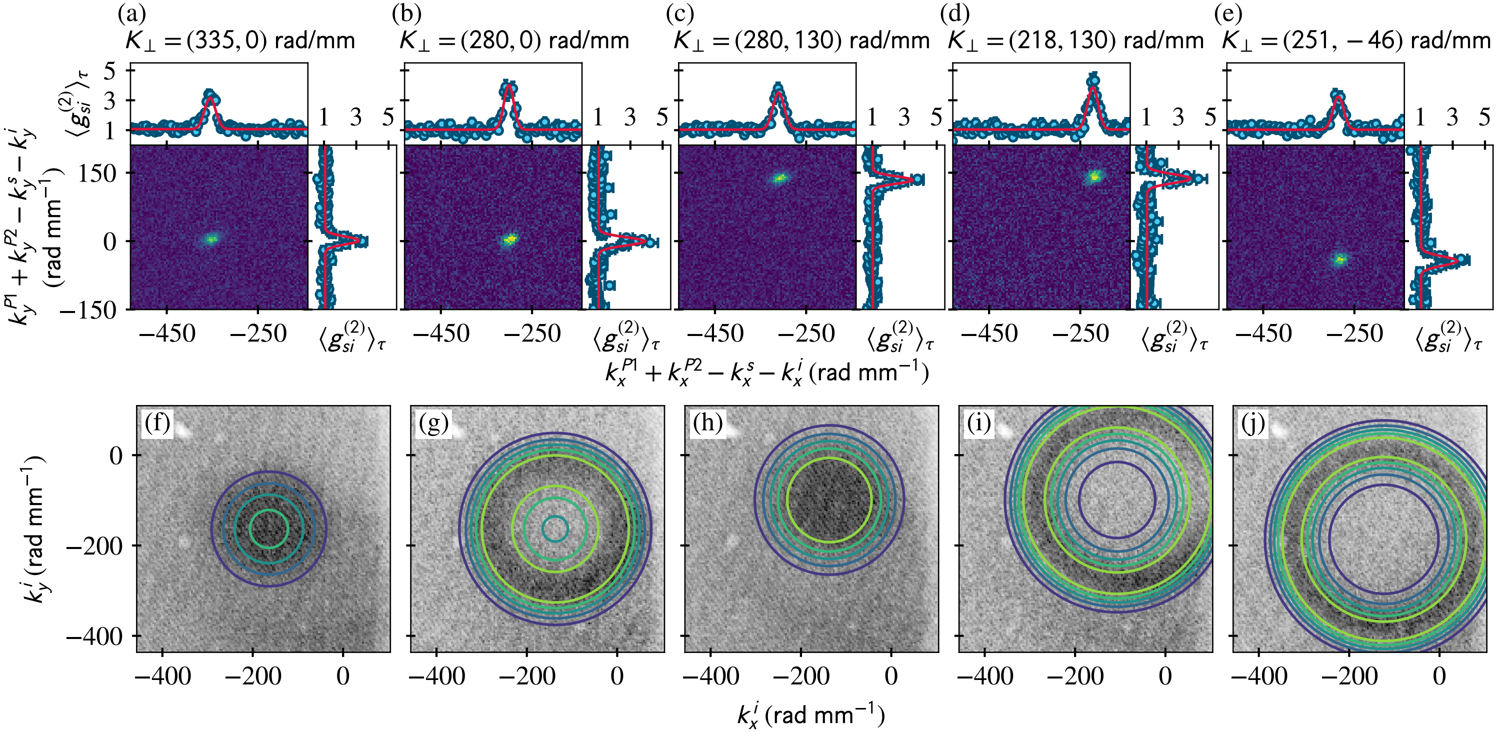

FIGURE 8.7: Correlation functions and superradiant emission patterns measured for a set of the ground-state spin-wave wavevectors. The top row presents the measurements of the time-averaged second-order correlation function for different transverse-wavevectors of the initial spin wave B. The bottom row presents the absolute measured idler intensities (total counts). The contour plots are the theoretical predictions of the phase matching. The data correspond to the same experimental situation column-wise.

We match the expected shape of phase-matched regions described by

$$\langle g_{si}^{(2)} \rangle_\tau - 1 \propto e^{-2\Delta K_z(\mathbf{k}_{s\perp},\mathbf{k}_{i\perp})^2 \sigma_z^2} \tag{8.11}$$

with the observed shapes of regions of increased idler counts rate. Without fitting (since all parameters are determined from correlation measurement), we observe very good agreement between experiment and theoretical prediction. It is worthy to compare various regimes we observe. In 8.7(f) we do not attain perfect phase matching even in the centre. The shape is thus roughly Gaussian. The opposite of that is presented in Figs. 8.7(i-j), where the the phase-matching rings become large and narrow. Figures 8.7(g-h) are in the intermediate regime where we either observe a broad ring as in (g) or a flattened Gaussian as in (h).

8.4 Conclusions and perspectives

In conclusion, we have demonstrated spin-wave based control of superradiance in the six-wave mixing process. Our experiments pave the way towards new schemes involving specifically prepared atomic states that lead to non-standard emission, such as for example sub-radiance [Jen17] as well as interference in the superradiant emission. Interesting perspectives arise due to the increased range of possibilities in the wavevector space.

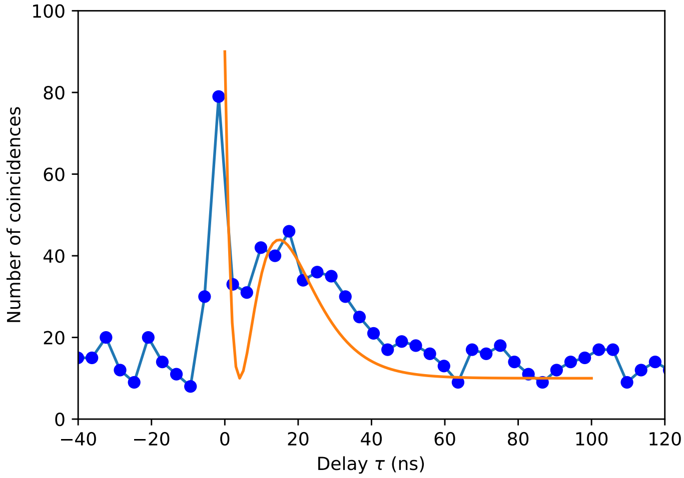

FIGURE 8.8: Signal-idler coincidences for a rotated polarization. A small dip in the middle of the decay is visible, potentially corresponding to destructive interference between faster and slower superradiant decay paths.

One interesting experiment involves interference of different decay paths, in the spirit of multi-path interference in four-wave mixing (see Ref. [PW15]). We could generate a superposition of different spin waves in the ensemble, that would later interfere during emission of the idler photon. We did a preliminary measurement in which we rotated the detected polarization of both signal and idler onto two orthogonal, elliptical polarization. With such, it should be possible to interfere the two decay paths either constructively or destructively. With superradiance, we would expect the coincidence signal to either disappear or be enhanced. With superradiance, however, the two decay paths should be characterized by different decay times, they will also interfere non-trivially in time. In particular, we would expect to see a dip (Fig. 8.8) where the amplitudes of two biphoton wavefunctions equalize. We did observe a potential indication of this phenomenon, yet most definitely better timing resolution is required to resolve the dip. It would be quite interesting to prove or disprove this hypothesis, as it would experimentally explain or demonstrate how should we treat effective dipole moments in superradiance. Potentially, the problem also requires extensive theoretical treatment.

8.4.1 Towards photonic triplets

Experimental attempts As already noted, one of the goals is to obtain a source of photonic triplets. Until now, however, the observation of such emission remains elusive. In an unsuccessful experiment, we have tried removing the seed beam from the scheme described in this Chapter. Instead, we first coupled the seed beam into a single-mode fibre, and after removing the seed light we tried to herald we the write photon detected in this mode. With such, we expected to observe a high third-order correlation function $g^{(3)}_{wsi}$ between the write, signal and idler photons. However, if one starts with a detection probability p_w for the write photon, corresponding to a hypothetical triplet generation rate p, we expect an accidental triplet detection proportional to p^3 and proper triplet detection rate proportional to p^2, since only the final idler emission is directional.

In consequence, we have been unable to observe a significantly high third-order correlation. The main reason for that is a still too low coherent excitation efficiency of the ground-state spin wave B to the $g-c$ spin wave $\mathcal{S}$ that leads to subsequent emission. We expect that the most efficient way would be to use a very short laser pulse with an area of π to coherently excite the state in a Rabi-oscillation manner. An alternative way to enhance the probability of register a proper triplet would be to enhance the emission of write (similarly as in Ref. [SDA10]) or signal photon via a cavity mode. Finally, using a camera to observe all three photons (in three distinct, selected regions) would be very interesting. In particular, we expect a favourable M^2 scaling with the number of observed modes. A challenge remains to select a good phase-matching configuration to allow that; yet, from the results presented here it seems that observation of ca. 100 phase-matched modes should be feasible.

Hölder inequality During the search for photonic triplets, it has come to our attention that no proper inequality for the third-order correlations, analogous to the Cauchy-Schwarz inequality (Eq. 2.32) seems to be known. One work [Din15] formulated an analogous inequality, but a simple example and analysis of their proof show that it is, in fact, wrong (see Appendix F). Here we thus propose a proper analogue of the Cauchy-Schwarz inequality.

Let us write the photon number operators for the three modes in a short form: $\hat{n}_a$, $\hat{n}_b$ and $\hat{n}_c$. If we now consider the classical states, and the photon-number operators as classical random variables n_a, n_b and n_c with expectation values understood as ensemble averages, we may use the Hölder inequality to generalize the Cauchy-Schwarz inequality yielding:

$$\langle n_a n_b \rangle \leq \langle n_a^p \rangle^{1/p} \langle n_b^q \rangle^{1/q} \tag{8.12}$$

for $p, q \geq 1$ and $1/p + 1/q = 1$. We may now apply this result to the product of three variables treating the first pair as one operator and taking $p = 3/2$ and $q = 3$ to obtain:

$$\langle n_a n_b n_c \rangle \leq \langle n_a^{3/2} n_b^{3/2} \rangle^{2/3} \langle n_c^3 \rangle^{1/3}. \tag{8.13}$$

And subsequently apply the Cauchy-Schwarz inequality to the first component of the product:

$$\langle n_a^{3/2} n_b^{3/2} \rangle \leq \langle n_a^3 \rangle^{1/2} \langle n_b^3 \rangle^{1/2}. \tag{8.14}$$

Finally, we obtain:

$$\langle n_a n_b n_c \rangle \leq \langle n_a^3 \rangle^{1/3} \langle n_b^3 \rangle^{1/3} \langle n_c^3 \rangle^{1/3}, \tag{8.15}$$

which in terms of normalized correlation function can be cast as:

$$[g_{abc}^{(3)}]^3 \leq g_{aaa}^{(3)} g_{bbb}^{(3)} g_{ccc}^{(3)}. \tag{8.16}$$

This inequality is indeed satisfied for all classical states, and it is thus clear that proper third-order auto-correlations (or other high-order correlations as can be implied for the generalized Hölder inequality) need to be measured to certify nonclassicality.

Finally, we would like to note a physical reason for the necessity to measure higher order auto-correlations. In the low-photon number regime, it becomes clear that one must check whether triples of photons do not appear randomly, to certify that the cross-correlation is nonclassical. Sole measurement of $g^{(2)}$ correlation is however only sensitive to pairs and generally does not give any information about triple counts.

Chapter 9

Conclusions and Perspectives

In the thesis I have concentrated on harnessing the multimode potential of a quantum memory in new ways. A quantum memory setup based on cold rubidium atoms has been constructed and optimized, which led to a demonstration of a memory operating in hundreds of spatial modes.

Next, a new method of manipulating spin waves stored in the memory has been developed. With the worked-out methods the Hong-Ou-Mandel interference of two spin waves residing in different spatial modes of an atomic ensemble has been demonstrated for the first time. The experiment marked the fundamental advance in controlling single collective excitations stored in the memory.

The framework has been then used to operate a temporally-multimode quantum memory. Our work greatly extended the capabilities originally demonstrated by *Hosseini et al.* [Hos09]. We have been able to program the interference of stored optical pulses paving the way towards a multi-input multi-output programmable interferometer.

Finally, the spin wave has been used as a pump in a parametric down-conversion process. The experiment exposed new intricacies lying in the superradiant behaviour of the system, its link with the phase matching, and interplay with noise. The fundamental studies allow better understanding of collective light-atom interactions.

In this final concluding chapter we would like to lay out new schemes that can be implemented as a continuation of the described research. In some particular cases, we already proposed extensions - for example the protocol for generating photonic triplets. Here, we will shortly discuss three issues: technological development needed to operate an enhanced, multiplexed photon source discussed in Chapter 4, proposed techniques to achieve non-linear interaction for spin-wave processing, and finally several new protocols that arise through understanding of the phase matching in the system.

9.1 Feedback-based photon generation

In Chapter 4 we have considered the multiplexed photon generation protocol. While the feedback is to yet possible due to the delays introduced by spatially-resolved single-photon detection, it is worth considering how to actually transfer emitted read photons into a single mode. Three particular configurations may be considered. In the simplest one, an acousto-optic deflector with variable drive frequency would be used to adaptively change the direction of emitted photon. The main disadvantage stems from loosing efficiency for angles largely deviating from the central one. Still, it seems feasible to efficiently deflect approx. 100 modes in one dimension.

The problem could also be completely mitigated, by adjusting the angle at which read beam is sent into the ensemble. The wavevector $\mathbf{k}_{R\perp}$ should be adjusted to $\mathbf{k}_{R\perp} = \mathbf{k}_{W\perp} - \mathbf{K}_{\perp} + \mathbf{k}_{0\perp}$, where $\mathbf{K}_{\perp}$ is known from measuring $\mathbf{k}_w = \mathbf{k}_W - \mathbf{K}_{\perp}$ so that $\mathbf{k}_r = \mathbf{k}_{0\perp}$, where $\mathbf{k}_{0\perp}$ is a pre-selected direction. The problem with this approach is that it only may be effective in the co-propagating configuration, where only a very small region of spin-wave wavevetors is properly phase-matched. In the counter-propagating configuration tilting the write and read beams spoils the phase-matching for almost all wavevectors. However, we could actively correct K_z of the spin wave with ac-Stark or magnetic gradient to always guarantee phase matching.

This directly leads us to the last method in which the entire wavevector of the spin wave would be adjusted so that the read photon is always emitted in the same direction. Notably, emission in this particular direction could be enhanced with a cavity [Zha09].

In all the discussed schemes (except the last one) the frequency of the photon is modified in each shot, since acousto-optic defection also changes light frequency. If photons of specified frequency are required at the output, one could easily fix that with an additional AOM in a double-pass configuration or a properly configured EOM.

9.2 Processing, interference and deserialization of pulses

The protocols introduced in Chapter 7 already featured manipulations in two different dimensions of the k-space. Using these two dimensions brings about many new possibilities. A particularly interesting one is to transduce pulses from the temporal to spatial domain, or vice versa. In a proposed protocol, we use a FIFO-like storage by shifting the stored pulse in a memory by $\mathbf{K} = (K_x, 0, K_z)$. A train of stored pules will thus occupy a skewed line in the k-space. By sending a read beam at an angle, all pulses could be now retrieved at once, as shown in Fig. 9.1(b), since they all will be phase-matched. While this works preferably in the planar approximation for phase matching, we could also arrange the pulses on a

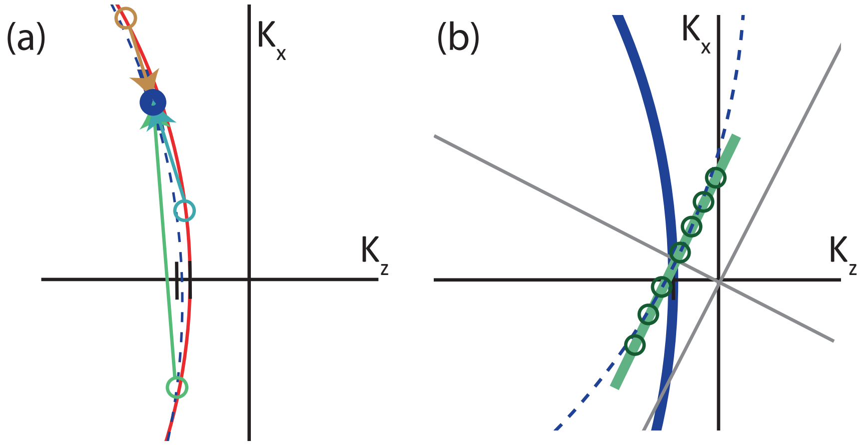

FIGURE 9.1: Two example protocols exploiting the properties of phase matching. In (a) we use the ac-Stark modulation to adaptively move the spin-wave mode into the same place in K-space, so it is always efficiently retrieved in the same direction. This particular mode can also be enhanced with a cavity. Different thin circles correspond to single-photon detections. We detect their transverse momentum, and calculate K_z from Eq. 2.90. Then, they are all shifted to a single location in K-space, marked by the small thick circle. In (b) we store a train of pulses using one control beam (main coordinate system, solid line) by moving them with ac-Stark modulation in a skewed direction in K-space. Next, we apply another control (read) beam (grey coordinate system, dashed line) to retrieve all modes at once, yet in different directions in space.

proper arc. The protocol can also be easily reversed to send pulses stored in parallel one-by-one. Another interesting possibility arises as a potential realization of a superadditivie optical receiver, proposed by S. Guha [Guh11; Kli16]. Such receiver can increase the information transmitted by one photon in classical communications via encoding the information in the Hadamard code (where symbols are encoded with binary phase shift keying), and then transforming the message into the pulse-position modulation format for measurement. The transformation that needs to be applied is a Hadamard matrix on the input temporal modes. As briefly demonstrated in Fig. 9.2 for four pulses our quantum memory could realize such a transformation via subsequent (or simultaneous) application of two distinct z-periodic gratings for a train of pulses stored in the memory. The interference induced by the gratings would realize exactly the desired transformation.

9.3 Enhancing interactions and nonlinearities

Finally, we discuss three ways to enhance the strength of interactions in the memory, to potentially allow for both more efficient operation as well as new class of photon-photon interaction.

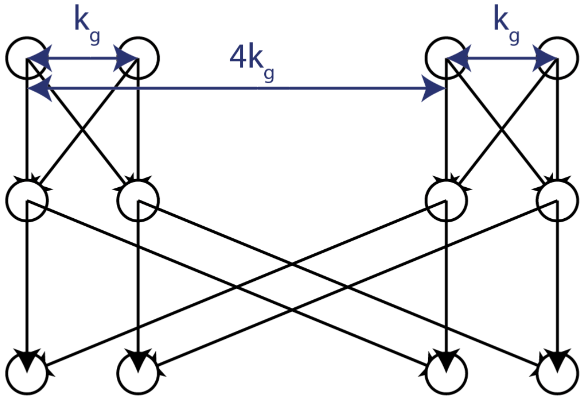

FIGURE 9.2: The idea for realization of a Hadamard transform for the input temporal modes. The four pulses enter in pairs, with a larger delay in between. They are thus arranged in pairs in the K_z space. We than apply a low-spatial-frequency modulation mixing each pair, and then a high-spatial-frequency modulation mixing modes across the pairs.

The efficiency is limited by the optical depth of the atomic ensemble. The best way to increase the optical depth is to create a longer ensemble, yet, in a spatially-multimode quantum memory like the one discussed here this creates more problems with phase matching. An alternative solution is to embed the ensemble in an optical cavity. The cavity can enhance emission of the write photon, leading to significant noise suppression, or increase the optical depth for the read photon, and thus increase the efficiency.

With high optical depth or with a cavity a possibility arises to keep the light inside atoms for a long time. With this in mind, a variety of protocols utilizing such stationary light has been proposed to facilitate effective photon-photon interactions via cross-phase modulation based on ac-Stark shifts.

Finally, a similar possibility could also be provided by Rydberg atoms. The complexity of the experiment, however, rises significantly, and it remains unknown if the blockade strength and radius would be enough to facilitate proper interactions in a large atomic ensemble with which we operate.

Regardless of these future challenges, I believe that still a plethora of unexplored schemes and potentially quite a few fundamentally new effects are to be unraveled with our quantum memory.

Appendix A

Additional Derivations

A.1 Unidirectional Pulse Propagation Equation

To be able to solve Eq. 2.3 for a generic medium polarization we will employ a set of approximations. Let us first rewrite the wave equation (Eq. 2.3) in the Fourier domain in terms of transverse spatial variables and time. Via Fourier transform the time derivative transforms as $\partial_t^2 \to -\omega^2$ and the transverse Laplacian as $\Delta_\perp = \partial_x^2 + \partial_y^2 \to -k_x^2 - k_y^2$. We obtain the following equation [1]:

$$\left(\frac{\partial^2}{\partial z^2} - \underbrace{(k_x^2 + k_y^2)}_{k_\perp^2 = |\mathbf{k}_\perp|^2} + \frac{\omega^2}{c^2} \right) \mathbf{E}(\mathbf{k}_\perp, z, \omega) = -\frac{\omega^2}{\epsilon_0 c^2} \mathbf{P}(\mathbf{k}_\perp, z, \omega) \tag{A.1}$$

The *unidirectional pulse propagation equation* (UPPE) is obtained by first factoring the propagator on the LHS of wave equation given in Chapter 2, Eq. 2.1 into a product of backward and forward propagators:

$$\left(\frac{\partial}{\partial z} + i\sqrt{\frac{\omega^2}{c^2} - k_\perp^2} \right) \left(\frac{\partial}{\partial z} - i\sqrt{\frac{\omega^2}{c^2} - k_\perp^2} \right) \mathbf{E}(\mathbf{k}_\perp, z, \omega) = -\frac{\omega^2}{\epsilon_0 c^2} \mathbf{P}(\mathbf{k}_\perp, z, \omega). \tag{A.2}$$

We now make the first approximation by assuming that the pulse propagated only in the forward direction. In such case the value of $\partial_z \mathbf{E}(\mathbf{k}_\perp, z, \omega)$ is always close to $i\sqrt{\frac{\omega^2}{c^2} - k_\perp^2}\mathbf{E}(\mathbf{k}_\perp, z, \omega)$[2]. In the right (forward) propagator in Eq. A.2 the two components will be close to cancelling out, while in the left (backward)

---

[1] Note that in most cases we will drop denote the transformed fields always by the same symbol, as often only some variables will be Fourier transformed. In any case it will be clear from the name of arguments (t - ω or x - k) in which domain the field is represented.

[2] This is true as long as we accept a complex solution of the wave equation of the form $\mathbf{E} \sim e^{ikz}$ with $k > 0$. For a physical real-valued solution we would need to write separate equations for two terms (rotating and counter-rotating) and make separate approximations for each of them. Importantly, the final result would be the same.

propagator they will approximately yield $2i\sqrt{\frac{\omega^2}{c^2}-k_\perp^2}$. The approximated equation is called UPPE:

$$\frac{\partial}{\partial z}\mathbf{E}(\mathbf{k}_\perp,z,\omega)=i\sqrt{\frac{\omega^2}{c^2}-k_\perp^2}\mathbf{E}(\mathbf{k}_\perp,z,\omega)-\frac{\omega^2}{2i\epsilon_0 c^2\sqrt{\frac{\omega^2}{c^2}-k_\perp}}\mathbf{P}(\mathbf{k}_\perp,z,\omega). \quad \text{(A.3)}$$

Note that the equation cannot be easily transformed back into the spatio-temporal domain due to a problem in understanding a square root of the laplacian; yet it can be solved in the Fourier domain numerically and the result (as well as the input) can be re-transformed.

A.2 UPPE for slowly-varying envelope

Here we introduce the slowly-varying envelopes for electric field and polarization:

$$\mathbf{E}(\mathbf{r},t)=\frac{1}{2}\mathbf{A}(\mathbf{r},t)e^{-i\omega_0 t+ik_0 z}+c.c., \quad \text{(A.4)}$$

$$\mathbf{P}(\mathbf{r},t)=\frac{1}{2}\boldsymbol{\mathcal{P}}(\mathbf{r},t)e^{-i\omega_0 t+ik_0 z}+c.c., \quad \text{(A.5)}$$

The UPPE (Eq. A.3) for $\mathbf{A}(\mathbf{k}_\perp,z,\omega)$ takes the following form:

$$\left(\frac{\partial}{\partial z}-i\sqrt{\frac{\omega^2}{c^2}-k_\perp^2}\right)\left(\mathbf{A}(\mathbf{k}_\perp,z,\omega+\omega_0)e^{ik_0 z}\right)= \\ =-\frac{\omega^2}{2i\epsilon_0 c^2\sqrt{\frac{\omega^2}{c^2}-k_\perp}}\boldsymbol{\mathcal{P}}(\mathbf{k}_\perp,z,\omega+\omega_0)e^{ik_0 z}. \quad \text{(A.6)}$$

We will now expand z-derivative and substitute $\omega'=\omega+\omega_0$, where ω' becomes the frequency deviation from the central carrier frequency. This procedure yields:

$$\left(\frac{\partial}{\partial z}+ik_0-i\sqrt{\frac{(\omega'-\omega_0)^2}{c^2}-k_\perp^2}\right)\mathbf{A}(\mathbf{k}_\perp,z,\omega')= \\ =-\frac{(\omega'-\omega_0)^2}{2i\epsilon_0 c^2\sqrt{\frac{(\omega'-\omega_0)^2}{c^2}-k_\perp^2}}\boldsymbol{\mathcal{P}}(\mathbf{k}_\perp,z,\omega'). \quad \text{(A.7)}$$

Let us now transfer to the frame of reference co-moving with the considered pulse, which is done by transforming: $z\to z$, $t\to t-z/c$, which for the z-derivative and ω corresponds to: $\partial_z\to\partial_z-i\omega'/c$, $\omega'\to\omega'$. We will simultaneously expand the square roots present in the expressions in the $-2\omega'\omega_0+\omega'^2$. On the LHS we obtain:

$$\left[\frac{\partial}{\partial z} - i\frac{\omega'}{c} + ik_0 - i\sqrt{\frac{\omega_0^2}{c^2} - k_\perp^2}\left(1 + \frac{1}{2}\frac{-2\omega'\omega_0 + \omega'^2}{\frac{\omega_0^2}{c^2} - k_\perp^2} + \dots\right)\right]\mathbf{A}(\mathbf{k}_\perp, z, \omega'), \tag{A.8}$$

Finally, apply the slowly varying envelope approximations, which simply states that $|\omega'| \ll \omega_0$ in the Fourier (frequency) domain[3]. We immediately drop the ω'^2 and higher terms, which reduced the expression to:

$$\left[\frac{\partial}{\partial z} - i\left(\sqrt{k_0^2 - k_\perp^2} - k_0\right) + i\frac{\omega'}{c}\left(1 - \frac{k_0}{\sqrt{k_0^2 - k_\perp^2}}\right)\right]\mathbf{A}(\mathbf{k}_\perp, z, \omega'). \tag{A.9}$$

The last term proportional to ω' is simlutaneously in the lowest order in transvere momentum proportional to $k_\perp^2$. Such term corresponds to a third-order spatio-temporal derivative, and may be dropped as well in comparison with the second term also proportional in the first order to $k_\perp^2$. In other words we need to assume $|\frac{\omega' k_\perp^2}{2ck_0^2}| \ll |\frac{k_\perp^2}{2k_0}|$ which is equivalent to an already existing assumption $|\omega'| \ll \omega_0$. However, as we expand the square roots further in $k_\perp^2$ we obtain stricter conditions, in particular $3|\omega'| \ll \omega_0$, $5|\omega'| \ll \omega_0$, etc., which in consequence puts a limit on $k_\perp^2$. In practice, the limit is much less strict than in the typical paraxial approximation. We correctly take into account all terms of the order of $(k_\perp)^{2j}$ for all j that satisfy $(2j+1)|\omega'| \ll \omega_0$ thus the requirement is roughly $(k_\perp)^{2\frac{\omega_0}{\omega'}} \ll (k_0)^{2\frac{\omega_0}{\omega'}}$. For the RHS of Eq. A.7 we obtain a analogous scenario:

$$-\frac{\omega_0^2 + \omega'\omega_0 + \omega'^2}{2i\epsilon_0 c^2\sqrt{\frac{\omega_0^2}{c^2} - k_\perp^2}}\left(1 - \frac{1}{2}\frac{2\omega'\omega_0 + \omega'^2}{\frac{\omega_0^2}{c^2} - k_\perp^2} + \dots\right)\boldsymbol{\mathcal{P}}(\mathbf{k}_\perp, z, \omega') \tag{A.10}$$

and with the same assumptions we obtain:

$$-\frac{\omega_0^2}{2i\epsilon_0 c^2\sqrt{k_0^2 - k_\perp^2}}\boldsymbol{\mathcal{P}}(\mathbf{k}_\perp, z, \omega'). \tag{A.11}$$

Note that in the time domain the condition is equivalent to $|\frac{\partial^2\boldsymbol{\mathcal{P}}}{\partial t^2}| \ll \omega_0|\frac{\partial\boldsymbol{\mathcal{P}}}{\partial t}| \ll \omega_0^2|\boldsymbol{\mathcal{P}}|$. The full equation, in which the frequency dependence is eliminated, takes

---

[3] Such relation may be translated to the time domain yielding the typical SVEA condition $|\frac{\partial^2\mathbf{E}}{\partial t^2}| \ll \omega_0|\frac{\partial\mathbf{E}}{\partial t}| \ll \omega_0^2|\mathbf{E}|$.

on a form:

$$\boxed{\left[\frac{\partial}{\partial z} - i\left(\sqrt{k_0^2 - k_\perp^2} - k_0\right)\right]\mathbf{A}(\mathbf{k}_\perp, z, t) = \underbrace{\frac{ik_0^2}{2\epsilon_0\sqrt{k_0^2 - k_\perp^2}}}_{\approx\frac{ik_0}{2\epsilon_0}}\boldsymbol{\mathcal{P}}(\mathbf{k}_\perp, z, t).} \tag{A.12}$$

This equation is used as Eq. 2.8 in its simplified version (the underbrace approximation) throughout our calculations.

A.3 Field quantization in the propagating mode basis

Let us approximate ω_l in the square root by ω_0 in Eq. 2.14 and rewrite the slowly varying envelope operator in a different set of modes $u_{sk}(\mathbf{r}, t)$, that are understood as pulses propagating along the z axis in the co-moving frame ($z \to z$, $t \to t - \frac{z}{c}$), in which z defines whether a pulse already passed through an atomic ensemble or at which transverse plane we consider it, and t is the local pulse time. They obey the relation:

$$\int \mathrm{d}x\,\mathrm{d}y\,c\mathrm{d}t\,u_{sk}(\mathbf{r}, t)u_{sj}^*(\mathbf{r}, t) = \delta_{kj} \tag{A.13}$$

at each z. Note that the transformation is possible thanks to the assumption of the quasi-monochromatic wave[4]. The coordinate transformation into the co-moving frame is implicitly incorporated into the mode function. The following must be satisfied in the co-moving frame:

$$\hat{\mathbf{A}}(\mathbf{r}, t) = \sum_{sl} i\sqrt{\frac{2\hbar\omega_0}{\epsilon_0}}\hat{a}_{sl}e^{-i(\omega_l-\omega_0)(t-\frac{z}{c})+ik_0z}U_{sl}(\mathbf{r})\boldsymbol{\epsilon}_s = i\sqrt{\frac{2\hbar\omega_0}{\epsilon_0}}\sum_{sk}\hat{a}_{sk}u_{sk}(\mathbf{r}, t)\boldsymbol{\epsilon}_s \tag{A.14}$$

Note that the sum on the right runs through a different set of indices. In particular, we are actually interested in propagating modes that are certain superpositions of the normal modes. One might imagine our typical mode of interest as a pulse propagating along a shape of a Gaussian beam. The relation can be reversed by integrating both sides with a conjugate mode function to give a definition of such pulsed mode annihilation operator:

$$\hat{a}_{sl} = -i\sqrt{\frac{\epsilon_0}{2\hbar\omega_0}}\int \hat{\mathbf{A}}(\mathbf{r}, t)\cdot\boldsymbol{\epsilon}_s u_{sl}^*(\mathbf{r}, t)\mathrm{d}x\,\mathrm{d}y\,c\mathrm{d}t \tag{A.15}$$

---

[4] A much more rigorous quantization of the paraxial wave packets (or the slowly varying envelope in the paraxial approximation) has been presented by *Deutsch and Garrison* [DG91].

A.4 Cauchy-Schwarz inequality and antibunching

Here we present proofs of two essential nonclassicality criteria presented in Sec. 2.1.3.

The mathematicians' version of the Cauchy-Schwarz inequality states that:

$$\left|\sum_{i=1}^{N} u_i \bar{v}_i\right|^2 \leq \sum_{j=1}^{N} |u_j|^2 \sum_{k=1}^{N} |v_k|^2, \tag{A.16}$$

where u_i and v_i are complex vector component.

We first consider two classical, positive random variables that are the numbers of registered photons n_a and n_b in two modes. The following is then satisfied due to the Cauchy-Schwarz inequality:

$$\left|\sum_{i} n_a^{(i)} n_b^{(i)}\right|^2 \leq \sum_{j} (n_a^{(j)})^2 \sum_{k} (n_b^{(k)})^2. \tag{A.17}$$

We divide both sides by N^2 (with N being the number of process realizations) and by the product of means of n_a and n_b, arriving immediately to our inequality of interest (Eq. 2.32).

For the antibunching criterion we may again use the Cauchy-Schwarz inequality (taking $u_i = n_a^{(i)}$ and $v_i = 1$) to obtain:

$$\left|\sum_{i} n_a^{(i)}\right|^2 \leq N\left(\sum_{i} (n_a^{(i)})^2\right), \tag{A.18}$$

which we then divide by N^2 to obtain:

$$\langle n_a \rangle^2 \leq \langle n_a^2 \rangle. \tag{A.19}$$

After finally dividing both sides by $\langle n_a \rangle^2$ we see that indeed:

$$g_{aa}^{(2)} = \frac{\langle n_a^2 \rangle}{\langle n_a \rangle^2} \geq 1. \tag{A.20}$$

A.5 Rotation wave approximation

To justify crossing out of the rapidly rotating terms, it is worth rewriting the non-approximated interaction Hamiltonian $\hat{H}_I$ (Eq. 2.43) as a sum of a time-independent (I') and oscillating (O) part:

$$\hat{H}_I = \underbrace{-\hbar\Delta\hat{\sigma}_{ee} - \hbar\frac{\Omega^*}{2}\hat{\sigma}_{ge} - \hbar\frac{\Omega}{2}\hat{\sigma}_{eg}}_{\hat{H}'_I} + \underbrace{\left(-\frac{\mathbf{A}\mathbf{d}_{ge}}{2}e^{-2i\omega t}\hat{\sigma}_{ge} - \frac{\mathbf{A}^*\mathbf{d}_{eg}}{2}e^{2i\omega t}\hat{\sigma}_{eg}\right)}_{\hat{H}_O(t)} \tag{A.21}$$

Now treating $\hat{H}_O(t)$ as a perturbation and $\hat{H}'_I$ as a base Hamiltonian we introduce a new interaction picture in which we use the time-dependent perturbation theory to calculate the evolution operator up to the first order:

$$\begin{aligned}
&\mathcal{T}\exp\left(-\frac{i}{\hbar}\int_0^t \mathrm{d}t' e^{i\hat{H}'_I t'/\hbar}\hat{H}_O(t')e^{-i\hat{H}'_I t'/\hbar}\right) = \\
&\qquad = \mathbb{1} - \frac{i}{\hbar}\int_0^t \mathrm{d}t' e^{iH'_I t'/\hbar}H_O(t')e^{-iH'_I t'/\hbar} + \ldots = \\
&= \mathbb{1} + \left[\frac{\mathbf{A}^*\mathbf{d}_{eg}\left(-1 + e^{\frac{i(4\omega-\Omega^*)}{2}}t\right)}{4\hbar\omega - \hbar\Omega^*} + \frac{\mathbf{A}\mathbf{d}_{ge}\left(1 - e^{-\frac{i(4\omega-\Omega)t}{2}}\right)}{4\hbar\omega - \hbar\Omega}\right]\hat{\sigma}_{gg} + \\
&\qquad \left[\frac{\mathbf{A}\mathbf{d}_{ge}\left(1 - e^{-i(2\omega-\Delta)t}\right)}{4\hbar\omega - 2\hbar\Delta} - \frac{\mathbf{A}^*\mathbf{d}_{eg}\left(1 - e^{2i\omega t}\right)}{4\hbar\omega}\right]\hat{\sigma}_{ge} + \\
&\qquad + \left[\frac{\mathbf{A}\mathbf{d}_{ge}\left(1 - e^{-2i\omega t}\right)}{4\hbar\omega} - \frac{\mathbf{A}^*\mathbf{d}_{eg}\left(1 - e^{i(2\omega-\Delta)t}\right)}{4\hbar\omega - 2\hbar\Delta}\right]\hat{\sigma}_{eg} + \\
&+ \left[\frac{\mathbf{A}^*\mathbf{d}_{eg}\left(-1 + e^{i(2(2\omega-\Delta)+\Omega^*)t}\right)}{2\hbar(2\omega-\Delta) + \hbar\Omega^*} + \frac{\mathbf{A}\mathbf{d}_{ge}\left(1 - e^{-\frac{1}{2}i(2(2\omega-\Delta)+\Omega)t}\right)}{2\hbar(2\omega-\Delta) + \hbar\Omega}\right]\hat{\sigma}_{ee} + \ldots
\end{aligned} \tag{A.22}$$

where $\mathcal{T}$ signifies proper time ordering characteristic of the Dyson series. All terms in the resulting evolution operator vanish on the conditions that the transition frequency ω is much larger than both the detuning $|\Delta|$ and the Rabi frequency $|\Omega|$, as they all contain the dominant term $4\hbar\omega$ in their denominators. In consequence, the RWA corresponds to zeroth order approximation in this framework. Basic correction procedure involves transforming the system into the frame of reference counter-rotating with the optical field and obtaining the Bloch-Siegert shift (also called ac-Stark shift if the field is far off-resonant)[5].

---

[5] Note that this ac-Stark shift is distinct from the ac-Stark shift caused by the co-rotating field component

A.6 Density of spin waves

The local spatial density of spin waves $B^\dagger(\mathbf{r})B(\mathbf{r})$ on a coherent spin-wave state is calculated as:

$$\langle\beta|B^\dagger(\mathbf{r})B(\mathbf{r})|\beta\rangle = \frac{1}{n(\mathbf{r})(\delta V)^2}\sum_{i,j\in\delta V(\mathbf{r})}\langle\beta|\hat{\sigma}_{hg}^{(i)}\hat{\sigma}_{gh}^{(j)}|\beta\rangle =$$
$$= \frac{1}{n(\mathbf{r})(\delta V)^2}\left(\sum_{\substack{i\neq j\\ \in\delta V(\mathbf{r})}}\langle\beta|\mathbb{1}\otimes\ldots\otimes\underset{i}{\hat{\sigma}_{hg}}\otimes\ldots\otimes\underset{j}{\hat{\sigma}_{gh}}\otimes\ldots\mathbb{1}|\beta\rangle + \sum_{i\in\delta V(\mathbf{r})}\langle\beta|\hat{\sigma}_{hh}^{(i)}|\beta\rangle\right) =$$
$$= \frac{1}{n(r)(\delta V)^2}\Big(n(\mathbf{r})\delta V\big(n(\mathbf{r})\delta V-1\big)|\beta(\mathbf{r})|^2 + n(r)\delta V|\beta(r)|^2\Big) = n(\mathbf{r})|\beta(r)|^2. \tag{A.23}$$

The operator may also be integrated to yield a total number of excitations in the ensemble:

$$\hat{n}_{tot} = \int \mathrm{d}\mathbf{r}\hat{B}^\dagger(\mathbf{r})\hat{B}(\mathbf{r}) \tag{A.24}$$

For the separable state the expectation value is:

$$\langle\beta|\hat{n}_{tot}|\beta\rangle = \int \mathrm{d}\mathbf{r}n(\mathbf{r})|\beta(\mathbf{r})|^2, \tag{A.25}$$

which for a spatially-independent $\beta(\mathbf{r}) = \beta$ simply yields $N|\beta|^2$.

A.7 Spin waves in momentum space

Here we first show that the operator $\hat{B}(\mathbf{K})$, as given by Eq. 2.111 is a Fourier transform of $\hat{B}(\mathbf{r})$, as in Eq. 2.102. We will do this by calculating its expectation value on a coherent state $|\beta\rangle$ as in Eq. 2.107. The expectation value of $\hat{B}(\mathbf{K})$ as defined by Eq. 2.111 is calculated by replacing summation by integration ($\sum_i \to \int \mathrm{d}\mathbf{r}n(\mathbf{r})$) with a weight given by atom number density:

$$\langle\beta|\hat{B}(\mathbf{K})|\beta\rangle = \frac{1}{(2\pi)^{3/2}}\sum_i\frac{1}{\sqrt{n(\mathbf{r}_i)}}e^{-i\mathbf{K}\mathbf{r}_i}\beta(\mathbf{r}_i) = \frac{1}{(2\pi)^{3/2}}\int\mathrm{d}\mathbf{r}\sqrt{n(\mathbf{r})}\beta(\mathbf{r})e^{-i\mathbf{K}\mathbf{r}} \tag{A.26}$$

Simultaneously, we calculate the expectation value of the Fourier transform of $B(\mathbf{r})$:

$$\begin{aligned}\langle\beta|\frac{1}{(2\pi)^{3/2}}\int \mathrm{d}\mathbf{r}\hat{B}(\mathbf{r})e^{-i\mathbf{K}\mathbf{r}}|\beta\rangle &= \frac{1}{(2\pi)^{3/2}}\int \mathrm{d}\mathbf{r}\langle\beta|\hat{B}(\mathbf{r})|\beta\rangle e^{-i\mathbf{K}\mathbf{r}} = \\ &= \frac{1}{(2\pi)^{3/2}}\int \mathrm{d}\mathbf{r}\sqrt{n(\mathbf{r})}\beta(\mathbf{r})e^{-i\mathbf{K}\mathbf{r}} \quad \text{(A.27)}\end{aligned}$$

Indeed the result is the same as in Eq. A.26. Since the coherent states form an overcomplete basis, we conclude that $\hat{B}(\mathbf{K})$ is a proper Fourier transform of $B(\mathbf{r})$. From now on we will treat Eq. as the main definition of a spin-wave creation operator, as it is well-defined via considering all atoms in the ensemble.

Similarly as for $\hat{B}(\mathbf{r})$, in the wavevector-resolved case we may evaluate the commutator. In this case we unambiguously obtain:

$$\begin{aligned}[\hat{B}(\mathbf{K}),\hat{B}^\dagger(\mathbf{K}')] &= \frac{1}{(2\pi)^3}\sum_{ij}\frac{1}{\sqrt{n(\mathbf{r}_i)n(\mathbf{r}_j)}}e^{i\mathbf{K}'\mathbf{r}_j-\mathbf{K}\mathbf{r}_i}[\hat{\sigma}_{gh}^{(i)},\hat{\sigma}_{hg}^{(j)}] = \\ = \frac{1}{(2\pi)^3}\sum_i\frac{1}{n(\mathbf{r}_i)}e^{i(\mathbf{K}'-\mathbf{K})\mathbf{r}_i}(\hat{\sigma}_{gg}^{(i)}-\hat{\sigma}_{hh}^{(i)}) &\xrightarrow[\langle 0|.|0\rangle]{} \frac{1}{(2\pi)^3}\sum_i\frac{1}{n(\mathbf{r}_i)}e^{i(\mathbf{K}'-\mathbf{K})\mathbf{r}_i} = \\ &= \frac{1}{(2\pi)^3}\int \mathrm{d}\mathbf{r}e^{i(\mathbf{K}'-\mathbf{K})\mathbf{r}} = \delta(\mathbf{K}-\mathbf{K}') \quad \text{(A.28)}\end{aligned}$$

The first order correction to this commutator resulting from deviation of the considered state from the ground state is proportional to n_{tot}/N, where n_{tot} is the total number of excitations. At the single-excitation level we do not expect ant observable effects due to this fact.

A.8 Separability of coherent spin waves

Let us now consider a plane-wave coherent spin-wave state:

$$|\sqrt{N}\beta\rangle_{\mathbf{K},coh} = e^{-N|\beta|^2/2}\sum_m^\infty(\hat{b}_\mathbf{K}^\dagger)^m(\sqrt{N}\beta)^m|0\rangle \quad \text{(A.29)}$$

By assumption, the state contains $N|\beta|^2$ excitations. We will now show that this state approximately corresponds to a separable state of atoms, as previously also used in Eq. :

$$|\sqrt{N}\beta\rangle_{\mathbf{K},sep} = (1+|\beta|^2)^{-N/2}\bigotimes_i^N(|g_i\rangle+\beta e^{i\mathbf{K}\mathbf{r}_i}|h_i\rangle) \quad \text{(A.30)}$$

First, we expand the above tensor product into a multinomial:

$$\bigotimes_{i}^{N}(|g_i\rangle + \beta e^{i\mathbf{K}\mathbf{r}_i}|h_i\rangle) = \sum_{m}^{N} \beta^m \sum_{\Sigma\in\mathrm{C}(m,N)} e^{i\mathbf{K}\sum_i^m \mathbf{r}_{\Sigma(i)}} \sigma_{hg}^{(\Sigma(1))} \dots \sigma_{hg}^{(\Sigma(m))}|0\rangle \quad \text{(A.31)}$$

where $\mathrm{C}(m,N)$ are all m-fold combinations within the set of N numbers, the number of which is given by $\binom{N}{m}$. We now look at the first terms in two of the above expressions:

$$|\sqrt{N}\beta\rangle_{\mathbf{K},coh} = e^{-N|\beta|^2/2}(1 + \beta\sum_i e^{i\mathbf{K}\mathbf{r}_i}\sigma_{hg}^{(i)} + \beta^2\sum_{ij} e^{i\mathbf{K}(\mathbf{r}_i+\mathbf{r}_j)}\sigma_{hg}^{(i)}\sigma_{hg}^{(j)} + \dots)|0\rangle \quad \text{(A.32)}$$

$$|\sqrt{N}\beta\rangle_{\mathbf{K},sep} = (1+|\beta|^2)^{-N/2}(1+\beta\sum_i e^{i\mathbf{K}\mathbf{r}_i}\sigma_{hg}^{(i)} + \beta^2\sum_{i\neq j} e^{i\mathbf{K}(\mathbf{r}_i+\mathbf{r}_j)}\sigma_{hg}^{(i)}\sigma_{hg}^{(j)} + \dots)|0\rangle \quad \text{(A.33)}$$

The apparent difference is that the second expression the sum disregards all elements (atoms) with same indexes, while in the first expression the sums take all the elements. We observe however that $\sigma_{hg}^{(i)}\sigma_{hg}^{(i)} = 0$, so the sums actually yield the same result. This causes problem with normalization of $|\beta\rangle_{\mathbf{K},coh}$, but a look at expansions of the two normalizations constants reveals that each term matches in the leading order of the atom number $N \gg 1$:

$$e^{-N|\beta|^2/2} = 1 - \frac{|\beta|^2 N}{2} + \frac{|\beta|^4 N^2}{8} - \frac{|\beta|^6 N^3}{48} + \dots \quad \text{(A.34)}$$

$$(1+|\beta|^2)^{-N/2} = 1 - \frac{|\beta|^2 N}{2} + |\beta|^4\left(\frac{N^2}{8} + \frac{N}{4}\right) - |\beta|^6\left(\frac{N^3}{48} + \frac{N^2}{8} + \frac{N}{6}\right) + \dots \quad \text{(A.35)}$$

Note however that each of the terms in the above expansions is not necessarily small. Regardless, this proves that the both states are normalized and in fact $|\beta\rangle_{\mathbf{K},sep} = |\beta\rangle_{\mathbf{K},coh}$. The above correspondence provides valuable information about the noise characteristics in atomic measurement. In particular, in the measurement of the total number of excitations $N|\beta|^2$ the relative noise scales as $\frac{1}{\sqrt{N}|\beta|}$, which exposes the *atomic projection noise*, the variance of which is clearly proportional the the number of atoms N.

A.9 Solving coupled equations

Let us now bring together quantum optics of photons along with the quantum optics of spin waves. As we have seen, the interaction of the atomic coherence is described by a set of coupled equations. In Sec 2.1.2 we have been able to quantize the optical field in terms of its slowly varying amplitude. Quantization for the atomic coherence is even simpler - instead of writing the equations for the evolution of the coherence, we express them in terms of related operators - in the Heisenberg picture - for each atom. The equations must yield the same result in terms of expectation values. Thus, a coherence of the type $B = \sqrt{n}\rho_{hg}$ is replaced by a spin wave operator $\hat{B}$.

This section will provide solutions of the coupled equations for write and read processes in a simplified, one-dimensional scenario. First we consider the process in which A_2 is the classical, coupling field. At this point we will also rewrite the equations into the one-dimensional form, in order to obtain the simplest possible result. We disregard the diffraction terms and replace the operators with their one-dimensional counterparts as. Via this transformation the atomic density n becomes a linear density. The equations for operators become:

$$\frac{\partial \hat{A}_1}{\partial z} = -\frac{ik_1}{\epsilon_0 \hbar}\sqrt{n} d_{ge} \frac{d_{eh} A_2}{2\Delta} e^{i(k_2-k_1)z} \hat{B}, \tag{A.36}$$

$$\frac{\partial \hat{B}}{\partial t} = -\sqrt{n} \frac{d_{he} A_2^* / \hbar^2 e^{i(k_1-k_2)z}}{4i\Delta} d_{eg} \hat{A}_1. \tag{A.37}$$

Note that in general our approach here is quite orthogonal the the Hamiltonian approach [Chr16a], which poses problems with proper treatment of propagation. In the wave-equations approach [Mit09], proper treatment of propagation as well as proper setting of coupling constants is natural, thanks to the direct classical correspondence.

The can be easily solved formally, or rather transformed into the integral form. However, this form also leads directly to a first-order perturbative solution, in which the operator under integral is taken before the interaction, which is at $t = 0$ for $\hat{B}$ and $z = 0$ for $\hat{A}$. We will assume the atom number density is spatially uniform and extends to infinity in the transverse dimension, the interaction takes a total time of T along the ensemble of length L and the coupling field intensity does not change in time. The first-order solution is then:

$$\hat{A}_1(L,t) = \hat{A}_1(z=0,t) - \int_0^L \mathrm{d}z \frac{ik_1}{\epsilon_0 \hbar}\sqrt{n} d_{ge} \frac{d_{eh} A_2}{2\Delta} e^{i(k_2-k_1)z} \hat{B}(z, t=0) \tag{A.38}$$

$$\hat{B}(z,T) = \hat{B}(z,t=0) - \int_0^T \mathrm{d}t \sqrt{n} \frac{d_{he} A_2^* / \hbar^2 e^{i(k_1-k_2)z}}{4i\Delta} d_{eg} \hat{A}_1(z=0,t) \tag{A.39}$$

Finally, the solution can be re-normalized and integrated, which allows expressing it in terms of discrete operators of photons and spin waves:

$$\begin{aligned}\underbrace{\int_0^T c\mathrm{d}t\left(-i\sqrt{\frac{\epsilon_0}{2\hbar\omega_1}}\frac{1}{\sqrt{cT}}\hat{A}_1(L,t)\right)}_{\hat{a}_{\mathrm{out}}} &= \underbrace{\int_0^T c\mathrm{d}t\left(-i\sqrt{\frac{\epsilon_0}{2\hbar\omega_1}}\frac{1}{\sqrt{cT}}\hat{A}_1(z=0,t)\right)}_{\hat{a}_{\mathrm{in}}} - \\ &- cT\sqrt{n}\frac{\sqrt{\epsilon_0}A_2 d_{ge}d_{eh}}{2\sqrt{2\hbar\omega_1 c}\Delta\hbar^2}\frac{\sqrt{L}}{\sqrt{cT}}\underbrace{\int_0^L \mathrm{d}z\frac{1}{\sqrt{L}}e^{i(k_2-k_1)z}\hat{B}(z,t=0)}_{\hat{b}_{\mathrm{in}}}\end{aligned} \tag{A.40}$$

$$\begin{aligned}\underbrace{\int_0^L \mathrm{d}z\frac{1}{\sqrt{L}}e^{i(k_2-k_1)z}\hat{B}(z,T)}_{\hat{b}_{\mathrm{out}}} &= \underbrace{\int_0^L \mathrm{d}z\frac{1}{\sqrt{L}}e^{i(k_2-k_1)z}\hat{B}(z,t=0)}_{\hat{b}_{\mathrm{in}}} + \\ &+ L\sqrt{n}\frac{\sqrt{\epsilon_0}A_2^* d_{eg}d_{he}}{2\sqrt{2\hbar\omega_1}\Delta\hbar^2}\frac{\sqrt{cT}}{c\sqrt{L}}\underbrace{\int_0^T c\mathrm{d}t\left(-i\sqrt{\frac{\epsilon_0}{2\hbar\omega_1}}\frac{1}{\sqrt{T}}\hat{A}_1(z=0,t)\right)}_{\hat{a}_{\mathrm{in}}}\end{aligned} \tag{A.41}$$

Remarkably, the coupling coefficients are the same in both of the two above equations. In particular, the coupling is constant can be written as:

$$\mathcal{G} = -\frac{\sqrt{\epsilon_0}A_2^* d_{eg}d_{he}}{2\sqrt{2\hbar\omega_1 c}\Delta\hbar^2}\sqrt{nLT}. \tag{A.42}$$

Note that the total number of atoms is $N = nL$. We may now write the above expression as a Bogoliubow transformation or an “IN-OUT” relation:

$$\begin{pmatrix}\hat{a}_{out}\\ \hat{b}_{out}\end{pmatrix} = \begin{pmatrix}1 & -\mathcal{G}\\ \mathcal{G}^* & 1\end{pmatrix}\begin{pmatrix}\hat{a}_{in}\\ \hat{b}_{in}\end{pmatrix}. \tag{A.43}$$

Since we assumed only first-order solution and thus $\mathcal{G}$ is implicitly small, the above transformation is a nearly unitary beamsplitter transformation. In practice it is feasible to replace 1 on the diagonal with $\sqrt{1-|\mathcal{G}|^2}$ to make the transformation purely unitary.

The above results clearly demonstrates the the interaction realizes a beamsplitter between light and atoms. Both light can be mapped onto the atomic coherence field (an operation which we will call “write-in”), and the spin waves can be mapped back onto light (“read-out”). Furthermore, a particular mode of atomic coherence is coupled to light. It is a spin wave with a mode function $\frac{1}{\sqrt{L}}e^{i(k_2-k_1)z}$. If we consider a different spin wave with a differing wavevector, it will interact with the light field weakly, with the coupling constant $\mathcal{G}$ multiplied by an overlap between the two mode functions. Such spin wave will then mostly remain in the memory during read-out.

Now we will perform a analogous procedure taking the A_1 field to be the coupling field and by $\hat{A}_2$ we will denote the quantum field. The two equation are:

$$\frac{\partial \hat{A}_2}{\partial z} = -\frac{ik_2}{\epsilon_0 \hbar}\sqrt{n} d_{he} \frac{d_{eg} A_1}{2(\Delta+\delta)} e^{i(k_1-k_2)z} \hat{B}^\dagger, \tag{A.44}$$

$$\frac{\partial \hat{B}}{\partial t} = -\sqrt{n} \frac{d_{eg} A_1/\hbar^2 e^{i(k_1-k_2)z}}{4i(\Delta+\delta)} d_{he} \hat{A}_2^\dagger. \tag{A.45}$$

We can first obtain the first-order solution:

$$\hat{A}_2(L,t) = \hat{A}_2(z=0,t) - \int_0^L \mathrm{d}z \frac{ik_2}{\epsilon_0 \hbar}\sqrt{n} d_{he} \frac{d_{eg} A_1}{2(\Delta+\delta)} e^{i(k_1-k_2)z} \hat{B}^\dagger(z,t=0) \tag{A.46}$$

$$\hat{B}(z,T) = \hat{B}(z,t=0) - \int_0^T \mathrm{d}t \sqrt{n} \frac{d_{eg} A_1/\hbar^2 e^{i(k_1-k_2)z}}{4i(\Delta+\delta)} d_{he} \hat{A}_2^\dagger(z=0,t) \tag{A.47}$$

Performing the analogous procedure we obtain the input-output relation:

$$\hat{a}_{out} = \hat{a}_{in} + \mathcal{G}\hat{b}_{in}^\dagger \tag{A.48}$$

$$\hat{b}_{out} = \hat{b}_{in} + \mathcal{G}\hat{a}_{in}^\dagger \tag{A.49}$$

with $\mathcal{G} = -\frac{\sqrt{\epsilon_0} A_1 d_{eg} d_{he}}{2\sqrt{2\hbar\omega_2 c}(\Delta+\delta)\hbar^2}\sqrt{nLT}$. This very distinct Bogoliubov transformation mixes operators and their hermitian conjugates, and as we have already shown corresponds to two mode squeezing. Here, it is customary to write $\mathcal{G} = \sinh\xi$, where ξ is the squeezing parameter. Here we see that the interaction produces pairs of photons and spin waves, and that the spin waves that are created in the atomic ensemble have the same mode function $\frac{1}{\sqrt{L}} e^{i(k_2-k_1)z}$ as in the case of beamsplitter.

A.10 Coupled equations and phase matching

Here we will consider the full 3D+1 scenario with diffraction, where the interaction will occur in a Gaussian-shape cloud of atoms. However, we will still neglect atomic dispersion and losses. We will also always assume $\delta = 0$ for simplicity and neglect any decoherence, effectively setting $\Gamma = \gamma = 0$ and disregarding power broadening. Finally, by $s_n(k_x, k_y, z)$ we will denote the square root of atomic density expressed in the transverse-Fourier domain as:

$$s_n(k_x, k_y, z) = \frac{1}{2\pi} \int \mathrm{d}x\mathrm{d}y \sqrt{n(x,y,z)} e^{-ik_x x - ik_y y} \tag{A.50}$$

A.10.1 Read interaction

Let us first consider the case previously depicted in Fig. 2.5(a), where the weak field now described by the $\hat{A}_r$ operator will interact with the atomic coherence $\hat{B}$ with the help of a strong coupling field A_R. Since this interaction will feature an exchange between the optical and atomic field, we will call it the read interaction, and denote the weak optical field by $\hat{A}_r$ and the strong drive field by A_R. The quantized amplitude then evolves as follows:

$$\frac{\partial \hat{A}_r}{\partial z} - i(\sqrt{k_r^2 - k_x^2 - k_y^2} - k_r)\hat{A}_r = -\frac{ik_r}{\epsilon_0 \hbar} d_{ge} \frac{d_{eh} A_R}{2\Delta} e^{i(k_R - k_r)z} \frac{s_n * \hat{B}}{2\pi}, \tag{A.51}$$

where the two-dimensional convolution in the k_x, k_y variables is denoted by $*$. The terms on the LHS correspond to propagation and diffraction, while RHS describes the interaction with the spin wave. The basis for this equation is Eq. 2.92 with the full diffraction term included. We may expect that only spin waves with the spatial dependence compensating this term will contribute to the interaction, as otherwise fast spatial oscillation will be averaged out. Simultaneously, the collective spin-wave coherence obeys a coupled equation:

$$\frac{\partial \hat{B}}{\partial t} = -\frac{d_{he} A_R^* / \hbar^2 e^{i(k_r - k_R)z}}{4i\Delta} d_{eg} \frac{s_n * \hat{A}_1}{2\pi}. \tag{A.52}$$

To simplify the situation we first substitute the optical field by:

$$\hat{A}_r = \hat{\hat{A}}_r e^{i(\sqrt{k_r^2 - k_x^2 - k_y^2} - k_r)z}, \tag{A.53}$$

where $\hat{\hat{A}}_r$ is a new operator with intrinsic time and space dependencies. For a homogenous equation constant $\hat{\hat{A}}_r$ yields a complete solution. Here, we substitute it the full inhomogeneous equation A.51 to obtain a simplified form:

$$\frac{\partial \hat{\hat{A}}_r}{\partial z} = -\frac{ik_r}{\epsilon_0 \hbar} d_{ge} \frac{d_{eh} A_R}{2\Delta} e^{i(k_R - k_r)z} e^{-i(\sqrt{k_r^2 - k_x^2 - k_y^2} - k_r)z} \frac{s_n * \hat{B}}{2\pi}, \tag{A.54}$$

The first-order solution in the coupling strength (proportional to A_R) for $\hat{A}_r$, disregarding a global phase factor of $e^{-i(\sqrt{k_1^2 - k_x^2 - k_y^2} - k_1)L}$, where $L \to \infty$ would be a total length of the atomic ensemble[6], reads:

$$\hat{A}_r(k_x, k_y, z = \infty, t) = \hat{A}_r(k_x, k_y, z = -\infty, t) - \int_{-\infty}^{\infty} \mathrm{d}z \frac{ik_r}{\epsilon_0 \hbar} d_{ge} \frac{d_{eh} A_R}{2\Delta} e^{i(k_R - \sqrt{k_r^2 - k_x^2 - k_y^2})z} \frac{(s_n * \hat{B})(k_x, k_y, z, t = 0)}{2\pi} \tag{A.55}$$

$$\hat{B}(k_x, k_y, z, T) = \hat{B}(k_x, k_y, z, t = 0) - \int_{0}^{T} \mathrm{d}t \frac{d_{he} A_R^* / \hbar^2 e^{i(k_R - \sqrt{k_r^2 - k_x^2 - k_y^2})z}}{4i\Delta} d_{eg} \frac{(s_n * \hat{A}_r|_{z=0})(k_x, k_y, z, t)}{2\pi} \tag{A.56}$$

These two equations show that part of the atomic coherence is mapped onto the optical field, and vice versa. Furthermore, there is a "blur" associated with finite extent of the atomic ensemble, here emerging as a convolution with s_n. In Appendix A.9 we show that in a slightly simplified case this interaction may be considered a simple beamsplitter on discrete modes.

Here, for illustration, let us consider read-out of a coherent spin wave with expectation value $\langle \hat{B} \rangle = \sqrt{n} \beta e^{i\mathbf{Kr}}$ in position space. We take the Fourier transform of this dependence in the transverse momentum space to match our equation expressed in these coordinates, obtaining $\beta s_n(k_x - K_x, k_y - K_y, z) e^{iK_z z}$. To calculate how the spin wave is converted into the optical field, we take Eq. A.55 and plug in the expectation value instead of the $\hat{B}$ operator, obtaining:

$$\int_{-\infty}^{\infty} \mathrm{d}z \frac{ik_r}{\epsilon_0 \hbar} d_{ge} \frac{d_{eh} A_R}{2\Delta} e^{i(k_R - \sqrt{k_r^2 - k_x^2 - k_y^2} + K_z)z} \tilde{n}(k_x - K_x, k_y - K_y, z) \tag{A.57}$$

where $\tilde{n}$ is a Fourier-transformed atomic density, here arising due to the two-dimensional convolution of s_n from the expectation value and s_n from Eq. A.55, as $s_n * s_n = 2\pi \tilde{n}$. Most importantly, we observe that typically the output light amplitude takes on a transverse shape of the atomic ensemble, as witnessed by the $\tilde{n}$ term. To be precise, we should indicate that this shape is slightly modified due to the preceding phasor. We may, however, assume that the main factor contributing to the shape of output light beam is the atomic density, and that the phase changes very insignificantly over the peak momentum-space distribution of $\tilde{n}$ (the entire expression is thus peaked around K_x, K_y). We may thus replace most occurrences of k_x and k_y by K_x and K_y and single out the phase-matching factor to the total read-out efficiency by first writing the atom-number density as

---

[6] The term corresponds to free-space propagation and only changes the phase of the output light when we look at the far field. We assume that the curvature of this phase factor will be insignificant as long as we look at reasonable distances. Regardless, it will not impact the intensity that we actually measure.

$n = n_0 e^{-\frac{x^2+y^2}{2\sigma_\perp^2} - \frac{z^2}{2\sigma_z^2}}$, obtaining the integral in a simple form as the efficiency of phase matching:

$$\eta_{\mathrm{phm}}(K_x, K_y, K_z) = \left| \int_{-\infty}^{\infty} \mathrm{d}z e^{i(k_R - \sqrt{k_r^2 - K_x^2 - K_y^2} + K_z)z - \frac{z^2}{2\sigma_z^2}} \right|^2 . \tag{A.58}$$

On the other hand, in some infrequent cases (see for example Ref. [LPW17a]), if phase matching changes significantly over the range of considered emission angles (which could correspond to an ensemble of very small transverse size or a very narrow phase-matching condition), full expression as in Eq. A.57 still needs to be considered and subsequently integrated to obtain η_{phm}.

These results allow us to draw important conclusions. During read-out, a spin wave with a transverse wavevector $\mathbf{K}_\perp$ is converted into a photon with a transverse mode amplitude determined by the shape of the atomic ensemble and a central wavevector of:

$$\mathbf{k}_{r\perp} = \mathbf{K}_\perp . \tag{A.59}$$

For the read-out process to be maximally efficient, the wavevector of the spin wave should also satisfy the relation:

$$\Delta K_z = k_R - \sqrt{k_r^2 - K_x^2 - K_y^2} + K_z = 0 \tag{A.60}$$

We illustrate this relation in a two-dimensional $(K_x,\ K_z)$ space of spin waves in Fig. 2.6(a). The spin waves that can be retrieved efficiently form a circle. Importantly, these are also the spin waves that can be created with the particular coupling field considered. Together, Eqs. A.59 and A.60 constitute the law of momentum conservation for photons and spin waves.

A.10.2 Write interaction

As in Sec. 2.3.1, the second scenario incorporate A_1 as the strong field, which we call A_W and A_2 as the weak quantum field to which we associate the operator $\hat{A}_w$. The equations of evolution are derived accordingly. Here, we just give the result in the first order:

$$\begin{aligned} &\hat{A}_w(k_x, k_y, z = \infty, t) = \hat{A}_w(k_x, k_y, z = -\infty, t) - \\ &\int_{-\infty}^{\infty} \mathrm{d}z \frac{ik_w}{\epsilon_0 \hbar} d_{eg} \frac{d_{he} A_W}{2\Delta} e^{i(k_W - \sqrt{k_w^2 - k_x^2 - k_y^2})z} \frac{(s_n * \hat{B}^\dagger)(-k_x, -k_y, z, t = 0)}{2\pi} \end{aligned} \tag{A.61}$$

$$\hat{B}(k_x,k_y,z,T)=\hat{B}(k_x,k_y,z,t=0)- \int_0^T \mathrm{d}t \frac{d_{eg}A_W/\hbar^2 e^{i(k_W-\sqrt{k_w^2-k_x^2-k_y^2})z}}{4i\Delta} d_{he}\frac{(s_n * \hat{A}_w^\dagger|_{z=0})(-k_x,-k_y,z,t)}{2\pi} \tag{A.62}$$

As in the read interaction, we may give the simple interpretation. In Sec. 2.1.2 (Eqs. 2.22 and 2.23) we have seen that if an operator transformation involves such particular mixing of creation and annihilation operators, the resulting interaction is two-mode squeezing. Thus, pairs of photons and atomic excitations are created. In Appendix A.9 we also show that in a simplified scenario the interaction is purely a two-mode squeezing in terms of discrete operators.

Here, we will concentrate on spatial properties and thus the wavevectors involved. Assuming a very wide ensemble, we see that here a coherence with a transverse wavevector $\mathbf{K}_x$, $\mathbf{K}_y$ will couple with an optical field with wavevector $-\mathbf{k}_x$, $-\mathbf{k}_y$, so that we have:

$$\mathbf{k}_{w\perp}=-\mathbf{K}_\perp. \tag{A.63}$$

This can be seen by examining the argument of operators in RHS of Eqs. A.61 and A.62. Mathematically, this inverse situation (minus instead of plus) stems from the fact that taking the Fourier transform of a Hermitian conjugate produces a conjugate operator taken at minus argument. Physically, the interaction is only effective if we have:

$$\Delta K_z = k_W-\sqrt{k_w^2-K_x^2-K_y^2}-K_z=0, \tag{A.64}$$

which together with Eq. A.63 again constitutes the law of momentum conservation. This can be checked with a coherent spin wave plugged in into Eqs. A.61 and A.62. Only spin wave with a proper wavevector will be then parametrically amplified in the interaction. The spin waves created in the two-mode squeezing interaction are portrayed in Fig. 2.6(b).

In both cases (read and write) it is often assumed that phase matching is perfectly satisfied, and the conservation laws supplemented by the wavevectors of coupling beams are written as:

$$\boxed{\mathbf{k}_r=\mathbf{k}_R+\mathbf{K},} \tag{A.65}$$

$$\boxed{\mathbf{k}_w=\mathbf{k}_W-\mathbf{K}.} \tag{A.66}$$

This simple form helps with many practical considerations.

In particular, if we register a photon with a transverse wavevector $\mathbf{k}_{w\perp}$, the associated spin wave state is given by $\hat{b}_{\mathbf{K}}^\dagger|0\rangle$ with $\mathbf{K}=\mathbf{k}_W-\mathbf{k}_w$ and the spin-wave mode function as in Eq. 2.113.

The framework introduced here allows drawing many more conclusions. In particular, if we consider the subsequent write and read process, we may obtain a direct form of the biphoton wavefunction, as will be presented in Appendix A.11.1.

A.11 The full process: correlation functions for photons

At last, let us join two types of interaction and calculate the spatial correlation function for two emerging photons. Assume that we first perform squeezing from time $t=0$ to $t=T$ and then from $t=T$ to $t=2T$ we read-out the spin wave. Let us denote the subsequent fields in the squeezing process as A_W for the strong coupling field, A_w for Stokes field, and in the beamsplitter interaction A_R for read-out coupling field, and A_r for read-out, anti-Stokes photons.

$$\begin{aligned}\hat{A}_w(k_x,k_y,z=\infty,t)&=\hat{A}_w(k_x,k_y,z=-\infty,t)-\\ &\int_{-\infty}^{\infty}\mathrm{d}z\frac{ik_w}{\epsilon_0\hbar}d_{eg}\frac{d_{he}A_W}{2(\Delta_w+\delta_w)}e^{i(k_W-\sqrt{k_w^2-k_x^2-k_y^2})z}\frac{(s_n*\hat{B}^\dagger)(-k_x,-k_y,z,t=0)}{\sqrt{2\pi}}\end{aligned} \tag{A.67}$$

$$\begin{aligned}\hat{B}(k_x,k_y,z,T)&=\hat{B}(k_x,k_y,z,t=0)-\\ &\int_0^T\mathrm{d}t\frac{d_{eg}A_W/\hbar^2e^{i(k_W-\sqrt{k_w^2-k_x^2-k_y^2})z}}{4i(\Delta_w+\delta_w)}d_{he}\frac{(s_n*\hat{A}_w^\dagger)(-k_x,-k_y,z=0,t)}{\sqrt{2\pi}}\end{aligned} \tag{A.68}$$

The result for $\hat{B}$ is then plugged in into the expression for read-out field:

$$\begin{aligned}\hat{A}_r(k_x,k_y,z=\infty,t+T)&=\hat{A}_r(k_x,k_y,z=-\infty,t+T)-\\ &\int_{-\infty}^{\infty}\mathrm{d}z\frac{ik_r}{\epsilon_0\hbar}d_{ge}\frac{d_{eh}A_R}{2\Delta_r}e^{i(k_R-\sqrt{k_r^2-k_x^2-k_y^2})z}\frac{(s_n*\hat{B})(k_x,k_y,z,t=T)}{\sqrt{2\pi}}\end{aligned} \tag{A.69}$$

A.11.1 First order correlations

We are interested in an expectation value of time integrated operators:

$$\hat{a}_w(k_x,k_y)=-i\sqrt{\frac{c\epsilon_0}{2\hbar\omega_wT}}\int_0^T\mathrm{d}t\hat{A}_w(k_x,k_y,z=\infty,t), \tag{A.70}$$

$$\hat{a}_r(k_x,k_y)=-i\sqrt{\frac{c\epsilon_0}{2\hbar\omega_rT}}\int_0^T c\mathrm{d}t\hat{A}_r(k_x,k_y,z=\infty,t+T) \tag{A.71}$$

of type $\langle\hat{a}_r(k_x,k_y)\hat{a}_w(k'_x,k'_y)\rangle$. In calculation of such expectation value on the initial vacuum state most terms vanish except those that are anti-normally ordered.

In our case it will be the spin-wave operator $\hat{B}$, that yields:

$$(s_n * \hat{B})(k_x, k_y, z)(s_n * \hat{B}^\dagger)(-k'_x, -k'_y, z') = 2\pi\tilde{n}(k_x + k'_x, k_y + k'_y, z)\delta(z - z') \tag{A.72}$$

The final correlation function can be written as:

$$\langle \hat{a}_r(k_x, k_y)\hat{a}_w(k'_x, k'_y)\rangle = c|d_{he}|^2|d_{ge}|^2 \frac{A_R A_W}{4\Delta_r(\Delta_w + \delta_w)} \frac{k_r k_w}{\epsilon_0^2 \hbar^2} \frac{\epsilon_0}{2\hbar\sqrt{\omega_r \omega_w}} \times$$
$$\int_{-\infty}^{\infty} \mathrm{d}z \tilde{n}(k_x + k'_x, k_y + k'_y, z) e^{i(k_R - \sqrt{k_r^2 - k_x^2 - k_y^2} + k_W - \sqrt{k_w^2 - k_x'^2 - k_y'^2})z} \propto \Psi(\mathbf{k}_\perp, \mathbf{k}'_\perp) \tag{A.73}$$

This correlation function has the unique property of being proportional, by definition, to the biphoton wave function $\Psi(\mathbf{k}_\perp, \mathbf{k}'_\perp)$. In the low photon-number regime we simply write the state of the field as:

$$|\Psi\rangle = (1 + \epsilon \int \mathrm{d}\mathbf{k}_\perp \mathrm{d}\mathbf{k}'_\perp \Psi(\mathbf{k}_\perp, \mathbf{k}'_\perp) \hat{a}_r^\dagger(\mathbf{k}_\perp) \hat{a}_w^\dagger(\mathbf{k}'_\perp))|0\rangle, \tag{A.74}$$

where $\epsilon \ll 1$. The essential property of the wave function is that it the photons are *anti-correlated* in momenta and the width of this correlation function is determined by the transverse shape of the atomic cloud. By these virtues, it relates to the number of modes by the Schmidt decomposition as proposed by Rzążewski, Law and Eberly. Furthermore, we will see that in typical experimental scenarios the second-order correlation function will be roughly proportional to the absolute value squared of this function, which will allow us to estimate the number of modes.

A.12 Holstein-Primakoff transformation

An alternative understanding to the Holstein-Primakoff approximation is to introduce a proper transformation we operators. In the main text we used a naive approach in which we define spin-wave operators and later just find that they are "nearly" bosonic. Here we will introduce the description of a collective state of many atoms. Let us define a collective spin operator for an ensemble of N atoms:

$$\hat{\mathbf{S}} = \sum_i^N \hat{\mathbf{S}}^{(i)} \tag{A.75}$$

where $\hat{\mathbf{S}}^{(i)} = (\hat{\sigma}_x^{(i)}, \hat{\sigma}_y^{(i)}, \hat{\sigma}_z^{(i)})$ is a spin operator for the i-th atoms (and unity operation for all other atoms) with $\hat{\sigma}_i$ begin the Pauli matrix operators for our two-level system. In this system the spin excitations and be added or subtracted via the ladder operators $\hat{S}_\pm = \hat{S}_x \pm i\hat{S}_y$. These operators satisfy commutation relation:

$$[\hat{S}_+, \hat{S}_-] = 2\hat{S}_z \tag{A.76}$$

Holstein and Primakoff [HP40] have proposed to introduce a new operator $\hat{b}$ which we will call a spin-wave operator, that would satisfy a bosonic commutation relation $[\hat{b}, \hat{b}^\dagger] = 1$. This operator satisfies the following relations:

$$\hat{S}_+ = \sqrt{2N}\sqrt{1 - \frac{\hat{b}^\dagger\hat{b}}{2N}}\hat{b} \approx \sqrt{2N}\hat{b}, \tag{A.77}$$

$$\hat{S}_+ = \sqrt{2N}\hat{b}^\dagger\sqrt{1 - \frac{\hat{b}^\dagger\hat{b}}{2N}} \approx \sqrt{2N}\hat{b}^\dagger, \tag{A.78}$$

$$\hat{S}_z = N - \hat{b}^\dagger\hat{b} \approx N \tag{A.79}$$

Where the approximation is made in the limit $N \gg 1$. In this limit we may explicitly write the spin wave operators as

$$\hat{b}^\dagger \approx \frac{1}{\sqrt{N}}\sum_i^N \hat{\sigma}_{hg}^{(i)}, \tag{A.80}$$

$$\hat{b} \approx \frac{1}{\sqrt{N}}\sum_i^N \hat{\sigma}_{gh}^{(i)}, \tag{A.81}$$

which reproduces our original definitions.

Appendix B

The *photonpacket*

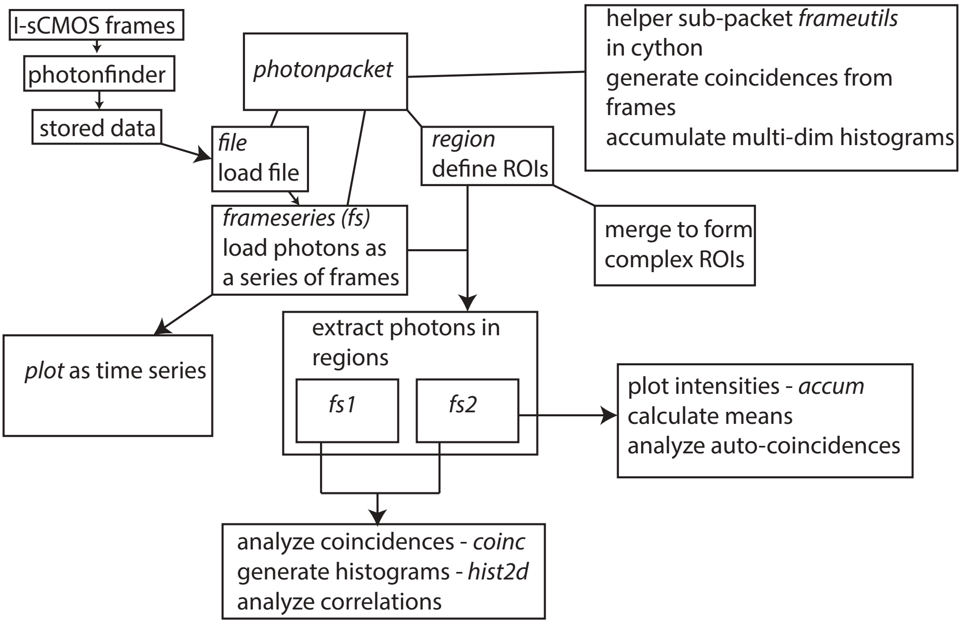

FIGURE B.1: A diagram of workflow and dataflow within the *photonpacket* for analysing data from the I-sCMOS camera.

Here we present a sample code using the *photonpacket* software I developed. The program below loads data accumulated with I-sCMOS and makes a very simple analysis. It is intended to be run with Spyder.

Figure B.1 also presents the typical workflow of the software in terms of classes used. Documentation can also be found at `http://www.fuw.edu.pl/~mparniak/photonpacket/`.

Potential applications of this software, after some tweaking, will also extend to purely one-dimensional data obtained from 1D arrays of APDs (x), purely temporal data, two-dimensional $x-t$ data from such arrays, or even three-dimensional $x-y-t$ data from devices such as the TimepixCam or PImMS cameras [FLN16; Bro08].

```
from matplotlib import pyplot as plt
import numpy as np
import photonpacket as pp
#%% load data
Nframes=100000
filename = 'mydata.dat'
f=pp.file.read(filename,Nframes=Nframes)
fs=f.getframeseries()
#%% define regions (ROIs)
c1 = pp.square(80,(112,162))
c2 = pp.square(80,(118,557))
#%% plot regions and total accumulated photons
d=fs.accumframes()
plt.clf()
plt.imshow(d)
c1.plot()
c2.plot()
plt.show()
#%% filter frameseries by ROIs
fs1 = c1.getframeseries(fs, reshape=True)
fs2 = c2.getframeseries(fs, reshape=True)
#%% accumulate coincidences/plot maps
dcoinc=pp.accum.accumcoinc2d(fs1,fs2,axis=1)
dacoinc=pp.accum.acccoinc(fs1.accumframes(),
        fs2.accumframes(), axis=1)/Nframes
subscoinc=dcoinc-dacoinc
plt.imshow(subscoinc)
#%% calculate total g2, plot 2D-histogram
print pp.stat2d.g2(fs1,fs2,uncert=True)
h=pp.hist2d.fromfs(fs1,fs2)
h.plot(showvalues=True)
```

Appendix C

Ac-Stark control of hyperfine coherence

Selection of detunings and laser power is essential for proper ac-Stark shift based control of hyperfine coherence at the single-excitation level. We found that the optimal setting is to red-detune the ac-Stark laser by $\delta_S/2\pi = 0.5$–3.0 GHz from the "empty" state $|h\rangle$ (here we calculate the detuning from $5^2S_{1/2}F = 2 \rightarrow 5^2P_{3/2}$ transition centroid, lying 193.7 MHz below the $F = 2 \rightarrow F = 3$ transition), so the energy shift of the $|h\rangle$ state is much larger than for the $|g\rangle$ state. While this causes some scattering from the $|h\rangle$ state, we avoid exciting atoms from the $|g\rangle$, which could generate spurious spin-wave excitations that would later be retrieved as noise. Furthermore, by making the ac-Stark light z-polarized (π polarization), we ensure that $|h\rangle$ is an eigenstate of the effective ac-Stark shift Hamiltonian. Note that this setting is very different from the proposal of *Sparkes et al.* [Spa10] who considered much larger detunings. In their setting, the ac-Stark light is coupled to $|g\rangle$ and $|h\rangle$ with nearly the same strength and the differential phase shift only appears when circular polarizations are used and in only several specific spin-wave magnetic configurations. Such an operation requires multi-watt power levels to obtain reasonable differential ac-Stark shifts. Furthermore, while the scattering rate would be indeed small, the noise generation rate has not been considered and could become a significant problem.

To evaluate the above predictions we model the full behaviour of the multi-level atom described by a density matrix ρ subject to an off-resonant ac-Stark field, using the framework described by Eq. 2.46. First we prepare a spin-wave state as $(|g\rangle + \epsilon|h\rangle)/\sqrt{1+\varepsilon^2}$ (with $\varepsilon \ll 1$) and track the behaviour of the atomic state in the subspace spanned by $|h\rangle$ and $|g\rangle$. The relative phase is calculated as $\varphi = \mathrm{Arg}(\rho_{hg})$ and the ac-Stark shift as $\Delta_S = \left.\frac{\mathrm{d}\varphi}{\mathrm{d}t}\right|_{t=0}$. The scattering rate $\Gamma_S = -\varepsilon^{-2} \left.\frac{\mathrm{d}\rho_{hh}}{\mathrm{d}t}\right|_{t=0}$ quantifies decay of the spin-wave population. For the noise rate Γ_n we take an atom prepared in a pure $|g\rangle$ state and we again calculate the rate as $\Gamma_n = \left.\frac{\mathrm{d}\rho_{hh}(\varepsilon=0)}{\mathrm{d}t}\right|_{t=0}$. The results are plotted in Fig. C.1 as a function of ac-

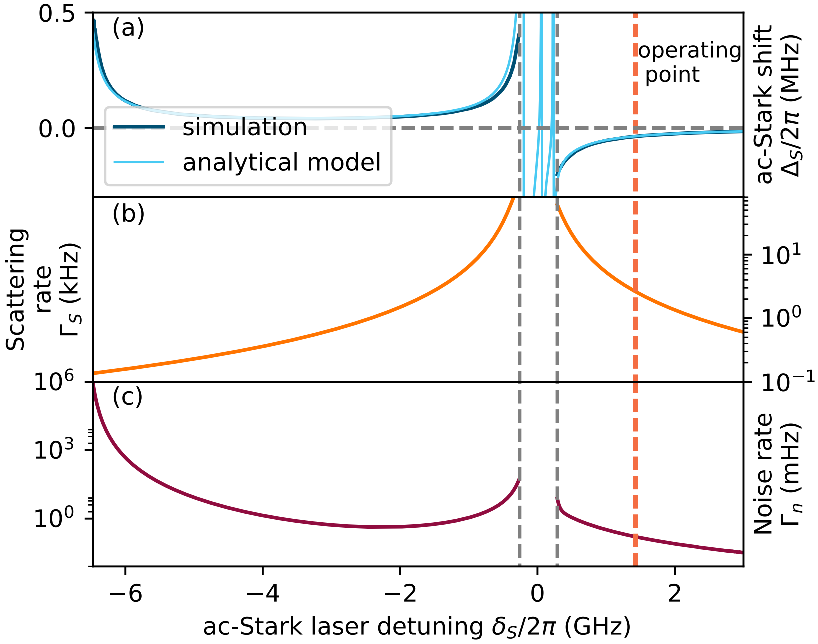

FIGURE C.1: Properties of the ac-Stark modulation. Panel (a) depicts the differential ac-Stark shift for the Rabi frequency of the ac-Stark beam equal with an intensity of 35 mW/cm^2, as a function of ac-Stark laser detuning δ_S from the $5^2S_{1/2}F = 2 \rightarrow 5^2P_{3/2}$ transition centroid. Both the simulation and the simplified analytical model are presented. A small deviation between the two can be noticed only close to resonance, as decoherence is not taken into account in the simplified model. Panels (b) and (c) portray incoherent scattering rate (decoherence rate) of spin-waves and generation rate of spurious excitations, respectively. The values are not plotted very close to the absorption resonance due to very high incoherent scattering rendering this region useless for the purpose of ac-Stark modulation.

Stark laser detuning δ_S. We find the differential splitting $\Delta_S/2\pi = -0.036$ MHz for the operation point at $\delta_S/2\pi = 1.43$ GHz and with approx. 40 mW of average power corresponding to an intensity of 35 mW/cm^2. Our experimental setup facilitates a peak power of 100 mW.

We can elucidate on these results by introducing a simple analytical model where we include all transitions via which the ac-Stark shift is induced in the far-detuned regime. The shifts of the two ground-state levels are:

$$\Delta_S^{(|g\rangle)} = \frac{|\mathcal{E}_S d|^2}{4\hbar}\left(\frac{5}{24}\frac{1}{\delta_S + \frac{5}{4}A_{0,1/2} - \frac{11}{4}A_{1,3/2}} + \frac{1}{8}\frac{1}{\delta_S + \frac{5}{4}A_{0,1/2} - \frac{3}{4}A_{1,3/2}}\right) \quad \text{(C.1)}$$

$$\Delta_S^{(|h\rangle)} = \frac{|\mathcal{E}_S d|^2}{4\hbar}\left(\frac{1}{40}\frac{1}{\delta_S - \frac{3}{4}A_{0,1/2} - \frac{1}{4}A_{1,3/2}} + \frac{1}{24}\frac{1}{\delta_S - \frac{3}{4}A_{0,1/2} - \frac{3}{4}A_{1,3/2}} + \frac{4}{15}\frac{1}{\delta_S - \frac{3}{4}A_{0,1/2} + \frac{9}{4}A_{1,3/2}}\right) \quad \text{(C.2)}$$

with $\mathcal{E}_S$ being the field of the ac-Stark beam, $d = 3.58 \times 10^{-29}$ Cm being the transition dipole matrix element for the D2 line, and $A_{0,1/2}/2\pi = 3.42$ GHz, $A_{1,3/2}/2\pi = 85$ MHz being the hyperfine coupling dipole constants.

The differential ac-Stark shift is calculated as:

$$\Delta_S = \Delta_S^{(|h\rangle)} - \Delta_S^{(|g\rangle)} \quad \text{(C.3)}$$

The field amplitude can be calculated as:

$$\mathcal{E}_S = \sqrt{\frac{2I_s}{c\epsilon_0}}. \quad \text{(C.4)}$$

In general, the detuning-independent factor thus becomes $I_S d^2/(2c\epsilon_0\hbar)$. The Rabi frequencies (for the specific power considered here) corresponding to subsequent transitions are: 13.0 MHz ($F = 1 \to F = 1$), 10.1 MHz ($F = 1 \to F = 2$), 4.5 MHz ($F = 2 \to F = 1$), 5.8 MHz ($F = 2 \to F = 2$) and 14.7 MHz ($F = 2 \to F = 3$). Due to detuning, only the latter three transition contribute significantly. This setting provides a total phase shift of $\varphi_S = \Delta_S T$ of the order of 0.45 rad with the manipulation time $T = 2$ μs. We find the scattering rate $\Gamma_s = 390$ Hz, which results in destruction of less than 0.1% of the spin waves due to incoherent excitation. Finally, we find a very little noise generation rate per atom $\Gamma_n = 1$ mHz (cf. with significantly higher noise rate when ac-Stark laser is tuned closer to the $|g\rangle$ state at $\delta_S/2\pi \approx -6.8$ GHz in Fig. C.1). If we assume that photons from these spurious excitations are scattered randomly during read-out to all far-field modes the number of which we estimate as $\sigma_z\sigma_\perp^2/\lambda^3 \approx 7 \times 10^8$ with $\sigma_z = 4$ mm, $\sigma_\perp = 0.3$ mm (longitudinal and transverse sizes of the ensemble, respectively), $\lambda = 795$ nm (wavelength of the read laser) and $N = 10^8$ (number of atoms), we estimate the probability of emitting a noise photon per mode of less than 3×10^{-10}, which is completely negligible compared with e.g. noise introduced by imperfect optical pumping.

Appendix D

Modeling the beamsplitter network

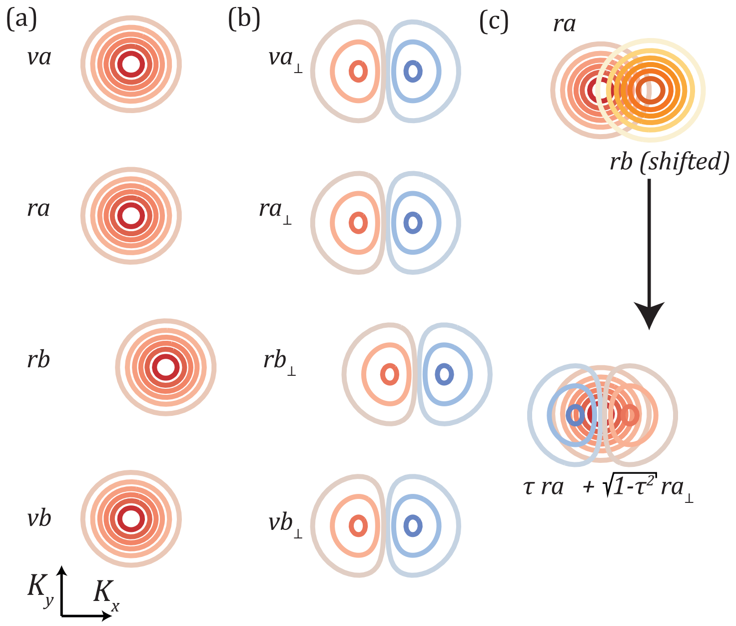

FIGURE D.1: Choice of wavevector-space basis for the beamsplitter network theoretical analysis: (a) proper modes ra and rb are selected in positions of the collection fibers, (b) orthogonal modes $ra_\perp$ and $rb_\perp$ are selected to allow construction of a shifted proper mode, as demonstrated in (c) where rb is constructed as a superposition of $ra_\perp$ and ra. The in top panel of (c) the ra mode is shown for reference, while the bottom panel of (c) shows two modes into which rb is decomposed. For small shifts ΔK_x the overlap $\tau \approx 1$ and the orthogonal modes are simply first Hermite-Gauss modes.

While in Fig. 6.8 the shapes of the presented theoretical curves roughly correspond to the shape of the fiber detection mode $u_\perp(\mathbf{K}_\perp)$ (in terms their widths and very roughly shapes), to properly describe these shapes as well as to obtain quantitative agreement of correlation functions a more elaborate model is required. We model the process in three steps: heralded generation, manipulation, read-out and detection that also adds noise during photons' detection. For the generation stage we assume a total of 8 pairs of squeezed modes: four of them correspond to read-out modes ra, rb, va and vb as denoted in Fig. 4 of the main text. They have associated write photon modes wa, wb that we detect, while the to other write photon modes are not detected. These modes are arranged in the K_y direction. In the K_x direction for each of these modes we also assume another pair of *orthogonal* modes ($ra_\perp$, $rb_\perp$, etc.), that are squeezed in the same way (these constitute another 4 mode pairs, yielding a total of 8). As we change mode positions in the K_x direction we assume that proper modes move accordingly (see Fig. D.1). During manipulation a three-way splitter operation is applied in the K_y direction, mixing modes with same K_x. The corresponding three-way splitter Bogoliubov transformation for modes ra, rb, va and vb is:

$$\mathrm{Tws}(vb, rb, ra, va) = \frac{1}{\sqrt{3}} \begin{pmatrix} 1 & 0 & 1 & 0 & 0 & 0 & 0 & 0 \\ 0 & 1 & 0 & 1 & 0 & 0 & 0 & 0 \\ -1 & 0 & 1 & 0 & 1 & 0 & 0 & 0 \\ 0 & -1 & 0 & 1 & 0 & 1 & 0 & 0 \\ 0 & 0 & -1 & 0 & 1 & 0 & 1 & 0 \\ 0 & 0 & 0 & -1 & 0 & 1 & 0 & 1 \\ 0 & 0 & 0 & 0 & -1 & 0 & 1 & 0 \\ 0 & 0 & 0 & 0 & 0 & -1 & 0 & 1 \end{pmatrix} \tag{D.1}$$

where subsequent rows correspond to operators: $\hat{b}_{vb}$, $\hat{b}^\dagger_{vb}$, $\hat{b}_{rb}$, $\hat{b}^\dagger_{rb}$, $\hat{b}_{ra}$, $\hat{b}^\dagger_{ra}$, $\hat{b}_{va}$, $\hat{b}^\dagger_{vb}$. However, if the modes are separated in the K_x direction we need to consider that for instance ra mixes both with rb and $rb_\perp$, as in the following beamsplitter transformation:

$$\mathrm{Bs}(rb, rb_\perp) = \begin{pmatrix} \tau & 0 & \sqrt{1-\tau^2} & 0 \\ 0 & \tau & 0 & \sqrt{1-\tau^2} \\ -\sqrt{1-\tau^2} & 0 & \tau & 0 \\ 0 & -\sqrt{1-\tau^2} & 0 & \tau \end{pmatrix} \tag{D.2}$$

We thus apply the three-way splitter transformation sandwiched between a basis change transformation that mixes rb and $rb_\perp$ (we may disregard mixing of unheralded modes, since they are not detected). The basis change is a beamsplitter transformation with transmission given by mode overlap equal:

$$\tau = \int \mathrm{d}K_x \mathrm{d}K_y u_\perp(K_x, K_y) u^*_\perp(K_x + \Delta K_x, K_y + \Delta K_y) \tag{D.3}$$

(in our case $\Delta K_y = 0$). The results is a Gaussian function for our Gaussian-shaped modes. The total transformation, including initial two-mode squeezings, is:

$$\mathrm{Bs}(rb, rb_{\perp})^T \left(\mathrm{Tws}(vb, rb, ra, va) \otimes \mathrm{Tws}(vb_{\perp}, rb_{\perp}, ra_{\perp}, va_{\perp})\right) \\ \mathrm{Bs}(rb, rb_{\perp}) \left(\bigotimes_{i=1}^{8} \mathrm{Sq}(w_i, r_i)\right) \tag{D.4}$$

where the two-mode squeezing transformation is:

$$\mathrm{Sq}(w, r) = \begin{pmatrix} \frac{1}{\sqrt{1-p^2}} & 0 & 0 & \frac{p}{\sqrt{1-p^2}} \\ 0 & \frac{1}{\sqrt{1-p^2}} & \frac{p}{\sqrt{1-p^2}} & 0 \\ 0 & \frac{p}{\sqrt{1-p^2}} & \frac{1}{\sqrt{1-p^2}} & 0 \\ \frac{p}{\sqrt{1-p^2}} & 0 & 0 & \frac{1}{\sqrt{1-p^2}} \end{pmatrix} \tag{D.5}$$

with p being the fundamental pair generation probability, and subsequent rows correspond to operators $\hat{b}_r$, $\hat{b}_r^{\dagger}$, $\hat{b}_w$, $\hat{b}_w^{\dagger}$.

Finally, we obtain output modes rc and rd and calculate proper expectation values on vacuum, including influence of dark counts as p_{dark}/η (where η is the net detection efficiency) in the read-out modes (write photon modes contain several times more photons and thus the dark counts there are negligible). For instance, within this framework the correlation function $g^{(2)}_{rc,rd|wa,wb}$ is calculated with the help of Mathematica:

$$\begin{aligned} g^{(2)}_{rc,rd|wa,wb} = {} & (\langle \hat{n}_{rc}\hat{n}_{rd}\hat{n}_{wa}\hat{n}_{wb}\rangle + p_{\mathrm{dark}}/\eta \langle \hat{n}_{rc}\hat{n}_{wa}\hat{n}_{wb}\rangle + \\ & p_{\mathrm{dark}}/\eta \langle \hat{n}_{rd}\hat{n}_{wa}\hat{n}_{wb}\rangle + (p_{\mathrm{dark}}/\eta)^2 \langle \hat{n}_{wa}\hat{n}_{wb}\rangle)\langle \hat{n}_{wa}\hat{n}_{wb}\rangle / \\ & (\langle \hat{n}_{rc}\hat{n}_{wa}\hat{n}_{wb}\rangle + p_{\mathrm{dark}}/\eta \langle \hat{n}_{wa}\hat{n}_{wb}\rangle) \\ & (\langle \hat{n}_{rd}\hat{n}_{wa}\hat{n}_{wb}\rangle + p_{\mathrm{dark}}/\eta \langle \hat{n}_{wa}\hat{n}_{wb}\rangle) = \\ = {} & \eta^2 \left(9p^2 + 6p\left(\tau^2 + 1\right) + \left(\tau^2 - 1\right)^2\right) - \\ & 6\eta p_{\mathrm{dark}} \left(3p^2 + p\left(\tau^2 - 2\right) - \tau^2 - 1\right) + 9(p-1)^2 p_{\mathrm{dark}}^2 \\ & / \left(\eta\left(3p + \tau^2 + 1\right) - 3(p-1)p_{\mathrm{dark}}\right)^2 . \end{aligned} \tag{D.6}$$

Analogous expressions are obtained for all other correlation functions using a computer algebra system. We obtain a very good agreement with experimental observations in all cases by setting $p = 0.05$ and $p_{\mathrm{dark}}/\eta = 0.017$.

Appendix E

XMDS2 code

The code here is a very simple simulation in the XMDS2 package [DHJ13] that implements a two-pulse FIFO storage. The exact equations solved are expressed similarly as in Ref. [Maz18]. The code published in the thesis of *M. Hosseini* [Hos12] served as a basis for this simulation.

```
<?xml version="1.0" encoding="UTF-8"?>
<simulation xmds-version="2">
<name>CSWPSOP</name>
<author> M.Parniak </author>
<description>
Three level atom + acstark mod + acstark shift
FIFO storage
</description>
<features>
<benchmark/>
<error_check/>
<bing/>
<fftw plan="patient"/>
<globals>
<![CDATA[

const real samplelength = 1; //cm

const real time_input1 = 2.851;
const real time_input2 = 4.252;

const real time_signal_input1 = 2.851;
const real time_signal_input2 = 4.252;


const real time_output1 = 5.87;
const real time_output2 = 7.52;
```

```
const real sigma = 0.135;

const real sigma1 = 0.14;
const real sigma2 = 0.095;
const real sigma3 = 0.14;
const real sigma4 = 0.14;

const real sigmasig1 = 0.13;
const real sigmasig2 = 0.11;

const real inp_hgt1 = 0.0;
const real inp_hgt2 = 0.01;

const real timeswitch1 = 3.15;
const real timeswitch2 = 3.97;

const real timeswitch3 = 4.65;
const real timeswitch4 = 5.47;

const real timeswitch5 = 6.3;
const real timeswitch6 = 7.12;

const real sa = 0.1; // atoms width
const real g = 230 / (sa*sqrt(3.1415926));
const real Delta = 6.28318*18;
const real delta = 6.28318*0;
const real OmegaAmp = 6.28318*8.2;
const real Gammac = 6.28318*5.9;
const real gammac = 6.28318*0.01;
const real chartime = 0.014;

const real K = 200/6.28;
const real fi=6.85;

]]>
</globals>
</features>

<geometry>
<propagation_dimension>t</propagation_dimension>

<transverse_dimensions>
```

```
<dimension name="z" lattice="200" domain="(0,1)"/>
</transverse_dimensions>
</geometry>

<vector name="main" initial_space="z" type="complex">
<components> rho12 </components>
<initialisation>
<![CDATA[
rho12 = 0;
]]>
</initialisation>
</vector>

<vector name="cross1" initial_space="z" type="complex">
<components>
E
</components>
</vector>

<computed_vector type="complex" name="drive" dimensions="">
<components>Omega</components>
  <evaluation>
          <![CDATA[
            complex om1 = OmegaAmp*0.25*
            (1+tanh((t-(time_input1-sigma1))/chartime))*
            (1+tanh((-t+(time_input1+sigma1))/chartime));
            complex om2 = OmegaAmp*0.25*
            (1+tanh((t-(time_input2-sigma2))/chartime))*
            (1+tanh((-t+(time_input2+sigma2))/chartime));
            complex om3 = OmegaAmp*0.25*
            (1+tanh((t-(time_output1-sigma3))/chartime))*
            (1+tanh((-t+(time_output1+sigma3))/chartime));
            complex om4 = OmegaAmp*0.25*
            (1+tanh((t-(time_output2-sigma4))/chartime))*
            (1+tanh((-t+(time_output2+sigma4))/chartime));

            Omega = om1+om2+om3+om4;
            ]]>
  </evaluation>
</computed_vector>
```

```
<sequence>
<integrate algorithm="ARK89" interval="10"
 steps="1600" tolerance="1.0e0">
<samples>1600 1600</samples>
<operators>
    <operator kind="cross_propagation" algorithm="RK4"
     propagation_dimension="z">
        <integration_vectors>cross1</integration_vectors>
        <dependencies>main drive</dependencies>
        <boundary_condition kind="left">
        <![CDATA[
                complex E1 = inp_hgt1*0.25*
                (1+tanh((t-(time_signal_input1-sigmasig1))
                /chartime))*
                (1+tanh((-t+(time_signal_input1+sigmasig1))
                /chartime));
                complex E2 = inp_hgt2*0.25*
                (1+tanh((t-(time_signal_input2-sigmasig2))
                /chartime))*
                (1+tanh((-t+(time_signal_input2+sigmasig2))
                /chartime));
                E = E1+E2;
        ]]>
        </boundary_condition>
        <![CDATA[
            dE_dz = - i * g * (conj(rho12) * Omega + E)
            /(2*Delta+i*Gammac) * exp(-(z-0.5)*(z-0.5)/(sa*sa));
        ]]>
    </operator>

<integration_vectors>main</integration_vectors >
<dependencies>drive</dependencies>
<![CDATA[
real dp = .12;
real triangle = abs(2*(K*z-floor(K*z+0.5)));
complex swa = triangle*
(t < timeswitch2 & t>timeswitch1 ? (1.0+i*dp):0.0);
complex swb = triangle*
(t < timeswitch4 & t>timeswitch3 ? -(1.0-i*dp):0.0);
complex swc = triangle*
(t < timeswitch6 & t>timeswitch5 ? (1.0+i*dp):0.0);
complex sw=(swa+swb+swc);
```

```
drho12_dt = (0.5*i*Omega*conj(E))/(2*Delta - i*Gammac) +
 (-4*i*delta*Delta*rho12 - 2*Delta*gammac*rho12 -
  2*delta*Gammac*rho12 + gammac*Gammac*i*rho12
  + i*Omega*rho12*Omega)/(2*(2*Delta - i*Gammac))
 + i*fi*sw*rho12;
]]>
</operators>
</integrate>
</sequence>
<output format="binary" filename="fifo.xsil">
<group>
<sampling basis="z(200)" initial_sample="yes">
<moments> alpreal12 alpimag12 </moments>
<dependencies> main </dependencies>
<![CDATA[
alpreal12 = (rho12).Re();
alpimag12 = (rho12).Im();
]]>
</sampling>
</group>
<group>
<sampling basis="z(200)" initial_sample="no">
<moments> probereal probeimag ctrlr ctrli </moments>
<dependencies> cross1 </dependencies>
<![CDATA[
probereal = E.Re();
probeimag = E.Im();

]]>
</sampling>
</group>
</output>
</simulation>
```

Appendix F

Photonic-triplet inequality

In Ref. [Din15] *Ding et al.* tried to derive an inequality analogous to the well-known Cauchy-Schwarz inequality for the case of three modes and for the third-order correlation function[1]. The arrived at the following inequality, allegedly satisfied for all classical states:

$$[g^{(3)}_{abc}]^2 \leq g^{(2)}_{aa} g^{(2)}_{bb} g^{(2)}_{cc}. \tag{F.1}$$

The known results is that for a pair of modes characterized by annihilation operators, $\hat{a}$ and $\hat{b}$, all classical states satisfy the Cauchy-Schwarz inequality (Eq. 2.32):

$$[g^{(2)}_{ab}]^2 \leq g^{(2)}_{aa} g^{(2)}_{bb}, \tag{F.2}$$

where by $\langle . \rangle$ we denote an expectation value on a considered quantum state of light and

$$g^{(2)}_{aa} = \frac{\langle \hat{a}^\dagger \hat{a}^\dagger \hat{a} \hat{a} \rangle}{\langle \hat{a}^\dagger \hat{a} \rangle^2} \tag{F.3}$$

is the autocorrelation function.

Let us now consider three modes of an optical field characterized by their respective annihilation operator: $\hat{a}$, $\hat{b}$ and $\hat{c}$. The three-mode correlation between these modes is well characterized by a third order correlation function:

$$g^{(3)}_{abc} = \frac{\langle \hat{a}^\dagger \hat{a} \hat{b}^\dagger \hat{b} \hat{c}^\dagger \hat{c} \rangle}{\langle \hat{a}^\dagger \hat{a} \rangle \langle \hat{b}^\dagger \hat{b} \rangle \langle \hat{c}^\dagger \hat{c} \rangle}. \tag{F.4}$$

The value of this function counts the number of triple photon counting events normalized to statistically random events.

In Ref. [Din15] the authors claim that the violation of inequality F.1 should

---

[1] We have discovered this inequality with Mateusz. I have proposed an alternative, correct inequality and disproven the inequality from [Din15] by providing the example. Mateusz identified the error in the proof of *Ding et al.*

certify nonclassical correlation. Here we show that this inequality is violated by a classical state. Let us consider a single-mode thermal state directed onto a three-way equal-amplitude splitter into modes $\hat{a}$, $\hat{b}$ and $\hat{c}$. Following the Glauber-Sudarshan P-representation we may write its density matrix as:

$$\hat{\rho}_{abc} = \int \mathrm{d}^2\alpha \frac{1}{\pi\bar{n}} \exp(-|\alpha|^2/\bar{n}) |\frac{\alpha}{\sqrt{3}}, \frac{\alpha}{\sqrt{3}}, \frac{\alpha}{\sqrt{3}}\rangle\langle\frac{\alpha}{\sqrt{3}}, \frac{\alpha}{\sqrt{3}}, \frac{\alpha}{\sqrt{3}}| = \\ = \int \mathrm{d}^2\alpha \mathrm{d}^2\beta \mathrm{d}^2\gamma P(\alpha,\beta,\gamma)|\alpha,\beta,\gamma\rangle\langle\alpha,\beta,\gamma| \quad \text{(F.5)}$$

with the following P-function:

$$P(\alpha,\beta,\gamma) = \frac{3}{\pi\bar{n}} \exp(-3|\alpha|^2/\bar{n})\delta(\alpha-\beta)\delta(\alpha-\gamma), \quad \text{(F.6)}$$

where $\bar{n}$ is the mean number of photons incident on the three-way splitter. For such state, the value of third-order cross-correlation will be equal to the value of auto-correlation of the state impinging on the three-way splitter, which we may strictly calculate using the optical equivalence theorem and Eq. F.6 as the distribution:

$$g^{(3)}_{abc} = \frac{\int \mathrm{d}^2\alpha |\alpha|^6 \frac{3}{\pi\bar{n}} \exp(-3|\alpha|^2/\bar{n})}{(\bar{n}/3)^3} = 6. \quad \text{(F.7)}$$

Each of the modes a, b and c contains also a single-mode thermal state, thus $g^{(2)}_{aa} = g^{(2)}_{bb} = g^{(2)}_{cc} = 2$. Consequently, the LHS of Eq. F.1 equals 36, while the RHS is only 8; the inequality is thus not satisfied even though the thermal state is clearly classical.

The error in the proof of inequality F.1 given in the Supplementary Material of Ref. [Din15] lies in the transition from Eq. (S3) to Eq. (S4) therein. Even though Eq. (S3) is correct, it does not imply Eq. (S4), as the transition from summations to averages requires division by the number of samples in each product sum. The products however contain two sums on the LHS, and three sums on the RHS. The number of samples thus cannot be factored out, and Eq. (S4) is incorrect.

In Ref. [Din15] the authors obtained a high value of third-order cross-correlation function $g^{(3)}_{abc} = 11.03 \pm 1.95$. This clearly suggests, along with strong temporal correlation and low values of second-order auto-correlation functions, the presence of true nonclassical photonic triplets. However, no correct inequality is violated, the actual nonclassicality remains to be determined since classical highly-fluctuating states can in principle achieve arbitrarily high values of $g^{(3)}_{abc}$.

Bibliography

[Afz09] M. Afzelius, C. Simon, H. De Riedmatten and N. Gisin, 'Multimode quantum memory based on atomic frequency combs', Phys. Rev. A **79**, 052329 (2009).

[Alb16] B. Albrecht, Y. Meng, C. Clausen, A. Dareau, P. Schneeweiss and A. Rauschenbeutel, 'Fictitious magnetic-field gradients in optical microtraps as an experimental tool for interrogating and manipulating cold atoms', Phys. Rev. A **94**, 061401 (2016).

[Alb15] B. Albrecht, P. Farrera, G. Heinze, M. Cristiani and H. de Riedmatten, 'Controlled Rephasing of Single Collective Spin Excitations in a Cold Atomic Quantum Memory', Phys. Rev. Lett. **115**, 160501 (2015).

[And14] G. Andersen, P. Gelsinger-Austin, R. Gaddipati, P. Gaddipati and F. Ghebremichael, 'Fast, compact, autonomous holographic adaptive optics', Opt. Express **22**, 9432 (2014).

[ABR10] M. Auzinsh, D. Budker and S. Rochester, *Optically polarized atoms : understanding light-atom interactions* (Oxford University Press, 2010).

[Aws18] D. D. Awschalom, R. Hanson, J. Wrachtrup and B. B. Zhou, 'Quantum technologies with optically interfaced solid-state spins', Nat. Photonics **12**, 516–527 (2018).

[BZL03] M. Bajcsy, A. S. Zibrov and M. D. Lukin, 'Stationary pulses of light in an atomic medium', Nature **426**, 638–641 (2003).

[Bec13] F. E. Becerra, J. Fan, G. Baumgartner, J. Goldhar, J. T. Kosloski and A. Migdall, 'Experimental demonstration of a receiver beating the standard quantum limit for multiple nonorthogonal state discrimination', Nat. Photonics **7**, 147 (2013).

[Bec08] F. E. Becerra, R. T. Willis, S. L. Rolston and L. A. Orozco, 'Nondegenerate four-wave mixing in rubidium vapor: The diamond configuration', Phys. Rev. A **78**, 013834 (2008).

[Beh13] N. Behbood, F. Martin Ciurana, G. Colangelo, M. Napolitano, M. W. Mitchell and R. J. Sewell, 'Real-time vector field tracking with a cold-atom magnetometer', Appl. Phys. Lett. **102**, 173504 (2013).

[BB05] I. Bialynicki-Birula, ‘Photon wave function’, Prog. Opt. **36**, 245–294 (2005).

[Boy08] V. Boyer, A. M. Marino, R. C. Pooser and P. D. Lett, ‘Entangled Images from Four-Wave Mixing’, Science **321**, 544–547 (2008).

[BYL18] B. B. Brandt, C. Yannouleas and U. Landman, ‘Interatomic interaction effects on second-order momentum correlations and Hong-Ou-Mandel interference of double-well-trapped ultracold fermionic atoms’, Phys. Rev. A **97**, 053601 (2018).

[BGR10] G. Brida, M. Genovese and I. Ruo Berchera, ‘Experimental realization of sub-shot-noise quantum imaging’, Nat. Photonics **4**, 227–230 (2010).

[Bro08] M. Brouard, E. K. Campbell, A. J. Johnsen, C. Vallance, W. H. Yuen and A. Nomerotski, ‘Velocity map imaging in time of flight mass spectrometry’, Rev. Sci. Instrum. **79**, 123115 (2008).

[Bus17] H. Busche, P. Huillery, S. W. Ball, T. Ilieva, M. P. A. Jones and C. S. Adams, ‘Contactless nonlinear optics mediated by long-range Rydberg interactions’, Nat. Phys. **13**, 655 (2017).

[Cai17] Y. Cai, J. Roslund, G. Ferrini, F. Arzani, X. Xu, C. Fabre and N. Treps, ‘Multimode entanglement in reconfigurable graph states using optical frequency combs’, Nat. Commun. **8**, 15645 (2017).

[Cam12] G Campbell, M Hosseini, B. M. Sparkes, P. K. Lam and B. C. Buchler, ‘Time- and frequency-domain polariton interference’, New J. Phys. **14**, 033022 (2012).

[Cam14] G. Campbell, O. Pinel, M. Hosseini, T. Ralph, B. Buchler and P. Lam, ‘Configurable Unitary Transformations and Linear Logic Gates Using Quantum Memories’, Phys. Rev. Lett. **113**, 063601 (2014).

[Cer18] A. Cerè, B. Srivathsan, G. K. Gulati, B. Chng and C. Kurtsiefer, ‘Characterization of a photon-pair source based on a cold atomic ensemble using a cascade-level scheme’, Phys. Rev. A **98**, 023835 (2018).

[CH15] T. Chanelière and G. Hétet, ‘Light-shift-modulated photon-echo’, Opt. Lett. **40**, 1294 (2015).

[Che16] L. Chen, Z. Xu, W. Zeng, Y. Wen, S. Li and H. Wang, ‘Controllably releasing long-lived quantum memory for photonic polarization qubit into multiple spatially-separate photonic channels’, Sci. Rep. **6**, 33959 (2016).

[Che15] P. Chen, C. Shu, X. Guo, M. Loy and S. Du, ‘Measuring the Biphoton Temporal Wave Function with Polarization-Dependent and Time-Resolved Two-Photon Interference’, Phys. Rev. Lett. **114**, 010401 (2015).

[Che06] S. Chen, Y.-A. Chen, T. Strassel, Z.-S. Yuan, B. Zhao, J. Schmiedmayer and J.-W. Pan, 'Deterministic and Storable Single-Photon Source Based on a Quantum Memory', Phys. Rev. Lett. **97**, 173004 (2006).

[Che07] Z.-B. Chen, B. Zhao, Y.-A. Chen, J. Schmiedmayer and J.-W. Pan, 'Fault-tolerant quantum repeater with atomic ensembles and linear optics', Phys. Rev. A **76**, 022329 (2007).

[Cho16] Y.-W. W. Cho, G. T. Campbell, J. L. Everett, J. Bernu, D. B. Higginbottom, M. T. Cao, J. Geng, N. P. Robins, P. K. Lam and B. C. Buchler, 'Highly efficient optical quantum memory with long coherence time in cold atoms', Optica **3**, 100–107 (2016).

[Cho11] K. S. Choi, 'Coherent control of entanglement with atomic ensembles', PhD thesis (California Institute of Technology, 2011).

[Chr16a] R. Chrapkiewicz, 'Generation and characterization of spatially structured few-photon states of light', PhD thesis (University of Warsaw, 2016).

[CW12] R. Chrapkiewicz and W. Wasilewski, 'Generation and delayed retrieval of spatially multimode raman scattering in warm rubidium vapors', Opt. Express **20**, 29540–29552 (2012).

[CDW17] R. Chrapkiewicz, M. Dąbrowski and W. Wasilewski, 'High-Capacity Angularly Multiplexed Holographic Memory Operating at the Single-Photon Level', Phys. Rev. Lett. **118**, 063603 (2017).

[CWB14] R. Chrapkiewicz, W. Wasilewski and K. Banaszek, 'High-fidelity spatially resolved multiphoton counting for quantum imaging applications.', Opt. Lett. **39**, 5090–5093 (2014).

[Chr16b] R. Chrapkiewicz, M. Jachura, K. Banaszek and W. Wasilewski, 'Hologram of a single photon', Nat. Photonics **10**, 576–579 (2016).

[Cla10] C. Clausen, I. Usmani, F. Bussieres, N. Sangouard, M. Afzelius, H. de Riedmatten and N. Gisin, 'Quantum Storage of Photonic Entanglement in a Crystal', Nature **469**, 508–511 (2010).

[CTDR72] C. Cohen-Tannoudji and J. Dupont-Roc, 'Experimental Study of Zeeman Light Shifts in Weak Magnetic Fields', Phys. Rev. A **5**, 968–984 (1972).

[Col13a] G. Colangelo, R. J. Sewell, N. Behbood, F. M. Ciurana, G. Triginer and M. W. Mitchell, 'Quantum atom–light interfaces in the Gaussian description for spin-1 systems', New J. Phys. **15**, 103007 (2013).

[Col13b] M. Collins, C. Xiong, I. Rey, T. Vo, J. He, S. Shahnia, C. Reardon, T. Krauss, M. Steel, A. Clark and B. Eggleton, 'Integrated spatial multiplexing of heralded single-photon sources', Nat. Commun. **4**, 3413–3415 (2013).

[Col07] O. A. Collins, S. D. Jenkins, A Kuzmich and T. A. B. Kennedy, 'Multiplexed memory-insensitive quantum repeaters.', Phys. Rev. Lett. **98**, 060502 (2007).

[Cou11] A. Couairon, E. Brambilla, T. Corti, D. Majus, O. de J. Ramírez-Góngora and M. Kolesik, 'Practitioner's guide to laser pulse propagation models and simulation', Eur. Phys. J. Spec. Top. **199**, 5–76 (2011).

[CJDD17] J. Czajkowski, M. Jarzyna and R. Demkowicz-Dobrzański, 'Superadditivity in communication of classical information through quantum channels from a quantum parameter estimation perspective', New J. Phys. **19**, 073034 (2017).

[Dai12] H.-N. Dai, H. Zhang, S.-J. Yang, T.-M. Zhao, J. Rui, Y.-J. Deng, L. Li, N.-L. Liu, S. Chen, X.-H. Bao, X.-M. Jin, B. Zhao and J.-W. Pan, 'Holographic storage of biphoton entanglement.', Phys. Rev. Lett. **108**, 210501 (2012).

[Dąb18] M. Dąbrowski, M. Mazelanik, M. Parniak, A. Leszczyński, M. Lipka and W. Wasilewski, 'Certification of high-dimensional entanglement and Einstein-Podolsky-Rosen steering with cold atomic quantum memory', Phys. Rev. A **98**, 42126 (2018).

[DPW17] M. Dąbrowski, M. Parniak and W. Wasilewski, 'Einstein-Podolsky-Rosen paradox in a hybrid bipartite system', Optica **4**, 272–275 (2017).

[DCW14] M. Dąbrowski, R. Chrapkiewicz and W. Wasilewski, 'Hamiltonian design in readout from room-temperature Raman atomic memory', Opt. Express **22**, 26076 (2014).

[DeR03] H. De Riedmatten, I. Marcikic, W. Tittel, H. Zbinden and N. Gisin, 'Quantum interference with photon pairs created in spatially separated sources', Phys. Rev. A **67**, 022301 (2003).

[DSK13] A. B. Deb, B. J. Sawyer and N. Kjærgaard, 'Dispersive probing of driven pseudospin dynamics in a gradient field', Phys. Rev. A **88**, 063607 (2013).

[DDJK15] R. Demkowicz-Dobrzański, M. Jarzyna and J. Kołodyński, 'Quantum Limits in Optical Interferometry', Prog. Opt. **60**, 345 (2015).

[DHJ13] G. R. Dennis, J. J. Hope and M. T. Johnsson, 'XMDS2: Fast, scalable simulation of coupled stochastic partial differential equations', Comput. Phys. Commun. **184**, 201 (2013).

[DG91] I. H. Deutsch and J. C. Garrison, 'Paraxial quantum propagation', Phys. Rev. A **43**, 2498–2513 (1991).

[Din16] D. S. Ding, K. Wang, W. Zhang, S. Shi, M. X. Dong, Y. C. Yu, Z. Y. Zhou, B. S. Shi and G. C. Guo, 'Entanglement between low- and high-lying atomic spin waves', Phys. Rev. A **94**, 052326 (2016).

[Din15] D.-S. Ding, W. Zhang, S. Shi, Z.-Y. Zhou, Y. Li, B.-S. Shi and G.-C. Guo, 'Hybrid-cascaded generation of tripartite telecom photons using an atomic ensemble and a nonlinear waveguide', Optica **2**, 642 (2015).

[Din13] D.-S. Ding, Z.-Y. Zhou, B.-S. Shi, G.-C. Guo and S. E. Harris, 'Single-photon-level quantum image memory based on cold atomic ensembles', Nat. Commun. **4**, 183601 (2013).

[Dis16] E. Distante, A. Padrón-Brito, M. Cristiani, D. Paredes-Barato and H. de Riedmatten, 'Storage Enhanced Nonlinearities in a Cold Atomic Rydberg Ensemble', Phys. Rev. Lett. **117**, 113001 (2016).

[Dis17] E. Distante, P. Farrera, A. Padrón-Brito, D. Paredes-Barato, G. Heinze and H. de Riedmatten, 'Storing single photons emitted by a quantum memory on a highly excited Rydberg state', Nat. Commun. **8**, 14072 (2017).

[Dua01] L.-M. M. Duan, M. D. Lukin, J. I. Cirac, P. Zoller, I. Cirac, P. Zoller, J. I. Cirac and P. Zoller, 'Long-distance quantum communication with atomic ensembles and linear optics.', Nature **414**, 413–418 (2001).

[Dud10] Y. O. Dudin, A. G. Radnaev, R. Zhao, J. Z. Blumoff, T. A. B. Kennedy and A. Kuzmich, 'Entanglement of Light-Shift Compensated Atomic Spin Waves with Telecom Light', Phys. Rev. Lett. **105**, 260502 (2010).

[Ech08] S. de Echaniz, M. Koschorreck, M. Napolitano, M. Kubasik and M. W. Mitchell, 'Hamiltonian design in atom-light interactions with rubidium ensembles: A quantum-information toolbox', Phys. Rev. A **77**, 032316 (2008).

[Edg12] M. Edgar, D. Tasca, F. Izdebski, R. Warburton, J. Leach, M. Agnew, G. Buller, R. Boyd and M. Padgett, 'Imaging high-dimensional spatial entanglement with a camera', Nat. Commun. **3**, 984 (2012).

[EPR35] A. Einstein, B. Podolsky and N. Rosen, 'Can Quantum-Mechanical Description of Physical Reality Be Considered Complete?', Phys. Rev. **47**, 777–780 (1935).

[Eve16] J. L. Everett, G. T. Campbell, Y.-W. Cho, P. Vernaz-Gris, D. Higginbottom, O. Pinel, N. P. Robins, P. K. Lam and B. C. Buchler, 'Dynamical observations of self-stabilizing stationary light', Nat. Phys. **13**, 68 (2016).

[Fak14] J. S. Fakonas, H. Lee, Y. A. Kelaita and H. A. Atwater, 'Two-plasmon quantum interference', Nat. Photonics **8**, 317–320 (2014).

[Fic16] R. Fickler, G. Campbell, B. Buchler, P. K. Lam and A. Zeilinger, 'Quantum entanglement of angular momentum states with quantum numbers up to 10,010', Proc. Natl. Acad. Sci. **113**, 13642–13647 (2016).

[Fin18] R. Finkelstein, E. Poem, O. Michel, O. Lahad and O. Firstenberg, ‘Fast, noise-free memory for photon synchronization at room temperature’, Sci. Adv. **4**, eaap8598 (2018).

[FLN16] M. Fisher-Levine and A. Nomerotski, ‘TimepixCam: a fast optical imager with time-stamping’, J. Instrum. **11**, C03016–C03016 (2016).

[Gao18] Y. Y. Gao, B. J. Lester, Y. Zhang, C. Wang, S. Rosenblum, L. Frunzio, L. Jiang, S. Girvin and R. J. Schoelkopf, ‘Programmable Interference between Two Microwave Quantum Memories’, Phys. Rev. X **8**, 021073 (2018).

[Gen16] M. Genovese, ‘Real applications of quantum imaging’, J. Opt. **18**, 073002 (2016).

[GSM06] J. M. Geremia, J. K. Stockton and H. Mabuchi, ‘Tensor polarizability and dispersive quantum measurement of multilevel atoms’, Phys. Rev. A **73**, 1–14 (2006).

[Ger11] S. Gerlich, S. Eibenberger, M. Tomandl, S. Nimmrichter, K. Hornberger, P. J. Fagan, J. Tüxen, M. Mayor and M. Arndt, ‘Quantum interference of large organic molecules’, Nat. Commun. **2**, 263 (2011).

[Giu15] M. Giustina, M. A. Versteegh, S. Wengerowsky, J. Handsteiner, A. Hochrainer, K. Phelan, F. Steinlechner, J. Kofler, J.-Å. Larsson, C. Abellán, W. Amaya, V. Pruneri, M. W. Mitchell, J. Beyer, T. Gerrits, A. E. Lita, L. K. Shalm, S. W. Nam, T. Scheidl, R. Ursin, B. Wittmann and A. Zeilinger, ‘Significant-Loophole-Free Test of Bell’s Theorem with Entangled Photons’, Phys. Rev. Lett. **115**, 250401 (2015).

[GWT16] A. N. Glaudell, E Waks and J. M. Taylor, ‘Serialized quantum error correction protocol for high-bandwidth quantum repeaters’, New J. Phys. **18**, 93008 (2016).

[Gol14] N Goldman, G Juzeliūnas, P Öhberg and I. B. Spielman, ‘Light-induced gauge fields for ultracold atoms’, Reports Prog. Phys. **77**, 126401 (2014).

[GRE99] R. Grobe, K. Rzążewski and J. H. Eberly, ‘Measure of electron-electron correlation in atomic physics’, J. Phys. B **27**, L503–L508 (1999).

[GGZS12] A. Grodecka-Grad, E. Zeuthen and A. S. Sørensen, ‘High-capacity spatial multimode quantum memories based on atomic ensembles’, Phys. Rev. Lett. **109**, 133601 (2012).

[Guh11] S. Guha, ‘Structured Optical Receivers to Attain Superadditive Capacity and the Holevo Limit’, Phys. Rev. Lett. **106**, 240502 (2011).

[Gul16] M. Gullans, J. Thompson, Y. Wang, Q.-Y. Liang, V. Vuletić, M. Lukin and A. Gorshkov, ‘Effective Field Theory for Rydberg Polaritons’, Phys. Rev. Lett. **117**, 113601 (2016).

[Gün13] M. Gündoğan, M. Mazzera, P. M. Ledingham, M. Cristiani and H. de Riedmatten, 'Coherent storage of temporally multimode light using a spin-wave atomic frequency comb memory', New J. Phys. **15**, 045012 (2013).

[Gün15] M. Gündoğan, P. M. Ledingham, K. Kutluer, M. Mazzera and H. De Riedmatten, 'Solid State Spin-Wave Quantum Memory for Time-Bin Qubits', Phys. Rev. Lett. **114**, 230501 (2015).

[HAK11] M. A. Hall, J. B. Altepeter and P. Kumar, 'Ultrafast Switching of Photonic Entanglement', Phys. Rev. Lett. **106**, 053901 (2011).

[HBT56] R. Handbury Brown and R. Q. Twiss, 'Correlation between Photons in two Coherent Beams of Light', Nature **177**, 27–29 (1956).

[HKZ13] R. W. Heeres, L. P. Kouwenhoven and V. Zwiller, 'Quantum interference in plasmonic circuits', Nat. Nanotechnol. **8**, 719–722 (2013).

[HZ12] P. R. Hemmer and T. Zapata, 'The universal scaling laws that determine the achievable resolution in different schemes for super-resolution imaging', J. Opt. (United Kingdom) **14**, 083002 (2012).

[HGO15] G. Hétet and D. Guéry-Odelin, 'Spin wave diffraction control and readout with a quantum memory for light', New J. Phys. **17**, 073003 (2015).

[HP40] T. Holstein and H. Primakoff, 'Field Dependence of the Intrinsic Domain Magnetization of a Ferromagnet', Phys. Rev. **58**, 1098–1113 (1940).

[HOM87] C. K. Hong, Z. Y. Ou and L. Mandel, 'Measurement of subpicosecond time intervals between two photons by interference', Phys. Rev. Lett. **59**, 2044–2046 (1987).

[Hon17] S. Hong, R. Riedinger, I. Marinković, A. Wallucks, S. G. Hofer, R. A. Norte, M. Aspelmeyer and S. Gröblacher, 'Hanbury Brown and Twiss interferometry of single phonons from an optomechanical resonator.', Science **358**, 203–206 (2017).

[Hos11] M Hosseini, B. M. Sparkes, G Campbell, P. K. Lam and B. C. Buchler, 'High efficiency coherent optical memory with warm rubidium vapour', Nat. Commun. **2**, 174 (2011).

[Hos12] M. Hosseini, 'Quantum Optical Storage and Processing Using Raman Gradient Echo Memory', PhD thesis (Australian National University, 2012).

[Hos09] M. Hosseini, B. M. Sparkes, G. Hétet, J. J. Longdell, P. K. Lam and B. C. Buchler, 'Coherent optical pulse sequencer for quantum applications.', Nature **461**, 241–5 (2009).

[Hou18] Z. Hou, J.-F. Tang, J. Shang, H. Zhu, J. Li, Y. Yuan, K.-D. Wu, G.-Y. Xiang, C.-F. Li and G.-C. Guo, 'Deterministic realization of collective measurements via photonic quantum walks', Nat. Commun. **9**, 1414 (2018).

[Hüb10] H. Hübel, D. R. Hamel, A. Fedrizzi, S. Ramelow, K. J. Resch and T. Jennewein, 'Direct generation of photon triplets using cascaded photon-pair sources', Nature **466**, 601–603 (2010).

[Hum14] P. C. Humphreys, W. S. Kolthammer, J. Nunn, M. Barbieri, A. Datta and I. A. Walmsley, 'Continuous-variable quantum computing in optical time-frequency modes using quantum memories', Phys. Rev. Lett. **113**, 130502 (2014).

[Jac16] M. Jachura, R. Chrapkiewicz, R. Demkowicz-Dobrzański, W. Wasilewski and K. Banaszek, 'Mode engineering for realistic quantum-enhanced interferometry', Nat. Commun. **7**, 11411 (2016).

[JC15] M. Jachura and R. Chrapkiewicz, 'Shot-by-shot imaging of Hong-Ou-Mandel interference with an intensified sCMOS camera', Opt. Lett. **40**, 1540 (2015).

[JBB16] K. Jachymski, P. Bienias and H. P. Büchler, 'Three-Body Interaction of Rydberg Slow-Light Polaritons', Phys. Rev. Lett. **117**, 053601 (2016).

[Jar16] M. Jarzyna, V. Lipińska, A. Klimek, K. Banaszek and M. G. A. Paris, 'Phase noise in collective binary phase shift keying with Hadamard words', Opt. Express **24**, 1693 (2016).

[Jen17] H. H. Jen, 'Phase-imprinted multiphoton subradiant states', Phys. Rev. A **96**, 023814 (2017).

[Jen15] H. H. Jen, 'Superradiant cascade emissions in an atomic ensemble via four-wave mixing', Ann. Phys. (N. Y). **360**, 556–570 (2015).

[JC16] H. H. Jen and Y.-C. Chen, 'Spectral shaping of cascade emissions from multiplexed cold atomic ensembles', Phys. Rev. A **93**, 013811 (2016).

[JTL07] L. Jiang, J. M. Taylor and M. D. Lukin, 'Fast and robust approach to long-distance quantum communication with atomic ensembles', Phys. Rev. A **76**, 012301 (2007).

[Jia09] L. Jiang, J. M. Taylor, K. Nemoto, W. J. Munro, R. Van Meter and M. D. Lukin, 'Quantum repeater with encoding', Phys. Rev. A **79**, 032325 (2009).

[Jin13] J. Jin, J. A. Slater, E. Saglamyurek, N. Sinclair, M. George, R. Ricken, D. Oblak, W. Sohler and W. Tittel, 'Two-photon interference of weak coherent laser pulses recalled from separate solid-state quantum memories', Nat. Commun. **4**, 2386 (2013).

[Kac18] K. T. Kaczmarek, P. M. Ledingham, B. Brecht, S. E. Thomas, G. S. Thekkadath, O. Lazo-Arjona, J. H. D. Munns, E. Poem, A. Feizpour, D. J. Saunders, J. Nunn and I. A. Walmsley, 'High-speed noise-free optical quantum memory', Phys. Rev. A **97**, 042316 (2018).

[Kan17] F. Kaneda, J. Chapman, F. Xu, P. G. Kwiat, J. Chapman and P. G. Kwiat, 'Quantum-memory-assisted multi-photon generation for efficient quantum information processing', Optica **4**, 1034 (2017).

[Kan15] F. Kaneda, B. G. Christensen, J. J. Wong, H. S. Park, K. T. McCusker and P. G. Kwiat, 'Time-multiplexed heralded single-photon source', Optica **2**, 1010–1013 (2015).

[KD33] P. L. Kapitza and P. A. M. Dirac, 'The reflection of electrons from standing light waves', Math. Proc. Cambridge Philos. Soc. **29**, 297 (1933).

[Kau14] A. M. Kaufman, B. J. Lester, C. M. Reynolds, M. L. Wall, M Foss-Feig, K. R. A. Hazzard, A. M. Rey and C. A. Regal, 'Two-particle quantum interference in tunnel-coupled optical tweezers.', Science **345**, 306–9 (2014).

[Kel18] Kelly, Julian, *A Preview of Bristlecone, Google's New Quantum Processor*, 2018.

[Kli16] A. Klimek, M. Jachura, W. Wasilewski and K. Banaszek, 'Quantum memory receiver for superadditive communication using binary coherent states', J. Mod. Opt. **63**, 2074–2080 (2016).

[KLM01] E. Knill, R. Laflamme and G. J. Milburn, 'A scheme for efficient quantum computation with linear optics.', Nature **409**, 46–52 (2001).

[Kok07] P. Kok, W. J. Munro, K. Nemoto, T. C. Ralph, J. P. Dowling and G. J. Milburn, 'Linear optical quantum computing with photonic qubits', Rev. Mod. Phys. **79**, 135–174 (2007).

[Kon18] C. Kong, X. Wei, J. Kang, S. Tan, K. Tsia and K. K. Y. Wong, 'Ultrabroadband spatiotemporal sweeping device for high-speed optical imaging', Opt. Lett. **43**, 3546 (2018).

[Kos11] M. Koschorreck, M. Napolitano, B. Dubost and M. W. Mitchell, 'High resolution magnetic vector-field imaging with cold atomic ensembles', Appl. Phys. Lett. **98**, 1–4 (2011).

[Kra11] H. Krauter, C. A. Muschik, K. Jensen, W. Wasilewski, J. M. Petersen, J. I. Cirac and E. S. Polzik, 'Entanglement Generated by Dissipation and Steady State Entanglement of Two Macroscopic Objects', Phys. Rev. Lett. **107**, 080503 (2011).

[Kre14] M. Krenn, M. Huber, R. Fickler, R. Lapkiewicz, S. Ramelow and A. Zeilinger, ‘Generation and confirmation of a (100 x 100)-dimensional entangled quantum system’, Proc. Natl. Acad. Sci. **111**, 6243–6247 (2014).

[KSH17] A. S. Kuraptsev, I. M. Sokolov and M. D. Havey, ‘Angular distribution of single-photon superradiance in a dilute and cold atomic ensemble’, Phys. Rev. A **96**, 023830 (2017).

[KMR17] K. Kutluer, M. Mazzera and H. de Riedmatten, ‘Solid-State Source of Nonclassical Photon Pairs with Embedded Multimode Quantum Memory’, Phys. Rev. Lett. **118**, 210502 (2017).

[Lad10] T. D. Ladd, F. Jelezko, R. Laflamme, Y. Nakamura, C. Monroe, J. L. O’Brien and J. L. O’Brien, ‘Quantum computers’, Nature **464**, 45–53 (2010).

[Lan09] S.-Y. Lan, A. G. Radnaev, O. A. Collins, D. N. Matsukevich, T. A. Kennedy and A. Kuzmich, ‘A multiplexed quantum memory’, Opt. Express **17**, 13639–13645 (2009).

[Lap17] C. Laplane, P. Jobez, J. Etesse, N. Gisin and M. Afzelius, ‘Multimode and Long-Lived Quantum Correlations Between Photons and Spins in a Crystal’, Phys. Rev. Lett. **118**, 210501 (2017).

[LE04] C. K. Law and J. H. Eberly, ‘Analysis and interpretation of high transverse entanglement in optical parametric down conversion’, Phys. Rev. Lett. **92**, 127903–1 (2004).

[Lee14] M.-J. Lee, J. Ruseckas, C.-Y. Lee, V. Kudriašov, K.-F. Chang, H.-W. Cho, G. Juzelianas, I. A. Yu, G. Juzeliānas and I. A. Yu, ‘Experimental demonstration of spinor slow light’, Nat. Commun. **5**, 5542 (2014).

[Lee16] Y.-S. Lee, S. M. Lee, H. Kim and H. S. Moon, ‘Highly bright photon-pair generation in Doppler-broadened ladder-type atomic system’, Opt. Express **24**, 28083 (2016).

[Lee17] Y.-S. Lee, S. M. Lee, H. Kim and H. S. Moon, ‘Single-photon superradiant beating from a Doppler-broadened ladder-type atomic ensemble’, Phys. Rev. A **96**, 063832 (2017).

[LPW17a] A. Leszczyński, M. Parniak and W. Wasilewski, ‘Phase matching alters spatial multiphoton processes in dense atomic ensembles’, Opt. Express **25**, 284–295 (2017).

[Les18] A. Leszczyński, M. Mazelanik, M. Lipka, M. Parniak, M. Dąbrowski and W. Wasilewski, ‘Spatially resolved control of fictitious magnetic fields in a cold atomic ensemble’, Opt. Lett. **43**, 1147 (2018).

[Li16] J. Li, M.-T. Zhou, B. Jing, X.-J. Wang, S.-J. Yang, X. Jiang, K. Mølmer, X.-H. Bao and J.-W. Pan, 'Hong-Ou-Mandel Interference between Two Deterministic Collective Excitations in an Atomic Ensemble', Phys. Rev. Lett. **117**, 180501 (2016).

[Lin17] Z. Lin, X. Peng, W. Li, H. Wang and H. Guo, 'Magneto-optical double resonance driven by fictitious fields', Opt. Express **25**, 7668 (2017).

[LPW18] M. Lipka, M. Parniak and W. Wasilewski, 'Microchannel plate cross-talk mitigation for spatial autocorrelation measurements', Appl. Phys. Lett. **112** (2018).

[LPW17b] M. Lipka, M. Parniak and W. Wasilewski, 'Optical frequency locked loop for long-term stabilization of broad-line DFB laser frequency difference', Appl. Phys. B **123** (2017).

[Lop15] R Lopes, A Imanaliev, A Aspect, M Cheneau, D Boiron and C. I. Westbrook, 'Atomic Hong–Ou–Mandel experiment', Nature **520**, 66–68 (2015).

[Lu18] H. H. Lu, J. M. Lukens, N. A. Peters, O. D. Odele, D. E. Leaird, A. M. Weiner and P. Lougovski, 'Electro-Optic Frequency Beam Splitters and Tritters for High-Fidelity Photonic Quantum Information Processing', Phys. Rev. Lett. **120** (2018).

[Lun11] J. S. Lundeen, B. Sutherland, A. Patel, C. Stewart and C. Bamber, 'Direct measurement of the quantum wavefunction', Nature **474**, 188–191 (2011).

[Ma11] X. S. Ma, S. Zotter, J. Kofler, T. Jennewein and A. Zeilinger, 'Experimental generation of single photons via active multiplexing', Phys. Rev. A **83**, 043814 (2011).

[Mag15] M. F. Maghrebi, N. Y. Yao, M. Hafezi, T. Pohl, O. Firstenberg and A. V. Gorshkov, 'Fractional quantum Hall states of Rydberg polaritons', Phys. Rev. A **91**, 033838 (2015).

[Man66] L. Mandel, 'Configuration-space photon number operators in quantum optics', Phys. Rev. **144**, 1071–1077 (1966).

[Mar17] N. Maring, P. Farrera, K. Kutluer, M. Mazzera, G. Heinze and H. de Riedmatten, 'Photonic quantum state transfer between a cold atomic gas and a crystal', Nature **551**, 485–488 (2017).

[Mat16] J. C. Matthews, X.-Q. Zhou, H. Cable, P. J. Shadbolt, D. J. Saunders, G. A. Durkin, G. J. Pryde and J. L. O'Brien, 'Towards practical quantum metrology with photon counting', npj Quantum Inf. **2**, 16023 (2016).

[Maz18] M. Mazelanik, M. Parniak, A. Leszczyński, M. Lipka and W. Wasilewski, 'Coherent spin-wave processor of stored optical pulses', (2018).

[MDW16] M. Mazelanik, M. Dąbrowski and W. Wasilewski, ‘Correlation steering in the angularly multimode Raman atomic memory’, Opt. Express **24**, 21995–22003 (2016).

[Mir17] I. Mirgorodskiy, F. Christaller, C. Braun, A. Paris-Mandoki, C. Tresp and S. Hofferberth, ‘Electromagnetically induced transparency of ultra-long-range Rydberg molecules’, Phys. Rev. A **96**, 011402 (2017).

[Mit09] M. W. Mitchell, ‘Parametric down-conversion from a wave-equation approach: Geometry and absolute brightness’, Phys. Rev. A **79** (2009).

[Møl17] C. B. Møller, R. A. Thomas, G. Vasilakis, E. Zeuthen, Y. Tsaturyan, M. Balabas, K. Jensen, A. Schliesser, K. Hammerer and E. S. Polzik, ‘Quantum back-action-evading measurement of motion in a negative mass reference frame’, Nature **547**, 191–195 (2017).

[MDL14] P. A. Moreau, F. Devaux and E. Lantz, ‘Einstein-Podolsky-Rosen Paradox in Twin Images’, Phys. Rev. Lett. **113**, 160401 (2014).

[Mor09] T. Moriyasu, D. Nomoto, Y. Koyama, Y. Fukuda and T. Kohmoto, ‘Spin manipulation using the light-shift effect in rubidium atoms’, Phys. Rev. Lett. **103**, 1–4 (2009).

[Mun10] W. J. Munro, K. A. Harrison, A. M. Stephens, S. J. Devitt and K. Nemoto, ‘From quantum fusiliers to high-performance networks’, Nat. Photonics **4**, 792–796 (2010).

[Mur16] S. Muralidharan, L. Li, J. Kim, N. Lütkenhaus, M. D. Lukin and L. Jiang, ‘Optimal architectures for long distance quantum communication’, Sci. Rep. **6**, 20463 (2016).

[Mur14] S. Muralidharan, J. Kim, N. Lütkenhaus, M. D. Lukin and L. Jiang, ‘Ultrafast and Fault-Tolerant Quantum Communication across Long Distances’, Phys. Rev. Lett. **112**, 250501 (2014).

[NW49] T. D. Newton and E. P. Wigner, ‘Localized States for Elementary Systems’, Rev. Mod. Phys. **21**, 400–406 (1949).

[Nic13] A. Nicolas, L. Veissier, L. Giner, E. Giacobino, D. Maxein and J. Laurat, ‘A quantum memory for orbital angular momentum photonic qubits’, Nat. Photonics **8**, 234–238 (2013).

[Nun13] J. Nunn, N. K. Langford, W. S. Kolthammer, T. F. M. Champion, M. R. Sprague, P. S. Michelberger, X.-M. M. Jin, D. G. England and I. A. Walmsley, ‘Enhancing multiphoton rates with quantum memories’, Phys. Rev. Lett. **110**, 133601 (2013).

[Nun08] J. Nunn, ‘Quantum Memory in Atomic Ensembles’, PhD thesis (University of Oxford, 2008).

[OG18] L. Ortiz-Gutiérrez, L. Muñoz-Martínez, D. Barros, J. Morales, R. Moreira, N. Alves, A. Tieco, P. Saldanha and D. Felinto, 'Experimental Fock-State Superradiance', Phys. Rev. Lett. **120**, 083603 (2018).

[Pan18] X.-L. Pang, A.-L. Yang, J.-P. Dou, H. Li, C.-N. Zhang, E. Poem, D. J. Saunders, H. Tang, J. Nunn, I. A. Walmsley and X.-M. Jin, 'A Hybrid Quantum Memory Enabled Network at Room Temperature', (2018).

[Par15] V. Parigi, V. D'Ambrosio, C. Arnold, L. Marrucci, F. Sciarrino and J. Laurat, 'Storage and retrieval of vector beams of light in a multiple-degree-of-freedom quantum memory', Nat. Commun. **6**, 7706 (2015).

[Par01] C. Y. Park, H. Noh, C. M. Lee and D. Cho, 'Measurement of the Zeeman-like ac Stark shift', Phys. Rev. A. At. Mol. Opt. Phys. **63**, 325121–325127 (2001).

[Par02] C. Y. Park, J. Y. Kim, J. M. Song and D. Cho, 'Optical Stern-Gerlach effect from the Zeeman-like ac Stark shift', Phys. Rev. A **65**, 033410 (2002).

[PKM17] J. Park, H. Kim and H. S. Moon, 'Two-photon interferences of nondegenerate photon pairs from Doppler-broadened atomic ensemble', Opt. Express **25**, 32064 (2017).

[Par18a] K.-K. Park, Y.-W. Cho, Y.-T. Chough and Y.-H. Kim, 'Experimental Demonstration of Quantum Stationary Light Pulses in an Atomic Ensemble', Phys. Rev. X **8**, 021016 (2018).

[Par18b] M. Parniak, S. Borówka, K. Boroszko, W. Wasilewski, K. Banaszek and R. Demkowicz-Dobrzański, 'Beating the Rayleigh Limit Using Two-Photon Interference', Phys. Rev. Lett. **121**, 250503 (2018).

[PLW16a] M. Parniak, A. Leszczyński and W. Wasilewski, 'Coupling of four-wave mixing and Raman scattering by ground-state atomic coherence', Phys. Rev. A **93**, 053821 (2016).

[PW14] M. Parniak and W. Wasilewski, 'Direct observation of atomic diffusion in warm rubidium ensembles', Appl. Phys. B **116**, 415–421 (2014).

[PW15] M. Parniak and W. Wasilewski, 'Interference and nonlinear properties of four-wave-mixing resonances in thermal vapor: Analytical results and experimental verification', Phys. Rev. A **91**, 023418 (2015).

[PLW16b] M. Parniak, A. Leszczyński and W. Wasilewski, 'Magneto-optical polarization rotation in a ladder-type atomic system for tunable offset locking', Appl. Phys. Lett. **108**, 161103 (2016).

[Par18c] M. Parniak, M. Mazelanik, A. Leszczyński, M. Lipka, M. Dąbrowski and W. Wasilewski, 'Multidimensional quantum optics of spin waves through ac-Stark modulation', (2018).

[PPW16] M. Parniak, D. Pęcak and W. Wasilewski, 'Multimode Raman light-atom interface in warm atomic ensemble as multiple three-mode quantum operations', J. Mod. Opt. **63**, 2039 (2016).

[Par17] M. Parniak, M. Dabrowski, M. Mazelanik, A. Leszczyński, M. Lipka and W. Wasilewski, 'Wavevector multiplexed atomic quantum memory via spatially-resolved single-photon detection', Nat. Commun. **8**, 2140 (2017).

[Pet17] D. Petrosyan, F. Motzoi, M. Saffman and K. Mølmer, 'High-fidelity Rydberg quantum gate via a two-atom dark state', Phys. Rev. A **96**, 042306 (2017).

[Pey12] T. Peyronel, O. Firstenberg, Q.-Y. Liang, S. Hofferberth, A. V. Gorshkov, T. Pohl, M. D. Lukin, V. Vuleti, V. Vuletić, V. Vuleti and V. Vuletić, 'Quantum nonlinear optics with single photons enabled by strongly interacting atoms', Nature **488**, 57 (2012).

[Phi98] W. D. Phillips, 'Nobel Lecture: Laser cooling and trapping of neutral atoms', Rev. Mod. Phys. **70**, 721–741 (1998).

[Pu17] Y.-F. Pu, N. Jiang, W. Chang, H.-X. Yang, C. Li and L.-M. Duan, 'Experimental realization of a multiplexed quantum memory with 225 individually accessible memory cells', Nat. Commun. **8**, 15359 (2017).

[Qia16] P. Qian, Z. Gu, R. Cao, R. Wen, Z. Ou, J. Chen and W. Zhang, 'Temporal Purity and Quantum Interference of Single Photons from Two Independent Cold Atomic Ensembles', Phys. Rev. Lett. **117**, 013602 (2016).

[RZZK07] A. Raczynski, J. Zaremba and S. Zielinska-Kaniasty, 'Beam splitting and Hong-Ou-Mandel interference for stored light', Phys. Rev. A **75**, 013810 (2007).

[Rad10] A. G. Radnaev, Y. O. Dudin, R. Zhao, H. H. Jen, S. D. Jenkins, A. Kuzmich and T. A. B. Kennedy, 'A quantum memory with telecom-wavelength conversion', en, Nat. Phys. **6**, 894–899 (2010).

[Rei12] K. F. Reim, J. Nunn, X.-M. Jin, P. S. Michelberger, T. F. M. Champion, D. G. England, K. C. Lee, W. S. Kolthammer, N. K. Langford and I. A. Walmsley, 'Multipulse Addressing of a Raman Quantum Memory: Configurable Beam Splitting and Efficient Readout', Phys. Rev. Lett. **108**, 263602 (2012).

[Rei16] C. Reimer, M. Kues, P. Roztocki, B. Wetzel, F. Grazioso, B. E. Little, S. T. Chu, T. Johnston, Y. Bromberg, L. Caspani, D. J. Moss and R. Morandotti, 'Generation of multiphoton entangled quantum states by means of integrated frequency combs', Science **351**, 1176–1180 (2016).

[RFN13] D. J. Richardson, J. M. Fini and L. E. Nelson, ‘Space-division multiplexing in optical fibres’, Nat. Photonics **7**, 354–362 (2013).

[RB14] G. Römer and P Bechtold, ‘Electro-optic and Acousto-optic Laser Beam Scanners’, Phys. Procedia **56**, 29–39 (2014).

[Roo16] S. Roof, K. Kemp, M. Havey and I. Sokolov, ‘Observation of Single-Photon Superradiance and the Cooperative Lamb Shift in an Extended Sample of Cold Atoms’, Phys. Rev. Lett. **117**, 073003 (2016).

[RSM90] M. Rosatzin, D. Suter and J. Mlynek, ‘Light-shift-induced spin echoes in a $J = 1/2$ atomic ground state’, Phys. Rev. A **42**, 1839–1841 (1990).

[Ros13] J. Roslund, R. M. de Araújo, S. Jiang, C. Fabre and N. Treps, ‘Wavelength-multiplexed quantum networks with ultrafast frequency combs’, Nat. Photonics **8**, 109–112 (2013).

[Sag14] E Saglamyurek, N Sinclair, J. A. Slater, K Heshami, D Oblak and W Tittel, ‘An integrated processor for photonic quantum states using a broadband light–matter interface’, New J. Phys. **16**, 065019 (2014).

[Sch13] J. Schneeloch, P. B. Dixon, G. A. Howland, C. J. Broadbent and J. C. Howell, ‘Violation of Continuous-Variable Einstein-Podolsky-Rosen Steering with Discrete Measurements’, Phys. Rev. Lett. **110**, 130407 (2013).

[SLR14] P. Schneeweiss, F. Le Kien and A. Rauschenbeutel, ‘Nanofiber-based atom trap created by combining fictitious and real magnetic fields’, New J. Phys. **16** (2014).

[SDA10] C. Simon, H. De Riedmatten and M. Afzelius, ‘Temporally multiplexed quantum repeaters with atomic gases’, Phys. Rev. A **82**, 010304(R) (2010).

[Sim07] J. Simon, H. Tanji, S. Ghosh and V. Vuletić, ‘Single-photon bus connecting spin-wave quantum memories’, Nat. Phys. **3**, 765–769 (2007).

[Sin17] N. Sinclair, D. Oblak, C. Thiel, R. Cone and W. Tittel, ‘Properties of a Rare-Earth-Ion-Doped Waveguide at Sub-Kelvin Temperatures for Quantum Signal Processing’, Phys. Rev. Lett. **118**, 100504 (2017).

[Sin14] N. Sinclair, E. Saglamyurek, H. Mallahzadeh, J. A. Slater, M. George, R. Ricken, M. P. Hedges, D. Oblak, C. Simon, W. Sohler and W. Tittel, ‘Spectral Multiplexing for Scalable Quantum Photonics using an Atomic Frequency Comb Quantum Memory and Feed-Forward Control’, Phys. Rev. Lett. **113**, 053603 (2014).

[Sip95] J. E. Sipe, ‘Photon wave functions’, Phys. Rev. A **52**, 1875–1883 (1995).

[Smi11] A Smith, B. E. Anderson, S Chaudhury and P. S. Jessen, ‘Three-axis measurement and cancellation of background magnetic fields to less than 50 µG in a cold atom experiment’, J. Phys. B At. Mol. Opt. Phys. **44**, 205002 (2011).

[Son17] C. Song, K. Xu, W. Liu, C.-p. Yang, S.-B. Zheng, H. Deng, Q. Xie, K. Huang, Q. Guo, L. Zhang, P. Zhang, D. Xu, D. Zheng, X. Zhu, H. Wang, Y.-A. Chen, C.-Y. Lu, S. Han and J.-W. Pan, ‘10-Qubit Entanglement and Parallel Logic Operations with a Superconducting Circuit’, Phys. Rev. Lett. **119**, 180511 (2017).

[Spa10] B. M. Sparkes, M. Hosseini, G. Hétet, P. K. Lam and B. C. Buchler, ‘ac Stark gradient echo memory in cold atoms’, Phys. Rev. A **82**, 043847 (2010).

[Spa13] B. M. Sparkes, J Bernu, M Hosseini, J Geng, Q Glorieux, P. A. Altin, P. K. Lam, N. P. Robins and B. C. Buchler, ‘Gradient echo memory in an ultra-high optical depth cold atomic ensemble’, New J. Phys. **15**, 085027 (2013).

[Sri13] B. Srivathsan, G. K. Gulati, B. Chng, G. Maslennikov, D. Matsukevich and C. Kurtsiefer, ‘Narrow Band Source of Transform-Limited Photon Pairs via Four-Wave Mixing in a Cold Atomic Ensemble’, Phys. Rev. Lett. **111**, 123602 (2013).

[Sri14] B. Srivathsan, G. K. Gulati, A. Cerè, B. Chng and C. Kurtsiefer, ‘Reversing the Temporal Envelope of a Heralded Single Photon using a Cavity’, Phys. Rev. Lett. **113**, 163601 (2014).

[Su17] S.-W. Su, S.-C. Gou, L. Y. Chew, Y.-Y. Chang, I. A. Yu, A. Kalachev and W.-T. Liao, ‘Setting a disordered password on a photonic memory’, Phys. Rev. A **95**, 061805 (2017).

[Sun17] W.-M. Sun, Q. Huang, Z.-J. Huang, P.-W. Wang and J.-H. Zhang, ‘All-Optical Vector Cesium Magnetometer’, Chinese Phys. Lett. **34**, 058501 (2017).

[Sur08] K. Surmacz, J. Nunn, K. Reim, K. C. Lee, V. O. Lorenz, B. Sussman, I. A. Walmsley and D. Jaksch, ‘Efficient spatially resolved multimode quantum memory’, Phys. Rev. A **78**, 033806 (2008).

[Tan15] J.-S. Tang, Z.-Q. Zhou, Y.-T. Wang, Y.-L. Li, X. Liu, Y.-L. Hua, Y. Zou, S. Wang, D.-Y. He, G. Chen, Y.-N. Sun, Y. Yu, M.-F. Li, G.-W. Zha, H.-Q. Ni, Z.-C. Niu, C.-F. Li and G.-C. Guo, ‘Storage of multiple single-photon pulses emitted from a quantum dot in a solid-state quantum memory’, Nat. Commun. **6**, 8652 (2015).

[Tas11] D. S. Tasca, R. M. Gomes, F. Toscano, P. H. Souto Ribeiro and S. P. Walborn, 'Continuous-variable quantum computation with spatial degrees of freedom of photons', Phys. Rev. A **83**, 052325 (2011).

[Tir16] A. Tiranov, J. Lavoie, P. C. Strassmann, N. Sangouard, M. Afzelius, F. Bussières and N. Gisin, 'Demonstration of Light-Matter Micro-Macro Quantum Correlations', Phys. Rev. Lett. **116**, 190502 (2016).

[Toy15] K. Toyoda, R. Hiji, A. Noguchi and S. Urabe, 'Hong–Ou–Mandel interference of two phonons in trapped ions', Nature **527**, 74–77 (2015).

[Ven07] M Vengalattore, J. M. Higbie, S. R. Leslie, J Guzman, L. E. Sadler and D. M. Stamper-Kurn, 'High resolution magnetometry with a spinor Bose-Einstein condensate', Phys. Rev. Lett. **98**, 200801 (2007).

[VG18] P. Vernaz-Gris, K. Huang, M. Cao, A. S. Sheremet and J. Laurat, 'Highly-efficient quantum memory for polarization qubits in a spatially-multiplexed cold atomic ensemble', Nat. Commun. **9**, 363 (2018).

[Vur18] H. Vural, S. L. Portalupi, J. Maisch, S. Kern, J. H. Weber, M. Jetter, J. Wrachtrup, R. Löw, I. Gerhardt and P. Michler, 'Two-photon interference in an atom–quantum dot hybrid system', Optica **5**, 367 (2018).

[Wan11] H. Wang, S. Li, Z. Xu, X. Zhao, L. Zhang, J. Li, Y. Wu, C. Xie, K. Peng and M. Xiao, 'Quantum interference of stored dual-channel spin-wave excitations in a single tripod system', Phys. Rev. A **83**, 043815 (2011).

[Wan12] J. Wang, J.-Y. Yang, I. M. Fazal, N. Ahmed, Y. Yan, H. Huang, Y. Ren, Y. Yue, S. Dolinar, M. Tur and A. E. Willner, 'Terabit free-space data transmission employing orbital angular momentum multiplexing', Nat. Photonics **6**, 488–496 (2012).

[WKF07] W. Wasilewski, P. Kolenderski and R. Frankowski, 'Spectral Density Matrix of a Single Photon Measured', Phys. Rev. Lett. **99**, 123601 (2007).

[Wei11] R. Wei, B. Zhao, Y. Deng, Y.-A. Chen and J.-W. Pan, 'Deterministic spin-wave interferometer based on the Rydberg blockade', Phys. Rev. A **83**, 63623 (2011).

[Wil11] R. T. Willis, F. E. Becerra, L. A. Orozco and S. L. Rolston, 'Photon statistics and polarization correlations at telecommunications wavelengths from a warm atomic ensemble', Opt. Express **19**, 14632 (2011).

[Wol08] F. Wolfgramm, X. Xing, A. Cerè, A. Predojević, A. M. Steinberg and M. W. Mitchell, 'Bright filter-free source of indistinguishable photon pairs', Opt. Express **16**, 18145 (2008).

[Wol11] F. Wolfgramm, Y. A. de Icaza Astiz, F. A. Beduini, A. Cerè and M. W. Mitchell, 'Atom-Resonant Heralded Single Photons by Interaction-Free Measurement', Phys. Rev. Lett. **106**, 053602 (2011).

[Wol12] F. Wolfgramm, C. Vitelli, F. A. Beduini, N. Godbout and M. W. Mitchell, 'Entanglement-enhanced probing of a delicate material system', Nat. Photonics **7**, 28–32 (2012).

[Xie15] Z. Xie, T. Zhong, S. Shrestha, X. Xu, J. Liang, Y.-X. Gong, J. C. Bienfang, A. Restelli, J. H. Shapiro, F. N. C. Wong and C. Wei Wong, 'Harnessing high-dimensional hyperentanglement through a biphoton frequency comb', Nat. Photonics **9**, 536–542 (2015).

[Xio16] C. Xiong, X. Zhang, Z. Liu, M. J. Collins, A. Mahendra, L. G. Helt, M. J. Steel, D. Y. Choi, C. J. Chae, P. H. W. Leong and B. J. Eggleton, 'Active temporal multiplexing of indistinguishable heralded single photons', Nat. Commun. **7**, 10853 (2016).

[Yan18] T. S. Yang, Z. Q. Zhou, Y. L. Hua, X. Liu, Z. F. Li, P. Y. Li, Y. Ma, C. Liu, P. J. Liang, X. Li, Y. X. Xiao, J. Hu, C. F. Li and G. C. Guo, 'Multiplexed storage and real-time manipulation based on a multiple degree-of-freedom quantum memory', Nat. Commun. **9**, 3407 (2018).

[Zha12] S. Zhang, J. F. Chen, C. Liu, S. Zhou, M. M. T. Loy, G. K. L. Wong and S. Du, 'A dark-line two-dimensional magneto-optical trap of 85Rb atoms with high optical depth', Rev. Sci. Instrum. **83**, 073102 (2012).

[Zha14] X.-W. Zhang, A Kalachev, P Hemmer, M. O. Scully and O Kocharovskaya, 'Quantum memory based on phase matching control', Laser Phys. **24**, 094016 (2014).

[Zha09] B. Zhao, Y.-A. Chen, X.-H. Bao, T. Strassel, C.-S. Chuu, X.-M. Jin, J. Schmiedmayer, Z.-S. Yuan, S. Chen and J.-W. Pan, 'A millisecond quantum memory for scalable quantum networks', Nat. Phys. **5**, 95–99 (2009).

[Zha07] B. Zhao, Z.-B. Chen, Y.-A. Chen, J. Schmiedmayer and J.-W. Pan, 'Robust Creation of Entanglement between Remote Memory Qubits', Phys. Rev. Lett. **98**, 240502 (2007).

[ZSD16] L. Zhao, Y. Su and S. Du, 'Narrowband biphoton generation in the group delay regime', Phys. Rev. A **93**, 033815 (2016).

[Zhi14] E. Zhivun, A. Wickenbrock, B. Patton and D. Budker, 'Alkali-vapor magnetic resonance driven by fictitious radiofrequency fields', Appl. Phys. Lett. **105**, 192406 (2014).

[Zho18] H.-S. Zhong, Y. Li, W. Li, L.-C. Peng, Z.-E. Su, Y. Hu, Y.-M. He, X. Ding, W. Zhang, H. Li, L. Zhang, Z. Wang, L. You, X.-L. Wang, X. Jiang, L. Li, Y.-A. Chen, N.-L. Liu, C.-Y. Lu and J.-W. Pan, '12-Photon Entanglement and Scalable Scattershot Boson Sampling with Optimal Entangled-Photon Pairs from Parametric Down-Conversion', Phys. Rev. Lett. **121** (2018).

[Zie98] M. Zielonkowski, J. Steiger, U. Schünemann, M. DeKieviet and R. Grimm, 'Optically induced spin precession and echo in an atomic beam', Phys. Rev. A **58**, 3993–3998 (1998).

[Zop18] M. Zopf, T. Macha, R. Keil, E. Uruñuela, Y. Chen, W. Alt, L. Ratschbacher, F. Ding, D. Meschede and O. G. Schmidt, 'Frequency feedback for two-photon interference from separate quantum dots', Phys. Rev. B **98**, 161302 (2018).